DGK Veröffentlichungen der DGK

Ausschuss Geodäsie der Bayerischen Akademie der Wissenschaften

Reihe C Dissertationen Heft Nr. 803

Alexander Georg Horvath

Retrieving geophysical signals from current and future satellite gravity missions

München 2017

Verlag der Bayerischen Akademie der Wissenschaften

ISSN 0065-5325 ISBN 978-3-7696-5215-4

Veröffentlichungen der DGK

Ausschuss Geodäsie der Bayerischen Akademie der Wissenschaften

Reihe C | Dissertationen | Heft Nr. 803

Retrieving geophysical signals from current and future satellite gravity missions

Von der Ingenieurfakultät Bau Geo Umwelt
der Technischen Universität München
zur Erlangung des akademischen Grades eines
Doktor-Ingenieurs (Dr.-Ing.)
genehmigte Dissertation

Vorgelegt von

Alexander Georg Horvath

München 2017

Verlag der Bayerischen Akademie der Wissenschaften

ISSN 0065-5325 ISBN 978-3-7696-5215-4

Adresse der DGK:

Ausschuss Geodäsie der Bayerischen Akademie der Wissenschaften (DGK)

Alfons-Goppel-Straße 11 ● D – 80 539 München

Telefon +49 – 331 – 288 1685 ● Telefax +49 – 331 – 288 1759

E-Mail post@dgk.badw.de ● http://www.dgk.badw.de

Prüfungskommission

Vorsitzender:	Prof. Dr. Ir. W. T. de Vries
Prüfer der Dissertation:	1. Prof. Dr. techn. R. Pail 2. Prof. Dr.-Ing. M. Horwath (TU Dresden) 3. Prof. Dr.-Ing. N. Sneeuw (Universität Stuttgart)

Die Dissertation wurde am 07.12.2016 bei der Technischen Universität München eingereicht und durch die Ingenieurfakultät Bau Geo Umwelt am 19.04.2017 angenommen.

Diese Dissertation ist auf dem Server der Deutschen Geodätischen Kommission unter http://dgk.badw.de/ sowie auf dem Server der Technischen Universität München unter https://mediatum.ub.tum.de/?id=1332207 elektronisch publiziert.

ISSN 0065-5325 ISBN 978-3-7696-5215-4

INGENIEURFAKULTÄT
BAU GEO UMWELT

Retrieving geophysical signals from current and future satellite gravity missions

Dissertation
von

Alexander Georg Horvath

TECHNISCHE UNIVERSITÄT MÜNCHEN

Technische Universität München

Lehrstuhl für Astronomische und Physikalische Geodäsie

Retrieving geophysical signals from current and future satellite gravity missions

Alexander Georg Horvath

Vollständiger Abdruck der von der Ingenieurfakultät Bau Geo Umwelt der Technischen Universität München zur Erlangung des akademischen Grades eines

Doktor – Ingenieurs

genehmigten Dissertation.

Vorsitzender:		Prof. Dr. Ir. W. T. de Vries
Prüfer der Dissertation:	1.	Prof. Dr. techn. R. Pail
	2.	Prof. Dr.-Ing. M. Horwath, Technische Universität Dresden
	3.	Prof. Dr.-Ing. N. Sneeuw, Universität Stuttgart

Die Dissertation wurde am 07.12.2016 bei der Technischen Universität München eingereicht und durch die Ingenieurfakultät Bau Geo Umwelt am 19.04.2017 angenommen.

Kurzfassung

Die vorliegende Arbeit beschäftigt sich mit der Schätzung geophysikalischer Massensignale aus zeitvariablen Schwerefeldern basierend auf Satellitenbeobachtungen. Diese Beobachtungen stammen entweder von aktuellen Missionen wie GRACE, oder aber von simulierten zukünftigen Schwerefeldmissionen. Die Arbeit greift bestehende Filterverfahren auf und analysiert diese hinsichtlich ihrer Leistungsfähigkeit in einer eigens dafür aufgestellten Simulationswelt. Darauf aufbauend werden diese Verfahren gezielt weiterentwickelt und durch Ergänzungen verbessert. Dies ermöglicht es, Massensignale und deren Trends aus zeitvariablen Schwerefeldlösungen mit besserer räumlicher Auflösung bzw. kleineren Unsicherheiten zu schätzen. Dies ist von großer Bedeutung, da ein besseres Verständnis von Massenverlagerungsprozessen im System Erde, beispielsweise hervorgerufen durch Prozesse in Hydrologie oder Kryosphäre, entschieden dazu beiträgt, das Klima und seine Zusammenhänge besser zu verstehen.

In Kapitel 1 werden die untersuchten Missionstypen vorgestellt und ein Ausblick auf die in Kürze startende, sich bereits im Bau befindliche GRACE-FollowOn Mission gegeben. Zusätzlich wird ein aus Konzeptstudien abgeleitetes vielversprechendes zukünftiges Missionsszenario näher vorgestellt, für welches die Anwendbarkeit der untersuchten und entwickelten Filtermethoden geprüft wird.

Kapitel 2 führt die theoretischen Grundlagen zur Darstellung des Schwerefelds und wichtige Werkzeuge und Methoden zur Auswertung und Verarbeitung desselben ein. Dies sind insbesondere die Ausgleichsrechnung nach der Methode der kleinsten Quadrate, die Regularisierung nach Tikhonov und verschiedene Maßzahlen zur Bewertung von Schwerefeldlösungen in sphärisch harmonischer Reihendarstellung. Ein weiterer Aspekt ist die Einführung in die Thematik des durch Unterabtastung hervorgerufenen sogenannten zeitlichen Aliasing.

Die für die Bewertung und Entwicklung der untersuchten Filtermethoden aufgestellte Simulationswelt wird in Kapitel 3 näher erläutert. Hierbei wird insbesondere darauf eingegangen, auf welcher Grundlage die verschiedenen Testdatensätze generiert wurden und welche Eigenschaften diese besitzen. Diskutiert wird die Erstellung verschiedener Rauschzeitreihen zur Charakterisierung der auf den Satelliten verwendeten Sensoren als stochastische Größen. Zuschaltbare deterministische Störeinflüsse, hervorgerufen durch simulierte fehlerhafte Reduktion hochfrequenter Signalbestandteile aus Atmosphäre, Ozean und Ozeangezeiten werden ebenso erläutert wie die rauschfreien Bestandteile wie beispielsweise die verwendeten Satellitenorbits.

Kapitel 4 widmet sich daran anschließend der Bestimmung bzw. Schätzung geophysikalischer Signale aus zeitvariablen Schwerefeldlösungen. Das Kapitel gliedert sich in drei Unterbereiche, dessen erster die bestimmbaren geophysikalischen Signale einführt. Im zweiten werden die Verarbeitungsschritte, ausgehend von der ungefilterten Schwerefeldlösung hin zu Massenvariationen in einem bestimmten Zielgebiet beschrieben. Wichtige Parameter dabei sind der geeignete Entwicklungsgrad der verwendeten Schwerefeldlösung in sphärisch harmonischer Reihendarstellung, notwendige Korrekturgrößen um GRACE-Schwerefeldlösungen zu ergänzen (beispielsweise Terme des Grads 1 und der C_{20} Term) sowie der Umgang mit der spektralen Begrenztheit von endlichen Reihendarstellungen und deren Auswirkung auf zu bestimmende geophysikalische Signale. Ein weiterer betrachteter Parameter ist die Einführung geeigneter Flächenintegrale, welche zum Einen die Umstände der spektralen Begrenztheit der Reihendarstellung und zum Anderen die Korrelationsstrukturen der Fehler in den Lösungen im Ortsraum zur Ermittlung von Massensignalen in Zielgebieten berücksichtigen. Der dritte Unterbereich beinhaltet eine Diskussion und Bewertung aktueller Schwerefeldlösungen hinsichtlich ihrer Eignung zur Bestimmung geophysikalischer Massensignale. Darüber hinaus wird ein

Überblick über relevante und aktuell in der Literatur besprochene Filter- und Prozessierungsmethoden im Zusammenhang mit GRACE gegeben.

Die im Detail analysierten und erweiterten Filtermethoden werden in Kapitel 5 besprochen. Dabei wird insbesondere auf zwei Varianten des empirischen Dekorrelationsfilters nach Swenson & Wahr eingegangen. Es werden geeignete Filterparameter für verschiedene Anwendungsfälle, v.a. den Entwicklungsgrad der zu filternden Lösung untersucht und bewertet. Eines der Kernstücke der vorliegenden Arbeit, der zeitvariable Dekorrelationsfilter *VADER* (variable decorrelation), wird im weiteren Verlauf des Kapitels eingehend untersucht. Dabei wird insbesondere auf die einzelnen Bestandteile des Filters, die Signalvarianz und Fehlerkovarianz Augenmerk gerichtet. Ein wichtiger Aspekt bei der Anwendung von Filtern ist die Evaluierung der Signalverfälschung durch die Filteranwendung. Diese wird für den VADER-Filter eingehend analysiert. Das zweite Anwendungsbeispiel in Kapitel 7 liefert hierzu weitere aufschlussreiche Erkenntnisse. Zum Abschluss von Kapitel 5 wird eine Einordnung der gewonnen Erkenntnisse präsentiert sowie eine Empfehlung zur Filterung GRACE-artiger zeitvariable Schwerefeldlösungen ausgesprochen.

Die Bewertung der Übertrag- und Anwendbarkeit der in Kapitel 5 herausgearbeiteten Ergebnisse zu den untersuchten Filtermethoden auf zukünftige Missionsszenarien wird in Kapitel 6 vorgenommen. Dabei wird die Wirkungsweise sowohl auf Einzel- als auch auf Doppelpaarmissionsszenarien untersucht. Die Grundlage hierfür liefert eine eingehende Untersuchung der stochastischen Eigenschaften der aus zukünftigen Missionsszenarien gewonnenen Schwerefeldlösungen.

Kapitel 7 zeigt zwei Anwendungsbeispiele. Das erste Beispiel widmet sich der Bestimmung von Eismassenänderungen im Bereich der Antarktis und ihrer Teilgebiete. Hier werden ausgehend von den ungefilterten Lösungen beispielhaft alle notwendigen Korrekturen zur Ergänzung der Lösung angebracht, um dann die Zeitreihe von Schwerefeldlösungen mit dem aus Kapitel 5 entwickelten VADER-Filter zu filtern. Begleitet wird der Prozess von einer Schätzung zeitvariabler Fehlerbudgets für die Einzelmonate sowie eines Fehlermaßes für das geschätzte Massensignal im jeweiligen Zielgebiet. Das zweite Beispiel baut auf einem synthetischen Datensatz aus der Simulationswelt auf und betrachtet den Einfluss verschiedener Filtermethoden auf die Phase und Amplitude von hydrologischen Signalen in Flusseinzugsgebieten. Dies ist insbesondere von Interesse, als dass durch die Filterung möglichst keine Änderung der geophysikalischen Signale hervorgerufen werden soll, um einer späteren Fehlinterpretation vorzubeugen.

Die Arbeit schließt in Kapitel 8 mit einer Zusammenfassung der erzielten Erkenntnisse zu geeigneten Filtermethoden zeitvariabler Schwerefelder für aktuelle und zukünftige Missionsszenarien ab. Ein zentrales Ergebnis ist hierbei die Feststellung, dass das Konzept des VADER-Filters sowohl für aktuelle GRACE als auch für zukünftige Szenarien bestens geeignet ist, um wertvolle Erkenntnisse zu Massenverlagerungsprozessen aus zeitvariablen Schwerefeldlösungen zu gewinnen. Des Weiteren wird ein Ausblick auf vielversprechende weiterführende Untersuchungs- und Analysemöglichkeiten, aufbauend auf den besprochenen Filtermethoden gegeben.

Insgesamt lässt sich feststellen, dass der VADER-Filter ein geeignetes Werkzeug zur Nachbearbeitung von zeitvariablen Schwerefeldlösungen ist. Die Bewertung verfügbarer GRACE-Zeitreihen hat ergeben, dass die ITSG-Grace2016 Zeitreihe mit ihren monatlichen formalen Fehlerkovarianzmatrizen am besten geeignet ist, um für die Schätzung geophysikalischer Signale herangezogen zu werden. Die Korrelationsmuster der formalen Fehler im Ortsbereich sind nach der Filterung mit dem VADER-Filter entgegen der Charakteristik vor der Filterung annähernd isotrop und schnell abfallend. Dies ist ein entscheidender Vorteil des Filters, da diese Eigenschaften den Einsatz regional begrenzterer Faltungsoperatoren zur Gebietsintegration ermöglichen.

Abstract

This thesis investigates the retrieval of mass transport phenomena, namely hydrological and ice mass change, derived from time variable gravity field solutions. The main focus is set on the evaluation and development of dedicated post-processing methods for retrieving the target signals. The investigations cover the assessment of suitable time series in spherical harmonics derived from GRACE observations, rate existing and further developed filter methods, describe all relevant corrections coping with deficiencies in the original GRACE estimates, discuss a comprehensive assessment of error budget contributions for mass change estimates, and give recommendations regarding suitable filter and processing strategies for GRACE. The assessment is accompanied by in-depth validation of the techniques investigated within a closed loop simulation environment. This provides a better understanding of the filter and processing methods. In the closed loop environment the design and setup of all relevant algorithms can be tailored towards best performance before being applied to real data.

The post-processing methods investigated in particular are two versions of the empirical decorrelation filter [Swenson and Wahr 2006] and a further developed form of the DDK filter [Kusche 2007]. The latter is called time variable decorrelation (VADER) filter and has non-stationary characteristics. The key parameters forming the VADER filter are month-to-month formal error covariance matrices and a cyclo-stationary signal variance. This configuration shows best performance with respect to all other filters and post-processing methods that have been tested within the frame of this thesis. Using the VADER filter does not only cause smallest filter induced deviation of the filter results from the target signals in terms of attenuation and phase shift of seasonal signals, it also has a favorable impact on the error correlation patterns. The correlation length of errors, especially in the along-track direction, is significantly reduced, allowing to apply less complex averaging functions to retrieve mass signals in the respective area of interest. The filter exhibits an adaptive behavior capable of adequate filter performance not only in nominal, but also in special months encountering short repeat cycles or months with weak data coverage.

To build a bridge to upcoming gravity field missions like GRACE-FO and future mission scenarios, the post-processing concepts for GRACE are rated regarding their applicability to future scenarios, especially a double pair mission scenario with one polar and one inclined pair. Based on simulated time series, among all investigated methods the VADER filter is identified to deliver the most promising performance for such missions. The double pair mission analysis also reveals improved gravity field solutions in the areas only covered by the polar pair.

Apart from theoretical investigations, two practical applications demonstrate the characteristics and capabilities of the filters tested. The first case study covers the process of estimating ice mass trends in the region of Antarctica and its subregions based on the ITSG-Grace2016 time series, which was identified to provide the most reliable formal error description of all series tested. The estimate is accompanied by a comprehensive error characterization of the filtered monthly solutions and the estimated trend. The total error is diverted into single error budget contributors like GRACE, degree one and C_{20} corrections, and GIA. The second case study illustrates the impact of the filters on estimates of hydrological signals of river basins based on a simulated time series. This allows evaluating the impact of the filters on the retrieved amplitude and phase. The VADER filter shows superior performance especially with respect to signal attenuation, phase shifts, and induced leakage.

The goal to contribute to the better understanding of mass transport phenomena by improving post-processing methods is reached. The VADER filter shows clear advantages with respect to the other filters tested. It allows increasing the spatial resolution of retrieved signal while minimizing

signal attenuation. An additional benefit is its positive effect on the error correlation patterns. This is of great importance as such achievements can serve for the better understanding of climatological and mass change processes as well as coupling mechanisms in the system Earth.

Table of content

Abbrevations

ACC	accelerometer
AIS	Antarctic ice sheet
AO	atmosphere and ocean (signal)
AP	Antarctic Peninsula
ARMA	autoregressive moving average
ASD	amplitude spectral density
CF	center of figure
CHAMP	Challenging Minisatellite Payload
CL	closed loop
CM	center of mass
CSR	Center for Space Research at the University of Texas at Austin
EAIS	East Antarctic ice sheet
EOF	empirical orthogonal function
ESA	European Space Agency
EWH	equivalent water height
GFZ	Geoforschungszentrum Potsdam
GIA	glacial isostatic adjustment
GMB	gravimetric mass balance
GOCE	Gravity field and steady-state Ocean Circulation Explorer
GRACE	Gravity Recovery and Climate Experiment
GRACE-FO	Gravity Recovery and Climate Experiment – Follow On
HIS	hydrological, ice, and solid earth (signal)
ICGEM	International Centre for Global Earth Models
IMBIE	international mass balance intercomparison experiment
ITRF	international terrestrial reference frame
JPL	Jet Propulsion Laboratory
LCLA	linear closed loop approach

LoS	line of sight
LRI	laser ranging instrument
MSE	mean square error
MWI	microwave interferometer
NGGM-D	next generation gravity field mission – Deutschland
OT	ocean tide
RACMO	regional Antarctic climate model
RMS	root mean square
S&W filter	Swenson & Wahr filter
SGG	satellite gravity gradiometry
SH	spherical harmonic
SLR	satellite laser ranging
SMB	surface mass balance
SST-ll/-hl	satellite to satellite tracking – low-low/high-low
VADER	time variable decorrelation
WAIS	West Antarctic ice sheet

Introduction

The motivation to perform the work presented within this thesis is to better understand mass change phenomena primarily induced by hydrological or cryospheric processes. They are, among other processes like solid earth, atmospheric, and ocean mass change phenomena, the major components of the outer Earth system. Their dynamics, interaction, and coupling are driven by solar irradiation, which serves as their motor, responsible for the Earth's climate. Key observations for the work presented are spaceborne satellite gravimetry observations from existing and future mission scenarios. The main goal of this thesis is to assess and further develop post-processing strategies for retrieving mass change estimates with increased spatial resolution and better understanding of its errors from time variable gravity field estimates. The core mission for this field of research is GRACE [Tapley et al. 2004], which was launched in 2002 and is, as from today (November 2016), still operational. With GRACE numerous achievements for a better understanding of mass transport phenomena have been reached. Due to the huge success of GRACE, a GRACE Follow On mission (GRACE-FO) is on its way and foreseen to be launched in 2017/2018. The main mission concept is the same as for GRACE (polar orbit, single pair, and microwave link for low-low satellite to satellite tracking (ll-SST)). An additional sensor implemented as demonstrator is a laser link for increased accuracy of ll-SST observations. Accordingly the thesis is focusing not only on operational missions, but also investigates the applicability of today's post-processing methods to future mission scenarios. A better understanding of the Earth system to which this work intends to contribute supports the interpretation of the Earth's climate system and its coupling effects. This advancement is not only important from a pure scientific perspective, but has also social and economic aspects. The public awareness for changes in the Earth system is rising, as sea level rise and large scale events like El-Niño create broad media attention. Delivering rock solid foundations and facts of how the climatological system works and how the processes evolve and change over time is fundamental to serve as basis for decision making processes on political, societal, and economic level.

The foundation for such work is a profound analysis of the available data and existing post-processing algorithms and their strengths and weaknesses. For this thesis two approaches have been identified and selected for in-depth analysis, the first being the empirical decorrelation filter [Swenson and Wahr 2006] and the second the DDK decorrelation filter [Kusche 2007]. For both filters the performance and possible enhancements are evaluated in a closed loop environment. This environment allows testing the impact and the consequences of changing individual parameters of the filter design and to identify weak points. The concept of the DDK filter turned out to be most promising, as it follows a more analytical than empirical approach, delivering superior results with respect to all other filters tested. The weak point of the DDK is its stationary design. Therefore one of the key parts of this thesis is to develop a non-stationary variant of the DDK filter, the time variable decorrelation filter VADER. One should note that for such a filter full monthly error covariance information, provided by the GRACE level-2 processing centers, needs to be available. In the recent past more and more processing centers decided to provide such datasets. Upon investigation of the available time series providing full month-to-month error covariance information, the ITSG-Grace2016 time series was identified to provide the most reliable and realistic error characterization. This time series is employed in the application example of estimating ice mass change in the region of Antarctica and its subregions.

Another aspect investigated is the characterization of the error and correlation structures inherent in up-to-date GRACE time series. Investigations exhibit significant differences between the processing centers. Working with full normal equation or error covariance matrices also allows deriving month-to-month post-filter error estimates by error propagation. This error budget

contribution, complemented with other error budget contributors, forms a total error budget estimate for monthly solutions.

The improvement of post-processing methods also helps to avoid empirical enhancements like the application of scale factors on, e.g., estimates of hydrological signals.

As the lifespan of the GRACE mission is turning towards its end (e.g. increasing battery problems and unintended outages), filter and post-processing concepts need to be tested regarding their applicability to future gravity field missions. As the soon (2017/2018) to be launched GRACE-FO mission has a very similar design as the GRACE mission, current methods are rated as being transferable to the new mission. Also for future realistic double pair mission scenarios the VADER filter proves being a very efficient tool for retrieving mass change estimates.

This work provides hints and recommendations for retrieving mass balance estimates from time variable gravity field solutions, incorporating tailored filter techniques as well as a description of the GRACE and overall mass balance error budget. The findings on error correlation patterns help to define suitable integration and averaging functions and to account for leakage in an adequate way.

In the following the general outline of the thesis is presented and the contents of the individual chapters are introduced in detail.

Chapter 1 introduces the mission types investigated, namely the GRACE and GRACE-FO mission. A promising future mission double pair scenario, described within a recent ESA study, is additionally introduced in order to analyze the potential gain and the applicability of today's filter methods in retrieving geophysical mass signals using such scenarios.

Chapter 2 delivers theoretical foundations for working with gravity field estimates represented in spherical harmonics. Among others, least squares adjustment theory, Tikhonov regularization, digital filters, and various measures to analyze gravity field solutions parameterized in spherical harmonics are described. Another important topic discussed is temporal aliasing, since this phenomenon is responsible for many difficulties retrieving high quality results from time variable gravity field estimates.

The closed loop simulation environment is introduced in chapter 3. It serves as basis for the development and evaluation of the investigated filter algorithms. It allows tuning the filter design towards optimal performance and to test the impact of variations in parameters, such as observing geometry, sensor performance, and de-aliasing error levels. A realistic testing environment assures the transferability of the findings regarding favorable filter designs, made within the closed loop environment, to real world data.

Chapter 4 discusses all relevant processing steps from initial gravity field estimates to mass trends. The three sections of the chapter discuss the target signals and their characteristics, the processing steps from time variable gravity field estimates to mass trends, and state of the art GRACE gravity fields and filter methods. The processing steps discussed involve especially the determination of a suitable maximum degree of SH expansion, all applicable corrections (e.g. degree one and C_{20}) to cope with deficiencies within the GRACE solutions, the issue of spatial and temporal leakage, and considerations on the design of averaging kernels to derive mass signals for the respective area of interest. In the last part of the chapter available GRACE time series are rated with respect to their characteristics and whether they are suited for estimating mass signal trends. This evaluation is accompanied by a review of state of the art filter and processing methods in the context of GRACE.

The in-depth analysis and tuning respectively further development of the two dedicated filter methods is discussed in chapter 5. The first one is the empirical decorrelation filter following the

concept by Swenson and Wahr [2006]. Two variants of this filter are rated regarding their characteristics and suitability for filtering GRACE time series. Secondly, being one of the core parts of this thesis, a further development of the DDK filter [Kusche 2007], the time variable decorrelation filter named VADER, is introduced. All its constituents, the error covariance matrices, the signal variance information, and the weighting coefficients, are discussed and evaluated within closed loop and real data experiments. Chapter 5 closes with a recommendation regarding a suitable setup of post-processing methods for retrieving geophysical signals from GRACE time series.

In chapter 6 the findings regarding the design and setup of post-processing methods for GRACE time series, with respect to the transferability to future mission scenarios, are evaluated. Analysis covers especially the changes in error correlation structures switching from single- to double-pair mission scenarios. The applicability of the analyzed post-processing strategies is rated not only, but also, with respect to the special conditions in the transition zone switching from double to single pair coverage. The chapter closes with recommendations on favorable strategies for double pair mission scenarios.

Two applications of the post-processing methods are presented in chapter 7. The first case study deals with retrieving ice mass variations in the region of Antarctica and its subregions. The experiment covers all processing steps from selecting a suitable time series, applying all necessary corrections, and employing the VADER filter with a setup suited for the conditions in the target region. The whole process is accompanied by estimating a total error budget for the individual filtered monthly solutions as well as for the estimated linear mass change signals. Individual error budget contributors accounted for are GRACE itself, the applied corrections, and GIA. The second case study is based on a closed loop experiment. The effect of the filter methods investigated within this thesis on retrieved hydrological signals is tested. Focus is set on the filter induced attenuation and shift of the amplitude and phase of seasonal signals. Target regions are six large and medium scale river basins on different continents. It is of major importance to rate filters with respect to their impact on retrieved signals, because altering the results by filtering should be minimized in order to avoid misinterpretation of hydrological or other geophysical signals.

The thesis closes with chapter 8, giving a summary of the major findings elaborated with respect to filter and post-processing methods for time variable gravity fields from current and future gravity field missions. One main advantage is the adaptability of the VADER filter and its superior performance with respect to the other filters tested, not only for GRACE but also for future mission scenarios on retrieving mass transport signals. Moreover, based on the work presented within this thesis, the chapter presents possible further developments and analyses.

For reasons of better readability some figures within this thesis are implemented as vector graphics, allowing for zooming in the digital version of this thesis. All figures available as vector graphics are marked with *.

Happy reading!

1. Gravity field missions

The gravity field of the Earth can be measured and modelled from terrestrial, air-, and space-borne observations. Different mission types can be used to study the gravity field and its temporal variation. To do so, one first needs to determine which kind of variations one intends to measure, since they exhibit different properties in terms of e.g. spectral composition and amplitudes or spatial and temporal resolution. The second step then is to define suitable observation strategies or mission scenarios to cover the target signals aimed at. In this thesis different existing or feasible future scenarios are discussed in detail. Operational or near operational missions are introduced in section 1.1, and one out of several proposed future mission scenarios is discussed in section 1.2. The abovementioned target signals like hydrological, ice, and solid earth mass redistribution (to mention the most significant ones) are discussed in section 4.1 regarding their characteristics in spatial and temporal variability. As one can see from section 4.1, there are also other signals like atmospheric and ocean mass redistribution, causing variations in the Earth's gravity field. The issue of measuring such signals or reducing them from the estimated solution (the de-aliasing issue) is discussed in section 2.5.

Time variable gravity field estimates originating from the concept of high-low Satellite to Satellite Tracking (hl-SST) were first derived from the CHAllenging Minisatellite Payload (CHAMP) mission [Reigber et al. 1999; 2002]. The second mission making use of this concept, in low-low mode, and being one of the main study objects of this thesis, is the Gravity Recovery And Climate Experiment (GRACE) mission [Tapley et al. 2004]. A third realized dedicated gravity field mission using the hl-SST approach is the Gravity field and steady-state Ocean Circulation Explorer (GOCE) mission [ESA 1999] with the first implementation of satellite gradiometry [Rummel et al. 2011]. Observing the gravity field from space has several significant advantages. The most striking one, of course depending on the orbital design parameters like e.g. inclination and height, is the ability to carry out measurements with homogeneous global coverage and accuracy, being independent of political boundaries or harsh climate conditions. This circumstance helps for solving the Earth's gravity field parameterized in spherical harmonics in a stable manner.

The two different principles of SST, hl- and ll-SST, and the concept of satellite gradiometry (SGG) are illustrated in Figure 1-1.

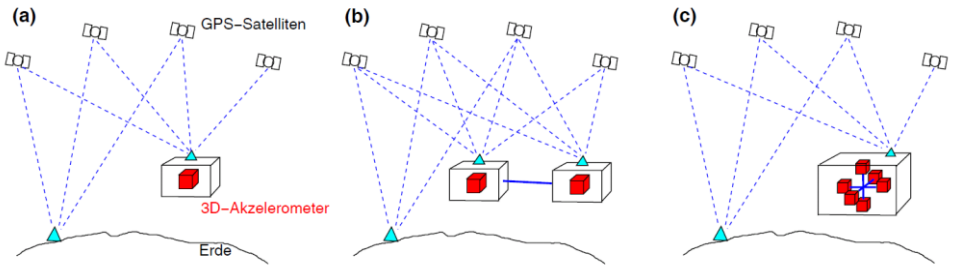

Figure 1-1: Schematic view of hl-SST in panel a, ll-SST in panel b, and SGG+hl-SST in panel c. Reference: Horwath 2008.

The aforementioned missions related to the implementations of SST are CHAMP for panel a, GRACE for panel b, and GOCE for panel c (for the hl-SST part). The most relevant concept for the investigation carried out in the following is the ll-SST. The basic component for such a

mission is a ranging instrument to determine the distance between at least two low flying spacecraft very precisely. The required precision of the ranging instrument is, as discussed in chapter 3, in the range of micro- to nanometers to allow meaningful gravity field estimates. Complementary an accelerometer is necessary to separate gravitational and non-gravitational forces, since for studying the gravity field only the gravitational forces are of interest and other forces like atmospheric or solar drag must be separated. The required accuracies and the source of potentially disturbing forces, as they are measured by an accelerometer positioned in the center of mass of a satellite, are discussed in more detail in chapter 3.

In the following two sections, the different mission concepts, based on the ll-SST approach, are presented. They serve as basis for the experiments of this thesis regarding the retrieval of geophysical signals and the development and tuning of dedicated post-processing methods. The missions are: The GRACE mission [Tapley et al. 2004], which consists of one pair of spacecraft in operation since 2002. The GRACE Follow-On mission (GRACE-FO), currently built and planned for launch in the period from December 2017 to February 2018 [Flechtner et al. 2016b], also consisting of one pair of spacecraft, and as third mission a double pair concept for 2020+, which is proposed, analyzed, and assessed within the study "*Assessment of Satellite Constellations for Monitoring the Variations in Earth Gravity Field*" (SC4MGV) [Iran Pour et al. 2015].

1.1 GRACE + GRACE-FO

The GRACE mission [Tapley et al. 2004] was launched in 2002 and is, as of today (November 2016), still operational. The constellation is composed of one pair of almost identical satellites flying in a polar orbit at 89° inclination, separated by an average distance of 200 km in along-track direction. One of the key scientific instruments is the inter-satellite ranging system to perform the ll-SST measurements. For GRACE this system is built from a microwave interferometer, operating in the K-band [Dunn et al. 2003]. In the case of GRACE-FO, the K-Band ranging (KBR) system is named as microwave interferometer (MWI). Additional key instruments are GPS receivers (allowing to also conduct hl-SST) and a 3-axis accelerometer on each spacecraft. The initial average altitude of GRACE was around 500km and subsequently decreased until today to about 350km (cf. Figure 5-17). This decrease in altitudes has, as discussed later in e.g. chapter 2 and section 4.3.2, a significant impact on the retrievability of gravitational signal and also feeds back on the specific properties of estimated gravity fields and the subsequently applied post-processing methods. With GRACE, numerous achievements in the understanding of mass redistribution processes have been made so far. Mass balance estimates for Antarctica [Shepherd et al. 2012], determining the contribution of melting ice sheets to sea level rise [King et al. 2012], monitoring of global sea level variations [Cazenave et al. 2009], detection of groundwater depletion in India [Tiwari et al. 2009], changes in solid earth signals induced by major earthquakes [Wang et al. 2012], and hydrological investigations [Reager et al. 2014], to name only a few.

As GRACE allows estimating mass variations on the Earth independent from other observation techniques, it can serve as an independent reference for evaluating the plausibility of e.g. climate models and output from other observational techniques like continental ice mass change estimates from radar altimetry or input-output methods. One important fact with studying gravity field variation is the superposition principle. GRACE or any other gravity field space mission observes the signal resulting from the sum of all mass transport processes, not distinguishing between the different phenomena like ice mass, the global water cycle or solid earth processes (cf. section 4.1). Therefore direct comparison between outputs from different measurement techniques is subject to careful consideration which phenomena (e.g. glacial isostatic adjustment; cf. section 4.2.2) are included in the respective sets of observations.

Since the continuity of measurement time series without data gaps, avoiding discontinuities, is of high importance for the development of the understanding of climate and solid earth processes, a successor of the GRACE mission is built and will be ready for launch in 2017/2018. Since the measurement concept and overall mission design is almost identical to GRACE, it is simply called GRACE Follow-On (GRACE-FO). One major difference between the two missions will be the more accurate inter satellite ranging instrument, a laser interferometer (LRI) [Sheard et al. 2012], complementary to an also installed K-band ranging instrument (MWI). The LRI serves as a technology demonstrator and is, as the initial concept is made up, only designed to operate for a shorter period (one year) and not throughout the whole nominal mission lifetime. The noise level of the ranging instrument will will decrease to, according to Flechtner et al. [2016a], 80 nm for the range or 9.9 nm/s for the range-rate, whereas the GRACE noise level is at 2.1 µm for the range resp. 0.24 µm/s for the range-rate. This gain in accuracy in SST performance will, according to Flechtner et al. [2016a], lead to only minor improvements in the recovery of geophysical signals. Figure 1-2, showing results from a simulation run performed by Flechtner et al. [2016a], gives an overview of degree amplitudes in terms of geoid height error for different error contributors in the MWI and LRI case. The thin lines represent the geoid height errors using the MWI, and the bold lines the ones using the LRI. The improvement of the SST error is significant, comparing the two green lines. This helps to reduce the total noise budget, but one should note the dominating error contributors indicated by the cyan (ocean tide error), aubergine-colored (atmosphere and ocean de-aliasing error), and orange curve (accelerometer error). They all show significantly higher amplitudes than the SST error and thus dominate the total error budget. The other error sources, like the static gravity (gray) and orbit error (magenta) do not play a major role since their amplitude is more than one order of magnitude smaller than the abovementioned contributors. Loomis et al. [2012] report the impact of an improvement in the SST accuracy only of minor or no value if the other error contributions of the whole system, especially the temporal aliasing, still dominate. They derive their findings, which are confirmed by Flechtner et al. [2016a], upon GRACE-FO system simulations. This insignificant improvement is illustrated by the almost coinciding all errors (dark red) lines. The mean HIS signal is indicated for comparison reasons (black).

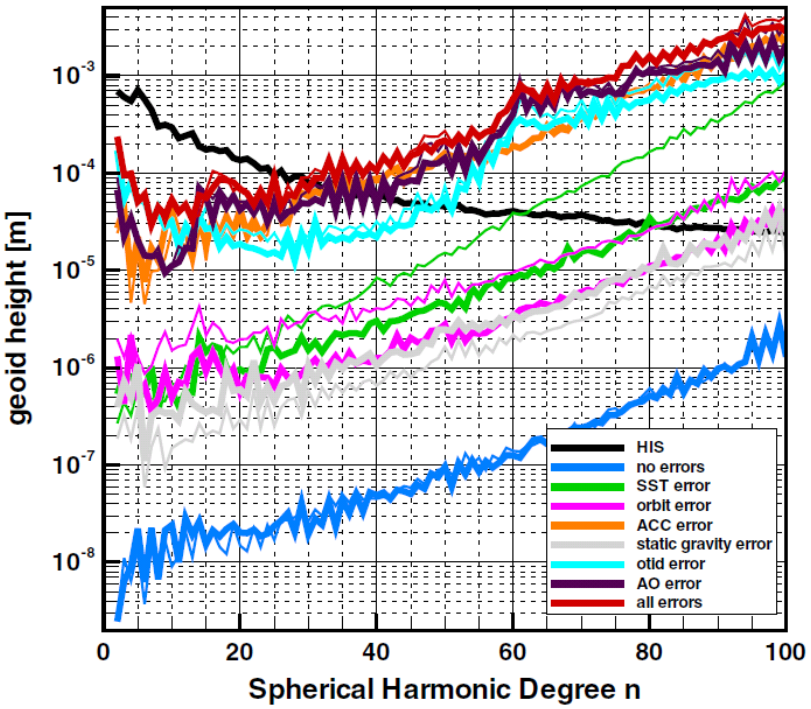

Figure 1-2: Degree amplitudes in terms of geoid height error in meters for a single simulated month for different individual instrument and model errors. Thin lines represent microwave interferometer results, bold lines represent laser interferometer results. Credits: Flechtner et al. 2016b

Nevertheless, some improvements in performance switching from GRACE to GRACE-FO can be expected. The follow-on mission e.g. carries a third star camera on board allowing more stable determination of the spacecraft's orientation, or an increased portion of digital instrumentation instead of analogue, allowing operations being less sensitive to the radiative environment conditions.

1.2 Future missions

Apart from the introduced currently flying or near operational missions, a second area of investigations, also being part of this thesis, are future mission concepts still being in the study phase. A number of studies and investigations were carried out in the recent past in order to identify meaningful constellations for future satellite gravity missions. These are, among others, two parallel studies regarding the *"assessment of a next generation mission for monitoring the variations of Earth's gravity" (NGGM and NG2)* [ESA 2010, 2011], the mission proposal *"e.motion"* submitted upon the call for ESA Earth Explorer 8 [Panet et al. 2013], and the DLR funded preparatory study *"e².motion"* [Gruber et al. 2014], which resulted in a response to the ESA Earth Explorer 9 call [Gruber et al. 2016]. They all evaluated and rated different mission configurations and concepts. Main aspects and parameters analyzed are the design of the orbit and the characterization of instrument performance in order to achieve the defined target performance. This target performance is measured by the recoverability of geophysical signals in terms of temporal and spatial resolution. The investigations carried out in the framework of this thesis regarding the design of the future mission scenario, e.g. the assumptions regarding the instrument and performance errors and the orbital design, are based on the findings and recommendations of the *SC4MGV* study [Iran Pour et al. 2015]. Among the different scenarios analyzed and assessed within the study, the so called "baseline scenario 5" was selected as prototype to be deployed for the future mission closed loop experiments design described in chapter 3.

Table 1-1: Future mission design parameters from SC4GMV "baseline scenario 5" [Iran Pour et al. 2015].

Pair	Orbit	Altitude	Inclination	Epoch (GPS time)
1	11/172 circular repeat orbit (3 day sub-cycle)	About 370 km	92°	01.01.1996 00:00 Ω=0°, ω=0°, M=0°
2	29/460 circular repeat orbit (7 day sub-cycle)	About 345 km	115°	01.01.1996 00:00 Ω=270°, ω=0°, M=0°

Table 1-1 summarizes the main orbit design parameters for both pairs. The numbers 11/172 mean 172 revolutions in an 11 day repeat period. The mean altitude of the two pairs, being 370 km respectively 345 km, is lower than the nominal height of the GRACE mission (cf. chapter 1.1). The numbers for longitude of the ascending node Ω, the argument of periapsis ω, and the mean anomaly M define the initial setup at the beginning of the one year simulation period. Figure 1-3 shows an exemplary ground track distribution for one day of the simulated orbit. The ground track of the polar pair is shown in blue, the one of the inclined pair in red. Double pair coverage is achieved for the area between 65° north and south. For the polar areas only one pair delivers observations. The impact of this setup on polar mass change estimation and the impact on applicable post-processing methods is one of the main focus areas of this thesis and discussed in

chapter 6. Apart from the orbit design, a second very important aspect of the mission design is the characteristics of the instruments and system noise. They are addressed in detail in chapter 3 regarding the setup of the closed loop simulation environment.

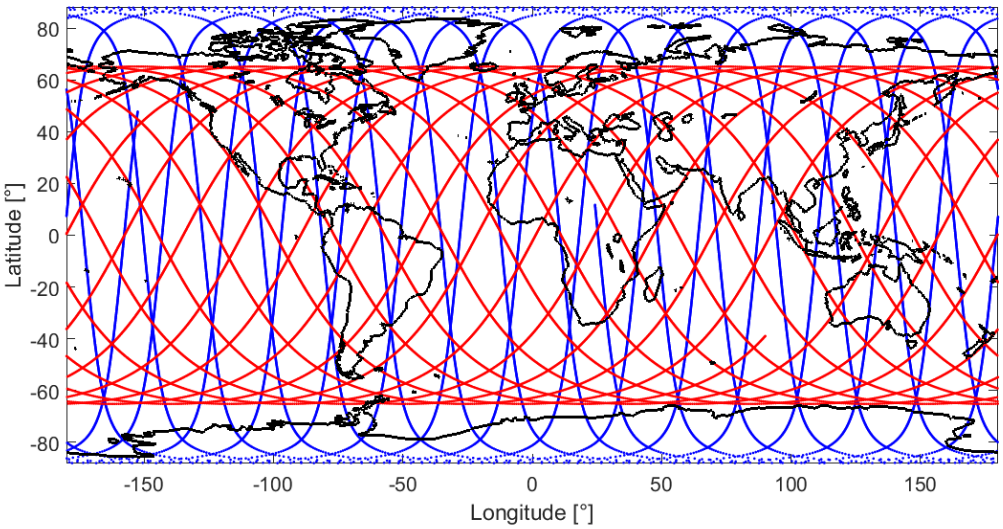

Figure 1-3: Exemplary ground track distribution from one day of near-polar (blue) and inclined (red) orbit configuration.

Limiting factors while operating such missions are, as already mentioned in the previous section in the context of GRACE-FO, the insufficient accuracy of today's AO de-aliasing products, and the lack of accurate enough ocean tide models. The assumptions regarding the accelerometer noise and the ranging accuracy are, as discussed in chapter 3, significantly better than for GRACE, leaving other system components as weakest part of the chain. Approaches and studies to overcome this problem by e.g. co-estimating the ocean tide signals are discussed in section 2.5 and chapter 8.

Notable other constellations, not subject of further investigations within this thesis, are pendulum and cartwheel configurations, investigated by e.g. the NGGM study [ESA 2010]. These concepts are very promising since they would lead to almost isotropic error correlation structures. Isotropic error correlation structures are preferable from the perspective of post-processing methods, as discussed later on within this thesis. One should note that a realization of such configurations cannot be expected within the next years, due to challenges from a technical and engineering perspective.

Studies investigating in the feasibility of hl-SST with laser links between GNSS satellites and low Earth orbiters, instead of GNSS observations, are investigated e.g. by Hauk et al. [submitted 2016].

2. The gravity field and theoretical foundations

The following chapter introduces briefly the theoretical background of the Earth's gravity potential, its associated gravity field, and its representation in the spectral domain using spherical harmonics (section 2.1). In addition basic theoretical foundations for analysis techniques applied in this thesis are outlined. Whilst working with time variable gravity fields (section 2.2), the key quantity of interest is mass transport, causing changes in the Earth's gravity field. In order to describe such variations, the estimation of signals is of importance. To do so, some foundations in estimation theory, especially least squares adjustment, are introduced in section 2.3. The section also contains an introduction to the following topics: Regularization as an amendment to the least squares adjustment, estimating the bias caused by applying regularization, and in the context of the closed loop simulation, replacing the weighting matrix P_{bb} by the use of autoregressive moving average (ARMA) filters.

Section 2.4 summarizes different measures to evaluate and analyze gravity fields in a spherical harmonic representation, and section 2.5 closes the chapter with introducing the issue of how to deal with short term variations of atmospheric and oceanic signals, undersampled by the measurement system, e.g. GRACE.

2.1 The gravity potential and spherical harmonics

For the representation of the Earth's gravity field, spherical harmonics are used within this thesis. A very comprehensive description of spherical harmonics can be found in Heiskanen and Moritz [1967]. Other representations, like e.g. mascons, exist and are discussed in section 4.3.1.

Following Heiskanen and Moritz [1967], the gravitational potential V of a solid body like the Earth reads

$$V(P) = G \iiint_{Earth} \frac{dm}{d} = G \iiint_{Earth} \frac{\rho}{d} dv \tag{2.1}$$

with G being the gravitational constant, dm an element of mass, and d the distance between the mass element and the attracted point P. dv is an element of volume and ρ its density. Numbers for all constants used within this thesis can be found in Table 2-1 at the end of this section. For a point P outside the attracting masses, V is a harmonic function and meets the Laplace equation (2.2)

$$\Delta V = 0 \tag{2.2}$$

Following this, the Earth's gravitational potential V can be described as a harmonic function at any location where equation (2.2) is valid. If P is outside a closed surface S (formed over all elements of mass dm), V will attenuate with $1/d$. According to Heiskanen and Moritz [1967], using spherical harmonic base functions, equation (2.1) can be expressed in spherical coordinates as

$$V(r,\theta,\lambda) = \frac{GM}{R}\sum_{l=0}^{\infty}\left(\frac{R}{r}\right)^{l+1}\sum_{m=0}^{l}\bar{P}_{lm}(\cos\theta)\left[\bar{C}_{lm}\cos m\lambda + \bar{S}_{lm}\sin m\lambda\right]. \tag{2.3}$$

r … radius (geocentric)
θ … spherical co-latitude
λ … spherical longitude
l … degree of expansion
m … order of expansion
R … reference radius of the Earth
M … reference mass of the Earth
$\bar{P}_{lm}$ … fully normalized Legendre polynomials
$\bar{C}_{lm}$ … fully normalized SH weighting coefficients for cosine term
$\bar{S}_{lm}$ … fully normalized SH weighting coefficients for sine term

The fully normalized Legendre polynomials $\bar{P}_{lm}$ are derived from the Legendre polynomials P_{lm} by

$$\bar{P}_{lm} = \sqrt{k(2l+1)\frac{(l-m)!}{(l+m)!}}P_{lm} \quad \text{with} \quad k = \begin{cases} 1 \text{ for } m = 0 \\ 2 \text{ for } m \neq 0 \end{cases} \tag{2.4}$$

The fully normalized SH weighting coefficients $\bar{C}_{lm}$ and $\bar{S}_{lm}$ are derived from the SH weighting coefficients C_{lm} and S_{lm} by

$$\begin{Bmatrix} \bar{C}_{lm} \\ \bar{S}_{lm} \end{Bmatrix} = \sqrt{\frac{(l+m)!}{k(2l+1)(l-m)!}}\begin{Bmatrix} C_{lm} \\ S_{lm} \end{Bmatrix} \quad \textit{with} \quad k = \begin{cases} 1 \text{ for } m = 0 \\ 2 \text{ for } m \neq 0 \end{cases} \tag{2.5}$$

Further details regarding the calculation of Legendre polynomials and a more detailed explanation of the underlying idea and concept of the SH series expansion can be found in Heiskanen and Moritz [1967] and Torge and Müller [2012]. One should note that the base functions fulfill the criterion of orthogonality. The normalization is applied in a way that the integral over a unit sphere equals 4π.

The representation in equation (2.3) illustratively shows the content of the triangular plots of spherical harmonic coefficients. The left part of the triangle is composed by the $\bar{S}_{lm}$, and the right part by the $\bar{C}_{lm}$ coefficients.

The term $(R/r)^{l+1}$ from equation (2.3) is of special importance, since it introduces a relation of the potential V with the radius of the Earth R and the distance r of the point being evaluated. As one can see from the exponent $l+1$, there is a strong damping factor for locations with increasing distance from the Earth's surface. This relation plays a key role for the design of gravity satellite missions and the retrievability of gravitational signals. The lower a satellite can fly, the larger the gravity potential is and the less sensitive an instrument needs to be to observe a certain signal.

Following equation (2.3), the full potential V can be split up into a reference or static potential V^{ref}, and a residual time variable potential ΔV.

$$\begin{aligned}\Delta V(\theta,\lambda,r) &= V(\theta,\lambda,r) - V^{\mathrm{ref}}(\theta,\lambda,r) \\ &= \frac{GM}{R}\left[\sum_{l=0}^{\infty}\left(\frac{R}{r}\right)^{l+1}\sum_{m=0}^{l}\bar{P}_{lm}(\cos\theta)\left[\bar{C}_{lm}\cos m\lambda + \bar{S}_{lm}\sin m\lambda\right] - \right. \\ &\quad \left.\sum_{l=0}^{\infty}\left(\frac{R}{r}\right)^{l+1}\sum_{m=0}^{l}\bar{P}_{lm}(\cos\theta)\left[\bar{C}^{\mathrm{ref}}_{lm}\cos m\lambda + \bar{S}^{\mathrm{ref}}_{lm}\sin m\lambda\right]\right] \\ &= \frac{GM}{R}\sum_{l=0}^{\infty}\left(\frac{R}{r}\right)^{l+1}\sum_{m=0}^{l}\bar{P}_{lm}(\cos\theta)\left[\left(\bar{C}_{lm}-\bar{C}^{\mathrm{ref}}_{lm}\right)\cos m\lambda + \left(\bar{S}_{lm}-\bar{S}^{\mathrm{ref}}_{lm}\right)\sin m\lambda\right] \\ &= \frac{GM}{R}\sum_{l=0}^{\infty}\left(\frac{R}{r}\right)^{l+1}\sum_{m=0}^{l}\bar{P}_{lm}(\cos\theta)\left[\Delta\bar{C}_{lm}\cos m\lambda + \Delta\bar{S}_{lm}\sin m\lambda\right]\end{aligned} \tag{2.6}$$

The terms residual and time variable can be understood as small variations with respect to the reference potential. Reason causing such potential differences can be, among others, a redistribution of mass. Because such mass redistribution processes are subject to e.g. seasonal variability, the difference to a reference field is not static but also varying in time. Since this thesis deals with geophysical signals or mass transport phenomena derived from gravity field observations, these potential differences ΔV play a key role.

In equations (2.3) to (2.6), the harmonic series is expanded to infinity. In real world applications the expansion has to be cut at a certain maximum degree $l_{\max}$. The performed degree of expansion can be translated by a rule of thumb [Gruber 2000] into spatial resolution by

$$\lambda_{\min}\left[\mathrm{km}\right] = 20000\mathrm{km}/l_{\max} \tag{2.7}$$

with $\lambda_{\min}$ as the lower bound of spatial resolution in kilometers (half wavelength resolution). Detailed thoughts regarding suitable degrees of expansion related to the target signals are presented in section 4.2.1.

A given set of residual time variable coefficients $\Delta\bar{C}_{lm}$ and $\Delta\bar{S}_{lm}$ from equation (2.6) can be transferred to different functionals. The ones important for mass transport studies are geoid height differences ΔN and the equivalent water height differences ΔEWH on the sphere. A more general term for EWH would be surface density variation per unit area. The term equivalent water height applies only if assuming a density of 1 kg/m². But this still contradicts the definition of mass, being density per volume. The underlying idea is to condense the mass variations causing a differential potential to an infinitely thin layer. According to the equivalent source principle we could not assign a varying potential measured at satellite altitude to a change of mass at a specific coordinate (e.g. r,θ,λ). Accordingly the assumption is based on the idea that mass variations occur in a region very close to the Earth's surface, approximated by the surface density. This restricts the possible solutions in the infinite solution space drastically [Wahr et al. 1998; Horwath 2008]. In the following the spherical approximation of the Earth's figure is used.

$$\Delta N(\theta,\lambda) = R\sum_{l=0}^{\infty}\sum_{m=-l}^{l}\bar{P}_{lm}(\cos\theta)\left[\Delta\bar{C}_{lm}\cos m\lambda + \Delta\bar{S}_{lm}\sin m\lambda\right] \tag{2.8}$$

$$\Delta EWH(\theta,\lambda) = \frac{M}{4\pi R^2}\sum_{l=0}^{l_{\max}}\left(\frac{2l+1}{1+k_l}\right)\sum_{m=0}^{l}\bar{P}_{lm}(\cos\theta)\left[\Delta\bar{C}_{lm}\cos m\lambda + \Delta\bar{S}_{lm}\sin m\lambda\right] \tag{2.9}$$

with k_l being the load Love number [Farrell 1972] for the respective degree l. In principle the series expansion shown in equation (2.9) for surface mass density variations is starting from degree zero. According to Wahr et al. [1998] and e.g. Horwath [2008], the expression is valid from SH degree 2 onwards. The degree zero term vanishes since conservation of mass is assumed. The degree one terms, however, need special consideration, as gravity field estimates are usually referred to the center of mass of the Earth, which is subject to change due to redistribution of mass. A detailed discussion of this issue can be found in section 4.2.2.

Table 2-1: Constants used within this thesis

Symbol	Name	Value
GM	Product of gravitational constant and the Earth's mass	$3.986005\ 10^{14}$ m^3s^{-2}
R	Earth's reference radius	6378137 m (GRS80)
ω_E	Earth's angular velocity of rotation	$7.292115\ 10^{-5}$ rad s^{-1}

2.2 Time variable gravity fields

With equation (2.6) residual time variable potential fields have been introduced. Figure 2-1 shows a full static field in gray in terms of SH degree RMS (cf. equation (2.26)). The parameter degree RMS and other measures to evaluate gravity field signals represented in spherical harmonics are introduced in section 2.4. The static field in this case is the GOCO02S gravity field [Goiginger et al. 2011], which also will be used in the closed loop experiments in the following chapters. As exemplary time variable or residual field (solid black curve) serves the ITSG-Grace2016 2010-01 [Mayer-Gürr et al. 2016a] field with its associated formal error (dashed black curve). This residual field contains, in addition to noise, to a large proportion five time variable geophysical constituents such as atmospheric (blue), oceanic (orange), hydrological (green), ice (cyan), and solid earth (brown) signals. To illustrate an approximate signal characteristic of these five constituents, average monthly variations from the AOHIS model by Dobslaw et al. [2015b] are drawn as SH degree RMS in the respective abovementioned colors. Figure 2-1 shows only a snapshot for one month (2010-01), and since residual gravity field estimates and all its constituents like noise and geophysical signals do vary over time, an explanation of the main frequencies and their relation to geophysical phenomena, also called target signals, are discussed in chapter 4.1.

Especially at lower SH degrees ($l < 25$) the degree RMS for the five geophysical constituents is at or within the range of the residual GRACE signal. The formal error of the GRACE estimate is also up to the same extent below the geophysical signal degree RMS. From degree 30 onwards one can observe a steady increase in degree RMS for the residual signal which coincides with its formal error. The quantity responsible for the observed increase is, as one can see in later chapters, noise (cf. Figure 4-20 in chapter 4.3.3) in combination with the $(R/r)^{l+1}$ term. In the following the residual field will be called "raw" or "unfiltered", since it is unfiltered and not treated with any post-processing method. For degrees 30 and higher the gap between the degree RMS of the five geophysical signals and the residual GRACE field increases. To reduce this gap by applying suitable post-processing methods and thus to extract as much as possible geophysical signal out of residual gravity fields is one of the main objectives of this thesis.

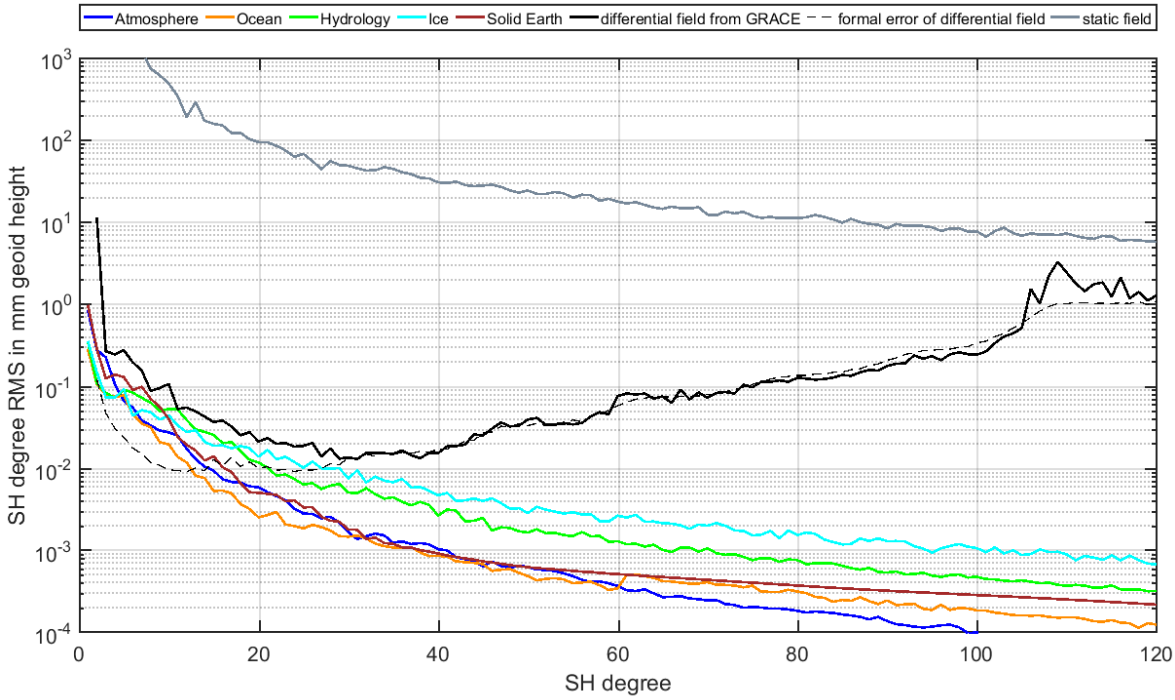

Figure 2-1: SH degree RMS of a full (gray) and differential gravity field (black) and its associated formal error (dashed black), in combination with atmospheric (blue), ocean (orange), hydrological (green), ice (cyan), and solid earth (brown) signal degree RMS in mm geoid height.

2.3 Least squares adjustment, regularization, and ARMA filters

Least squares adjustment is used for two major tasks in this thesis. The first aspect is estimating the SH weighting coefficients $\bar{C}_{lm}$ and $\bar{S}_{lm}$ from equation (2.3). This is necessary in order to derive a representation of the Earth's gravity potential field in spherical harmonics from the observations in the closed loop simulation environment (cf. chapter 3). The second aspect is estimating constant, linear, and periodic signals in series of time variable gravity fields. Both tasks rely on the same foundations briefly laid out in the following. A comprehensive compendium regarding estimation theory can be found in e.g. Koch [1987] or Niemeier [2002].

The basic equation expressing the relation between observations l, unknowns x, and residuals v is $f(x) = l + \hat{v}$, with $\hat{v}$ being the a-posteriori residuals fulfilling the minimum requirement $\hat{v}^T P_{ll} \hat{v} \rightarrow \min$ in least squares sense. P_{ll} is the weighting matrix for the observations. It is the inverse of the covariance matrix Q_{ll} ($P_{ll} = Q_{ll}^{-1}$). This matrix contains information regarding the correlation between observations (off-diagonal elements) and their accuracy (diagonal elements). This leads to the solution for the a-posteriori unknowns $\hat{x}$:

$$\hat{x} = \left(A^T P_{ll} A \right)^{-1} A^T P_{ll} l \tag{2.10}$$

with A being the design matrix (also called Jacobi matrix) containing the partial derivatives $\partial f(x)/\partial x$ of the functional model $f(x)$ with respect to the unknowns x. The formal covariance matrix $Q_{\hat{x}\hat{x}}$ of the a-posteriori unknowns is

$$Q_{\hat{x}\hat{x}} = \left(A^T P_{ll} A \right)^{-1}. \tag{2.11}$$

In the case of the decorrelation process, introduced in the following (cf. equation (2.18)) and discussed in section 5.3, the a-posteriori covariance matrix $Q_{\hat{x}\hat{x}}$, originating from the process of estimating the spherical harmonic coefficients $\bar{C}_{lm}$ and $\bar{S}_{lm}$, is called N^{-1}.

The a-posteriori residuals $\hat{v}$ are

$$\hat{v} = A\hat{x} - l \tag{2.12}$$

and the unit weight variance $\hat{\sigma}_0^2$ is

$$\hat{\sigma}_0^2 = \frac{\hat{v}^T P_{ll} \hat{v}}{n-u} \tag{2.13}$$

with n being the number of observations l, and u being the number of unknowns x. The difference between n and u is called redundancy and needs to be at least 0 to allow for unambiguously solving the equation system.

The a-posteriori covariance matrices, scaled by the unit weight variance of the unknowns $\hat{K}_{\hat{x}\hat{x}}$, residuals $\hat{K}_{\hat{v}\hat{v}}$, and observations $\hat{K}_{\hat{l}\hat{l}}$ are

$$\begin{aligned}
\hat{K}_{\hat{x}\hat{x}} &= \hat{\sigma}_0^2 Q_{\hat{x}\hat{x}} = \hat{\sigma}_0^2 \left(A^T P_{ll} A \right)^{-1} \\
\hat{K}_{\hat{v}\hat{v}} &= \hat{\sigma}_0^2 Q_{\hat{v}\hat{v}} = \hat{\sigma}_0^2 \left(Q_{ll} - A Q_{\hat{x}\hat{x}} A^T \right)^{-1} \\
\hat{K}_{\hat{l}\hat{l}} &= \hat{\sigma}_0^2 Q_{\hat{l}\hat{l}} = \hat{\sigma}_0^2 A Q_{\hat{x}\hat{x}} A^T = Q_{ll} - Q_{\hat{v}\hat{v}}
\end{aligned} \tag{2.14}$$

In the following an extension of equation (2.10) is introduced. It deals with the concept of regularization and embeds a second uncorrelated set of observations l_2, which leads to

$$\hat{x} = \left(A_1^T P_{ll1} A_1 + A_2^T P_{ll2} A_2 \right)^{-1} \left(A_1^T P_{ll1} l_1 + A_2^T P_{ll2} l_2 \right). \tag{2.15}$$

Within this thesis, the concept of the so called Tikhonov regularization [Tikhonov and Arsenin 1977] is pursued. Other concepts like the truncated singular value decomposition and the ridge regression exist, but are not applied for the analyses carried out within this thesis. An overview discussing different regularization techniques in the context of geodesy can be found in e.g. Bouman [1998].

The Tikhonov regularization is based on the idea to introduce a so called penalty term with the aim to constrain the solution. This leads to an extended minimization term in least squares sense.

$$v^T P_{ll} v + \alpha x^T R x \rightarrow \min \tag{2.16}$$

Derived from the criterion in equation (2.16) the solution for the a-posteriori unknowns $\hat{x}_\alpha$ is

$$\begin{aligned}
\hat{x}_\alpha &= \left(A^T P_{ll} A + \alpha R \right)^{-1} A^T P_{ll} l \\
&= N_\alpha^{-1} A^T P_{ll} l
\end{aligned} \tag{2.17}$$

with the regularization matrix R and its weighting factor α. The weighting factor α is steering the regularization. If it becomes zero, no regularization is applied and the solution of equation (2.17) would be the same as equation (2.10). Connecting equation (2.17) with (2.15) allows introducing the idea of zero observations in the sense of the aforementioned penalty term. The observations l_2 in equation (2.15) are zero with the consequence for the term $A_2^T P_{ll2} l_2$ being zero as well. The term $A_2^T P_{ll2} A_2$ is not zero and still contains the normal equation part $A_2^T A_2$ with the preferred stochastic characteristics contained in P_{ll2}. We can now easily see the equivalence of equation (2.17) and (2.15) assuming zero observations or a penalty term. This equivalence can

also be extended to the VADER filter approach introduced here and extensively discussed in chapter 5.3. The general form of the VADER filter is

$$\begin{aligned}\hat{x}_\alpha^{VADER} &= W_\alpha \hat{x} \\ &= \left(N + \alpha M\right)^{-1} N\hat{x} \\ &= \left(A^T P_{ll} A + \alpha M\right)^{-1} A^T P_{ll} A\hat{x} \\ &= \left(A^T P_{ll} A + \alpha M\right)^{-1} \underbrace{A^T P_{ll} A\left(A^T P_{ll} A\right)^{-1}}_{=I} A^T P_{ll} l \\ &= \left(A^T P_{ll} A + \alpha M\right)^{-1} A^T P_{ll} l\end{aligned} \tag{2.18}$$

Equation (2.18) shows the equivalence of the VADER filter with the introduced form of a regularization following Tikhonov. With respect to equation (2.17), the regularization matrix R is replaced by M, representing the signal variance matrix used in the context of the VADER filter (cf. chapter 5.3). The idea to apply such a filter or decorrelation concept to monthly GRACE solutions is discussed e.g. in Kusche [2007], Kusche et al. [2009], and Klees et al. [2008]. One can also see that it is possible to split the process of estimating the a-posteriori filtered unknowns $\hat{x}_\alpha^{VADER}$ into a two-step approach. First a processing center, having a level-2 processing chain at hand, estimates the unknowns $\hat{x}$. Second an interested user can take this gravity field estimate and perform regularization as desired or necessary to derive certain target signals. The only information, apart from the SH coefficients $\hat{x}$, to be provided by the processing center is the $A^T P_{ll} A = N$ normal equation matrix or its inverse. Discussions and analysis regarding the requirements to be met by the normal equations and the possibility to generalize or approximate them with respect to GRACE, GRACE-FO and future mission data post-processing or filtering, are presented in sections 4.3, 5.3, and chapter 6. This discussion also explains the difference between the aforementioned implementations of a filter approach following equation (2.18) and the implementation elaborated within this thesis.

A measure to assess the impact or strength of the regularization is to compute the regularization bias Δx_α. A detailed description of the following brief introduction of the regularization bias can be found in Xu [1992] and is e.g. applied in the context of smoothing techniques in the recovery of regional gravity fields by Xu and Rummel [1994] or in the context of spherical cap regularization techniques by Metzler [2007].

Towards the regularization bias, first a look is taken at the difference between the two solutions, the true solution x, and the biased solution $\hat{x}_\alpha$, following Louis [1989] and Metzler [2007]:

$$\begin{aligned}\hat{x}_\alpha - x &= N_\alpha^{-1} A^T P_{ll} l - N^{-1} A^T P_{ll} l_e \\ &= N_\alpha^{-1} A^T P_{ll} l - N_\alpha^{-1} A^T P_{ll} l_e + N_\alpha^{-1} A^T P_{ll} l_e - N^{-1} A^T P_{ll} l_e \\ &= N_\alpha^{-1} A^T P_{ll} \left(l - l_e\right) + \left(N_\alpha^{-1} - N^{-1}\right) A^T P_{ll} l_e\end{aligned} \tag{2.19}$$

l … observations containing noise
l_e … observations noise free
x … true solution
x_α … regularized solution

The last line of equation (2.19) is composed of two parts: The first product represents, in the terminology of Metzler [2007], the data error. The second part represents the regularization error.

The data error can be derived by applying covariance propagation for the regularization onto the original normal equation $N = A^T P_{ll} A$. This leads to the covariance matrix $Q_{\hat{x}\hat{x}}^{\alpha}$ of the regularized solution:

$$\begin{aligned} Q_{\hat{x}\hat{x}}^{\alpha} &= \left(A^T P_{ll} A + \alpha R\right)^{-1} A^T P_{ll} A \left(A^T P_{ll} A + \alpha R\right)^{-1} \\ &= \left(A^T P_{ll} A + \alpha R\right)^{-1} - \left(A^T P_{ll} A + \alpha R\right)^{-1} \alpha R \left(A^T P_{ll} A + \alpha R\right)^{-1} \\ &\neq \left(A^T P_{ll} A + \alpha R\right)^{-1} \end{aligned} \tag{2.20}$$

From equation (2.20), representing the data error, one can see a difference between the covariance matrix of the unknowns in a standard least squares adjustment procedure, as noted in equation (2.11), versus the one originating from a filtered or regularized solution. The regularization error can be computed upon knowledge of the true solution. This truth is not known e.g. in the field of real world gravity field estimation. But it is known in the closed loop simulation environments created e.g. within this thesis to investigate the characteristics and capabilities of different post-processing methods. Since applying a regularization violates the assumption of an unbiased estimator $E\{\hat{x}_{\alpha}\} \neq x$, causing the abovementioned regularization error, the expectation value for the regularized solution is

$$\begin{aligned} E\{\hat{x}_{\alpha}\} &= \left(A^T P_{ll} A + \alpha R\right)^{-1} A^T P_{ll} E\{l\} \\ &= \left(A^T P_{ll} A + \alpha R\right)^{-1} A^T P_{ll} A x \\ &= \left(A^T P_{ll} A + \alpha R\right)^{-1} \left(A^T P_{ll} A + \alpha R - \alpha R\right) x \\ &= x - \left(A^T P_{ll} A + \alpha R\right)^{-1} \alpha R x \\ &\neq x \end{aligned} \tag{2.21}$$

As Metzler [2007] concludes, and as one can see from equation (2.21), the magnitude of the bias is

$$\Delta x_{\alpha} = -\left(A^T P A + \alpha R\right)^{-1} \alpha R x \tag{2.22}$$

According to Xu [1992], a full error description of a regularized solution is given by the so called Mean Square Error (MSE). It is composed of the covariance and the bias term, leading to the expression

$$MSE(x) = Q_{\hat{x}\hat{x}}^{\alpha} + \Delta x_{\alpha} \Delta x_{\alpha}^T, \tag{2.23}$$

aggregating equation (2.20) and (2.22).

The bias term Δx_{α} increases with stronger regularization, whereas the propagated covariance $Q_{\hat{x}\hat{x}}^{\alpha}$ decreases with stronger regularization. This allows finding an optimum in terms of minimum RMS of the two components, leading to a minimum MSE and determining the optimal balance between regularization strength and signal to noise ratio improvement in the closed loop experiments where the true x is known. Section 5.3, especially 5.3.3, shows some practical applications and investigations regarding the aforementioned topic and the consistency of the minimal MSE criterion with other measures of best filter setups.

By taking the square root of the diagonal of the MSE matrix one can derive the difference between the true solution and the biased estimate. This quantity is referred to as residuals of e.g. cumulative geoid errors in section 5.3. Within the closed loop experiments, the square root of the diagonal of the MSE and residuals are the same quantity. The approach investigating the MSE

allows, contrary to the residuals, distinguishing between the different components causing the overall gap between truth and the filtered solution.

A second variant to alter equation (2.10) in the case of correlated observations is replacing the a-priori weighting matrix P_{ll} by filtering the design matrix A and the observations l. This is of great importance when dealing with a large number of observations. A typical solution, estimated within the experiments carried out for this thesis, has a maximum degree of $l_{\max} = 120$. This results in a total number of unknowns of $121^2 = 14641$. The corresponding A matrix has therefore 14641 columns. The usual number of observations lies within a range of 250000 for a typical 30 day solution based on 10 second sampling. Setting up the full system $A^T P_{ll} A$ would result in enormously large matrices. A full A matrix with the aforementioned parameters would already need about 30GB of memory in double precision ($14641 \cdot 250000 \cdot 8\,\text{byte}$). One way to overcome this issue is to take advantage of the concept called *Autoregressive Moving Average* (ARMA) filter [Schuh 1996; Siemes 2008; Stetter 2012]. Equation (2.10) can be extended as follows:

$$\begin{aligned}
\hat{x} &= \left(A^T P_{ll} A\right)^{-1} A^T P_{ll} l \\
&= \left(A^T F^T I F A\right)^{-1} A^T F^T I F l \\
&= \left((FA)^T I F A\right)^{-1} (FA)^T I F l \\
&= \left(\tilde{A}^T I \tilde{A}\right)^{-1} \tilde{A}^T I \tilde{l} \\
&= \left(\tilde{A}^T \tilde{A}\right)^{-1} \tilde{A}^T \tilde{l}
\end{aligned} \tag{2.24}$$

with a transformation or filter matrix F. The covariance matrix of the filtered observation $\tilde{P}_{ll} = I$ equals the identity, implying uncorrelated observations $\tilde{l}$. $\tilde{A}$ and $\tilde{l}$ are now transformed by F to another basis. The key advantage is the possibility to perform the filtering as a sequence of operations in time. This allows filtering very long time series without explicitly setting up full equation systems like the first row of equation (2.24). One drawback of the ARMA filter approach, although very small in the context of the experiments carried out within this thesis, is the so called filter warm-up time as discussed in Schuh [2003]. Its impact and how it is dealt with is addressed in chapter 3. Whilst understanding F as filter matrix, one can add white or colored noise to the system using the inverse function of the filter response. The design of a filter matrix F and its application in the context of the mission simulation environment is also addressed in chapter 3.

2.4 Measures to evaluate gravity field solutions in spherical harmonics

Performing the processing of gravity field estimates in the spectral domain has some big advantages. From a perspective of computational costs and efficiency, working in the frequency domain is by far more efficient than working in the spatial domain. In the frequency domain filter operations can be formulated as simple multiplications, whereas in the spatial domain they become complex convolution operations (cf. section 4.3.3 and 4.3.4). An also very important fact is the storage of covariance information $Q_{\hat{x}\hat{x}}$ (since these matrices are fully populated) in the spectral domain. A representation of covariance information in the spatial domain would need to be made for every grid point the potential field is evaluated for. Since grids are usually at least at a one degree resolution (360 by 180 grid points), this would be 64800 matrices of 518 KB each or 33.59 GB in total compared to 1.71 GB for a spectral representation up to $l_{\max} = 120$. The calculation regarding the hard disk storage requirements assumes double precision. These

circumstances suggest working in the spectral domain as long as possible during the processing algorithm and just perform a SH synthesis (cf. equation (2.3)) to finally visualize the results.

Measures for assessing the quality and properties of potential or residual potential fields represented in spherical harmonics are:

Degree variances

$$c_l^2 = \sum_{m=0}^{l} \left(\bar{C}_{lm}^2 + \bar{S}_{lm}^2 \right) \tag{2.25}$$

Degree amplitudes

$$c_l = \sqrt{c_l^2} = \sqrt{\sum_{m=0}^{l} \left(\bar{C}_{lm}^2 + \bar{S}_{lm}^2 \right)} \tag{2.26}$$

Cumulative degree amplitudes

$$c_l^{\text{cum}} = \sqrt{\sum_{n=l_{\min}}^{l} c_l^2 \left(n \right)} \tag{2.27}$$

Order variances

$$o_m^2 = \sum_{l=m}^{l_{\max}} \left(\bar{C}_{lm}^2 + \bar{S}_{lm}^2 \right) \tag{2.28}$$

Phase and amplitude of SH coefficients

$$\text{phase}\left(lm \right) = \arctan\left(\bar{S}_{lm} \Big/ \bar{C}_{lm} \right) \quad \text{with} \quad \text{phase}\ \left(lm \right) \in \left[-\pi,\ \pi \right] \tag{2.29}$$

$$\text{amplitude}\left(lm \right) = \sqrt{\bar{C}_{lm}^2 + \bar{S}_{lm}^2} \tag{2.30}$$

By applying the factor R_E to the quantities above, they can also be expressed in terms of geoid height. The operation expressed by equations (2.25) to (2.27) can be applied not only to SH coefficients, but also to their variance respectively standard deviations delivering e.g. error degree amplitudes. These error degree amplitudes or variances must not be mixed up with the cumulative geoid errors from the closed loop experiments which are computed from residuals.

Not only the analysis of formal variance or covariance information is of interest, but also investigations regarding empirical covariance information from gravity field time series. A comparison of formal and empirical covariance information allows testing the match of their characteristics and provides information about the features of the stochastic modelling during the estimation process. In section 4.3.2 a description is provided of how empirical error covariance matrices are derived and how they can be evaluated. Measures to evaluate them are e.g. correlation patterns in the spatial domain or RMS of correlations between specific SH degrees and/or orders.

2.5 Treatment of AO and OT variations – The de-aliasing problem

This section gives a brief overview of the problem of undersampling signals. One basic relation in the context of undersampling high frequency signals is given by the Nyquist theorem [Shannon 1949] $f_{Ny} = 1/2\Delta t$, with the Nyquist frequency f_{Ny} and the sampling interval Δt. Following e.g. the explanations regarding aliasing in the context of gravity satellite missions by Murböck [2015],

with f_{Ny} defining the lower bound of the sampling frequency, one must sample a signal x at least with the frequency f_x. If this criterion is violated, f_x cannot be reconstructed and, as a result, aliasing occurs. The frequency of the aliased signal f_{alias} equals to $f_{alias} = \left|\mathrm{mod}\left(f_x + f_{Ny}, 2f_{Ny}\right) - f_{Ny}\right|$. From the above one can understand the effect of choosing sampling frequencies of a target signal too low, illustrated in Figure 2-2. It illustrates on the basis of a simple 1D example of a continuous cosine series with 10 second period (black curve) the aliasing introduced by undersampling the target frequency. The red dots and blue circles show exemplary the discrete sampling points using 3 second (red) or 8 second (blue) sampling intervals. The blue dashed line illustrates the reconstructed signal from the 8 second sampling intervals. By comparing the black and dashed blue line, conclusively the target signal was not mapped with a sufficient sampling rate.

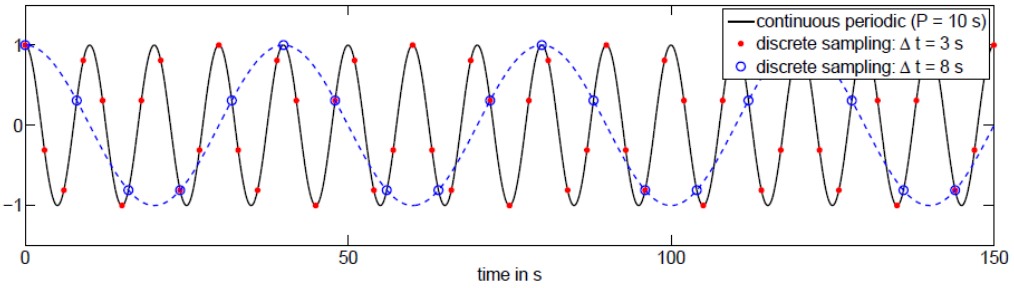

Figure 2-2: Temporal aliasing in case of a 1D time series. A normalized continuous cosine time series with 10 second period (black), sampled with 3 (red) and 8 (blue) second sampling. Reconstructed signal from 8 second sampling in dashed blue line. Credits: Murböck [2015].

This effect of undersampling can be transferred to gravity field missions. Several studies investigating the effect of aliasing and its impact on gravity field retrieval, using GRACE observations, have been carried out [Han et al. 2004; Thompson et al. 2004; Seo et al. 2008; Visser et al. 2010]. Undersampling, and thus aliasing, occurs with every satellite mission to a certain extent. Since the ground track separation has a finite distance, the temporal resolution of the observations made has a limited sampling rate, and the stretch of observations is confined in time. In real world applications temporal aliasing occurs and cannot be avoided. In the case of GRACE nearby locations on the Earth's surface, which are subject to changes in e.g. hydrological or atmospheric conditions in time, are observed with large temporal difference. This is due to properties of the orbit. Accordingly the observations contain different states of atmospheric or hydrological conditions. Since these variations are within the timeframe of one gravity field estimate, this single set of SH coefficients does not allow for reconstructing the variations, leading to errors or noise. This circumstance cannot be totally avoided and is compensated by the use of model data to minimize these effects. In the actual GRACE processing (cf. e.g. [Dahle 2014]), the high frequency AO variations are reduced using a specific de-aliasing product, namely the AOD1B products (cf. [Flechtner et al. 2015]). The ocean tide signal is reduced by using again model information from an ocean tide model (cf. [Savcenko and Bosch 2012]). As further analysis will show, the de-aliasing products and procedures apparently inherit certain deficits, which result in distorted solutions. By inspecting the cyan (ocean tide error) and aubergine-colored (atmosphere and ocean de-aliasing error) lines in Figure 1-2, one can identify them being among the most dominant contributors to the GRACE error budget.

As introduced, different sources causing aliasing exist in the context of GRACE-like missions: aliasing induced by non-tidal and tidal signals. Aliasing periods caused by tides are e.g. given by Ray [2003]. One tidal period considered in subsequent investigations (cf. section 4.3.2) is the S_2 161-day period. It is part of the functional model applied for estimating trends, since its amplitude is influencing the estimation process for mass trend signals. Characteristics of the AO signals are discussed in section 4.1.

Another interesting aspect is how de-aliasing errors map to certain sets of SH coefficients. Murböck et al. [2014] summarize, based on the findings of the semi-analytical approach [Sneeuw 2000], the relation of orbit defining Kepler elements and resonances within specific SH orders in gravity field solutions. Foundations in this context also can be found in Kaula [1966] and Lambeck [1988]. For the rate (rad/s) of the argument of the latitude $\dot{u}$ and the longitude of the ascending node $\dot{\Lambda}$ holds:

$$\dot{u} = \dot{\omega} + \dot{M} = n + \frac{3}{2} n J_2 \left(\frac{a_e}{a_s} \right)^2 \left(4\cos^2 i - 1 \right) \tag{2.31}$$

$$\dot{\Lambda} = \dot{\Omega} - \dot{\theta} = -\frac{3}{2} n J_2 \left(\frac{a_e}{a_s} \right)^2 \cos i - \dot{\theta} \tag{2.32}$$

ω … argument of perigee
M … mean anomaly
Ω … right ascension of the ascending node
i … inclination
θ … Greenwich sidereal time
n … mean motion
a_e … Earth's semi-major axis
a_s … satellites semi-major axis
J_2 … Earth's flattening (cf. section 4.2.2)

Following Sneeuw [2000], it reads for the orbital angular variable and signal spectrum $\dot{\psi}_{mk}$, using equation (2.31) and (2.32),

$$\dot{\psi}_{mk} = k\dot{u} + m\dot{\Lambda} \tag{2.33}$$

with $-l_{max} \le k \le l_{max}$ and $0 \le m \le l_{max}$. The rates, given in units of rad/s, can be transformed to frequencies, in units of 1/s = Hz, by dividing them by 2π. Murböck et al. [2014] evaluate the relation given by equation (2.33) for GRACE orbits in a simulation environment. The absolute minimum frequencies derived from $\dot{\psi}_{mk}$ exhibit local maxima for orders m being integer multiples of ≈ 15. The number of approximately 15 is correlated with the number of revolutions of the spacecraft around the Earth per day N_{rev}/N_{day} . For GRACE this number nominally lies between 15 and 16. Murböck et al. [2014] further analyze residual order variances (cf. equation (2.28)) of a series of real monthly GRACE solutions and compare them with the absolute minimum frequencies obtained from the orbit configuration analysis described above. They report very good agreement between the occurrence of dominant order resonances and the absolute minima of the respective frequencies from $\dot{\psi}_{mk}$ in terms of order m and time.

These findings suggest AO and OT de-aliasing errors being projected to specific sets of coefficients. These coefficients are predominantly the ones with SH orders being multiples of ≈ 15 and lower SH degree. Seo et al. [2008] elaborate similar conclusions, performing experiments on how de-aliasing errors map to specific groups of SH coefficients. They not only find specific orders predominantly influenced by de-aliasing errors, but also reveal that errors map on coefficients differentiated by even and odd SH degree. Seo et al. [2008] subsume after testing the influence of single frequency error contributions, that if introducing an error for a certain order m, the result is a linear combination of the error input and the Kaula resonance orders. It appears that SH coefficients of a certain SH order with same parity of the SH degree carry aliasing error. Such an error can, according to the above, be called correlated error. This finding is of great importance since e.g. the empirical filter approach by Swenson and Wahr [2006] is built on these properties (cf. section 5.2).

The investigations regarding the properties of actual GRACE time series in section 4.3.2 also exhibit such correlated structures embedded in the normal equation respectively the error covariance matrices. As outlined in the respective section, they exhibit changes in time since the

orbital configuration of GRACE is evolving. Murböck et al. [2016] show very good agreement between such SH order dominated correlations, derived from formal GRACE error covariance matrices, with the resonance frequencies deduced from $\dot{\psi}_{mk}$ in terms of order m.

In the context of future mission scenarios and the aim to minimize the influence of aliasing effects introduced by unfavorable orbit configurations, Murböck [2015] describes illustratively the connection between orbital mission parameters (e.g. height and repeat frequency) and the occurrence of temporal aliasing. Favorable orbital heights and inclinations to minimize the mapping of de-aliasing errors to the estimates solutions are identified. The findings on the temporal evolution of SH order resonances for GRACE orbits are in good agreement with the results of the investigations derived within this thesis from the correlation structure in GRACE normal equations (cf. section 4.3.2).

Seo et al. [2008] and Visser et al. [2010] state, among others, that the key factor for the advancement of future gravimetry missions, aiming for better spatial and temporal resolution, is to overcome the dependency on insufficient de-aliasing models. One option is to tailor the mission design parameters towards promising configurations [Visser et al. 2010; Murböck et al. 2014]. Another option discussed lately is changing the parametrization of the estimation process by e.g. co-estimating certain tidal constituents, or by estimating short term daily AO variations and reducing them on the level of normal equations [Kurtenbach 2011; Daras et al. 2015; Daras 2016; Mayer-Gürr et al. 2016a].

3. Simulation environment for closed loop tests

The following chapter explains the simulation environment used and sets focus on the design and implementation of deterministic and stochastic error contributions in the simulation runs. The design of the error budget is of high importance. It defines the rate of recoverability of the input signal, whether it is static or time variable, and creates, in conjunction with the orbits used, the different kinds of gravity field missions investigated. The setting needs to be made carefully since the rating of performance and applicability of different post-processing methods is based on the properties of the filtered residual field. Figure 3-1 gives a schematic overview of the simulation environment and illustrates all major steps carried out in order to derive from the input datasets a final gravity field estimate.

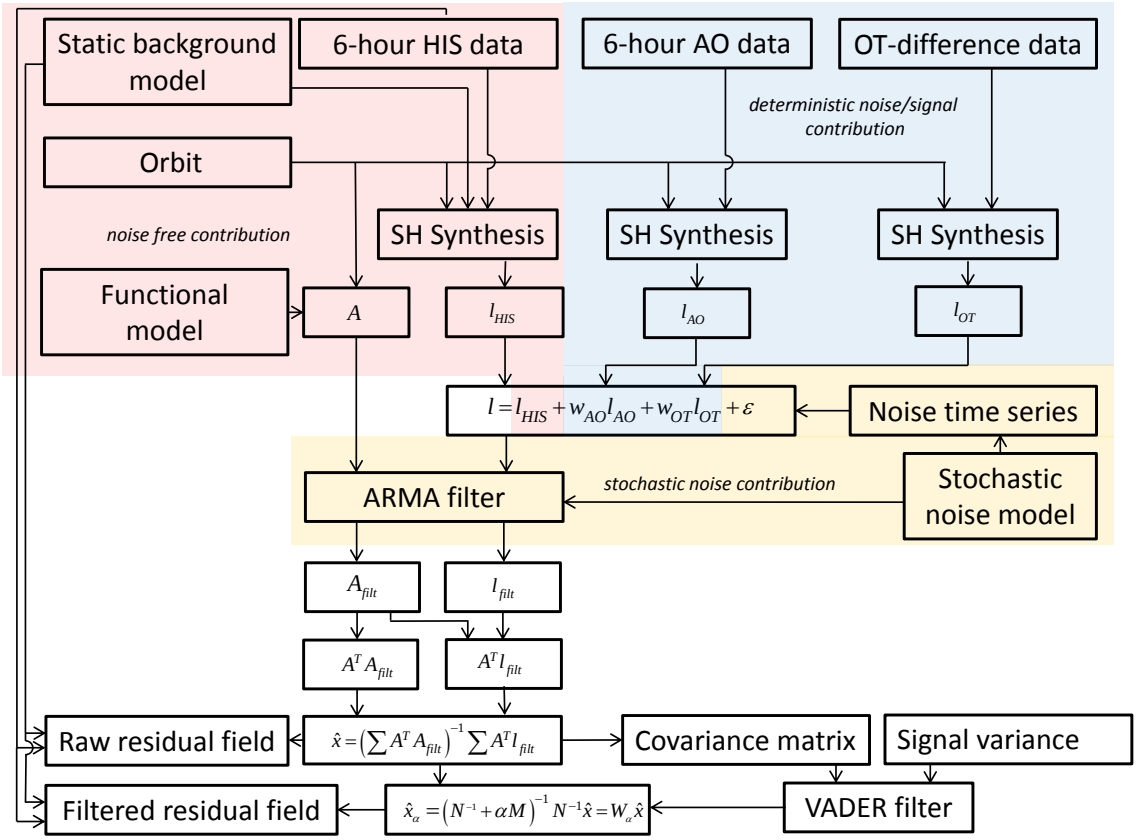

Figure 3-1: Flow chart illustrating the setup of the closed loop (CL) simulation environment.

The simulation approach implemented is the so called numerical "Linear Closed Loop approach" (LCLA) as described and implemented by e.g. Murböck et al. [2014]. It is based on the "acceleration approach" introduced by Rummel [1979]. It allows estimating a gravity field solution in e.g. spherical harmonics, derived from the acceleration differences experienced between e.g. two spacecraft without linearization or prior knowledge about the gravity field due to the linear relation between the acceleration differences and the unknown gravity field parameters C_{lm} and S_{lm}, represented by $\hat{x}$ in the simulator flowchart. Equation (3.1) gives the functional model for the application of the ll-SST principle in the estimation process.

$$\hat{\mathbf{l}}_{ll-SST} = \left\langle \Delta\mathbf{a}_{grav}, \Delta\mathbf{r}_0 \right\rangle \tag{3.1}$$

With $\hat{\mathbf{l}}_{ll-SST}$ being the acceleration differences along the line of sight (LoS) vector, calculated from $\Delta\mathbf{r}_0$, the unit vector pointing from satellite A to satellite B, and $\Delta\mathbf{a}_{grav}$, the difference in acceleration experienced between the two spacecraft, caused by the gravitational potential V outside the mass distribution of the acting body, located at different positions.

The accelerations experienced by each of the two spacecraft are derived from the gravitational potential V at the corresponding spacecraft position. Rummel [1986] illustrates the connection between the acceleration vector $\Delta\mathbf{a}_{grav}$, the Marussi tensor $\mathbf{M}$, and the distance vector $\mathbf{d}$ between two spacecraft, based on Newton's second law of motion, as

$$\Delta\mathbf{a}_{grav} = \mathbf{M}\mathbf{d} \tag{3.2}$$

Not only gravitational accelerations (gravitational in the sense of caused by the body of the Earth) act on a satellite, but also non-gravitational accelerations $\mathbf{a}_{non-grav}$ like e.g. atmospheric drag or solar radiation pressure. Since all constituents of the total acceleration $\mathbf{a}_{total}$ are acting in a superimposed way, the non-gravitational accelerations need to be subtracted leaving a modified version of equation (3.1).

$$\begin{aligned} \hat{\mathbf{l}}_{ll-SST} &= \left\langle \Delta\mathbf{a}_{total}, \Delta\mathbf{r}_0 \right\rangle - \left\langle \Delta\mathbf{a}_{non-grav}, \Delta\mathbf{r}_0 \right\rangle \\ &= \left\langle \left(\Delta\mathbf{a}_{total} - \Delta\mathbf{a}_{non-grav} \right), \Delta\mathbf{r}_0 \right\rangle \end{aligned} \tag{3.3}$$

In the case of GRACE-like measurement systems, this issue is solved by the use of accelerometers on board each spacecraft, which measure the non-gravitational accelerations acting on the spacecraft. Other disturbing sources of gravitational acceleration like tides are reduced by using models. In the simulation environment implemented for the later discussed experiments, a noise budget accounting for the reduction of non-gravitational forces is introduced by applying a dedicated accelerometer noise time series. The error budget components applied are discussed in detail later within this section.

The total accelerations $\mathbf{a}_{total}$ contain, as Rummel [1979] or e.g. Liu [2008] note, not only a distance change or range rate dependent term $\ddot{\rho}$, but also a velocity change dependent term (fraction on the right side of the equation), as equation (3.4) shows.

$$\left\langle \Delta\mathbf{a}_{total}, \Delta\mathbf{r}_0 \right\rangle = \ddot{\rho} + \frac{\dot{\rho}^2 - \left\| \Delta\dot{\mathbf{r}} \right\|^2}{\rho} \tag{3.4}$$

This so called velocity term is not considered due to applied simplifications in the setup of the simulation environment. Rummel [1979] or Liu [2008] rate the omission of the velocity term having a significant impact on the quality of the retrieved solution. Numerical simulations by Murböck [2015] show no significant deficits by omitting this term, as the ranging noise is assumed to be dominant with respect to the error made by the omission of the velocity term.

Since within this thesis the role of simulated gravity field estimates with their full error covariance matrices, originating from the closed loop simulator, is to serve as test objects for post-processing methods, the main criterion here, for the applicability of the LCLA, is the structure of the error covariances. Detailed investigations regarding the properties and similarities of the error covariance matrices of the simulator output and real GRACE error covariance matrices, provided by different processing centers, showing good agreement between the two types of covariance matrices, are presented in section 5.3.1.

In the following, the input for the least squares adjustment process presented in the simulator flowchart in Figure 3-1, especially the three groups of contributors, the noise free contributions

(red), the deterministic noise or signal contributions (blue), and the stochastic noise contributions (yellow), are explained. An overview of the realized scenarios, naming the respective datasets used, can be found in Table 3-1. The three center columns give an overview for the mission simulations performed, whereas the very right column indicates the setup of the deterministic noise contribution runs.

Table 3-1: Summary of the most important simulation run setups conducted

Scenario:	GRACE like	Future mission single pair	Future mission double pair	Optional Deterministic noise
ACC noise	White noise	Colored noise	Colored noise	Noise free
SST noise	White noise	Colored noise	Colored noise	Noise free
Orbits	Real GRACE orbit	Real GRACE orbit	Synthetic orbit	Real GRACE orbit or Synthetic orbit
Timeframe	11 years	11 years	1 year	11/1 year
l_{max}	120	120	120	120
Temporal resolution	Monthly (as defined by GRACE orbit)	Monthly (as defined by GRACE orbit)	Monthly (30 day solutions)	Monthly (as defined by GRACE orbit or 30 day)
Static background model	GOCO02S	GOCO02S	GOCO02S	-
Target signal	HIS	HIS	HIS	AO or OT differences
Optional deterministic error	AO OT differences	AO OT differences	AO OT differences	

For the closed loop experiments carried out within the framework of this thesis, all input models are expanded to the same SH degree ($l_{max}=120$) as the estimated solutions. The only exception are the OT differences, used to simulate optional deterministic noise, developed up to $l_{max}=80$.

Noise free contribution

The noise free contributions summarize all input datasets not representing noise in the sense of intentionally introduced noise. They are considered as noise free observations. One of the key datasets are the orbits. As Table 3-1 shows, real GRACE orbits [Zehentner and Mayer-Gürr 2016] are used for the GRACE-like and an advanced future mission concept assuming to have a GRACE-like constellation. Real orbits are used for the future mission case, since they suffer from real mission operation problems resulting in e.g. data gaps or changes of the orbital altitude. This results, as experiments in section 4.3 and chapter 6 show, in more realistic correlation structures than using synthetic circular or perfect repeat orbits. For the double pair scenario real orbits are not available, and thus simulated orbits from the SC4GMV study have to be used instead. The

nominal sampling rate for the real GRACE orbits is 10 seconds, and for the synthetic SC4GMV orbits 5 seconds. The timeframe and number of observations fed into the monthly estimate is defined by the real GRACE orbits and varies within certain bounds. For the SC4GMV orbits, the solutions are exactly 30 days long. Although not necessary, a static background field is fed into the simulated scenario representing the constant part of the total gravity field. The time variable part, represented by the HIS component of a simulated geophysical signal dataset with 6-hourly sampling intervals by Dobslaw et al. [2015b], serves as target signal to be observed. Between the 6-hourly intervals of the model, a linear interpolation between the two closest model snapshots is performed to derive the HIS signal at the time of the observation defined by the orbit timestamp.

Stochastic noise contribution

In the following, the stochastic noise contribution and the two implementations or designs for the noise time series applied, are discussed. The closed loop simulator can in principle be fed with any noise time series (cf. Figure 3-1). The only limiting factor is the later discussed filter degree for the autoregressive moving average (ARMA) filter (cf. section 2.3), which should be kept reasonably low due to performance issues like computational speed. The two noise time series designs (cf. Table 3-1) presented in the following are one less complex, but simple to construct, white noise time series and a more complex, but therefore also more realistic colored noise time series, based on the colored noise characteristics of an accelerometer and ranging instrument.

A very general approximate assumption regarding the measurement and system noise is to assume white noise. This is, as discussed below, not the most accurate representation of the noise budget present in gravity field mission scenarios, but can be assumed to be a first order approximation. The assessment regarding the amplitude of white noise is determined following the outlined approach. Figure 3-2 illustrates the results and the assessment carried out to determine a suitable level for the white noise time series. First, a monthly GRACE gravity field solution with its associated formal errors is selected. In the present case, the ITSG-Grace2014 time series is chosen since its formal errors, compared to others time series, do not tend to be too optimistic (cf. chapter 4.3.2). In a second step the residual monthly field (black solid curve) is computed by subtracting a constant field (here GOCO02S, magenta solid curve; associated formal error in dashed magenta curve). The formal error of the residual ITSG-Grace2014 field is shown as black dashed curve. A propagation of the error for the residual field was spared, since the static field is assumed to be error free. As shown in Figure 3-2, this is not fully true, but the formal error of the static field is about one order of magnitude smaller than the one of the monthly field.

The blue, red, and green solid curves show the residual field obtained from simulator runs. Input, serving as observation for these simulation runs, is always the same static field GOCO02S. Therefore the residuals of the simulation runs represent the real discrepancy or error between the original observations and the output from the simulator and should therefore be understood as error of the simulated test case configuration without containing aliasing errors induced by time variable signals observed. The match with the associated formal errors, represented by the dashed curves in the respective colors, indicates a good choice for the functional model and prior error estimate of the observations. The posteriori unit weight variance $\hat{\sigma}_0^2$ is close to one. The residual real GRACE field on the other side represents the residual time variable component of the Earth's gravity field not represented by the long term static solution, which was subtracted. These residuals are mainly composed by time variable geophysical signal constituents like HIS. This observation is supported by the good agreement between the cyan solid curve, representing mean HIS signal from the model by Dobslaw et al. [2015b], with the residual GRACE curve (black solid) in the range of SH degrees smaller 20. These differences in the compounding of the residual curves explain the spread between the GRACE estimate and the simulation run results in the area between SH degree 2 to 20. A distinct feature of all residual curves is their positive slope

starting from about SH degree 20. This slope is mainly due to the increasing level of error with increasing SH degree. Static signals are reduced and the most important residual signal components like HIS decrease in signal strength with increasing SH degree, as the cyan solid curves shows. In general, a decrease in signal amplitude per SH degree of the gravity field signal has to be expected from *"Kaula's rule of thumb"* [Kaula 1966].

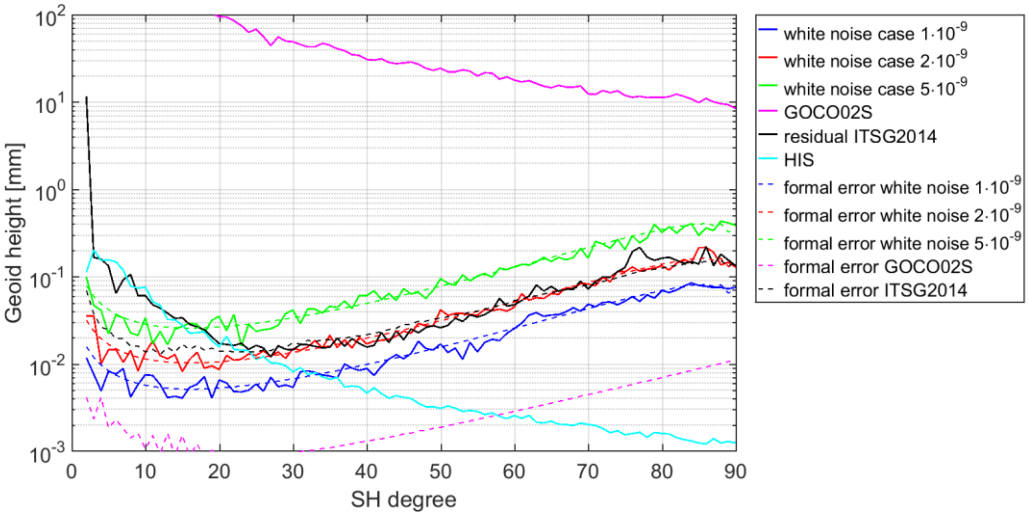

Figure 3-2: White noise test for closed loop experiments

The goal is now to find a system noise level (system stands for the simulation environment), which delivers an error behavior possibly matching the observed real world GRACE error. A choice for the white noise level of $2 \cdot 10^{-9}\,\mathrm{m\,s^{-2}}$ apparently fulfills this requirement. $1 \cdot 10^{-9}\,\mathrm{m\,s^{-2}}$ is too optimistic and $5 \cdot 10^{-9}\,\mathrm{m\,s^{-2}}$ is too pessimistic. In the following, a white noise level of $2 \cdot 10^{-9}\,\mathrm{m\,s^{-2}}$ serves as input used for the GRACE-like simulation runs analyzed in the subsequent chapters.

As mentioned above, the white noise characterization of the system error is fairly simple while easy to implement. Since more detailed knowledge regarding the contributors to the total system noise are known, a second refined noise model is set up and implemented in the course of work presented within this thesis. In the following, a colored noise model comprising accelerometer and satellite-to-satellite tracking noise is introduced. Other total noise budget contributors would be attitude errors. They are not addressed in the present study but could be included in future improvements of the closed loop simulation environment by projecting them as additional noise contribution into the LoS, respectively the ranging vector. They are to be considered containing a stochastic and deterministic part, since they depend on instrument characteristics and location resp. situation in space (solar drag, systematic mispointing etc.).

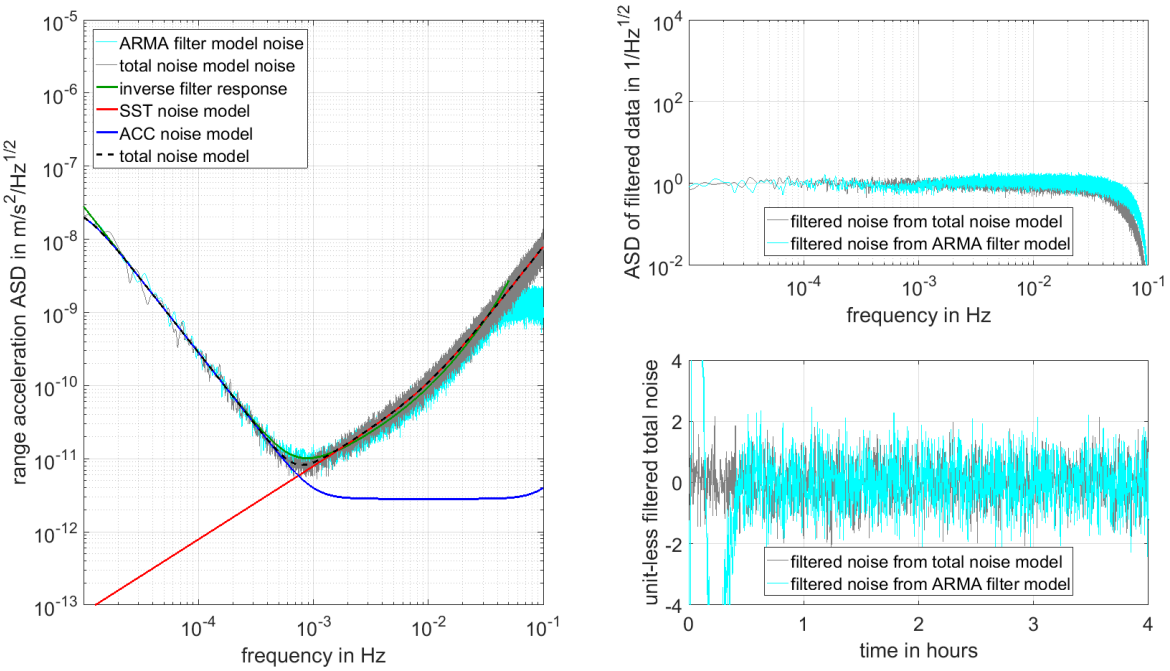

Figure 3-3: Colored noise case: Noise model and inverse filter

Figure 3-3 shows in the left panel the noise model for the assumptions regarding a, compared to GRACE, more advanced future mission scenario. The assumption on system performance for the accelerometer (ACC) and the satellite to satellite tracking (SST) device are aligned to the SC4MGV baseline 5 scenario. Detailed descriptions and discussions of how to derive such instrument characteristics can be found e.g. in [ESA 2010]. The blue line represents the performance of the ACC with respect to frequency. The ACC has a sensitivity introduced to the accelerometer error model of $2 \cdot 10^{-12}\,\mathrm{m\,s^{-2}}$ for frequencies f in the bandwidth $10^{-3}\,\mathrm{Hz} > f > 10^{-5}\,\mathrm{Hz}$. The blue line is drawn at $\sqrt{2} \cdot 2 \cdot 10^{-12}\,\mathrm{m\,s^{-2}}$ because the full system consists of two accelerometers, one on each satellite. The red line represents the noise model for the SST system (in this case a laser instrument instead of the K-band ranging instrument on GRACE). The total noise as an aggregation of ACC and SST noise is represented by the dashed black line. Since the use of an ARMA filter approach (cf. section 2.3) is very promising in terms of applicability and numerical efficiency, an inverse filter response (green) is approximated in order to best match the total noise model. Due to reasons of computational efficiency and simplicity of the filter function it was decided to implement a filter cascade consisting of, in this case, three simple filters. Namely a series of Butterworth type [Butterworth 1930] low and high pass filters of first and second order. From the two filter models now available (dashed black and solid green line) two noise time series can be constructed. The gray colored curve shows the ASD for the noise time series from the total noise model and the cyan curve the one from the ARMA filter model. As one can see from the upper right panel of Figure 3-3, this approximation appears valid since the ASD of the filtered noise time series filtered by the noise model (gray) is coinciding very well with the one filtered with the approximated ARMA model (cyan). A deviation from 1 indicates a non-confirming alignment between filter response and total noise model. One could estimate a higher order ARMA filter (cf. Stetter 2012), matching even better with the total noise model, but no significant benefit compared to the additional costs is expected. Tests have revealed a difference between the estimated signal from observations filtered with the noise model and the ARMA filter model of a factor of 50-100 smaller than the magnitude of the actual observed signal.

The only drawback of using an ARMA filter approach, in order to introduce a stochastic weighting in the least squares estimation process, is the filter warmup time as mentioned in section 2.3. The lower right panel of Figure 3-3 shows the filtered noise time series from the ARMA filter model (cyan) and the total noise model (gray). Very prominent is the deviation from the expected scattering at the very beginning of the time series (approximately first half hour corresponding to about 180 observations at 10 second sampling). This deviation is due to the abovementioned warmup time the filter needs to be able to reproduce the desired noise characteristics. To avoid negative impact on the estimated final solution, the observations suffering from the application of this deviated noise model are excluded from further processing. Including a safety buffer, the first 500 observations are excluded from further processing. For a typical monthly solution this cutoff is considered not critical since it translates to omitting about 0.2% of the total number of observations for 10 second sampling and even less for 5 second sampling rates.

Deterministic noise contribution

The deterministic noise contribution is introduced, since questions regarding de-aliasing should also be addressed in the performance evaluation and further development of post-processing methods. The AO component of the model by Dobslaw et al. [2015b] is observed with the same setup as the static gravity field and time variable HIS signal contribution, with the only difference being the applied stochastic noise contribution. Since the target is to simulate the effect of temporal aliasing due to insufficient sampling of short term signal variations caused mainly by the design of the orbit, stochastic noise must not be introduced to allow isolating the effect of aliasing from the degradation of the observations by deficits of the observing instruments. Therefore satellite instruments, namely the accelerometer and the inter-satellite ranging device, are assumed to work noise free. The introduction of this deterministic error contribution into the least squares estimation process is done on the level of normal equations.

The OT deterministic noise or error contribution is set up by taking the differences of two ocean tide models as upper bound of the error. These models are the EOT08a [Savcenko and Bosch 2008] and the FES2004 [Lyard et al. 2006] model. This contribution is expanded up to the maximum SH degree of 80. For SH degrees beyond, an ocean tide error is not considered due to the low amplitudes of power spectrum density of OT models.

4. Retrieval of geophysical signals

The main goal of gravity field missions dedicated to the retrieval of time variable gravity fields is exploring geophysical signals. But the term time variable itself is a quite vague description. The underlying geophysical processes, responsible for changes in the Earth's gravity field, show periods, ranging from hours to decades to centuries, not even ending in millennia. A detailed explanation can be found in the following section (4.1). Depending on the origin, geophysical signals can be of very small extent, e.g. hundreds of meters, or range to large extents of thousands of kilometers. How well these features are observed with today's and near future gravity field missions is introduced in the following. A second aspect discussed are the different spectral properties of geophysical and atmospheric processes. This circumstance, coupled with finite sampling rates and aggregated averages of observations in time, leads to the aforementioned issue of aliasing (cf. section 2.5). Since geophysical signals are superimposed, solid earth, hydrological, and cryospheric signals are collated with each other. Finding methods of separating them into their different sources of origin is a difficult or sometimes even impossible task. To retrieve geophysical signal information from today's time variable gravity field estimates, certain processing steps are necessary to overcome some deficits coming along with the initial estimates. Questions like the right degree of expansion, applicable correction, or the issue of leakage and integration kernels are addressed in section 4.2. Section 4.3 recaptures the state of the art in GRACE post-processing by introducing the main types of gravity field solutions and giving an in-depth analysis of available level-2 products in the SH domain. An overview of established isotropic, anisotropic, and decorrelation technique dependent filters is provided to allow classifying the two filter concepts presented within this thesis.

4.1 Detectable geophysical signals

In September 2014 a consultation meeting was held in Herrsching (Germany), gathering together scientists from different peer groups such as hydrology, ocean, cryosphere, and solid earth science. The goal of the meeting was to define the user needs for future satellite gravity missions. Important aspects discussed were the identification of valuable target signals and the required observational accuracy and capabilities to reach these targets. Pail et al. [2015] describe the collected ideas and output from the meeting. Two major findings are of relevance with respect to the topics of this thesis. First, the assessment which geophysical signals can be observed with actual and near future satellite gravity field missions, and second the classification of the various signal sources in terms of spatial and temporal extent as well as signal amplitude. For hydrological and cryospheric processes, examples are given in Figure 4-1. The upper two panels describe the spatial extent of the different subcategories against the amplitude in mm EWH. The lower two panels characterize the same features with respect to their amplitude per year. The black, dark gray, and light gray lines represent the capabilities of GRACE (black), a future threshold scenario (dark gray), and an even more ambitious target scenario for the far future (light gray). The threshold scenario is in terms of performance similar to the polar only pair presented in chapter 1. A variety of features is shown in the different bubbles, indicating the spatial extent (resolution) of the signals against their amplitude respectively amplitude per year. As one can see from the GRACE performance curve (black), most of the features cannot be observed. Since the understanding of geophysical and climatological processes is not only interesting for science, but of major importance for mankind in general, any improvement made in raising the accuracy and retrievability of geophysical signals is of value.

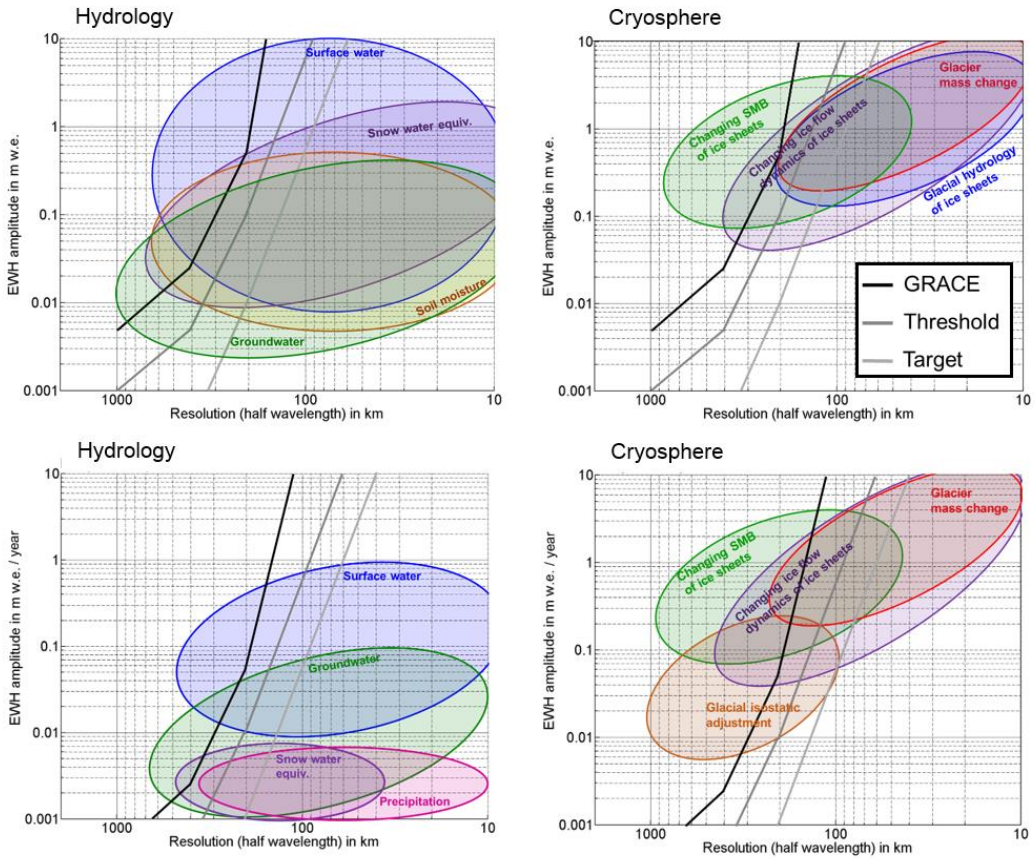

Figure 4-1: Hydrological and cryospheric features in terms of their spatial extent (resolution) against their amplitude (upper panels) and amplitude per year (lower panels). Credits: [Pail et al. 2015].

Some of the features observed with GRACE, mentioned in section 1.1, are as one can see from Figure 4-1, only the "tip of the iceberg". One particular process is groundwater. The groundwater depletion analyzed by Tiwari et al. [2009] is one of the major events of such kind. Another example is the depletion in California's Central Valley [Famiglietti et al. 2011]. There are numerous other places where groundwater depletion occurs but is not captured, as the black GRACE performance line indicates. Knowledge about such processes helps to understand the underlying individual processes of depletion and renewal and helps to sustain natural resources. A second particular process is the dynamics of ice sheets. In Figure 4-1, this general term is divided into several sub processes. By comparing the spatial extent and amplitudes of the ice mass trend derived from altimetry with the respective results from GRACE, as shown in Figure 4-3, it becomes clear which gap there is to close by improving gravity signal retrieval from space missions. Although one should keep in mind that a similar spatial accuracy as from radar altimetry cannot be achieved using gravity space missions, because of the decrease in potential with increasing orbital height, thus limiting the spatial resolution.

Figure 4-2 shows SH degree amplitudes for atmospheric (A) and ocean (O) signals compared to hydrological (H), ice (I), and solid earth (S) signals. A clear discrepancy between the frequencies, derived by a Fourier analysis of the AOHIS time series [Gruber et al. 2011] for January 2005, and the respective amplitude can be observed. HIS signals tend to show much smaller short term variations compared to AO signals. Since the GRACE averaging period is nominally 30 days for the monthly solutions, large signal variations of the AO component occur. These variations are, since they are undersampled and imperfectly reduced from the estimates, the reason for temporal non-tidal aliasing (cf. section 2.5). The blue solid line indicates the theoretical maximum SH order

of a gravity field solution calculated from the Colombo-Nyquist theorem [Weigelt et al. 2013]. For a double pair, with double the number of observations (referring to revolutions per day), the maximum retrievable SH order increases as indicated by the dashed blue line.

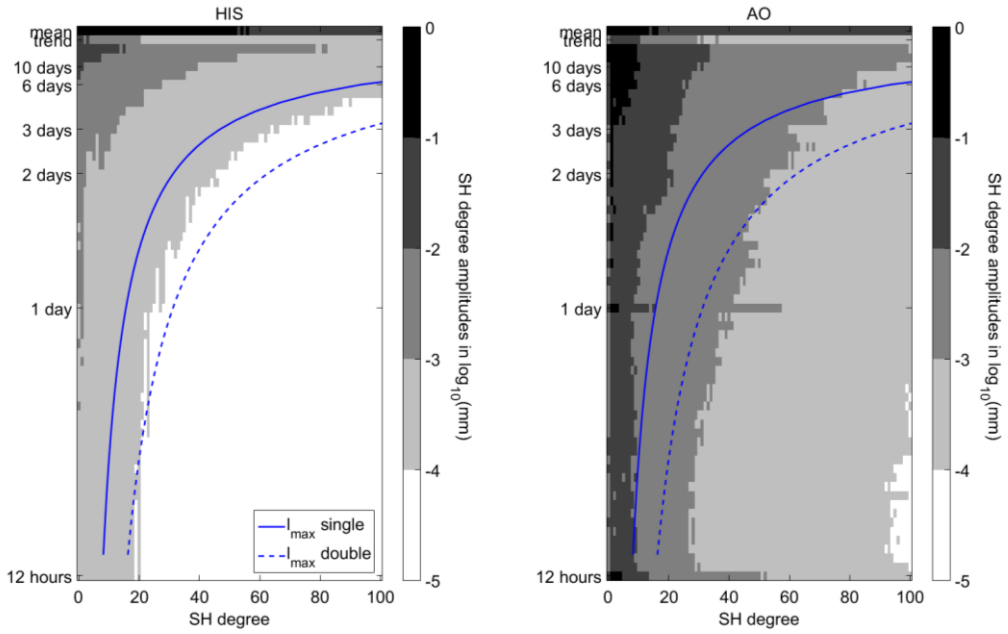

Figure 4-2: SH degree amplitudes in $\log_{10}$ (mm) geoid heights of non-tidal temporal HIS (left panel) and AO (right panel) variations depending on the period (days). The blue lines approximate the maximum possible SH degree of expansion for a single and double pair respectively. Credits: [Murböck 2015]

4.2 Processing steps from time variable gravity field solutions to mass trends

From the introduction of detectable geophysical signals in the previous section it is clear that the spatial resolution of GRACE is much too coarse to observe a large proportion of the target signals. Since gravity field solutions can only be estimated from GRACE observations to a certain degree of SH expansion, a proper definition has to be established up to which degree a SH expansion makes sense (section 4.2.1). To achieve the performance level in terms of signal retrieval indicated for GRACE in Figure 4-1, different corrections need to be applied to GRACE time series in order to cope with deficiencies in e.g. the C_{20} coefficients and other parameters (section 4.2.2). The issue of leakage induced by insufficient sampling of the target signals in terms of localization and spectral sampling (section 4.2.3) is addressed in conjunction with the mechanism to derive mass balance estimates from areas of interest (section 4.2.4).

4.2.1 The right degree of expansion

As explained in section 4.3.1, different series of gravity field solutions are available. They show different degrees of SH expansion, going from $l_{max} = 60$, 90 or 96 even up to 120. Consequently the question arises whether it makes sense to include information of higher degrees, e.g. from degree 61 to 90/96 or even beyond. From the investigations shown in section 4.3.2, it can be expected to encounter worse signal to noise ratio for higher degrees as the target signals decrease in amplitude by Kaula's rule of thumb whereas the noise is increasing. Does it make sense to include datasets into the analysis containing SH coefficients beyond $l_{max} = 60$ or even beyond $l_{max} = 90$? To examine this issue an experiment is conducted. Figure 4-3 shows examples of a linear trend, estimated from the CSR96-RL05 time series expanded up to $l_{max} = 60$ (panel a), up to $l_{max} = 90$ (panel b), a high resolution linear trend estimated from ICESat [Zwally et al. 2002] laser altimetry [Groh et al. 2014] (panel d), and the high resolution altimetry trend filtered with a 250 km Gaussian filter (panel c). The two results from GRACE are filtered with an optimized version of the S&W filter version two [Swenson and Wahr 2006]. For details on the filter parameters see section 5.2. For the unfiltered high resolution trend, a different colorbar limit is used for better readability. All four panels show results in mm EWH year^{-1}. Before the experiment is discussed, one should be aware that the direct comparison between GRACE and radar altimetry trends is only partially valid, since they observe different quantities. Altimetry mass change estimates are derived from surface height changes in a certain time interval, e.g. changes in geometry, resulting in volume changes. These volume changes are further combined with assumptions regarding the density of the volume body, e.g. the ice density, delivering mass change per time interval. A description of deriving mass change from radar altimetry observations can be found e.g. in Wingham et al. [2006]. GRACE derived mass change estimates on the other hand embed superimposed contributions from all mass redistribution processes whether they result in surface geometry variations or not. The main difference in mass change estimates from the two techniques is induced by glacial isostatic adjustment processes (cf. section 4.2.2). Another effect, potentially causing differences, are non-synchronous time frames covered by the respective measurement time series. This discrepancy is potentially causing different slopes for the linear component of the mass change estimate. The difference in the area of Dronning Maud and Enderby Land (cf. map of Antarctica in the Appendix section) is mainly due to such an only partially overlapping timeframe of the high resolution altimetry trend and the GRACE timeframe. Since the ICESat operational phase ended in 2009, the positive anomaly in these regions is not present in this dataset [Groh et al. 2014].

The comparison between GRACE and altimetry trends should at this stage only be made on a qualitative basis, comparing e.g. the signal amplitudes and general signal distribution patterns. A qualitative benchmark regarding amplitudes is set by the spectrally filtered solution in the lower left panel. It is, as mentioned, filtered with a 250km Gaussian filter and is therefore within the range of the spectral resolution of GRACE, which can be expected to be around 300 km [Murböck 2015]. By comparing the two upper panels (a) and (b) from Figure 4-3 with panel (c), one can observe a much better match in signal amplitudes for the trend derived from the SH expansion of $l_{max} = 90$, than for $l_{max} = 60$. The extremum in the Amundsen Sea Sector is –271 mm EWH year^{-1} for $l_{max} = 90$ and -231 mm EWH year^{-1} for $l_{max} = 60$ versus –276 mm EWH year^{-1} for the smoothed altimetry trend. For the positive trend in Marie Byrd Land the amplitudes are +56 mm EWH year^{-1} and +78 mm EWH year^{-1} for the $l_{max} = 60$ respectively $l_{max} = 90$ solutions against +77 mm EWH year^{-1} for the smoothed altimetry trend. The lower expansion apparently causes attenuation of the signal amplitudes and does not allow, due to its stronger spectral limitation, recovering the mass change signals with the required resolution. A higher degree of SH expansion allows representing signals having a glaciologically more plausible geographic attribution. This applies especially for the dominant signals in West Antarctica. The effect of glacial isostatic adjustment (GIA), discussed in section 4.2.2, is not addressed in this comparison. The impact of applying a

GIA correction can be derived from Figure 4-8 and lies within a range of –5 to +20 mm EWH year^{-1}.

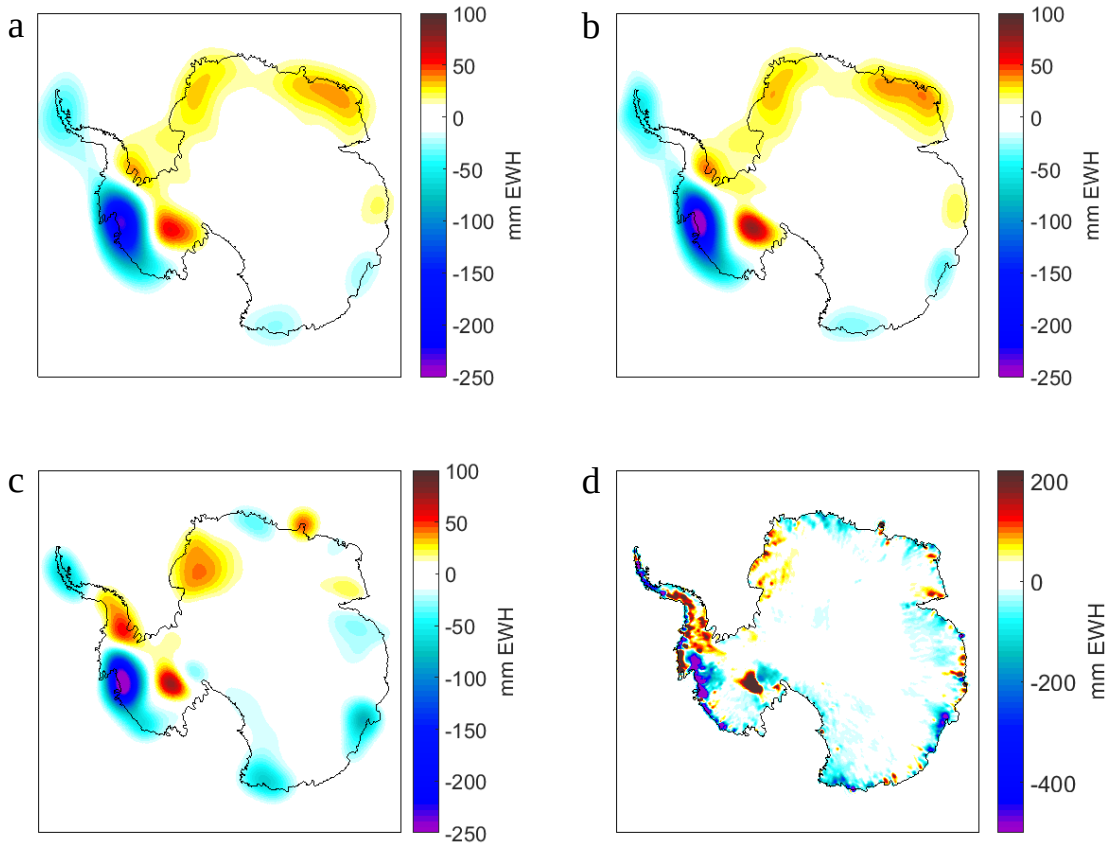

Figure 4-3: Linear trend estimates in mm EWH year^{-1} from CSR96-RL05 time series truncated to l_{max}=60 (a), from CSR96-RL05 time series without truncation (b), from high resolution altimetry trend filtered with a 250 km Gaussian filter (c), and from a high resolution altimetry trend without filtering (d). Note different scaling of the colorbar for panel (d).

Another feature to observe is the leakage-out effect (cf. section 4.2.3) for the solution developed to $l_{max} = 60$. Less pronounced leakage-out effect can be observed for the $l_{max} = 90$ trend signal, leading towards a more plausible distribution of trend signal. Large trend signals are not to be expected e.g. in ocean areas.

The second assessment regarding a suitable degree of expansion is the comparison of commission versus omission error in e.g. the region of Antarctica. The assessment follows an approach discussed by Horwath et al. [2013a]. The commission error is determined as the RMS of the formal error of the linear trend, taken over the region south of –60° latitude. The underlying monthly gravity field solutions are the CSR96-RL05 solutions. The omission error assessment is based on the altimetry-based high resolution trend $\kappa(\varphi,\lambda)$, shown in panel (d) of Figure 4-3, capturing the characteristics of both ice-dynamics and accumulation-driven signals. The omission error is then defined as $\mathrm{RMS}\left(\kappa - \kappa^{\mathrm{trunc}}\right)$, where κ^{trunc} is the spectrally truncated version of κ according to the chosen maximum SH degree. Figure 4-4 depicts the SH degree dependent development of the RMS of the linear mass trend expressed in mm EWH year^{-1}. The red line shows the evolution of the commission error, derived as described above, not intersecting the blue line representing the omission error for the region south of –60° latitude.

Even though quantitative details of this analysis depend on specifics of applied assumptions and techniques, the conclusion can be drawn that, for resolving the large Antarctic mass changes, a SH degree beyond 100 would be most appropriate. Specifics would be the degree of smoothing for

the commission error determination, or the degree of SH expansion for the high resolution altimetry trend, serving as benchmark of the signal content.

For regions closer to the equator this assumption cannot be upheld anymore, because of the different orbital coverage (larger ground track spacing) and higher noise level in the solutions (cf. e.g. Figure 4-11). In lower latitudes also larger problems due to temporal aliasing occur, since atmospheric and ocean mass variations have larger amplitudes between the polar circles [Kandel 1980], although the accuracy of the de-aliasing models is weaker in high latitudes.

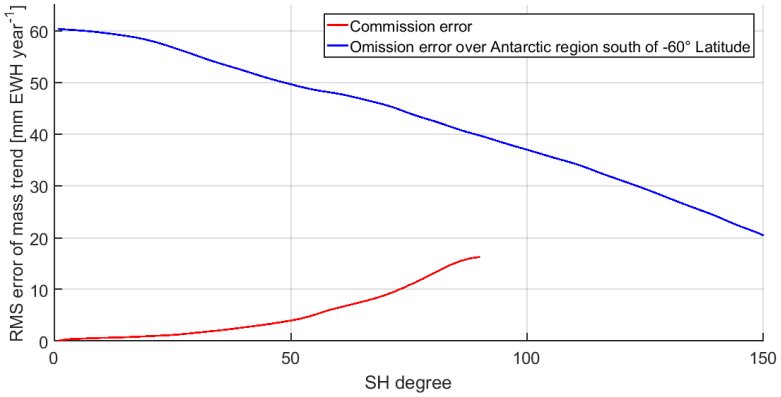

Figure 4-4: Errors of commission (based on the CSR96-RL05 series) and omission (based on a high resolution altimetry dataset) for Antarctic ice mass trends for different maximum degrees in mm EWH year^{-1}.

Wahr et al. [1998] expected, before GRACE was launched, meaningful signal to be extracted only for expansions of $l_{\max} \approx 100$. The experiments showed that at least for polar and high latitude regions, a SH degree beyond 100 for GRACE time variable models is appropriate.

4.2.2 Applicable corrections to cope with deficiencies in GRACE gravity field estimates

In the course of GRACE data processing some corrections, depending on the application, can be applied to cope with specific deficiencies in GRACE data, e.g. inaccurate C_{20} coefficients or missing degree one terms. Other corrections like the surface mass balance correction are less a classic correction but a technique to subtract high-frequency non-target geophysical signals from the time series in order to better resolve the actual target signal. The GIA is a classic geophysical correction separating superimposed signal contributions in order to retrieve target signals isolated from unwanted signal contributions. In the following the four mentioned corrections are introduced in more detail.

Each correction comes along with its own uncertainty. For the GIA correction, an uncertainty is estimated from analyzing the variability of an ensemble of GIA models. For the C_{20} and degree one coefficients, an error estimate is derived by analyzing the error noise from a residual mass time series. This residual mass time series is derived from the respective coefficients which are reduced by a six-parameter model. The reduction is performed to isolate portions of signal not induced by mass redistribution features. For the SMB correction no dedicated error budget contribution is estimated.

C_{20} correction

The reason for variations in the C_{20} coefficient, also called J_2 variations, is the dynamic in the Earth's oblateness. First reports of such C_{20} variations observed by satellite laser ranging (SLR) were made by Yoder et al. [1983]. They connect the variations observed mainly to tidal deformations, seasonal variations in groundwater, changes in mean sea level, and viscous rebound in northern Canada. Later analysis of longer SLR time series (e.g. Cheng and Tapley 2004) show changes in C_{20} due to periodical variations in the global distribution of atmosphere and water masses. The temporal extent ranges from seasonal or interannual over decadal and 18.6 year to secular periods. C_{20} variations due to long term (considering decadal or secular time frames) linear effects, induced by glacial isostatic adjustment processes, are described by e.g. Peltier [1983]. Since the GRACE measurement concept is not ideally designed to observe the C_{20} term, the initial estimates originating from GRACE observations exhibit deficits in accuracy. A common way to overcome this problem is to replace them with estimates originating from SLR observations. The C_{20} replacement coefficients used in the further processing are described in Cheng et al. [2013b] and are taken from the time series provided by GRACE technical note TN-07 [Cheng and Ries 2016].

One should note that the retrieval of C_{20} from GRACE itself underwent great improvements over the last years. Klinger and Mayer-Gürr [2016] report the C_{20} coefficient of the ITSG-Grace2016 time series being of almost equal quality when derived from GRACE itself as compared to the SLR derived coefficients. Figure 4-5 shows a comparison of C_{20} coefficients of the CSR96-RL05 (blue), ITSG-Grace2014 (orange), and ITSG-Grace2016 (green) GRACE time series compared to the time series derived from SLR observations (red; GRACE TN-07). A clear improvement is visible by switching from ITSG-Grace2014, which exhibits similar values for the C_{20} coefficient as the CSR-96 time series, to ITSG-Grace2016. This improvement is, as Klinger and Mayer-Gürr [2016] report, due to their more sophisticated accelerometer calibration. From 2015 onwards, the coefficients from ITSG-Grace2016 start to show significant deviations from the SLR coefficients. This deviation is due to changes in the GRACE operations, especially the change of the on-board temperature, leading to different accelerometer characteristics.

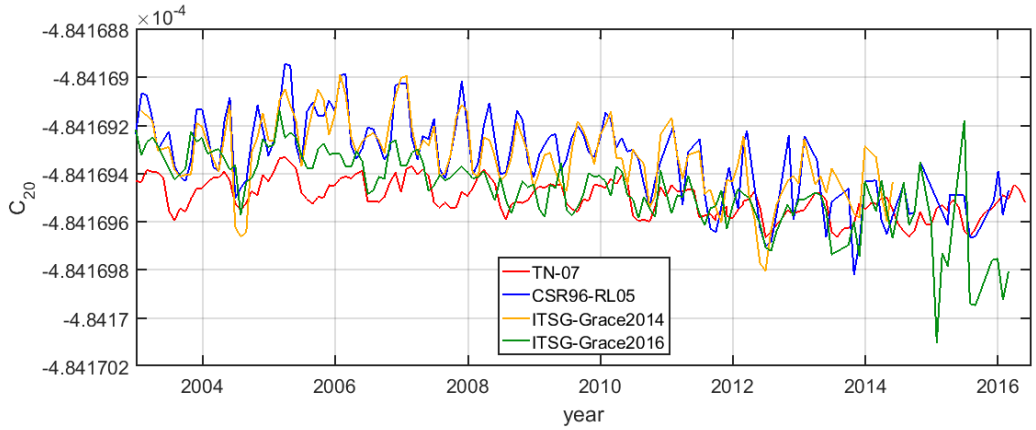

Figure 4-5: C20 coefficients from SLR (red) and the CSR96-RL05 (blue), ITSG-Grace2014 (orange), and ITSG-Grace2016 (green) GRACE time series over time.

Improving the GRACE estimate of the C_{20} coefficients has an impact on the results of the VADER filtered time series. Due to the properties of the VADER filter (W_α matrix is fully populated), all filtered coefficients are correlated with each other. This correlation causes energy being transferred between coefficients. Better consistency is achieved if the replacement coefficients are almost equal to the original ones, or if a replacement of the coefficients can be

omitted. Tests with the ITSG-Grace2014 time series, replacing the C_{20} coefficients with SLR derived coefficients before and after filtering the time series, revealed a difference for the estimated trend of 0.2 Gt year^{-1}. The 0.2 Gt year^{-1} are induced by distributing energy of the original inaccurate C_{20} coefficient to the filtered solution and cannot be cured by the replacement coefficient from SLR anymore. For the ITSG-Grace2016 time series this difference is below 0.1 Gt year^{-1}, which is a clear advantage with respect to the accuracy of the retrieved linear trend.

To assess the contribution of the C_{20} coefficients to the overall GRACE error budget of a monthly solution, the following assessment is performed. The variability of the C_{20} coefficients is, as stated above, induced by variations in the distribution of mass on Earth. The redistribution processes are associated with certain frequencies, such as seasonal variability. To estimate the contribution of the C_{20} coefficients to the uncertainty of a monthly mass signal estimate, the C_{20} coefficients are inspected independently from the other SH coefficients. This allows deriving a mass time series derived solely from the C_{20} coefficients. Such a time series exhibits seasonal variations and linear trend signals induced by the geophysical features discussed above. A residual C_{20} mass time series is derived by reducing a six-parameter model (constant, linear, annual and semiannual sine/cosine parameters). The choice of the parameters being reduced is aligned to the spectral analysis of C_{20} coefficients by Bloßfeld et al. [2015], revealing signal peaks for periods of 365.25 and 182.6 days. This residual time series is considered to be predominated by noise. To reduce remaining geophysical signal, a high-pass filter is applied to the residual mass time series. Filters tested are a 13-month moving average and a 13-month Gaussian average with preference given to the Gaussian average. The Gaussian average uses contrary to the simple moving average a Gaussian bell shaped function to calculate the moving average. The 13 months define the width (3-sigma) of the timeframe taken into account. The RMS of the respective residual high-pass filtered time series is then considered as approximate contribution to the total error budget of a monthly mass balance estimate from an individual GRACE solution. An analysis as described above is discussed e.g. in Nagler et al. [2016] (based on Wahr et al. 2006) in the context of estimating the error noise in a mass change time series of GRACE in general, not separating the individual contributors such as C_{20}, degree one and the remaining coefficients of $l=2$ but $m\neq 0$ and $l>2$. This concept of deriving the contribution of the replaced C_{20} coefficient to the total error budget is picked up again in the application chapter 7.

Degree one terms

The degree one terms are responsible for placing any SH representation of the gravity field estimate to the geocenter of the Earth. Geocenter in this context means center of mass (CM). Another very common reference in geodetic science is the center of figure (CF). Time variable gravity field estimates from GRACE usually do not contain an estimate for the degree one terms, since GRACE is, because of its configuration, not able to observe them. They are by definition set zero (which implies the center of the GRACE reference frame being in the Earth's center of mass) and are therefore constant, not telling anything regarding geocenter motion. The terrestrial reference frame, e.g. the ITRF2008 [Altamimi et al. 2011], is fixed at a certain epoch and does not necessarily coincide with the GRACE reference frame placed in the respective center of mass for each monthly solution. The center of mass is varying with annual and seasonal variations of several millimeters as depicted in Figure 4-6. These variations are induced by mass redistribution, primarily variations in atmosphere, oceans and hydrology [Dong et al. 1997]. Incorporating geometric space geodetic techniques such as SLR, variations of the geocenter location (CM) with respect to a superordinate reference frame can be measured. Following Torge and Müller [2012] it holds for the degree one coefficients

$$C_{10}=\frac{1}{aM}\iiint_{Earth} Z'\,dm \quad C_{11}=\frac{1}{aM}\iiint_{Earth} X'\,dm \quad S_{11}=\frac{1}{aM}\iiint_{Earth} Y'\,dm \tag{4.1}$$

with X', Y', and Z' being Cartesian coordinates of a point P', displaced by the vector r' from the origin of the geometric reference frame (e.g. the terrestrial reference frame ITRF). This point P' would be the CM for the respective monthly solution. If the origin of the geometric reference frame and the GRACE reference frame, placed in the center of mass, coincide, then X', Y', and Z' become zero. Consequently it holds $C_{10} = C_{11} = S_{11} = 0$. But this assumption does not hold in general as the center of figure is usually defined being static in time with respect to a certain reference epoch and not varying from month to month.

The effect of geocenter motion needs therefore special attention whilst combining mass estimates derived from e.g. geometric space geodetic techniques such as altimetry, being referenced to the center of figure, with estimates derived from GRACE. Omitting the degree one correction results, according to Chambers [2006b], in systematic errors of the estimated mass variations. Since especially the *z*-component (cf. Figure 4-6) exhibits a linear drift, locations sensitive to variations in *z*-direction (e.g. the poles) encounter a systematic effect.

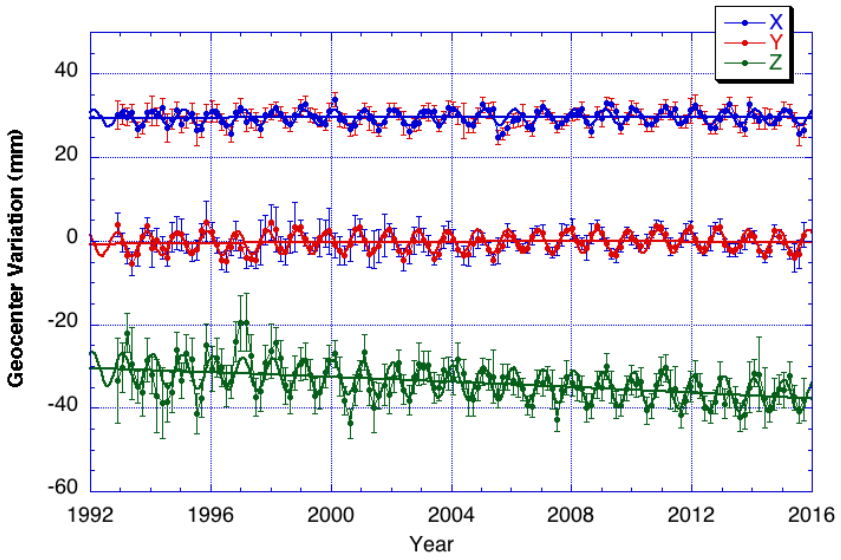

Figure 4-6: Geocenter variations (X',Y',Z') estimated from SLR observations. X' values are offset by +30mm, and Z' values by –30mm for better readability. Credits: [Kruizinga 2016; Cheng et al. 2013a]

Wrongful assumptions regarding the degree one correction can have a very strong impact on the final mass change estimates. An assessment of the uncertainty of degree one corrections is therefore inevitable whilst describing the accuracy of monthly GRACE solutions. Barletta et al. [2013] investigate the scattering of applying different degree one corrections. They detect a significant contribution of the degree one uncertainty to the total error budget and derive that 1 mm geocenter shift in *z*-direction results in a mass change of 89 Gt for the Antarctic ice sheet.

For the experiments conducted for the application section, namely the retrieval of ice mass change estimates in Antarctica (cf. section 7.1), degree one coefficients are applied following the concept of Swenson et al. [2008]. The coefficients are obtained from the GRACE Tellus web portal (http://grace.jpl.nasa.gov/). As their approach is based on the incorporation of CSR GRACE solutions and an ocean model for $l \geq 2$ to estimate the mass redistribution, some inconsistency might occur whilst applying the correction on the ITSG-Grace2016 time series. In order to validate the applicability of the GRACE Tellus degree one coefficients on any GRACE time series, not being further discussed within this thesis, one would need to assess the sensitivity of the approach with respect to the incorporation of different GRACE time series for deriving the mass transport estimates.

As the relation in equation (2.9), transforming Stokes coefficients to coefficients of EWH, is introduced only for $l>1$, the relation also needs to be extended to coefficients of $l=1$. A load love number of $k_{l=1}=0.021$ is, according to Blewitt [2003], suited for application in equation (2.9) and to transfer sets of Stokes coefficients with $l\geq 1$ to EWH coefficients.

The change of degree one coefficients over time is comparable to the one of C_{20} coefficients related to mass redistribution processes on Earth. The assessment of the error budget contribution of the degree one coefficients to the total monthly GRACE error budget is performed in a very similar way as for the C_{20} coefficients. Again a residual mass time series for an area of interest is computed by adjusting a six-parameter model and applying the same high-pass Gaussian average filter to diminish remaining signals. Numbers for the degree one error budget contribution are given in section 7.1 for the example of Antarctica.

The only term not discussed so far is the C_{00} term. According to e.g. Wahr et al. [1998], this term is related to the total mass of the Earth (solid plus "fluid" parts composed of e.g. oceans and atmosphere), which is assumed to be constant. Consequently no ΔC_{00} occurs in the context of analyzing GRACE time series and the term vanishes. Accordingly the load love number is $k_{l=0}=0$.

SMB

In the processing chain towards a comprehensive mass trend estimate one has to take into account interannual variations of surface mass balance (SMB). The reasons for such effects are variations in precipitation, in Antarctica mainly snowfall, ablation and drifting snow (blown by wind). Such variations, showing inter- and intra-annual variability, are a major source for non-linear temporal variations of the Antarctic gravity field. A large portion of the non-linear signal in geodetic mass and volume time series is well explained by modelled SMB fluctuation [Horwath et al. 2012; Horwath et al. 2013b]. The dataset used for further processing is the RACMO2-ANT27 regional atmospheric climate model [Lenaerts et al. 2012]. It has a 27km horizontal grid resolution and is driven by the ERA-interim (1979-2010) climate model [Balsamo et al. 2015]. For integration of the gridded product into the processing chain, a SH analysis was performed, and the SMB corrections are applied in the spectral domain.

Figure 4-7 shows in the central panel the RMS in mm EWH of monthly SMB corrections in the region of Antarctica (2003-01 until 2014-02), originating from the RACMO-ANT27 model. The areas of coastal East and West Antarctica exhibit large variations in surface mass variation, whereas the inner ice sheet, especially in East Antarctica, does not show significant variations at all. Reducing cumulative SMB anomalies has two effects, as one can see by comparing the red and blue lines in the four surrounding panels of Figure 4-7. The four panels show the linear trend component derived from the ITSG-Grace2016 time series before (blue) and after (red) SBM correction.

First, it may change the overall trend. This effect depends on the reference time interval to which the SMB anomalies are referred to. In order not to change the estimated linear trend, the set of SMB corrections, which are applied as monthly corrections, are de-trended over exactly the same time interval as the underlying GRACE time series. This choice corresponds to assuming the GRACE interval itself as the reference interval for the SMB anomalies. This leads to the same slope for the linear trend estimate (depicted in the black dashed line), estimated from the time series before and after the SMB correction applied.

The second effect of reducing SMB variation effects prior to a linear trend estimate is the reduction of the residuals with respect to a linear and seasonal signal. This effect is illustrated in Figure 4-7. From comparing again the red and blue lines in the surrounding panels, one can

observe different characteristics depending on the region or basin for which the graph is calculated. The regions used are the 27 Antarctic regions defined by Zwally and Giovinetto [2011] (cf. map of integration basins in the Appendix section). Basin 10, located in East Antarctica in Macrobertson Land, does not show large differences between the two curves, suggesting not much surface mass balance variations in this area. This is in agreement with the RMS of the corrections being almost zero. Close by, in Enderby Land, basin 7, the situation is very different. Here one can observe a strong discrepancy between the red and blue curve, especially between 2008 and 2009. This is due to a significant anomaly of snowfall in this period [Groh et al. 2014]. If one estimated a linear trend e.g. in the period of 2005-2009 (near zero) and compared it to one from the period 2008-2012 (significant positive slope), one would get very different results for the linear mass change estimate of this basin. The results for basin 13, area of Wilkes Land, also show a significant anomaly around the years 2008-2010, similar to basin 7. For basin 21, located in the Amundsen Sea Sector, the blue curve from before the SMB correction suggests, apart from a clear linear behavior, a quadratic shape (negative curvature), as e.g. reported by Velicogna et al. [2014]. After the SMB correction this feature becomes obsolete. Applying the SMB correction helps in this matter to avoid misinterpretation of time series. The formal errors of trend estimates also decrease since the residuals predominantly become smaller. After reducing SMB effects, the residuals of the GRACE gravity field trends are dominated by the errors inherent in the GRACE monthly solutions rather than by non-linear geophysical signals.

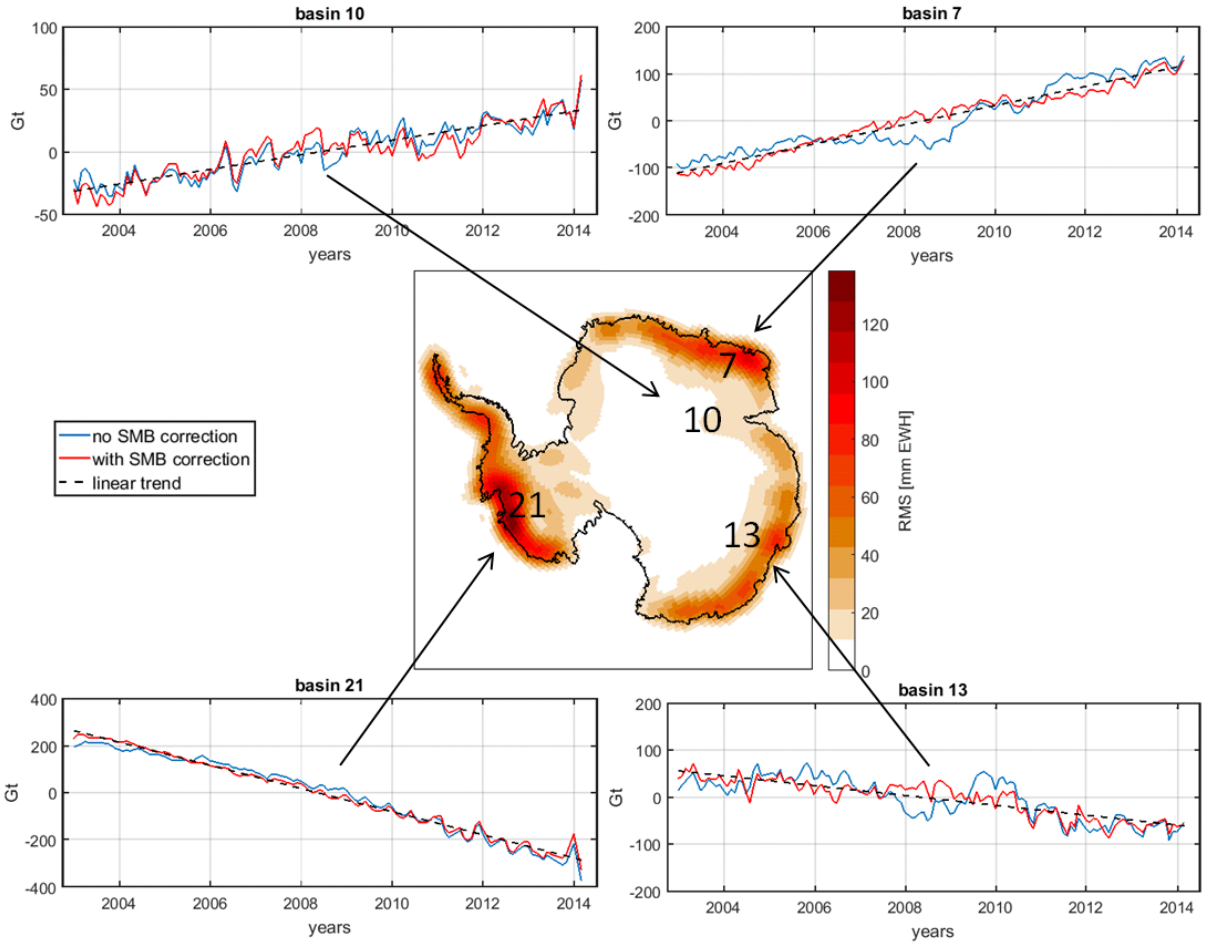

Figure 4-7: Integrated mass estimates per month and linear trend (dashed black) from the ITSG-Grace2016 time series with (red) and without (blue) SMB corrections applied for 4 different basins in Antarctica. The central panel shows the RMS of the monthly SMB correction originating from the RACMO-ANT27 model for the timeframe from 2003-01 until 2014-02 in mm EWH.

GIA

The GIA signal is the major contribution to the solid earth signal budget apart from mantle convection [Ghelichkhan et al. submitted 2016] and earthquake events. Areas with the strongest present day GIA effect can be found in e.g. Fennoscandia, eastern Canada (Hudson Bay area), and Antarctica. Additionally other regions with changes in ice loading since the past glacial maximum show rebound effects. GIA is not necessarily an uplift effect due to vanished past loading. Also areas with downward adjustment are known due to heavier present day loading than in the past. The effects originating from loading history since the past glacial maximum can be superimposed with older loading situations originating from events even further in the past. GIA models are derived by mainly two different approaches. The first approach [Ivins and James 2005; Peltier 2004; Whitehouse et al. 2012] is to combine an ice loading evolution for the last e.g. 21000 years with assumptions regarding the viscoelastic properties of the Earth's crust, leading to a GIA prediction for today. The second approach [Gunter et al. 2014; Riva, R. E. M. et al. 2009; Sasgen et al. submitted 2016b] is to combine measurements of different space geodetic techniques like GNSS, satellite gravimetry and satellite altimetry, again in conjunction with a viscoelastic Earth model, to derive an empirical estimate of GIA rates.

Figure 4-8 shows the GIA effect in mm EWH per year for two GIA models for the region of Antarctica. The model displayed on the left panel is the release 2 version of the model by Ivins and James [2005]. The difference between the original release 1 and release 2 is the incorporation of GPS constraints in the latter one. The model on the right panel is the so called best estimate by Whitehouse et al. [2012]. The common representation of GIA models is mm radial displacement or rates of mm geoid. In order to integrate the GIA effect into the mass estimation process and to compute the GIA contribution in rates of gigatons per year, the models have been transferred to mm EWH per year. Large discrepancies in GIA effects between East and West Antarctica can be observed for both models. Differences between models are, e.g., due to varying assumptions regarding the Earth's rheology or the loading history incorporated. The effect on mass trend estimates for different basins or regions in Antarctica is at the order of the estimated trend itself. Consequently the GIA correction plays a major role in the processing chain of estimating ice mass change. Assessing the contribution of the GIA correction to the uncertainty of the final estimate is therefore rated to be necessary. In the following an approach of estimating an uncertainty contribution for the GIA correction is briefly introduced. The GIA error budget assessment is performed similarly as e.g. van der Wal et al. [2015] do, by evaluating the spread of GIA corrections of a representative collection of recent GIA models in the respective area of interest. A numerical example for the region of Antarctica is shown in the case study for Antarctica in section 7.1.

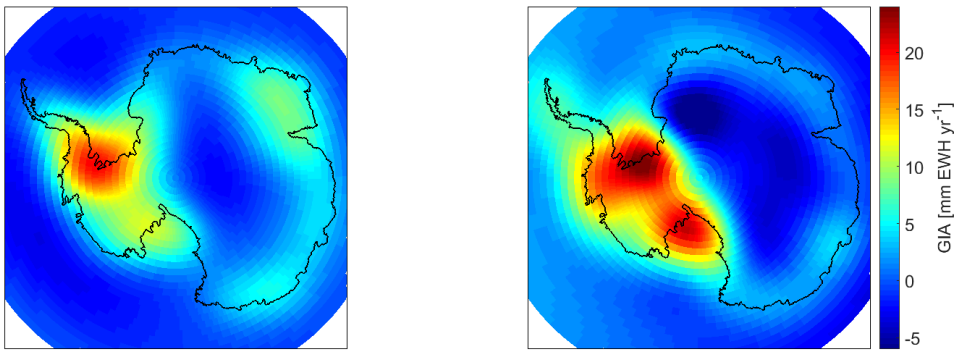

Figure 4-8: GIA effect from Ivins and James IJ05R2 (left panel) and Whitehouse W12a best (right panel) in mm EWH per year in the region of Antarctica

Ocean layer compensation

In case SMB variations or other model data originating from e.g. hydrological models are reduced, the issue of "conservation of mass" is of importance. This means: If one subtracts mass from one location on Earth, this mass does not vanish. It will be redistributed. To avoid violating the balance of mass on Earth, the reduced mass can be replenished by introducing an oceanic layer [Horwath and Dietrich 2009], equivalent in mass. This concept is pursued by introducing a uniform oceanic layer to assure conservation of mass for the application example of mass balance estimates in Antarctica (cf. section 7.1).

4.2.3 Leakage issue

GRACE measurements have a limited spatial resolution due to the truncation of the SH series expansion. The truncation is necessary due to the orbital height and the length of the baseline between the two spacecraft. A second contribution to the limited spatial resolution is the averaging of observations in space and time (usually monthly averages). A third factor is the superposition of signals of various sources with different spectral characteristics, making it difficult to separate e.g. only hydrological signals from the total signal. This all leads to deficiencies regarding the recovery of the actual signals present during the observation time. Additional signal attenuation is caused by filtering, which is necessary in order to suppress the noise, caused mainly from aliasing, within GRACE gravity fields.

Due to the described lack of sharp spatial delineation of signals originating from a specific source like e.g. continental hydrology, superposition occurs from the different catchments and signal contributors of the whole observed signal. By applying a region function (cf. section 4.2.4) for a single river catchment on a continent, signal from surrounding catchments leaks into the region of interest (leakage-in). Vice versa signal from the catchment of interest is also leaking into the neighboring areas (leakage-out). Landerer and Swenson [2012] address the issue of leakage and signal attenuation in the context of hydrological catchments. They estimate scaling factors for individual catchments in order to compensate the signal attenuation induced by filtering and the characteristics of the GRACE mission design itself. Since GRACE is, as mentioned, averaging observations in time, the recovered signal is an average over time. If now for two neighboring catchments the function of mass change is shifted by e.g. half a month, the recovered signals for the two basins are correlated due to the leakage, and thus the phase of each individual catchment is influenced by the neighboring catchment. This leads to biased estimates of amplitude and phase of the respective catchment signal. The issue of phase shift of recovered signals caused by leakage and techniques to cover for such effects is e.g. discussed by Vishwakarma et al. [2016].

The problem of leakage-out can also be observed in Figure 4-3. The mass change being closest to the real signal is represented by panel (c), originating from an altimetric measurement derived dataset. With the observational boundary conditions set for GRACE and the limited degree of SH expansion, the signal is, as described in section 4.2.1, attenuated and spatially disseminated due to the leakage-out effect (panels a and b).

For the application example in section 7.1, estimating mass change in Antarctica, the problem of leakage into ocean areas is compensated by extending the integration kernel into the oceanic area. The underlying idea, applicable for this specific region, is that the signals on land, induced by ice mass change, are orders of magnitude larger than the signal from the oceanic area. Consequently the error made by including the oceanic signal components into the mass estimate is much smaller than omitting the leaking signal from the ice mass change on land. This approach is in agreement with the findings from Horwath and Dietrich [2009].

Figure 4-9 shows an exemplary linear trend estimate for the region of the Antarctic ice sheet (AIS). Especially in the area of the Antarctic Peninsula and the Amundsen Sea Sector, signal is leaking into oceanic areas. In order not to omit the signal, the region function is extended by a 100 km zone into the ocean, indicated by the black dashed line closer to the coastline (solid black line). This extension is also done since the exact location of the land-sea boundary is changing over time. Especially grounding line locations, being the boundary where the ice cap is not lying on the bedrock anymore but starts floating in water, are subject to change. A discussion regarding the principles of the dynamics of ice cap margins at coasts and the principles of grounding line location and migration can be found e.g. in McMillan et al. [2014]. The second dashed line, further away from the coastline, represents the end of the transition zone described by the cosine taper:

$$\omega = \tfrac{1}{2}\cos\left(\pi \, d/300\,\mathrm{km}\right) + \tfrac{1}{2} \tag{4.2}$$

The value of 300 km is chosen by analyzing the correlation length of the VADER filtered monthly gravity field solutions (cf. section 5.4, Figure 5-19). ω represents the value or the region function with the distance d from the 100 km boundary, decreasing from 1 to 0.

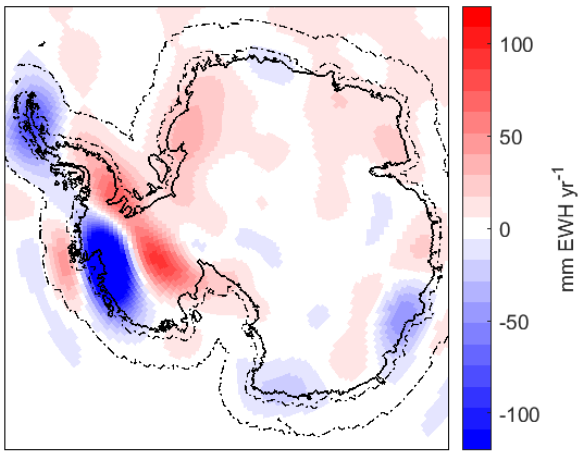

Figure 4-9: Integration kernel boundaries as implemented in application section 7.1 in dashed lines. Line closer to the coastline represents 100 km zone, second dashed line represents end of the transition zone from 1 to 0 according to equation (4.2).

4.2.4 Integration/averaging kernels

Integration or averaging kernels are applied on GRACE gravity field solutions, since contrary to e.g. altimetry, a point-wise localized measurement is not possible. If one is interested in the mass change of a certain region, one has to average over a basin or area of interest in order to retrieve a mass change signal with high signal to noise ratio. If the selected area is too small, the result is dominated by error. The goal is now to define suitable kernels which allow averaging enough to retrieve significant signals, but to make the kernel also as confined as possible to have fine spatial resolution. In literature different approaches regarding averaging kernels can be found [Wahr et al. 1998; Horwath and Dietrich 2009]. In principle averaging kernels can be applied in frequency domain as well as in spatial domain. For a suitable design of the kernels, one has to take into account also the issue of leakage, introduced in the previous section (4.2.3).

The following relation is, according to Horwath and Dietrich [2009], explaining the connection between Stokes coefficients transferred to coefficients of surface density variation $\Delta\kappa_{lm}$ (cf. equation (2.9), $\Delta\kappa_{lm} = \left\{\Delta C_{lm}^{EWH}, \Delta S_{lm}^{EWH}\right\}$), and mass change of a region of interest $\Delta m(t)$ for a specific time t.

$$\Delta m(t) = 4\pi R^2 \sum_{l=0}^{\infty} \sum_{m=0}^{l} \vartheta_{lm} \Delta\kappa_{lm}(t) \tag{4.3}$$

ϑ_{lm} stands for the spectral representation of a square-integrable region function on the sphere.

Since GRACE or other satellite derived estimates of surface density variations are limited in the degree of SH expansion and are dominated by noise in the higher SH degrees (cf. Figure 3-2), the equation (4.3) can be rewritten as

$$\Delta m^{GRACE}(t) = 4\pi R^2 \sum_{l=0}^{l_{max}} \sum_{m=0}^{l} \eta_{lm} \Delta\kappa_{lm}^{GRACE}(t) \tag{4.4}$$

Following Swenson and Wahr [2002], the region function ϑ_{lm} can be replaced by a weighting function η_{lm}, being composed of the region function ϑ_{lm} and a damping factor ω_{lm} to account for the properties of signal to noise ratio in the time variable GRACE gravity field estimates.

$$\eta_{lm} = \omega_{lm} \vartheta_{lm} \tag{4.5}$$

ω_{lm} can be understood as a type of filter parameter. Wahr et al. [1998] discuss different approaches like e.g. the Gaussian type filter for ω_{lm}. Horwath and Dietrich [2009] further investigate the population of the quantities in equation (4.5) and its subsequent implementation into equation (4.4) by analyzing approaches like the regional integration approach. Obstructive factors for ideal signal recovery are the problem of leakage (cf. section 4.2.3) and the damping of the observed signal, induced by filtering. They e.g. discuss the utilization of predefined mass change patterns to assess the optimal configuration for tailoring the integration kernel (sometimes also called sensitivity or averaging kernel) to assure good signal recovery. The spatial representation of equation (4.4) reads

$$\Delta m^{GRACE}(t) = \iint_{\Omega} \eta(\Omega) \Delta EWH(\Omega, t) R^2 d\Omega \tag{4.6}$$

with $\eta(\Omega)$ being a region function, combined with a damping factor as stated in equation (4.5), expressed in the spatial domain. The function is defined on the sphere with the surface Ω. $\Delta EWH(\Omega, t)$ are the surface mass density variations as derived from equation (2.9) spanning the surface of the sphere Ω, described by the dimensions θ and λ.

The simplest region function would consist of 1 inside the area of interest, and 0 outside. Within the framework of this thesis only relatively simple integration kernels are employed. One reason behind this decision are the properties of error correlation of VADER filtered monthly GRACE solutions, showing spatially confined and almost isotropic error correlation structures (cf. section 5.4, Figure 5-19). The second aspect, apart from the correlation of errors in the spatial domain, is leakage (cf. section 4.2.3). For the example shown in section 7.1, leakage occurs mainly as leakage-

out into the ocean. Figure 4-9 shows the integration kernel applied for the whole AIS. Within the region of interest, e.g. the AIS, the region function is 1. It is according to the description in section 4.2.3 amended by a 100 km extension zone, followed by a steady decrease from 1 to 0 according to equation (4.2). The design of weighting functions, composed of region and damping factors according to equation (4.5), is not subject of this thesis but is addressed again in the outlook chapter 8. Discussion regarding the design of more complex region or weighting functions, aggregating region and damping factors, can be found e.g. in the aforementioned work by Horwath and Dietrich [2009], Wahr et al. [1998], Swenson and Wahr [2002], or in the recent work by Groh and Horwath [2016].

4.3 State of the art of GRACE gravity field solutions

The following section describes a representative selection of the available GRACE time variable gravity field solutions (sections 4.3.1), with a detailed analysis of errors and noise contained in the GRACE time variable gravity field solutions (section 4.3.2). The main established post-processing methods applied in order to extract information about the geophysical signals from the time series are presented in the following. They cover isotropic (section 4.3.3), anisotropic, and other regularization type filters (section 4.3.4). All these methods have the common goal to improve the signal to noise ratio and to make geophysical signals interpretable.

4.3.1 Different solutions and their characteristics

Apart from the official GRACE ground segment processing centers Center for Space Research (CSR), Geoforschungszentrum Potsdam (GFZ), and Jet Propulsion Laboratories (JPL), an emerging number of independent processing centers publishes their own estimates of time variable gravity field solutions. The ICGEM web portal (http://icgem.gfz-potsdam.de/ICGEM/) hosts most of the series in the so called standard *icgem* format. A second repository for GRACE solutions and auxiliary data is the GRACE Tellus web portal (http://grace.jpl.nasa.gov/). The different solutions can be grouped into several clusters. These are classic spherical harmonic estimates of time variable gravity fields without significant further processing, forming the first cluster. A second cluster is formed by the solutions treated with different filters or regularization techniques. These solutions are still provided in spherical harmonics, but do not need any further filtering or smoothing (e.g. DDK filtered solutions on the ICGEM web portal). The third cluster contains solutions using different base functions like mascons. They are usually provided in grids and also do not need further smoothing or post-processing. A discussion on the performance and characteristics of mascon solutions can be found e.g. in Watkins et al. [2015]. One should note that the comparison of gravity fields in SH representation and mascons by Watkins et al. [2015] concentrates on SH solutions being truncated at degree 60 and treated with empirical decorrelation plus a subsequent 300km Gaussian filtering. According to the findings within this thesis (cf. section 4.2.1 and chapter 5) with respect to recommendable filter setups and degrees of expansion, this might not be the best possible post-processing method for GRACE data represented in SH coefficients.

All these solutions span different time periods for the used observations. The GRACE standard solution covers a 30 day time period usually matching calendar months, but also shorter periods like 10 or 11 day solutions or daily estimates are available.

Since the processing methods investigated and developed within this thesis only deal with gravity field estimates in the spherical harmonic domain, the focus within the following in-depth comparison of models is set on this subgroup of available models. The number of solutions is also limited by the prerequisite of the availability of full error covariance information throughout the whole time series (needed for the VADER filter).

Table 4-1 summarizes all time variable GRACE solutions used for investigations within this thesis.

Table 4-1: Overview of all GRACE time series used within this thesis

Name	Degree of expansion	Full error covariance	Reference
GFZ-RL5a	90	yes	Dahle 2014
CSR60-RL05	60	yes	Kruizinga 2015
CSR96-RL05	96	yes	Kruizinga 2015
ITSG-Grace2014	60/90/120	yes	Mayer-Gürr et al. 2014
ITSG-Grace2016	60/90/120	yes	Mayer-Gürr et al. 2016a

Remark: The CSR60 and CSR96 full error covariance matrices were made available only at the time this thesis was submitted. For completeness, the availability of full error covariance information is indicated, but the data is only partially integrated into the work of this thesis. The recent publication of more and more error covariance information shows an increased awareness for the benefits and opportunities the analysis of such dataset bears.

4.3.2 Analysis of available GRACE time series in the spherical harmonic domain

Only a minority of processing centers provide solutions accompanied by their formal covariance matrices (cf. Table 4-1). Both ITSG solutions from TU Graz provide the corresponding error covariance matrices with free web access. For the GFZ-RL5a solutions the error covariance matrices are available upon request. The CSR at the University of Texas provides for both times series, the CSR60-RL05 and CSR96-RL05, error covariance matrices with free web access. Other processing centers (as from November 2016) do not provide publicly accessible error covariance matrices. According to the aforementioned limited selection of available error covariance matrices, an in-depth analysis of model characteristics relevant for the VADER filtering and the overall usability of the solutions can be done only for these time series. Although the selection is small, it covers two of the three official processing centers and one independent center. Parameters for investigation presented in the following are the noise content of the time series and how close the formal errors are to empirically derived errors. This allows rating the applicability of the error covariance information to the processing of mass balance estimates.

To estimate and quantify the noise content an empirical error covariance is estimated. The first step towards such an empirical covariance is to compute residual time series dominated by noise. This is done by separating noise and target signals for each month. The approach used is a nine-parameter reduction model consisting of a constant (1), linear (2), annual cosine (3), annual sine (4), semi-annual cosine (5), semi-annual sine (6), 161-day cosine (7), 161-day sine (8), and quadratic term (9). Analysis has shown best reduction for reducing all nine parameters. The other options checked, but rejected, were reducing parameter one to four, and one to six. Comparing

the median line, the degree amplitudes for reducing only four or six parameters are larger by a factor of 1.1 to 1.5. As these residuals occur predominantly in the lower SH degrees, they can be attributed to residual geophysical signal rather than noise.

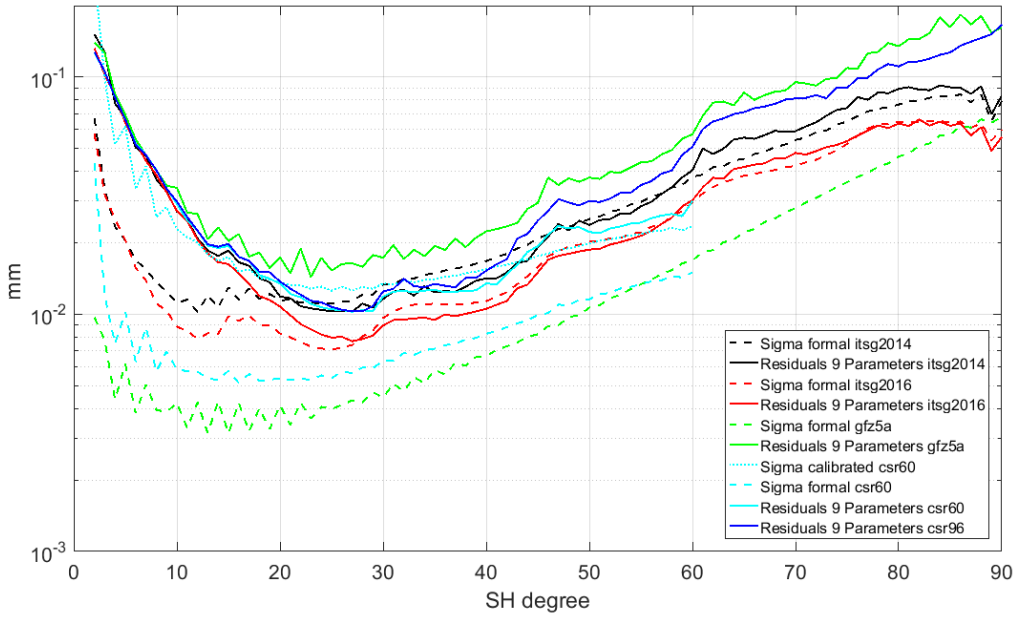

Figure 4-10: Degree amplitudes of residuals for different time series in comparison with the error degree amplitudes derived from the corresponding formal errors. All lines represent the median line derived from the full set of curves from each dataset.

Figure 4-10 shows the median lines of sets of different degree amplitudes estimated from residuals of different time series (solid lines). The reduction model used is composed of the nine abovementioned constituents. The corresponding error degree amplitudes are also shown as the median lines of each set (dashed lines). The display comprises data from ITSG-Grace2014 (black), ITSG-Grace2016 (red), GFZ-RL5a (green), CSR60-RL05 (cyan), and CSR96-RL05 (blue). For the CSR60-RL05 series the median line for the formal error degree amplitudes is computed from the timespan 2013-06 until 2016-01, since formal errors are not provided before via the distributed sets of SH coefficients. Complementary the CSR60-RL05 series provides calibrated standard deviations for each month. The median line of the calibrated standard deviations (dotted cyan line) is shown for comparison only. For the CSR96-RL05 series no formal errors are provided with the monthly solutions. Very good agreement between residuals and formal errors can be observed for the ITSG-Grace2016 series. From SH degree 25 and higher, both lines coincide very well. The same holds for ITSG-Grace2014, although the general level of noise is higher. For GFZ-RL5a, a significant gap between residuals and formal errors can be observed, leading to the conclusion that the formal errors are too optimistic. The same holds for the results originating from the CSR60-RL05 series, although the gap between formal errors and residuals is smaller. The only conclusion to be drawn from the CSR96-RL05 residuals is a lower noise level compared to the GFZ solution. The ITSG-Grace2016 results indicate best performance in terms of noise content of the unfiltered time series and the level of formal error being closest to the empirically derived approximation of the real error. The real error is of course unknown and is assumed to be similar but smaller than the residuals shown. The parameter model used for reduction covers most of the geophysically meaningful target signals, but some residual signal still remains in the estimated residuals which are dominated by noise. Analysis shows a higher residual geophysical signal content for the spectral band of SH degree 2 to 20 not totally captured by the reduction model. The residuals of this spectral band show, contrary to the higher SH degrees, geographic correlations with areas subject to the presence of strong geophysical signals. Geophysical features making random

contributions to the residuals can be large scale changes in hydrological processes, exceptional warm or cold periods in polar regions causing melt or accumulation of ice mass, or major earthquakes. The formal error in the band between SH degree 2 and 20 is also significantly lower than the residuals. From experiments carried out, the gap between residuals and formal error is assumed to be present for two reasons. First, the formal error in this region is too optimistic (too small), and second, the residual signal is too large. Both quantities are rated to contribute about equally to the gap. Nevertheless, the residuals from SH degree 20 and higher are assumed to represent a realistic assumption of the real error. A similar analysis, assessing the noise content in GRACE solutions, was performed by Schrama et al. [2007]. They used an empirical orthogonal function (EOF) approach to reduce geophysical signal from the monthly solution. An EOF approach instead of the 9 parameter reduction model was also tested, but not further pursued, since the properties of the residual signals did not show substantial differences.

The next analysis step is the computation of an empirical error covariance matrix $\mathbf{Q}^{\text{emp}}$ from the series of residuals for each time series. Equation (4.7) shows the basic relation for deriving $\mathbf{Q}^{\text{emp}}$ from SH coefficients.

$$\mathbf{Q}^{\text{emp}} = \frac{1}{T-1}\sum_{t=1}^{T}\left(\mathbf{x}_t - \bar{\mathbf{x}}\right)\left(\mathbf{x}_t - \bar{\mathbf{x}}\right)^T, \tag{4.7}$$

with $\mathbf{x}_t$ serving as placeholder for each vector with sets of SH coefficients with the index t running in the time domain. The time index of the series starts with 1 and ends with T.

$$\bar{\mathbf{x}} = \frac{1}{T}\sum_{t=1}^{T}\mathbf{x}_t \tag{4.8}$$

is the respective mean value of the set of SH coefficient vectors. The average is taken over the whole set of samples in the time domain. The number of samples used for the computation of the empirical covariance matrices investigated within this thesis is summarized in Table 4-2 and ranges from 123 to 151 samples. Evaluating the relation in equation (4.7) for a given time series developed up to $l_{\max}$ leads to a quadratic empirical covariance matrix $\mathbf{Q}^{\text{emp}}$ with the dimension $\left(l_{\max}+1\right)^2$ by $\left(l_{\max}+1\right)^2$.

The empirical covariance matrices shown in the following are derived, as summarized in Table 4-2, from the ITSG-Grace2016, ITSG-Grace2014, GFZ-RL5a, CSR96-RL05, and CSR60-RL05 time series.

Table 4-2: Composition of the empirical error covariance matrices analyzed

Time series	$l_{\max}$	Time frame	Total months	Skipped months
ITSG-Grace2016	90	2002-04 until 2016-03	145	2002-09, 2003-01, 2004-09, 2004-10, 2015-02
ITSG-Grace2014	90	2003-02 until 2014-06	123	2004-08, 2004-09, 2004-10, 2012-04, 2012-05, 2012-06
GFZ-RL5a	90	2002-04 until 2014-09	132	2003-01 and 2003-05
CSR96-RL05	96	2002-05 until 2016-04	146	2002-04, 2002-09, 2004-09
CSR60-RL05	60	2002-04 until 2016-03	151	not skipping any months

The reason for skipping certain months is because they exhibit comparably high residuals with respect to the other monthly solutions in the time series. The choice for excluding the

abovementioned months is made on the result of inspecting cumulated residuals (cf. equation (2.27)) per month. Experiments show higher consistency of the empirical covariance estimates excluding these months because they distort the correlation patterns embedded in the time series.

These empirical covariance matrices can now be compared to the formal error covariance matrices provided by the processing centers. This is of importance, since it needs to be validated how close the formal error covariance matches an empirical assessment of the error covariance. Since the monthly filters are constructed using formal error covariances, inaccurate error covariance information leads to inferior filter results.

The following two measures are taken to compare the empirical against the formal error covariance matrices. First, variances in the spatial domain are computed.

$$\begin{aligned} \boldsymbol{\sigma}^2(\theta,\lambda) &= tr\left(\mathbf{K}(\theta,\lambda)\right) \\ \boldsymbol{\sigma}^2_{\text{emp}}(\theta,\lambda) &= tr\left(\mathbf{K}^{\text{emp}}(\theta,\lambda)\right) \end{aligned} \tag{4.9}$$

$\mathbf{K}(\theta,\lambda)$ and $\mathbf{K}^{\text{emp}}(\theta,\lambda)$ from equation (4.9) are derived by

$$\begin{aligned} \mathbf{K}(\theta,\lambda) &= \mathbf{A}(\theta,\lambda)\,\mathbf{Q}\,\mathbf{A}(\theta,\lambda)^T \\ \mathbf{K}^{\text{emp}}(\theta,\lambda) &= \mathbf{A}(\theta,\lambda)\,\mathbf{Q}^{\text{emp}}\,\mathbf{A}(\theta,\lambda)^T \end{aligned} \tag{4.10}$$

The matrix $\mathbf{A}(\theta,\lambda)$ contains the partial derivatives of the spherical harmonics series expansion (2.3), extended by a factor for transforming the result to equivalent water heights (EWH, cf. (2.9)).

$$\mathbf{A}(\theta,\lambda) = P_{lm}(\cos\theta)\begin{Bmatrix}\sin m\lambda \\ \cos m\lambda\end{Bmatrix}\frac{M}{4\pi R^2}\frac{2l+1}{1+k(l)} \tag{4.11}$$

The number of rows in $\mathbf{A}$ is defined by the number of points (θ,λ). The number of columns is defined by the degree of expansion of the solution and depends on the maximum degree $l_{\max}$ leading to $(l_{\max}+1)^2$ columns. The memory requirement of a full covariance matrix in the spatial domain for a one degree resolution global grid is about 33,6 GB ($(180\cdot 360)^2 \cdot 8$ Bytes).

The evaluation of the correlations of a specific point of interest with all other points evaluated can be conducted by computing the correlation matrix ρ

$$\rho(a,b) = \frac{\mathbf{K}(\theta_a,\lambda_a,\theta_b,\lambda_b)}{\sqrt{\mathbf{K}(\theta_a,\lambda_a)}\cdot\sqrt{\mathbf{K}(\theta_b,\lambda_b)}} \tag{4.12}$$

with a,b being tuples of locations. If $a=b$, the correlation is 1, which implies a 100% positive correlation of the parameter with itself. All other correlations range between 1 (full positive correlation) and -1 (full negative correlation). 0 means no correlation.

Figure 4-11 gives an example for the square root of the formal error variance expressed in the spatial domain, using the relation expressed in equation (4.9). The data used is April 2004 from the ITSG-Grace2016 time series. A clear zonal dependency, typical for GRACE solutions (cf. Schrama, E. J. O. et al. 2007) of the spatial distribution of errors, can be observed (larger error in

low and mid latitudes, decreasing error towards the poles). The zonal dependency is mainly due to the spatial coverage of the Earth's surface. Since GRACE has a near-polar orbit (cf. chapter 1.1), the density of observations near the poles is much higher than around the equator, leading to smaller errors in high latitudes.

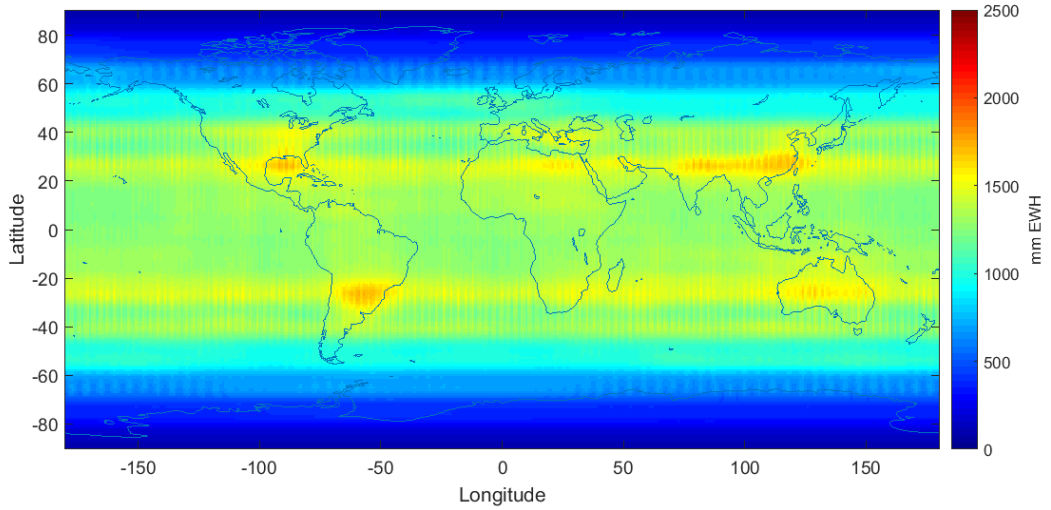

Figure 4-11: Global unfiltered square root of variance for ITSG-Grace2016 2004-04 monthly solution in the spatial domain derived from the formal error covariance matrix.

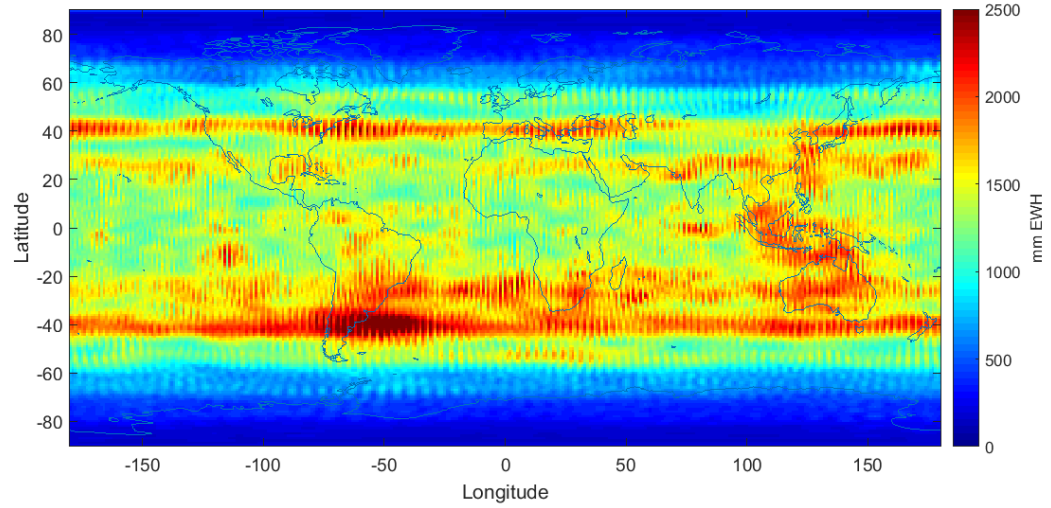

Figure 4-12: Global empirical unfiltered square root of variance from the ITSG-Grace2016 time series (145 months) in the spatial domain derived from the empirical error covariance matrix.

Another contributing factor for the spatial pattern of the errors is, in the case of the two ITSG time series, the introduction of stochastic information for the AOD1B de-aliasing applied [Mayer-Gürr et al. 2014; Mayer-Gürr et al. 2016b]. The other processing centers do not include such stochastic information in their processing, thus showing different and less realistic error structures.

Figure 4-12 shows the empirical errors derived as square root of the diagonal of the empirical covariance matrix (cf. equation (4.7) with (4.9)). Both formal and empirical errors show very good agreement. They exhibit a distinct zonal pattern and have comparable amplitudes and geographical correlations regarding their maxima and minima. Doing such a direct comparison, one should keep in mind that the formal errors are derived from one single monthly error covariance matrix, whereas the empirical errors are derived from the whole time series after

applying the aforementioned reduction. Therefore one must not expect a 100% agreement between the two figures, although the good agreement indicates a good match between the two entities. The magnitude of the formal errors, being on average 15% smaller than the empirical ones, appears to be in a range close to reality. Since the empirical errors still contain a portion of geophysical signals not captured by the reduction model as described above, they do not only show errors, thus leading to higher variances. Figure A 1 to Figure A 3 in the appendix section give corresponding examples for formal and empirical errors from the ITSG-Grace2014, CSR60-RL05, and GFZ-RL5a time series. The match between formal and empirical errors for the other time series is significantly lower than for the ITSG-Grace2016 series. Table 4-3 shows the correlation coefficient between formal and empirical error covariance in the spatial domain and the average attenuation of the square root of the variance (standard deviation), switching from empirical to formal error covariance.

Table 4-3: Correlation coefficient and amplitude relation of formal and empirical error covariance results in the spatial domain.

Series:	ITSG-Grace2016	ITSG-Grace2014	GFZ-RL5a	CSR60-RL05
Correlation coefficient:	0.83	0.76	0.84	0.83
Average attenuation:	15%	20%	370%	43%

The good agreement (0.76 to 0.84) of the correlation coefficient for the global spatial representation of the error covariance implies a match in the patterns of formal and empirical error covariances (e.g. the zonal dependency). The large differences in average attenuation originate from an underestimation of the formal error for e.g. the GFZ-RL5a time series. This finding is also supported by the difference in agreement between formal error degree amplitudes and degree amplitudes from the residuals of the respective time series depicted in Figure 4-10.

A better understanding of the properties of the formal and empirical errors and the differences between the processing centers can be developed by investigating their error correlation patterns derived from the covariances in the spatial domain.

Figure 4-13 shows correlation patterns for four different GRACE solution series, the GFZ-RL5a, ITSG-Grace2014, ITSG-Grace2016, and CSR60-RL05. In all eight panels of Figure 4-13, the correlation of the point located at 42° north and 90° west is evaluated in an area ranging from 90° north to 90° south and from 120° to 60° west. The location is chosen arbitrarily. For other locations tested (higher and lower latitudes) the patterns exhibit similar shapes. Examples for other locations (latitude and longitude) in the context of the analysis of future mission scenarios are given e.g. in section 6.1. For each series, the correlation derived from the formal and empirical covariances is shown according to the relation expressed in equation (4.12).

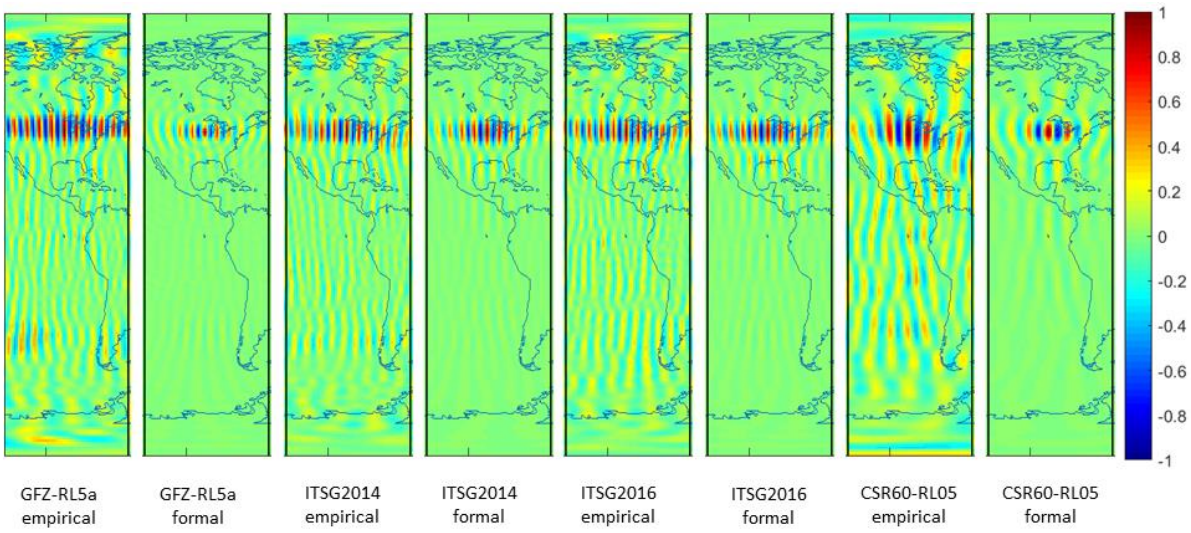

Figure 4-13: Spatial correlation patterns from different formal and empirical GRACE solutions. Central point located at 42° north and 90° west over the North American continent. Longitude of each box spans from 120° to 60° west and latitude from 90° to -90° north. Colorbar ranges from +1 (full positive correlation) to -1 (full negative correlation).

All results presented in this figure are based on unfiltered input datasets. The most important aspect to analyze is the correlation length of the errors. All eight patterns show significant differences for the patterns in east-west compared to north-south direction. The correlation length in east-west direction is much shorter than in north-south direction. This is clearly illustrated by the respective transects displayed in Figure 4-14.

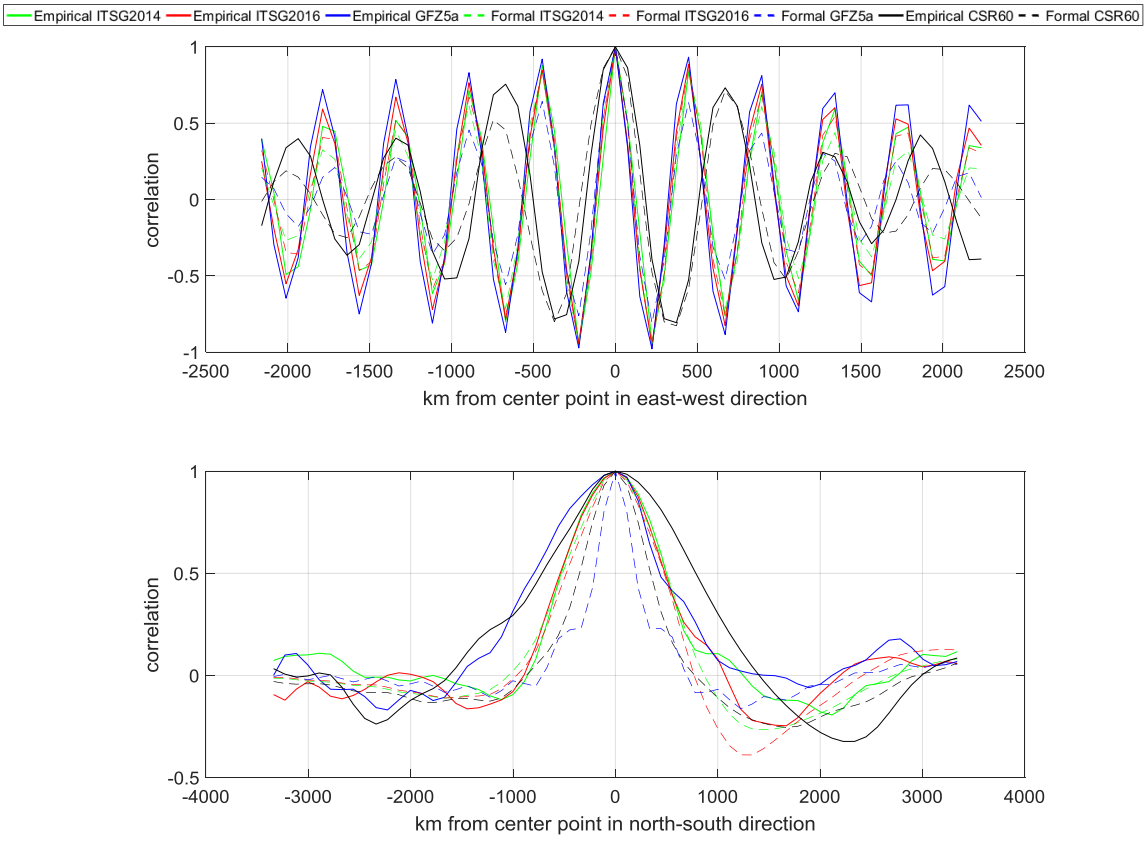

Figure 4-14*: Correlation patterns for the location 42° north and 90° west (same as Figure 4-13) derived from different formal and empirical error covariance matrices. Upper panel shows transects in east-west and lower panel in north-south direction.

As already deducted from Figure 4-13, best agreement between formal (dashed lines) and empirical (solid lines) correlations can be observed for the ITSG-Grace2016 solution (red) in both directions. For the time series expanded up to $l_{max} = 90$, the GFZ-RL5a series (blue) shows the largest gap between the two correlation curves, suggesting the formal covariance information being less realistic than for the ITSG solutions. The ITSG-Grace2014 series (green) lies in between the two other ones. The observation of generally higher noise content for e.g. the GFZ-RL5a series, with respect to the ITSG-Grace2016 series from Figure 4-10, can be supported by the properties of the correlation length and its convergence towards zero (especially in the north-south along-track direction), derived from the empirical error covariance information. The lower panel of Figure 4-14 exhibits a slower decrease of empirical error correlation for GFZ-RL5a than for the other series. The upper panel also always shows the highest correlation with respect to the distance for GFZ-RL5a compared to the other series. A distinct difference especially in the east-west direction can be found for the CSR60-RL05 series. The distance between the zeroing of the curves is larger than for the other three series. This is reasoned by the degree of SH expansion and the dominant SH order of correlation. By counting the zero-crossings with respect to the distance, one can determine a dominant order of correlation for the three series expanded up to $l_{max} = 90$ around 61. The CSR60-RL05 series (black) is only expanded up to $l_{max} = 60$ and therefore cannot have a dominant correlation around the SH order of 61. Its dominant correlation is carried by the SH order of around 45. These numbers for the SH orders of correlation are in good agreement with the findings of Murböck [2015], where dominant correlations for SH orders of around 15, 30, 45, 60 and 75 (investigating different GRACE and GRACE-like simulated solutions expanded up to $l_{max} = 90$) are described. Experiments carried out show very good agreement with these numbers whilst analyzing both formal and empirical error covariance matrices.

To better understand the properties of the correlations embedded in SH orders, a more detailed investigation is performed. Correlations following the relation expressed in equation (4.12) can also be evaluated for tuples of SH coefficients and their correlation. The RMS of correlation between coefficients sorted by SH order is computed and shown in Figure 4-15. Horizontal and vertical axis display the SH orders of the sets of tuples being evaluated. One pixel presented in the display of Figure 4-15 represents accordingly the RMS derived from all correlations between coefficients of the respective tuple of SH orders. The two panels show very clearly bands of higher correlation for specific SH orders. Both correlation matrices are computed from formal ITSG-Grace2016 error covariance matrices. The left panel of Figure 4-15 is based on the one from 2004-04 and the right panel originates from the one from 2016-01. Apart from the SH order, a second sorting criteria is applied. Each correlation between SH orders is set up by a two-by-two pixel box containing the contributions from odd and even SH degrees. The distinction regarding odd and even SH degrees in the context of correlated errors for GRACE solutions is documented e.g. by Swenson and Wahr [2006] and also addressed in section 5.2, discussing the Swenson and Wahr type filter approach [Swenson and Wahr 2006] in detail. The issue of correlations between coefficients of same order and parity of degree is furthermore addressed in the section regarding the aliasing problem (cf. section 2.5).

From Figure 4-16 a clear pattern regarding the correlation per SH order divided by parity of the SH degree can be observed. The figure shows a zoom-in of the left panel of Figure 4-15 for the sector spanning from SH order 0 to 20 against 50 to 70. As mentioned, the distinct linear features, either parallel or perpendicular to the diagonal, are composed of two-by-two pixel boxes. The upper left of each box refers to even, the lower right to odd SH degrees, the upper right and lower left to mixed contributions. It is apparent that even or odd contributions show significantly higher correlation than mixed ones. This can be expected from theoretical grounds explained in section 2.5.

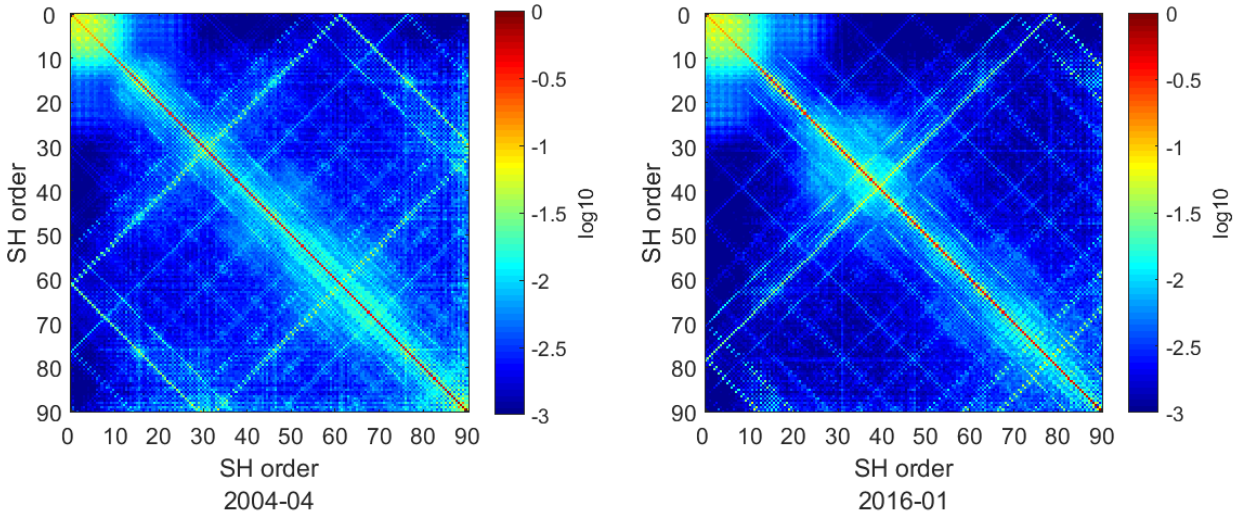

Figure 4-15: RMS of correlation per SH order distinguished between odd and even SH degree from two ITSG2016 formal error covariance matrices (left: 2004-04, right: 2016-01) in logarithmic ($\log_{10}$) scale.

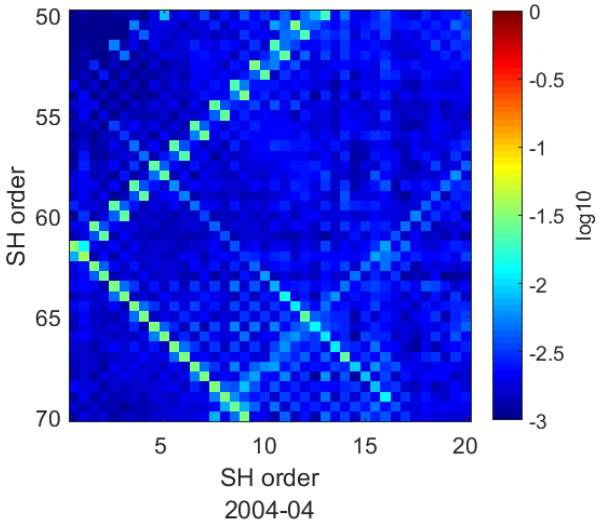

Figure 4-16: RMS of correlations per SH order divided by even and odd degrees as augmented display of the left panel of Figure 4-15. Display shows a sector from SH order 0 to 20 against 50 to 70 in logarithmic ($\log_{10}$) scale.

The following analysis is performed in order to analyze the distinct features, parallel or perpendicular to the diagonal, in more detail. Let m_x be the SH order on the horizontal axis of each panel of matrices as in Figure 4-15 and m_y the SH order of the vertical axis entries without applying the differentiation between even and odd SH degrees. By tracking the parallel features, it turns out that a constant value for the difference of the contributing orders is present (slope=-1). For the perpendicular features, the sum of the two contributing SH orders is constant (slope=1).

$$const_{parallel} = |m_x - m_y| \tag{4.13}$$

$$const_{perpendicular} = m_x + m_y \tag{4.14}$$

Since the features in the left and right panel of Figure 4-15 show different patterns, an evolution of the correlation structures in time can be assumed. To verify this impression, a further analysis of computing the RMS for each tuple with constant values for $|m_x - m_y|$ and $m_x + m_y$ from the RMS of the correlations matrix, evaluated by SH order, is performed. This is repeated for each available monthly solution. Figure 4-17 shows in the left panel the evolution of the SH order correlation patterns derived by all $m_x + m_y$ tuples. The right panel shows the analysis for the

$|m_x - m_y|$ tuples. The patterns agree very well with the order resonance frequencies computed by Murböck [2015] for GRACE orbits. The effect of the SH order resonances can be observed for $m < 2 \cdot l_{max}$. Distinct and prominent features correlated to e.g. deep resonance phases are: a strong resonance for m=61 in mid-2004, for m=168 in end 2006, for m=107 in 2009/2010, for m=46, 92, and 138 in mid-2012, and for m=31, 62, 93, 124, and 155 in the beginning of 2015. Not only are resonance peaks present in the figure, but also elongated features visible throughout the whole time series, representing resonance frequencies e.g. around m=61. The white horizontal lines represent data gaps with no monthly solution available. As decorrelation filters are based on the correlations, embedded in the normal equation matrices, such variable behavior needs to be taken into account. Section 5.3 addresses the impact of incorporating time variable versus static correlation patterns in detail.

As to be expected, correlations between coefficients are driven by the orbital configuration of the mission.

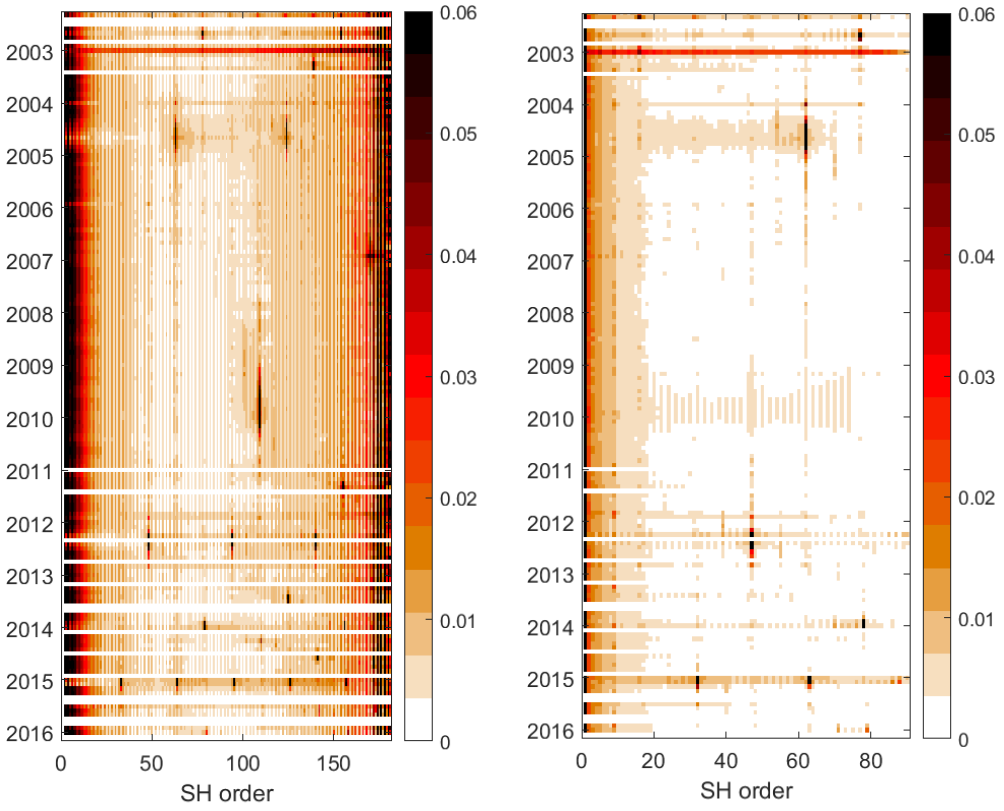

Figure 4-17: Evaluation of the RMS of tuples agreeing with equation (4.14) (left panel) and equation (4.13)(right panel) applied on the ITSG-Grace2016 time series.

Another way to analyze the correlation matrix of a specific time series is to compute the RMS of correlations of tuples differentiated by even and/or odd degrees. Figure 4-18 shows in the left panel the result for the ITSG-Grace2016 time series for the month 2004-04. The right panel of the figure shows the same analysis for the same month for the GFZ-RL5a series. Each panel is divided into four sectors. The upper left sector represents the RMS of correlations between tuples of odd/odd SH degree coefficients, whereas the lower right sector represents for tuples of even/even SH degree coefficients. The upper right and lower left corner represent the RMS for tuples of mixed even/odd resp. odd/even SH degrees.

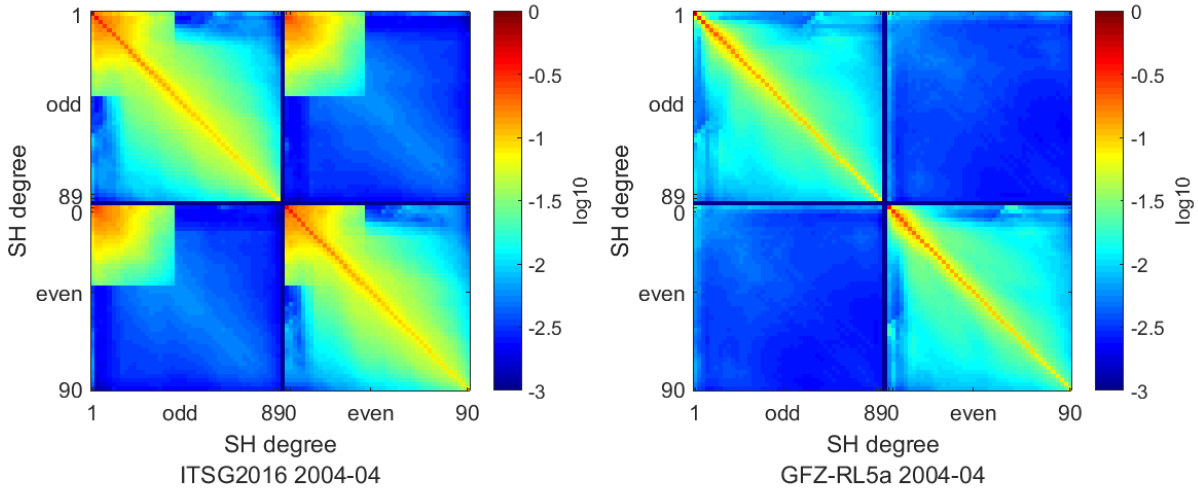

Figure 4-18: Degree RMS of correlations, split up in odd and even SH degrees, for the month 2004-04 of the ITSG-Grace2016 time series (left panel) and GFZ-RL5a series (right panel), in logarithmic scale.

One can observe a very distinct difference in the RMS of correlations between odd and even SH degrees for the two solutions. For the ITSG-Grace2016 solution in the left panel for even, odd, and mixed contributions, a very characteristic pattern of high correlation up to SH degree 40 can be observed. This is due to the processing concept of the ITSG-Grace2016 time series. According to Klinger et al. [2016], a daily solution up to SH degree 40, using a Kalman filter technique, is subtracted from the whole estimate on the basis of normal equations. Using a Kalman filter to estimate short, e.g. daily variations of the gravity field, is described e.g. by Kurtenbach [2011]. The application of a Kalman filter approach, embedding a state vector carrying prior information from one time step to the next one, apparently causes these very clear correlations. For both results (left and right panel) the correlations between SH degrees close to each other are significantly higher than for tuples of coefficients separated by a large number of SH degrees. This results in higher correlation values along the main diagonal and smaller values for far-off-diagonal elements. For the sectors representing the RMS of mixed tuple correlations, significantly smaller values are observed than for the odd/odd or even/even ones. This is in agreement with the findings by e.g. Swenson and Wahr [2006], who built their empirical decorrelation approach on this property of the GRACE solutions. By comparing the correlation patterns from Figure 4-18, one can draw the conclusion that a general assumption of correlations between different GRACE time series is only partially valid. Whilst using decorrelation filters based on the correlation structures embedded in the normal equations, a distinction regarding the respective time series appears advisable.

The correlation patterns per SH order derived from the empirical error covariance matrices do not show such sharp lines expressing strong correlations like the ones from a specific month. Mainly due to changes in the orbital configuration (e.g. the altitude and orbit repeat periods), a very blurred picture of the correlations can be seen. It contains superimposed contributions from all different orbital configurations the GRACE satellites ran through during the period under consideration. A general pattern of higher correlations between tuples of coefficients originating from close range SH degrees can be observed, similar to the pattern described from Figure 4-18.

Considering the findings regarding the properties of the GRACE time series investigated, the ITSG-Grace2016 time series appears to exhibit the most realistic formal error characteristics. It is chosen to serve as basis for the real data application discussed later on in this thesis. The temporal evolution of correlation characteristics is evident, and does justify taking into account time variable information to closely cover for the respective situation of the monthly solutions.

The benefits of employing time variable error covariance information instead of static one are addressed in detail in section 5.3. Since different time series exhibit distinct differences in correlation patterns, a generalization of the GRACE correlation pattern using "one average pattern" seems sub-optimal. If regularization type filters are used, it is recommended to employ for each time series the respective error covariance matrices, since the processing centers pursue different processing techniques, resulting in deviations of the correlation patterns.

4.3.3 Isotropic filters

A very common and widely used isotropic filter is the Gaussian type filter. It is described e.g. by Jekeli [1981], put in context with GRACE by Wahr et al. [1998], and used for real GRACE data processing e.g. by Swenson et al. [2003] and many others. Another example for an isotropic filter would be a standard cut off filter (also known as low pass filter). It cuts the set of SH coefficients at a certain degree, which represents the simplest limitation of a SH series expansion, and is thus avoiding the influence of unwanted signal content in the resulting solution. As one can see from section 2.2 (cf. Figure 2-1), the cut off filter does not comply with the need to perform a gradual separation of signal and noise by downweighting the coefficients containing a low signal to noise ratio or signal that is not part of the target signal. Figure 2-1 shows that this ratio is in a first order approximation strongly SH degree dependent, evolving as a function of the SH degree. Examples of weighting factors derived by equation (4.15) respective the recursive approach shown in equation (4.16) [Jekeli 1981] are presented in Figure 4-19.

$$W(\alpha) = \frac{b}{2\pi}\frac{e^{-b(1-\cos\alpha)}}{1-e^{-2b}} \tag{4.15}$$

$$\begin{aligned} W_0 &= 1 \\ W_1 &= \frac{1+e^{-2b}}{1-e^{-2b}} - \frac{1}{b} \\ W_l &= -\frac{2l-1}{b} W_{l-1} + W_{l-2} \end{aligned} \tag{4.16}$$

with

$$b = \frac{\ln 2}{1-\cos\varphi} \quad and \quad \varphi = \frac{r}{R} \tag{4.17}$$

The value of α in equation (4.15) represents the half width radius (also referred to as half-width-at-half-of-maximum) expressed as spherical distance (assuming $\alpha = \varphi$). Following Peters [2007], it holds $W(\alpha = \varphi) = 0.5 \cdot W(\alpha = 0)$. To derive weighting factors W_l between 1 and 0 for each SH degree, one needs to normalize the result from (4.15) by dividing by $W(\alpha = 0)$. This is realized in the recursive approach by setting $W_0 = 1$. Other isotropic filters known in the geodetic community are the Pellinen filter [Pellinen 1966] and Hann filter [Jekeli 1981]. They are both described in Jekeli [1981] and a discussion regarding their application in the context of filtering time variable GRACE gravity field solutions can be found e.g. in Peters [2007]. The Pellinen and Hann filters will not be used or discussed further on, since they do not allow separation of target signals from the residual signals and noise on a level of accuracy aimed for within this thesis.

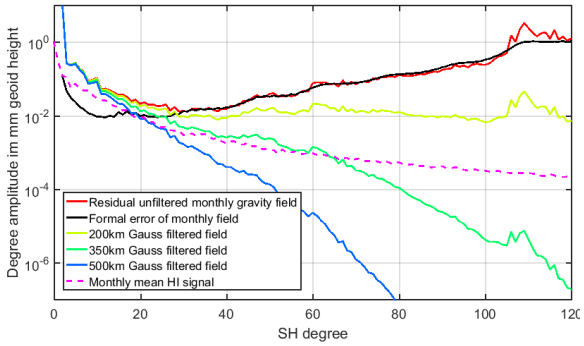

Figure 4-20: Degree amplitudes of one exemplary month (ITSG-Grace2016 2010-01) in unfiltered state with formal error and filtered states. Mean monthly HI signal as potential target signal for comparison from model [Dobslaw et al. 2015a] data.

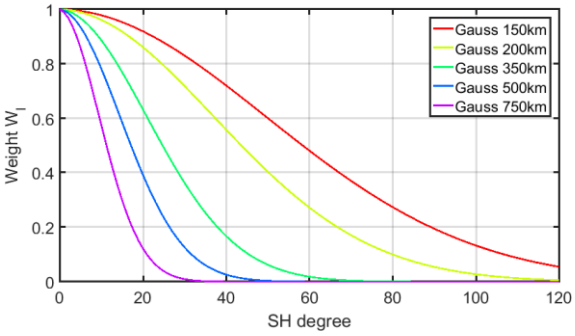

Figure 4-19: SH degree dependent Gaussian weighting factors W_l for different half width radii α.

From Figure 4-20 one can see the SH degree dependent evolution of the residual unfiltered signal in terms of degree amplitudes (red) with its associated formal error (black). For this example, the month 2010-01 from the ITSG-Grace2016 time series up to $l_{max} = 120$ is used. The static field subtracted to derive the residual field is GOCO02S [Goiginger et al. 2011]. To illustrate the behavior of the degree amplitudes of a potential target signal, the average HI signal [Dobslaw et al. 2015b] for January is shown as the purple dashed line. For the HI signal one can observe a decrease of amplitude with increasing SH degree, contrary to the unfiltered GRACE signal (especially for $l > 30$). Since formal error and signal amplitude for the unfiltered signal coincide for $l > 30$, one can conclude a non-significance of the unfiltered signal. In other terms, one could say the unfiltered signal is predominantly composed by noise. A discussion whether the formal error is realistic or not can be found in the previous section 4.3.2, rating the ITSG-Grace2016 formal error being realistic. The resulting degree amplitudes, after applying three different Gaussian type filters on the unfiltered residual solution, are shown in yellow (200km), green (350km), and blue (500km). The Gaussian filter with a half weight radius of 350 km shows, compared to the other two examples, best agreement with the target HI signal.

Further investigations presented in chapter 5 for the GRACE and GRACE-FO like missions will confirm a half weight radius in the area of about 350 km as suitable filter strength (cf. section 5.3). Suitable should be understood in terms of achieving the best compromise between the two opposing goals of preserving the target signal and suppressing noise and other signals (like residual AO signal remaining from imperfect de-aliasing). Since the only steering factor for the Gaussian filter is the half weight radius, it is not able to account for e.g. better spatial coverage and lower noise level in polar regions. It cannot account for varying representation of target signal by zonal, tesseral or sectorial coefficients, for varying spectral characteristics of potential target signals (cf. chapter 4.1), and for the north-south oriented striping pattern due to its isotropy. The effect of smearing locally concentrated high amplitude signals, caused by globally uniform and isotropic filter behavior, increases the effect of spatial leakage (cf. chapter 4.2.3). One advantage of the Gaussian filter, which makes it widely used, though it comes along with the aforementioned deficiencies, is its limited complexity, making it easy to be implemented in a processing chain. Interested readers can find a summary of different isotropic and anisotropic filter methods applied on a sphere in Devaraju [2015].

4.3.4 Anisotropic & regularization type filters

As the previous section 4.3.3 showed clear drawbacks using the isotropic Gaussian filter method, some more sophisticated anisotropic or regularization type filter methods are introduced. Among others, the methods by Han et al. [2005], Swenson and Wahr [2006], Sasgen et al. [2006], Kusche [2007], and Klees et al. [2008] are of particular interest. Han et al. [2005] describe the correlation structure as well as the amplitude ratio of signal and errors contained in GRACE solutions being not only degree, but also order dependent. Figure 4-21 gives an example for the ratio between geophysical signal from a model and a residual GRACE solution. The geophysical model is a monthly average of one month of 6-hour hydrological, ice and solid earth signal from the model by Dobslaw et al. [2015b]. The month used from GRACE is 2010-01 from the ITSG-Grace2016 time series.

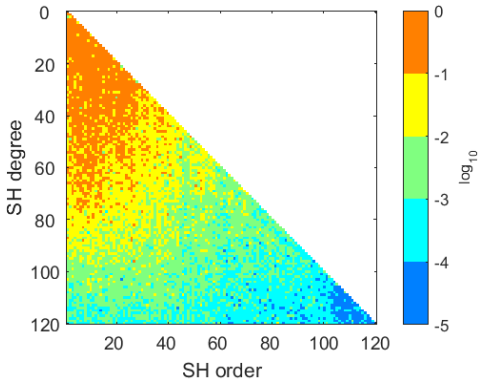

Figure 4-21: Amplitude ratio between target HI signal and unfiltered residual GRACE signal in $\log_{10}$ according to equation (4.18).

A clearly not only SH degree but also SH order dependent behavior of the amplitude ratio is visible in Figure 4-21. For lower SH orders of a specific SH degree, the ratio is higher than for higher SH orders of the same SH degree. The ratio γ_{lm} is derived by evaluating the following relation.

$$\gamma_{lm} = \frac{\sqrt{\left(C_{lm^{HI}}^2 + S_{lm^{HI}}^2\right)}}{\sqrt{\left(\Delta C_{lm^{GRACE}}^2 + \Delta S_{lm^{GRACE}}^2\right)}} \tag{4.18}$$

The indices HI and GRACE represent the target signal, respectively the unfiltered residual GRACE coefficients. Amending the concept of the Gaussian filter, downweighting coefficients dominated by noise, a variation of the weighting, also depending on the SH order, is introduced by Han et al. [2005] leading to a non-isotropic weighting function. Other anisotropic filter approaches are e.g. the Fan filter discussed by Zhang et al. [2009].

A second category of filters are regularization type filters. Prominent representatives are the Wiener filter by Sasgen et al. [2006], the DDK filter approach by Kusche [2007], and the ANS filter by Klees et al. [2008].

For the Wiener filter, the regularization only depends on the SH degree. For the DDK filter, basis for the VADER filter discussed within this thesis (cf. section 5.3), the regularization is based on a synthetic GRACE error covariance matrix, derived from orbit information, in combination with a static degree dependent signal variance (cf. equation (2.18)). DDK filtered solutions with 8 different filter strengths can be obtained for all ICGEM hosted GRACE time series via the ICGEM web portal. The ANS filter is designed as a part of the GRACE level-2 product

estimation itself and not solely as a post-processing method. It is based on the error covariance information of the respective month, originating from the estimation process and an iteratively derived signal variance. The iterative signal variance is initiated with a constant signal variance. A set of monthly GRACE time series solutions is filtered with this first setup of the filter. From the filtered time series containing signal, a new signal variance is estimated serving as input for the next iteration step. The process continues until the residuals of two consecutive signal variance estimates are below a certain threshold. The approach serves as basis for the DMT-1b time series [Liu et al. 2010], covering the timespan from 2003 until end 2010 (as from November 2016). A disadvantage of the ANS filtered DMT-1b solutions is the globally optimized filter design, not allowing to adjust the filter strength to specific target signals and target regions. Therefore it is not applicable as an adjustable post-processing method. Experiments comparing signal amplitudes from multiple GRACE time series indicate comparably low signal content for the DMT-1b solution, potentially due to the strength of the regularization applied.

Another tailored regularization approach is the concept leading to the GRGS solutions. A description of the approach is given by Bruinsma et al. [2010]. The regularization is performed as part of the inversion process. Accordingly this filter is contrary to the VADER filter not a dedicated post-processing strategy.

Other methods employed for filtering or smoothing GRACE solutions are e.g. empirical orthogonal function (EOF) filtering concepts [Wouters and Schrama 2007], or the empirical decorrelation approach (also known as a modified version of the Savitzky-Golay type filter [Savitzky and Golay 1964]) introduced by Swenson and Wahr [2006]. The latter filter is analyzed and rated in section 5.2.

5. Optimized filter strategies for GRACE and GRACE-FO

The following chapter focusses on the tuning and further development of filters respectively post-processing methods, in order to derive geophysical signals from GRACE or GRACE-like missions with improved quality. The main objective to reach is optimizing filter strategies in order to preserve as much signal as possible and to suppress as much noise as possible. Accordingly the term optimized should be understood as separating the target signal aimed for from residual signal and noise in the most effective way. As discussed in section 4.3, a differentiation regarding not only the target signal but also the target region must be made, since the noise level of GRACE-like solutions is at first order latitude dependent. In this context two approaches are presented. The first approach is the determination of an optimized configuration of the Swenson and Wahr type empirical decorrelation filter ([Swenson and Wahr 2006], cf. section 5.2). For reasons of simplicity, the filter is referred to as "S&W filter" in the following. The discussion of the approach ranges from the selection of suitable time series, in terms of degree of the SH expansion, to the choice of filter parameters and target regions, for deriving the target signals. The second approach discussed in-depth is the aforementioned time variable decorrelation filter approach (VADER filter). All constituents and various design options are evaluated and rated in order to derive a recommendable setup of the processing chain. Before discussing the two post-processing methods, a short section dealing with the differences to be expected as from today's perspective regarding the applicability of filter methods for GRACE time variable gravity fields on GRACE-FO like time variable gravity fields is presented.

The datasets used as input for the real data analysis for the VADER filter (section 5.3) are the ITSG-Grace2014 and ITSG-Grace2016 time series. The selection is based on the assessment of the available GRACE time series as presented in section 4.3.2. Compared to the other investigated time series, they both show best applicability for being employed in real data processing using the VADER filter. The closed loop white noise and colored noise datasets from the simulation environment (cf. section 3) are employed for assessing the design parameters to develop a deeper understanding of how the filter works, and to determine which configuration is suited best. For the optimized S&W empirical decorrelation filter, different GRACE time series can be used, since the filter does not depend on the quality and availability of e.g. the error covariance matrices. As for assessing the VADER filter, the closed loop white noise time series serves again as testing environment.

5.1 The resemblance between GRACE and GRACE-FO from the perspective of post-processing methods

As described in chapter 1.1, the major difference between GRACE and GRACE-FO is the instrumentation for the inter-satellite ranging system. Different levels of performance for system components change the proportion of deterministic and stochastic error budgets. According to Flechtner et al. [2016a], reduction in single components of the total error budget can be expected (cf. Figure 1-2). Nevertheless the total error budget level is expected to remain on a similar scale as for GRACE, since dominating error budget contributors, like AO and OT de-aliasing errors, are expected to be on almost equal level. This is due to the current design of the level-2 processing chain, as AO and OT de-aliasing depends on models [Dahle et al. 2012; Bettadpur 2012]. As long as there is no improvement in the quality of the de-aliasing models, de-aliasing errors will be responsible for correlated errors in GRACE or GRACE-FO solutions in a comparable way, thus

leading to similar correlation structures, as the orbital configuration is also a continuance of the GRACE configuration. As post-processing filters are either independent of the set of SH coefficients they are applied to, or depend, like the VADER and S&W filter, on correlations embedded either in the error covariance matrices respectively the SH coefficients, no major differences should be expected in the applicability of post-processing methods switching from GRACE to GRACE-FO solutions. If the processing concept is changed, as e.g. discussed in the outlook (cf. chapter 8), a readjustment of post-processing methods is likely to be necessary in order to deliver better results.

5.2 The Swenson & Wahr type empirical decorrelation filter: Assessment of opportunities and limits

The empirical destriping filter following Swenson and Wahr [2006] has proven to effectively reduce the typical north-south oriented and correlated error structures of GRACE monthly solutions [Werth et al. 2009]. The filter is based on the observation that the GRACE typical north-south oriented striping structures correspond to specific patterns in the SH coefficients, namely correlations among the coefficients of a given SH order and even or odd SH degree (cf. section 2.5). A possible way, depicted by Swenson and Wahr [2006], to remove these patterns is to fit polynomials to the respective sequences of SH coefficients individually for each month, which are subsequently reduced. The S&W filter belongs to the category of adaptive, inhomogeneous, and anisotropic filters. The basic parameters to choose are the degree of the polynomial n_{poly} and the minimum order m_{start} for which the filter procedure is applied (cf. Figure 5-1). Additional adjustable parameters are the maximum degree of expansion $L_{\max}$ the filter is applied to, and a window size w, confining the sampling points included for the polynomial fit. It holds $L_{\max} \leq l_{\max}$, since as later discussed, in some cases applying the filter is only practicable to a part of the whole set of coefficients. Equation (5.1) describes, following Swenson and Wahr [2006], the relation between filtered $\Delta C_{lm}^{\text{SW}}$ and unfiltered coefficients $\Delta C_{lm}^{\text{ewh}}$.

$$\Delta C_{lm}^{\text{SW}} = \sum_{\substack{n=l-s \\ n:\,even\ or\ odd}}^{l+s} \Lambda_{lnm} \Delta C_{nm}^{\text{ewh}} \tag{5.1}$$

Λ_{lnm} describes the filter, respectively the transfer function between filtered and unfiltered coefficients. The indices l and m describe the SH degree and order. n represents the degree. Whether it runs over even or odd parity with l, depending on the settings. The quantity w defines the window length, or in other words the number of the SH coefficients taken into account for the polynomial fit. It is defined by the sampling point $\pm$ the desired integer length of the sampling interval s ($w=1+2s$). This leads to an odd value for w. The parameter $L_{\max}$ is not shown in the equation, but implies either limiting the set of ΔC_{lm}^{ewh} to a desired maximum degree of SH expansion, or limiting the coefficients filtered to a maximum SH degree, which is order dependent (cf. [Chambers 2006a]). This could be e.g. $L_{\max} = m+40$. The filter Λ_{lnm} itself consists of a polynomial estimate, based on a specified set of sampling points. Two major versions of the polynomial fit and subsequent reduction of correlated noise are documented in literature.

The first version (later referred to as “version one”) of the approach is to apply a polynomial for each SH coefficient to be filtered separately, always taking into account a defined set of unfiltered sampling points. After evaluating the polynomial function at the respective SH coefficient, the result is subtracted from the unfiltered SH coefficient, leading to the filtered SH coefficient [Werth et al. 2009; Devaraju 2015].

The second version (later referred to as "version two") is to estimate the polynomial once for each set of coefficients of same m and even or odd parity for l, using again a defined set of sampling points from $l = m$ to $L_{\max}$. Subsequently this single polynomial is evaluated for all sampling points, leading to the filtered coefficients by subtracting the polynomial from the whole set of unfiltered sampling points [Chambers 2006a].

Since the SH coefficients derived from GRACE observations contain a portion of correlated noise or error, this empirical assessment works, as one can see e.g. from the examples in section 5.4. But not all noise contained in an unfiltered solution is correlated and can be removed with such an empirical approach. To suppress the uncorrelated or random noise, together with the noise contained in the unfiltered sections of the given set of SH coefficients (e.g. the ones with $m < m_{start}$ or the ones with $l > L_{\max}$), Swenson and Wahr [2006] recommend the application of a Gaussian filter (cf. section 4.3.3) as second step of a two-step filter cascade, completing the approach. With this second step, a new variable for the filter appears, and needs to be defined. Reviewing literature, most of the experiments are performed by using a Gaussian filter with half weight radii ranging between 300 km and 500 km (e.g. [Werth et al. 2009; Vishwakarma et al. 2016; Watkins et al. 2015]). Not all authors employ a Gaussian filter, but use other filters as second step of the cascade [Werth et al. 2009].

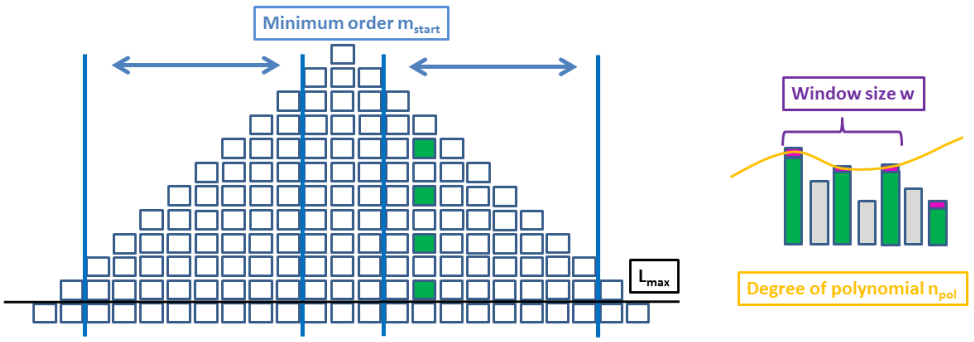

Figure 5-1: Scheme of the S&W empirical decorrelation filter with parameters m_{start}, $L_{\max}$, n_{poly}, and w.

Figure 5-1 gives a schematic overview of the parameters to be chosen whilst applying the S&W filter. From the minimum order m_{start} onwards, the filter is applied to all coefficients with $m < l_{\max} - 2n_{\text{poly}}$. As indicated by the vertical blue lines, part of the coefficients (represented by the rectangular shapes) is not filtered since the number of sampling points available is not high enough to fit the desired polynomial. For lower polynomial degrees, neglecting these coefficients does not have a major impact on the filtered solution, as this group of coefficients also exhibits the largest uncertainty. But for increasing polynomial degrees, neglecting more and more coefficients becomes a significant problem.

To apply the S&W filter, no error covariance information is needed. The S&W filter is built on the correlations embedded in the SH coefficients themselves, and thus the filter does not need any additional information or dataset than the set of SH coefficients to filter. Along with the simplicity of implementing the S&W filter, this circumstance can be seen as the most significant advantage of the approach with respect to the VADER filter, which needs more information to be successfully applied (cf. section 5.3). As one can see from Figure 5-1, the choice to make for the first assessment is the degree of polynomial n_{poly} and the minimum order m_{start}, from which onwards the filter is applied. A second prerequisite for the successful utilization of the S&W filter is the transformation of the SH coefficients to so called residual mass coefficients ΔEWH, which are in the words of Swenson and Wahr [2006] "*GRACE monthly anomalies converted to mass*", before applying the polynomial fit. The transformation from residual SH coefficients to mass coefficients can be applied by using the relation expressed in equation (2.9).

Figure 5-2 gives an example of unfiltered and S&W filtered coefficients, plotted separately for parity of the SH degree and sine/cosine coefficients. The blue curves illustrate the aforementioned correlation, expressed by the uniform and steady behavior of SH coefficients of same parity, separated by sine and cosine coefficients. The underlying residual (static GOCO02S field is subtracted) solution originates from the ITSG-Grace2016 time series and is transformed to ΔEWH coefficients. The black lines indicate a polynomial fit of degree seven, which is estimated from all available sampling points. The choice of a suitable polynomial degree is discussed later on. The red curves represent the empirically decorrelated coefficients. The degree of expansion shown in the example ranges up to $l_{\max} = 90$ and the coefficients shown are of SH order 31.

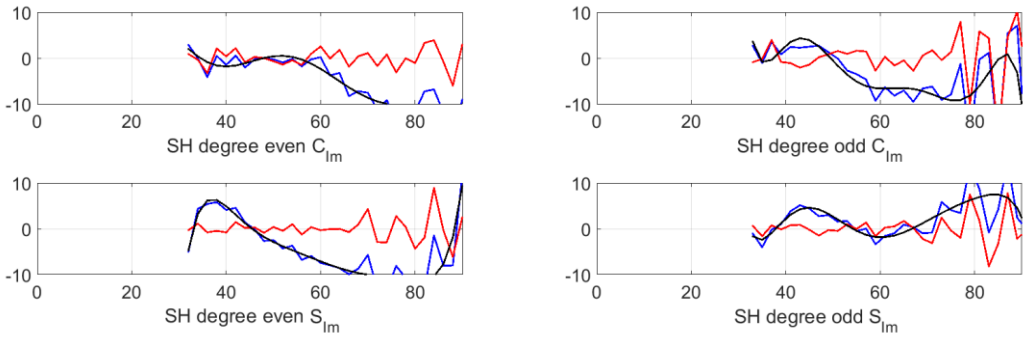

Figure 5-2: Example of unfiltered (blue) and S&W filtered (red) C and S coefficients separated by even and odd SH degrees for SH order 31. The fitted polynomial (black) is of degree 7.

For all sampling points with $l < 70$, very smooth and steady behavior can be observed for the unfiltered state. For $l \approx 70$ and higher, this steady behavior is apparently not present anymore and the nominal values of the coefficients start to become volatile. Analyzing the behavior of the SH coefficients for a solution expanded up to $l_{\max} = 120$ reveals even more unstable behavior for coefficients of same order and parity for higher SH degrees.

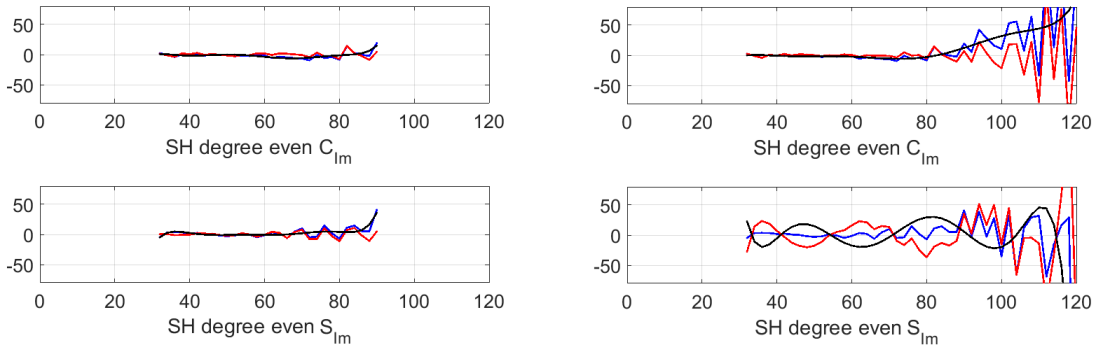

Figure 5-3: Example of unfiltered (blue) and S&W filtered coefficients (red) C and S coefficients of even SH degree for SH order 31 with a fitted polynomial of degree 7 (black). The SH expansion for the left panels is up to SH degree 90, and for the right panels up to SH degree 120.

Figure 5-3 shows in the left two panels the properties of SH coefficients (now only even $\Delta C_{lm}^{\mathrm{ewh}}$ and $\Delta S_{lm}^{\mathrm{ewh}}$) expanded up to $l_{\max} = 90$. In the right two panels the expansion is ranging up to $l_{\max} = 120$, originating from the very same dataset. Blue lines indicate unfiltered coefficients, and red lines the filtered coefficients. The fitted polynomial is again shown in black. Comparing the quality of the fit for the upper two examples reveals only minor difference between the two degrees of expansion. For the examples in the lower two panels, the fit shows for the expansion to $l_{\max} = 120$ strong oscillating behavior especially in the lower SH degrees. Comparing the lower left with the lower right filtered results (red curves), significant differences, causing artefacts in the

filtered result, occur. Ideally the filtered solution should look the same for a specific SH degree, whether expanded up to $l_{max} = 90$ or $l_{max} = 120$ (not considering e.g. omission errors). Since the fit is estimated from least squares adjustment, large residuals in higher SH degrees, caused by the volatile behavior of the coefficients, are forcing the solution to allow residuals in the lower degrees to fulfill the minimum criterion $\hat{v}^T P_{ll} \hat{v} \rightarrow \min$ (cf. section 2.3). One option to overcome this problem is to limit the maximum SH degree to which the filter, and therefore the polynomial fit, is applied to [Chambers 2006a]. Another option is to introduce a moving window, limiting the SH coefficients taken into account for the fit and the subsequent reduction for each individual coefficient derived by the fitted polynomial [Werth et al. 2009]. This approach leads, depending on the window size, to a decorrelation of the filtered coefficients, which are separated by a distance larger than the window size w (here the term decorrelation refers to the dependency or correlation induced by the polynomial fit between filtered coefficients of same order and parity of the SH degree, not to the reduction respectively filtering of correlated noise). A third option, which is not pursued in the course of this thesis, would be the introduction of weights by changing the P_{ll} matrix from identity to, e.g., a degree dependent function that downweights the volatile coefficients in the higher SH degrees, as they are expected to exhibit a low signal to noise ratio and an unstable behavior. The downweighting would result in not allowing such large residuals for the coefficients in smaller SH degrees, as visible in the lower right panel of Figure 5-3. In this context one should keep in mind that the filter cascade is non-commutative. Since the filter is, as mentioned above, applied in conjunction with a Gaussian filter of typical half widths of 350 to 500 km, the discussion regarding the handling of high SH degree coefficients becomes in a way less important. As shown in Figure 5-5, potentially remaining noise is down weighted by the application of a suitable Gaussian filter as step two of the cascade. This holds only as long as the higher SH degree coefficients do not feed back to the lower SH coefficients, as shown in the lower right panel of Figure 5-3. The mentioned Gaussian filter radii cause a downweighting of coefficients for the lower range of the filter strength (350 km) of already two orders of magnitude from degree 80 onwards (cf. Figure 4-19), thus suppressing the signal contained in this part of the spectrum. Applying the S&W filter on a solution expanded up to e.g. $l_{max} = 120$ leads therefore to a filtered solution limited in signal content to $l < l_{max}$.

In the following, investigations for optimizing the filter parameters n_{poly}, m_{start}, L_{max}, and w from closed loop experiments are presented.

Closed loop experiments assessing the potential of empirical decorrelation

For optimizing the filter setup regarding n_{poly}, m_{start}, L_{max}, and w, the closed loop simulation environment (cf. chapter 3) is employed. For determining the setup for filtering a GRACE-like monthly gravity field estimate, solutions from the white noise time series with additional deterministic AO de-aliasing error are employed (cf. Table 3-1). In the closed loop case, the criterion for a good solution, filtered by the S&W filter, is the magnitude of the cumulative degree amplitude (cf. equation (2.27)) of the residuals. The residuals are calculated as the difference between the filtered solution and the true target signal, in this case the monthly mean HIS signal. For this purpose the available monthly solutions are filtered with varying m_{start} ranging from 2 to 18, and n_{poly} ranging from 2 to 14 according to the version two of the S&W filter as introduced before. A limitation of the window length w is not introduced at this point, as this parameter is part of the version one of the S&W filter. The maximum degree of expansion is limited for all orders m at the same $L_{max} = l_{max} = 40, 60, 75,$ and 90. Figure 5-4 shows for the different degrees of expansion the obtained median cumulative degree amplitudes in mm EWH (cf. equation (2.27)) from each configuration of the S&W filter. The x-axis indicates the degree of polynomial n_{poly}, and the y-axis the minimum order to start m_{start}. The numbers above each panel indicate the respective L_{max}. Colorbar limits are chosen to be different for each panel in order to better

identify the local minima by eye. The limits for the y-axis, ranging from 2 to 18, are indicated only for the very left panel, but are valid for all four panels.

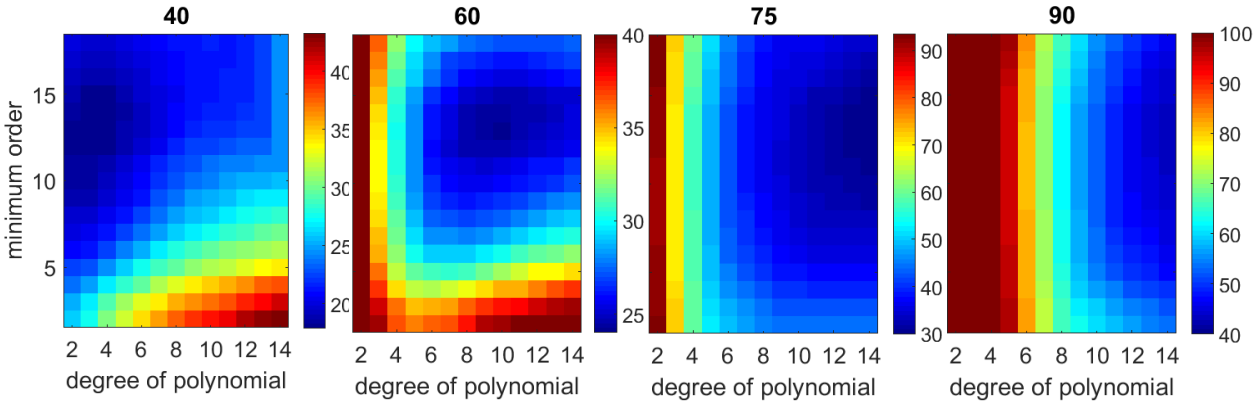

Figure 5-4: Median of cumulative residuals [mm EWH] from the closed loop white noise time series expanded up to different maximum SH degrees (indicated by number on top of each panel). The colorbar is chosen differently in order to better identify each local minimum per panel.

The very left panel of Figure 5-4 shows the residuals for an expansion up to SH degree 40. This is the same degree of SH expansion as within the experiment by Chambers and Bonin [2012], evaluating the filter setup in a similar way by minimizing the standard deviation of residuals with respect to ocean bottom pressure variations. Their finding of an optimal configuration of $n_{\text{poly}} = 5$ and $m_{\text{start}} = 15$ for the CSR-RL05 series can be confirmed with good agreement by the closed loop experiment, delivering a minimum of the residuals at $n_{\text{poly}} = 4$ and starting $m_{\text{start}} = 14$. The difference can be explained by the different time series used (real data versus simulated data) and the different target signal (ocean bottom pressure variations versus the true HIS signal of the closed loop environment). If just increasing the degree of SH expansion further on, the minima of the cumulative residuals are shifting for the degree of polynomial to higher degrees. This can be expected by looking at the decreasing steadiness for coefficients of same order and same parity of the SH degree (cf. Figure 5-3). The minimum order remains stable in a corridor between 12 and 15. The stability of the order is due to the first resonance order embedded in GRACE solutions around $m = 15$ (cf. section 4.3.2). Swenson and Wahr [2006] for example did also not observe a specific correlation pattern for $m < 8$ but for all higher SH orders. In the range of $8 \leq m < 12$ correlations are present but not strong enough for showing a global minimum in the panels of Figure 5-4 already at $m < 12$. The reason for the increasing degree of the polynomial can be found in the noise characteristics depending on the SH degree, and the way correlated errors are significantly represented by the respective SH coefficients. As Figure 5-3 illustrates, the behavior of the steadiness of the unfiltered coefficients is decreasing with increasing SH degree, thus requiring a higher degree polynomial to match the characteristics of the sampling points without introducing artefacts.

The properties of the version one of the S&W filter are better suited for handling solutions expanded to higher SH degrees, since the introduction of a moving window of a certain size makes the estimates, depending on the window size, independent of each other. The originally proposed polynomial is of degree 2 [Swenson and Wahr 2006]. Regarding the window size, no value is specified. Devaraju [2015] suggests to use a size of $w = 5$, whereas Werth et al. [2009] introduce a variable window size. The proposed settings for the window size by Werth et al. [2009] were tested and rejected upon inferior performance compared to the proposed setup by Devaraju [2015].

In the following, the results from the investigations regarding version one and two of the S&W filter are compared against each other. The best setup for version two of the S&W filter is, as one

can see from Figure 5-4, depending on l_{max} respectively L_{max}. The parameters derived from Figure 5-4 for the applied n_{poly} in Figure 5-5 are $n_{poly}=4$ for $l_{max}=40$, $n_{poly}=10$ for $l_{max}=60$, $n_{poly}=12$ for $l_{max}=75$, and $n_{poly}=14$ for $l_{max}=90$. Figure 5-4 might suggest that for the expansion to $l_{max}=90$, a higher polynomial might deliver a more pronounced minimum. Since polynomials of increasing degree need a higher number of sampling points, resulting in omitting an increasing number of coefficients (cf. Figure 5-1), and since the distribution of the sampling points leads to badly scaled inversion problems for polynomials of such high degrees, a further increase of polynomials degrees is not enforced.

The upper two panels of Figure 5-5 show the resulting median of the monthly degree RMS of the signal respectively the residuals, after applying filter parameters as introduced before, for version one and two of the S&W filter (label "S&W only"). The underlying dataset used for evaluating the performance is the 143 months long white noise closed loop time series, containing the monthly target HIS signals with additional ocean tide (OT) and atmosphere and ocean (AO) de-aliasing errors. To keep the number of variable parameters low, for all tests shown in Figure 5-5 and the metrics presented in Table 5-2, the minimum order is $m_{start}=12$. Using $m_{start}=8$ instead delivers, in the closed loop environment, results of almost equal performance. The lower two panels show the resulting SH degree RMS after also applying the second step of the filter cascade, the Gaussian filter (label "S&W+GAUSS"). The half width is set, again to limit the number of variable parameters, to 200 km for all S&W filters presented. To allow rating the performance of the filter, the unfiltered (solid black), 200km (dotted black), and 300km (dashed black) Gaussian filtered SH degree RMS are indicated for comparison in the upper panels. The mean HIS signal (cyan) is shown for comparison in all four panels. For both steps of the filter cascade, the resulting signal is shown in the left panels, whereas the residuals, with respect to the target HIS signal, are shown in the right panels.

The filter performance of only applying the S&W filter (upper left panel) delivers, especially for the lower SH degrees $l_{max}<30$, at first sight no significant differences in terms of the resulting signal RMS per SH degree. Inspecting the residuals carefully (upper right panel) reveals smaller residuals for the version one of the S&W filter (magenta) and the dedicated design for version two of the filter for $l_{max}=40$ (red) with respect to the other ones performing inferior in this spectral band. For $l_{max}=60, 75,$ and 90 the version one shows, compared to version two, significantly larger residuals for $l>40$. After applying the second step of the filter approach, these large residuals for version one are suppressed by the Gaussian filter, revealing residuals of lower amplitude, thus being in the range of the target signal. Although the version one exhibits larger residuals for $l>40$ compared to the ones originating from the version two approaches, the overall performance of version one is rated to be better for solutions of higher SH degree. The residuals for the version two filter for $l_{max}=60, 75, 90$ are higher, especially in the range of $12<l<30$, as the lower right panel reveals. This is due to the feedback mechanism induced by the polynomial fit over all sampling points spanning from $l=m$ to l_{max} (cf. Figure 5-3). For $l_{max}=40$, the version two outperforms version one. For reasons of comparison, the performance of the Gaussian filter is indicated as well. The performance of the 200km half width shows the filter performance of only applying the second step of the filter cascade, delivering unsatisfying results. The 300 km half width indicates a good match in terms of signal RMS per SH degree. Comparing the S&W filter against the Gaussian filter results shows an isotropic filter like the Gaussian one being outperformed in terms of residuals on all degrees of expansion $l>40$. The decrease of the signal RMS shortly before reaching the respective l_{max} is due to the way degree RMS is calculated. Since for each polynomial a certain number of coefficients needs to serve as sampling points, for orders $m>l_{max}-2n_{poly}$ no filtering can be applied. Thus these coefficients are omitted and contribute as zero to the degree RMS.

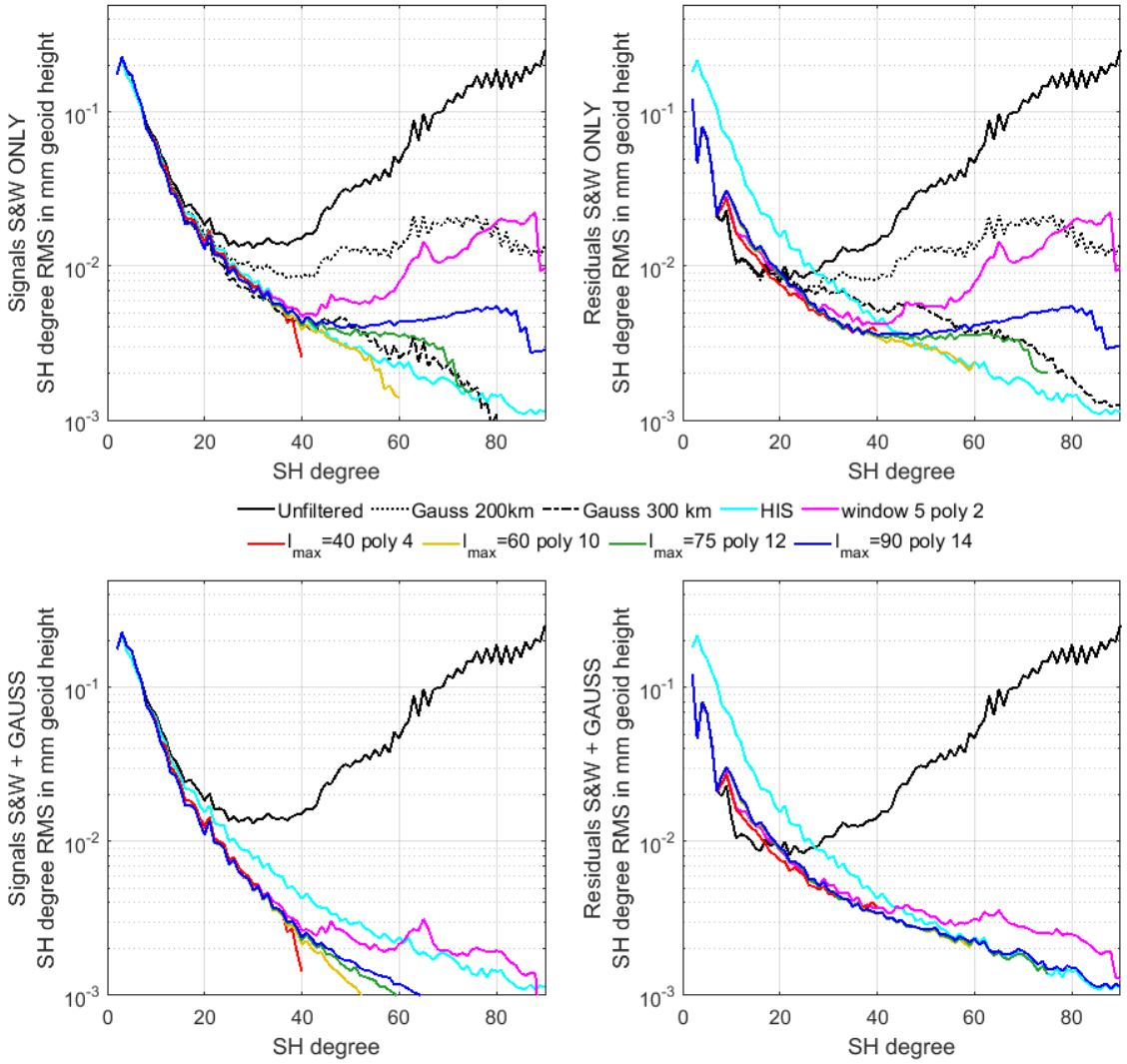

Figure 5-5: SH degree RMS of signal and residuals in mm geoid height, originating from different S&W filter setups and different degrees of expansion. Black lines represent unfiltered signal (solid), 200km (dotted) and 300 km (dashed) Gaussian filtered signals, respectively residuals. The cyan line indicates the average HIS signal for comparison reasons. Other colored lines represent the results from the respective S&W filter setup according to the legend. Left panels refer to resulting signals after filtering, whereas right panels refer to residuals with respect to the HIS signal.

Following from the experiments above, the S&W filter can be rated as suitable and effective for filtering GRACE-like temporal gravity fields expanded up to a SH degree of around 60 or even 90. If employing the version one with the moving window, an extension of the SH expansion can be made up to $l_{max} = 120$ without significant implications generated by oscillation effects in the lower SH degrees. The version two should, according to the experience gained, not be applied to such high degrees of SH expansion. For increasing degrees of expansion, the need for polynomials of comparably high degree is a clear drawback. High degree polynomials leave the problem of omitting large number of coefficients and tend to cause numerical problems by leaving the polynomial fit not well conditioned. Since usually the S&W filter is applied in a cascade with a Gaussian filter, expanding the set of coefficients further than 90 or 100 does only make sense if the half width of the Gaussian filter is chosen below or around 350 km (cf. Figure 4-19). Otherwise the downweighting would result in not only suppressing the noise but also all signal in the respective higher degrees. A summary of the findings derived from Figure 5-5 and the preceding analysis is given by listing the cumulative geoid errors, as presented in Table 5-2. In

addition, a comparison is made to the performance of the VADER filter (cf. section 5.3), also applied to different l_{max}. Exemplary results from both S&W filter versions, applied in the context of real data filtering and compared to other filter techniques, are presented in section 5.4.

5.3 VADER filter - Time variable decorrelation

The decorrelation approach adapted for the following experiments, filtering time variable gravity fields derived from satellite observation, was introduced by Kusche [2007]. Klees at al. [2008] rate their adapted version of the filter to be the optimal filter for filtering GRACE derived time variable gravity field solutions. Their adaption of the filter includes, contrary to the Kusche approach, already time variable filter properties, but is different from the approach pursued within this thesis (cf. section 4.3.4). In the following a time variable decorrelation filter (VADER) approach, which is applicable as a post-processing filter only, and is based solely on publicly available datasets, is discussed in detail. It does not depend on an own level-2 processing environment, giving access to normal equations or error covariance matrices for each monthly estimate, nor does it require complex techniques to estimate signal variance information. This makes the VADER approach, contrary to the one by Klees et al. [2008] and the subsequently derived time series and products by Liu et al. [2010], accessible for in depth analysis. It can be tailored to user needs, respectively to the requirements for determining mass balance estimates in the region of interest with the most suitable filter properties. As briefly introduced in section 2.3 (cf. equation (2.18)), the basic equation for the VADER filter reads

$$\begin{aligned} \hat{x}_{\alpha}^{VADER} &= \left(N + \alpha M\right)^{-1} N\hat{x} \\ &= W_{\alpha}\hat{x} \end{aligned} \tag{5.2}$$

The key components defining the filter matrix W_{α} are the the normal equation matrix N and the inverse of the signal variance matrix M. Both constituents are discussed regarding their setup, time variable behavior, and population (e.g. full, diagonal or order block structure) in the following sections (cf. section 5.3.1 and 5.3.2).

A measure to assess the impact of applying a regularization type filter on a gravity field solution, in terms of biasing the true solution, is presented in section 5.3.3.

The issue of applying time variable filters on time series and potential biases introduced by time variable or also static filter designs and filter strengths is addressed in section 5.3.4. An example using simulated datasets in order to assess the impact on estimated signals from decadal time series on the biasing of the true solution by either time variable or static filters is presented in the application chapter in section 7.2.

Section 5.4 summarizes the findings from the above sections and presents a suggestion for an optimal filter setup for retrieving geophysical signals from long term decadal GRACE time series.

In order to compare the filter strength, an approach to derive the approximate average filter strength in terms of a mean smoothing radius is discussed. To evaluate the average filter strength of a specific filter setup is beneficial in order to compare results from different filter strategies. Rietbroek [2015] estimates the average filter strength of DDK decorrelation filter DDK1 trough DDK8 by estimating the half width half weight radius of the convolution kernel at 0°, 30°, and 60° latitude in all four cardinal directions. This concept is picked up for making a fair comparison of the VADER and DDK filter strength based on same measures. This simple approach of only estimating the half width half weight of the convolution kernels for two transects is at first order

justified since the most significant difference in correlation type and length occurs in the along- versus cross-track, respectively north-south and east-west direction (cf. Figure 5-6). Other approaches like estimating a larger number of half width radii in azimuthal direction, e.g. every 5 degrees, are tested but no significant difference in the retrieved average smoothing radii are found. Another approach to assess the average smoothing radius tested is comparing the damping coefficient per SH degree originating from a Gaussian filtered solution and a VADER filtered solution. The damping coefficient is computed by taking the proportion between SH degree amplitudes of the unfiltered versus the filtered solution per SH degree. This approach shows high sensitivity regarding variations especially in the low SH degrees and is rejected upon not delivering reliable results for the average smoothing radius.

Figure 5-6 gives an example of the shape of a convolution kernel (left panel, for 30° northern latitude at 0° longitude) derived from the filter matrix W_α of the VADER filter. A clear anisotropic behavior is visible. The difference in along-track (north-south) and cross-track (east-west) direction is illustrated by the right panel of Figure 5-6, showing the traverse through the kernel center in east-west (blue) and north-south (red) direction. One can observe clear negative side lobes for the north-south traverse causing a sharpening or edge preserving effect in the along-track direction. The east-west averaging function is wider than the north-south one and does only show minor negative side lobes. This induces stronger smoothing in the cross-track direction, e.g. over the typical GRACE-like striping pattern. The application of the convolution kernel in the frequency domain is much more effective from a numerical point of view, since monthly solutions in spherical harmonics are available. It reduces to a simple matrix vector multiplication. In the spatial domain one would need to compute the convolution kernel for each grid point of the area investigated separately, due to the anisotropy and location dependency of the filter, and apply the kernel for each point individually. This is by far less effective or fast compared to filtering SH coefficients.

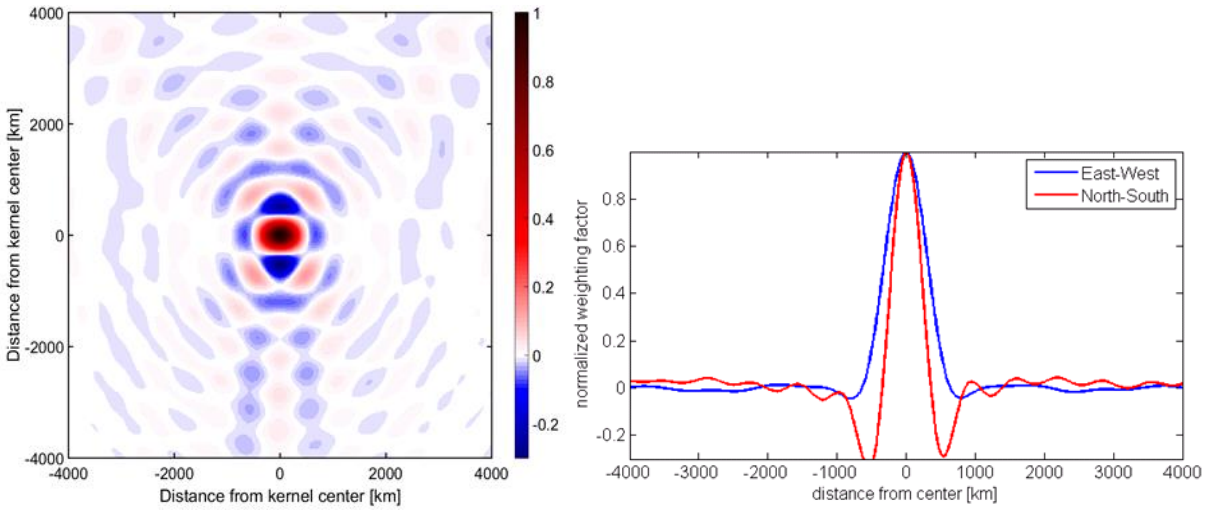

Figure 5-6 Example of a convolution kernel at 30° northern latitude for the kernel center (left panel) and the traverse trough the kernel center (right panel) in east-west (blue) and north-south (red) direction.

The numbers presented in Table 5-1, comparing the filter strength for the ITSG-Grace2016 time series filtered with the VADER filter and the average DDK filter radii, derived from the procedure outlined above, allow deciding which filters to compare with each other depending on the average filter strength. The grounds for the averaging procedure are the 12 distances in all four cardinal directions at three different latitudes estimated for each monthly solution of the time series. As one can see from Figure 5-15 in section 5.3.4, the average smoothing radius is subject to scattering for each monthly solution, depending whether a static or a time variable design is

chosen to build the VADER filter matrix W_α. In the case of a time variable design, the median value of the average smoothing radius is given, derived from all monthly solutions of a decadal time series.

Table 5-1: Average smoothing radii for different VADER ITSG-Grace2016, ITSG-Grace2014 (in brackets) and DDK filters.

VADER ITSG-Grace2016 (2014)	Average smoothing radius [km]		DDK
$\alpha = 0.001$	162 (178)		
$\alpha = 0.005$	183 (196)		
$\alpha = 0.01$	193 (207)		
$\alpha = 0.05$	224 (237)	232	7
$\alpha = 0.1$	240 (254)	267	6
$\alpha = 0.5$	287 (305)	285	5
$\alpha = 1$	312 (335)	333	4
$\alpha = 5$	389 (436)	360	3
$\alpha = 10$	431 (492)	475	2

Smaller radii occur for the ITSG-Grace-2016 than for the ITSG-Grace2014 series for the same α-values. Analysis of the respective error covariance matrices reveals numerically smaller values within matrices of the ITSG-Grace2016 series than corresponding ones of the ITSG-Grace2014 series. This implies a lower noise level for the 2016 series and is in agreement with the results depicted in Figure 4-10, comparing the red against the black dashed line. It also agrees with the result of the comparison of the empirical versus the formal error covariance matrices for the two time series (cf. Figure 4-11 and Figure A 1). A lower noise level requires less filtering, being directly influenced by the population of the error covariance matrix applied.

The relation between the filter strength of the VADER filter and the α-value is different for each time series since the level (numerical values) of normal equations, with respect to the signal variance applied, is not fixed. In case one would have the true error covariance and true signal variance, a value of $\alpha = 1$ would deliver the optimal solution.

One should also not misinterpret the average smoothing radius as the half width radius of the Gaussian filter, also known as half filter-width-at-half-of-maximum ($\frac{1}{2}$ FWHM). The filter-width-at-half-of-maximum (FWHM) represents, according to Devaraju and Sneeuw [2016], the spatial resolution of the filtered field. The spectral content of a solution filtered with the average smoothing radius, as indicated e.g. in Table 5-1, does result in a differing spectral content than the respective VADER filtered solution. Following this, the average smoothing radius should be understood only as an approximate value of the $\frac{1}{2}$ FWHM, whilst deriving the spatial resolution of the filtered field.

Figure 5-7 gives an impression of how the VADER filter is performing for different strengths (here denoted as VADER 1 to 9) for an example of the white noise simulated time series (cf. Table 3-1) containing HIS signal and OT de-aliasing error. The SH degree RMS for the unfiltered solutions is shown in gray lines. The dark gray bold solid line indicates the median for the set of monthly solutions. Some outliers can be identified showing significantly larger SH degree RMS. For all individual monthly solutions filtered with different filter strengths (shown in black lines), these outliers are not present anymore. The capturing of these outliers is exemplarily shown in section 5.4 for real data examples. The versicolored bold lines again indicate the median lines for each

family of filter results. The average HIS signal SH degree RMS is indicated in dashed yellow to give an impression which filter strengths are suitable for retrieving the target signal. Promising filter strengths can be expected for CL-VADER 4, 5, and 6. By inspecting the residuals of the signals, as displayed in Figure 5-8, this assumption regarding the promising results can be substantiated, as CL-VADER 4, 5, and 6 show lowest residuals throughout the whole band of $l < 60$.

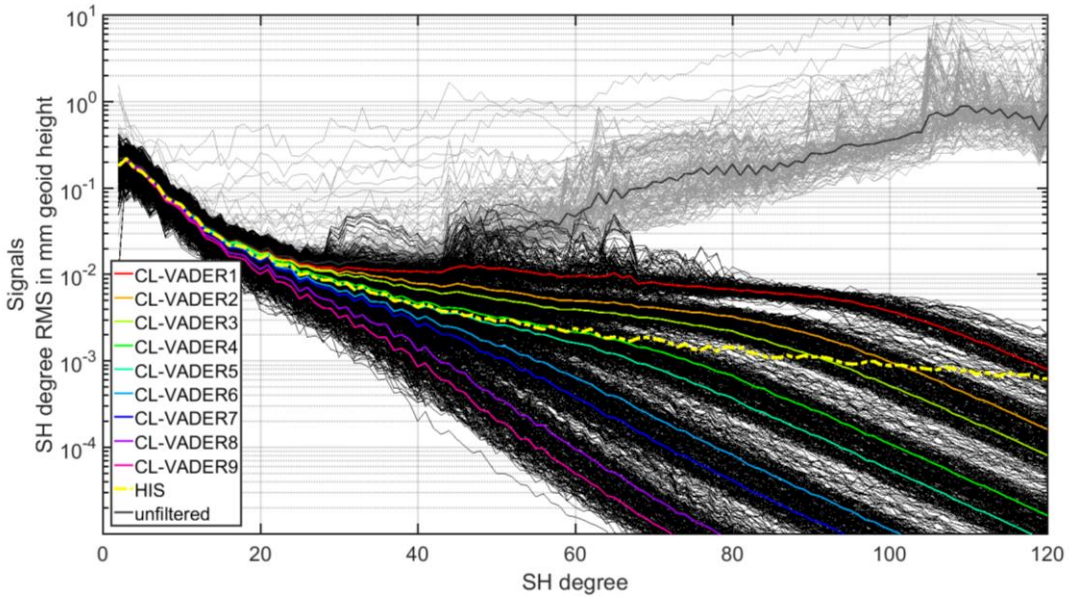

Figure 5-7: SH degree RMS for different VADER filters. Bold colored lines represent according to the legend the median degree RMS from a 143 months long time series. Thin lines represent the SH degree RMS from the respective single months. For comparison the yellow line indicates the average HIS signal.

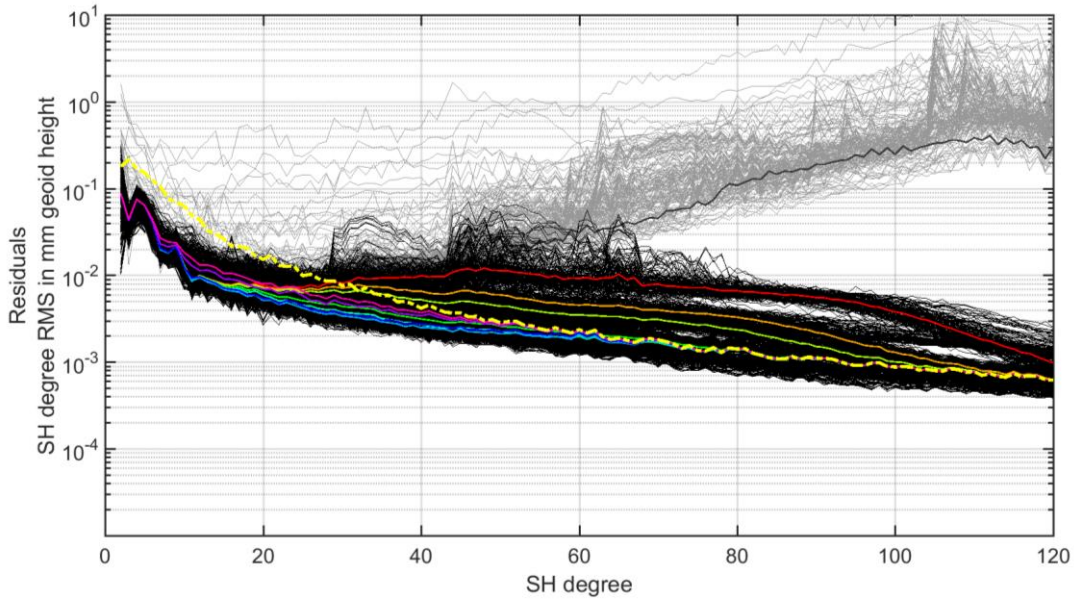

Figure 5-8: SH degree RMS of residuals with respect to the HIS signal (yellow) from different VADER filters according to the signals displayed in Figure 5-7.

The question now is which filter design suits the goal to retrieve most of the target signal best. The following two sections present investigations regarding the setup of the error covariance and signal variance information used to compute the filter matrix W_α.

5.3.1 The error covariance matrix

For the design of the error covariance matrix different options can be considered. A static approximate version, e.g. the one employed in the approach by Kusche [2007], is rejected upon the findings regarding the non-stationary behavior of correlations within a decadal GRACE time series (cf. section 4.3.2 and Figure 4-17). The impact of using non-stationary versus static error covariance information to build the filter is also addressed in section 5.3.4. Since error covariance matrices are difficult to handle from a data handling perspective, the question arises whether one should use fully populated, SH order block, or diagonal matrices. From the investigation regarding the correlation embedded in real data error covariance matrices [Murböck et al. 2016], an improvement can be expected by using the additional information regarding correlations between SH coefficients in off diagonal elements of the error covariance matrix. The gain from switching from order block to fully populated matrices is, according to these findings, less significant, but still makes a notable difference. Figure 5-9 shows the quality of geophysical signal retrieval for different setups of the error covariance matrix in terms of cumulative geoid errors of the residuals in the simulation environment. Best performance can be seen for the fully populated matrix (red). The gain switching between diagonal (blue) and order block (black) is, as expected, larger than from switching between order block and full population. The performance of the regularization using only a diagonal matrix is better than using a Gaussian filter (cyan dashed line).

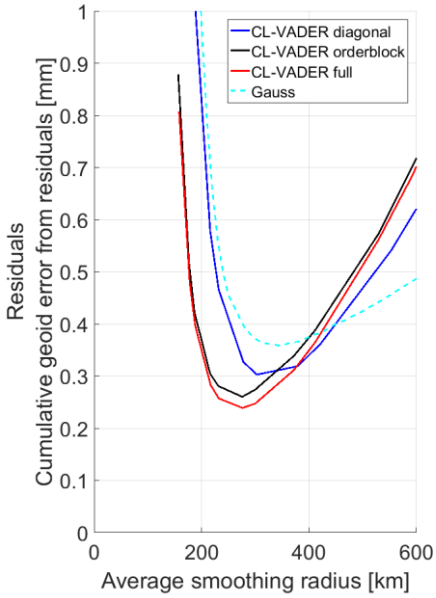

Figure 5-9: Performance of the VADER filter with different setups (diagonal/blue, order block/black, and full/red) of the error covariance matrices used to build the filter matrix. Performance of Gaussian smoothing for comparison reasons in dashed cyan line.

In the following always fully populated error covariance matrices are used.

Similarity of the formal error covariance with respect to the closed loop error covariance

An important question to answer is how realistic the closed loop error covariance matrices are with respect to the formal ones from real level-2 GRACE time series. A good agreement matters, since the results and findings from the closed loop experiments are picked up for the real data applications. The major driver for the properties of the VADER filter matrices are the correlations embedded within the error covariance matrices. To rate the transferability of the closed loop experiments regarding the design, a comparison of the error correlation structure in the spatial domain is performed. Figure 5-10 shows a comparison regarding the similarities in error correlation properties between formal real data and closed loop error covariance matrices. The figure shows in the right panel the correlation in the spatial domain for an evaluation point at 42° north and 90° west. The correlation varies from +1 (positive correlation) to -1 (negative correlation). In the left two panels of the figure, the respective traverses through the evaluation point are shown with respect to the distance from the center point in km. The three maps of the right panel give a general impression of the anisotropy of the error correlation resulting from formal error covariance matrices for ITSG-Grace2016 and GFZ-RL5a compared to the one derived from the closed loop simulations. All agree on first sight well with longer correlations in along-track (north-south) direction than in cross-track direction (east-west). Closer inspection reveals differences especially in the along-track direction (lower left panel). The correlation structure in along-track direction is influenced by the stochastic model applied for the observations. For the ITSG-Grace2016 time series, colored noise of the observations along the arc is introduced by the modelled stochastic properties of the de-aliasing products applied. According to Mayer-Gürr et al. [2016b], an empirical covariance function is introduced for the AOD1B products. This leads to correlations for the observations along the arc. For the GFZ-RL5a solution such a stochastic model is not utilized. This results in not introducing correlations between single observations when applying the de-aliasing product. The closed loop simulation environment is able to include stochastic modelling by applying a dedicated ARMA filter. The current implementation brings in correlations due to the characteristics of the accelerometer and SST ranging instrument (cf. chapter 3). These processing details especially explain the deviations of the correlation in along-track direction. Differences between the real data examples and the closed loop matrices can also be expected because of the use of different force models.

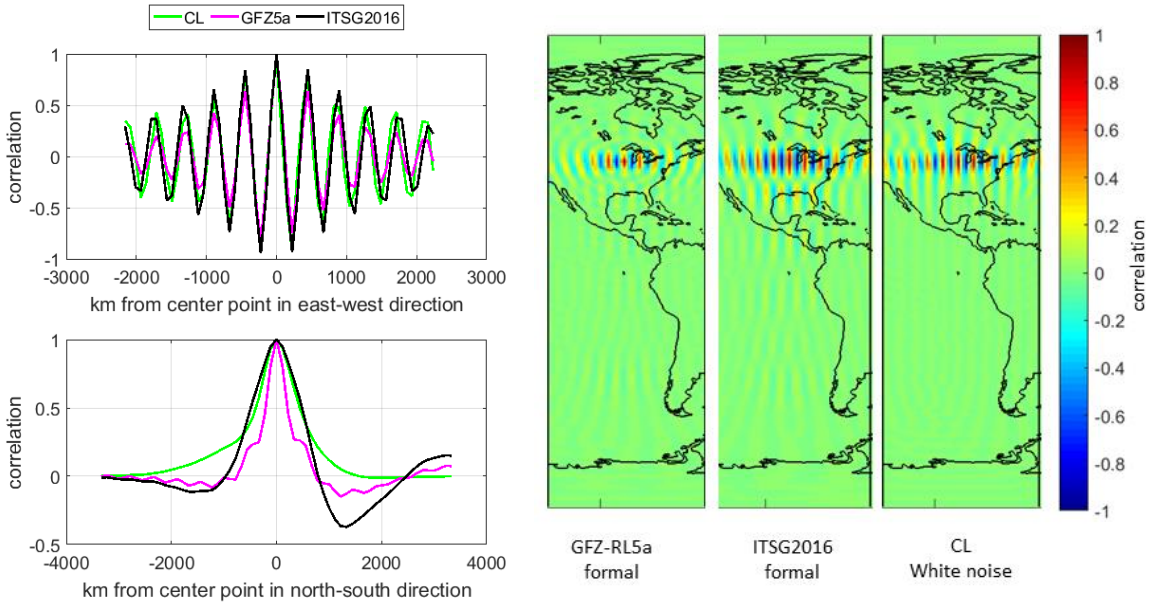

Figure 5-10: Comparison of formal and closed loop error covariance properties in cross-track (upper left panel) and along-track (lower left panel) direction. The right panel shows the respective spatial correlation pattern for a point at +42° latitude and -90° longitude on the North American continent.

The closed loop force model is built on acceleration difference only and does not consider e.g. hl-SST. For the cross-track direction, the agreement between the ITSG-Grace2016 and closed loop correlation is very good. The GFZ-RL5a time series shows for both directions significant deviations from the other two samples, which result from differences in the processing approach. Although differences in the along-track direction in terms of the correlation length exist between real GRACE time series and the one created with the closed loop simulator, transferring the outcome of the closed loop experiments as a proxy for the real data treatment is considered valid.

This conclusion becomes more persuasive by also comparing the temporal evolution of correlation patterns, embedded in the real data time series, to the simulated one. The features compared are in the following case the properties of the error covariance matrices, casing the perpendicular structures from correlations per SH order (cf. section 4.3.2 and equation (4.14)). Figure 5-11 shows the RMS of correlations of SH order $m_x + m_y$ evaluated for the ITSG-Grace2016 time series (left panel) against the closed loop white noise time series (right panel). Each row corresponds to a single monthly solution. Each element of the respective row is derived by taking the RMS of all entries of a matrix, similar to the one depicted in Figure 4-15, but only differentiated by SH order and not even and odd SH degree, meeting the criteria of $m_x + m_y$ equaling the SH order indicated in the x-axis of the figure below.

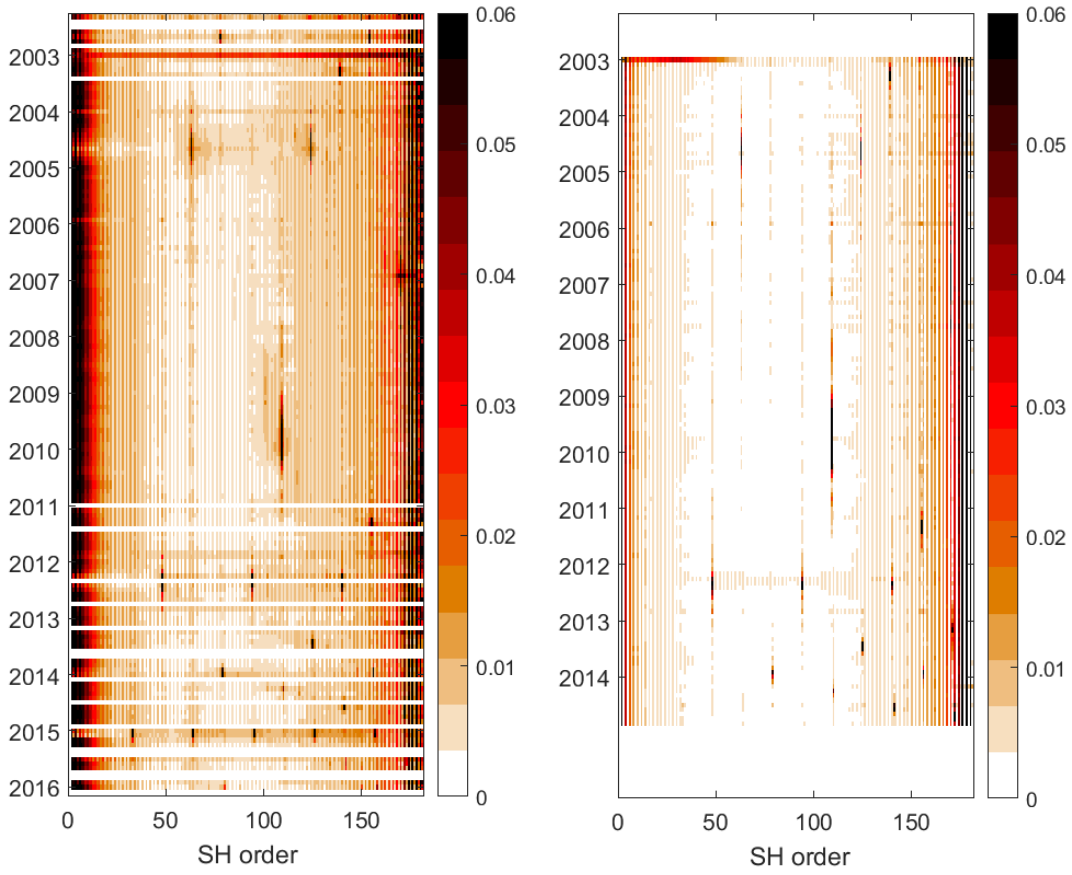

Figure 5-11: RMS of correlation m_x+m_y over time for the ITSG-Grace2016 (left) and closed loop (right) time series.

The left panel is the same display as the left panel in Figure 4-17. The white horizontal lines represent data gaps. For the right panel the same analysis is shown for the closed loop white noise time series. In general the level of correlation is a bit higher for the real data time series. The behavior with respect to the SH order although is very similar. High and fast decreasing RMS of correlation for the SH order from 0 onwards and lowest correlation for SH orders between 50 and 100 can be observed. For both series the RMS of correlations increases again from SH order 130

onwards. All of the distinctive features, high correlation for a short period of time localized within a specific SH order, can be found in both series. These are among others e.g. the local maximum in 2004 at m=61, the local maximum spanning throughout 2009 at m=107, and the three local maxima in mid-2012 at m=46, 92, and 138.

The increase in RMS of correlation for these specific snapshots in time correlate very well with deep resonance phases of the GRACE orbit causing problems due to e.g. fast repeat tracks for the gravity field recovery (cf. [Murböck et al. 2014; Murböck 2015]).

To transfer the experience gained within the closed loop experiments, regarding the error covariance matrix setup for the VADER filter, is considered to be valid upon the investigations outlined above.

5.3.2 The signal variance matrix

The second major component of the VADER filter design is the signal variance information. In literature different approaches can be found. For the DDK filter series, the signal variance is derived by a power law rule and is static in time [Kusche 2007]. Klees et al. [2008] derive their signal variance information from the solution itself in an iterative approach as part of the level-2 processing chain. Due to the estimation of signal variance information for each month individually, their signal variance is changing in time.

Since the VADER filter is designed as a pure post-processing filter strategy, the estimation of the signal variance from the solutions themselves is excluded. The following methods are investigated to determine the setup of the signal variance. The target signals aimed for are geophysical signals like hydrological or ice mass variations. To get an idea of the spectral properties of such signals and their time dependency, data from the AOHIS Earth model by Dobslaw et al. [2015b] is utilized. Figure 5-12 shows in five solid lines the median of the cumulative geoid error derived from different setups of the signal variance matrix for different filter strengths. "True signal" means introducing the monthly average HI signal in spherical harmonics. The term "calendar month mean" represents long term average signals for a specific calendar month, e.g. January, February, March, etc. The term "l-rule" stands for a power law rule depending on the SH degree l. A detailed discussion of the calendar month mean or cyclo-stationary approximation of the signal variance can be found later in this section. The power law approximation for the signal variance follows the relation

$$S(l) = al^b \tag{5.3}$$

with $S(l)$ being the approximated signal for the respective SH degree l. a and b represent the power law coefficients responsible for the scaling and steepness of the curve. Similar approximations of signal, as a function of SH degree, can be found e.g. in Sasgen et al. [2006] and are built upon the principle of *Kaula's rule of thumb* [Kaula 1966]. One would expect the best filter performance whilst using the true signal observed in the closed loop environment as prior for the filter design to deliver the best performance. As Figure 5-12 depicts, this is not the case. For both examples consisting of real signal, the performance is significantly inferior to the versions using a power law signal variance. The reason behind this effect is of numerical nature. Whilst using the true signal, SH coefficients of very small amplitude are introduced in the generation of the filter matrix. As the variable M is the inverse of the squared prior signal, very small values of the signal SH coefficients lead to instabilities, which result in false weighting of certain coefficients. The retrieved filtered solution devides therefore from the power law solutions by 20% on average, as shown by the difference between the local minima of the five cases shown in Figure 5-12.

Since for real world applications the true signal variance is not known, the use of real month-to-month signal variances is not possible. The signal variance can only be co-estimated from the solution itself (to a limited degree of SH expansion like 40) or approximated from models. The results depicted with the term "l-rule" in Figure 5-12 originate from model information. As one can see from the almost coinciding patterns of the curves (red, cyan, black), the retrieval seems not to be very sensitive to variations in the signal variance (at least within reasonable bounds). All three cases, power law approximations of the real monthly signal, the calendar month average, and the overall average deliver results of on average comparable quality. The impact of using static or variable signal variance is also addressed in detail in section 5.3.4 (Figure 5-15).

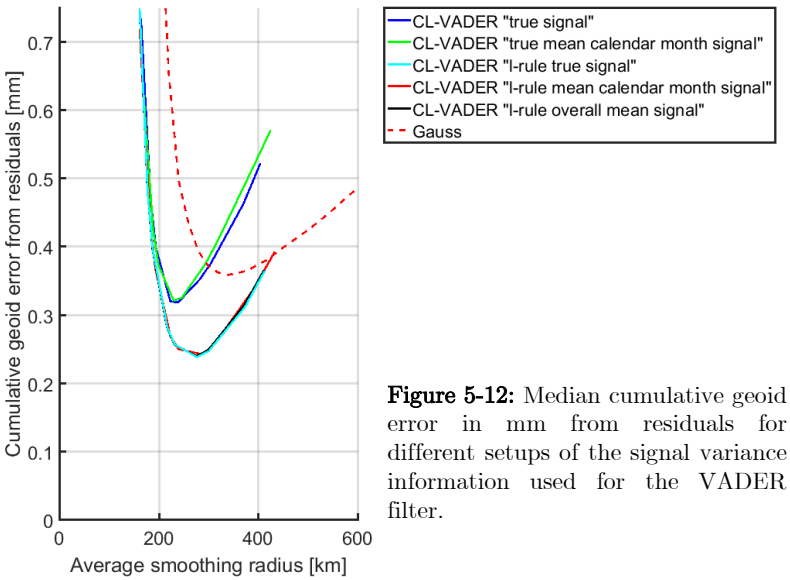

Figure 5-12: Median cumulative geoid error in mm from residuals for different setups of the signal variance information used for the VADER filter.

The best signal variance information to be implemented in the filter process is of course one which closely matches the true properties of the target signal. The following experiment addresses the applicability of calendar month mean or cyclo-stationary signal properties. From the findings of Devaraju [2015] regarding the variability of the signal variances, a significant cyclo-stationary pattern is deducted. The average power law, according to equation (5.3), is estimated for each month for the HIS component of the model [Dobslaw et al. 2015b] separately and averaged over the available timeframe.

The coefficients a and b, estimated from the model data, are shown in Figure 5-13 in solid red lines. To assess the reliability and plausibility of these estimates, the a and b coefficients are also estimated from a residual DDK filtered time series. The series used is the ITSG-Grace2016 series already filtered with DDK4, as it can be obtained as a ready-to-use product from the ICGEM web portal (http://icgem.gfz-potsdam.de/ICGEM/). The DDK filter is, regarding its filter strength and behavior, static in time, as explained before. Thus, one can assume that the variability of the a and b coefficients is not induced by the filter. Rather it is inherent in the time series itself. Since the signal to noise ratio is expected to be good for SH degrees below 30 (cf. section 4.3.2 and Figure 4-10), the a and b coefficients are only estimated from this first part of the spectrum. Otherwise the result would be predominated by the remaining noise of the GRACE solutions. Months coinciding with deep resonance phases of the GRACE orbit are excluded from the analysis to allow meaningful results. The resulting coefficients are shown in blue. At first sight, a good agreement between the coefficients can be observed.

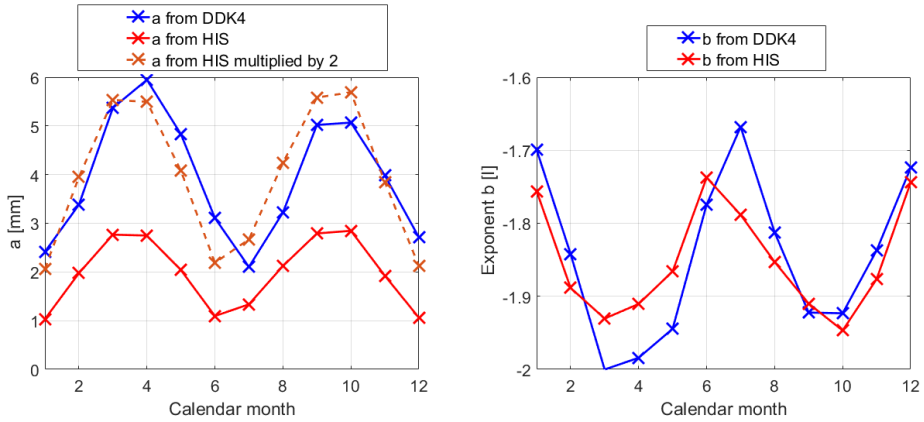

Figure 5-13: a (geoid height) and b coefficients per calendar month according to equation (5.3) computed from the monthly average HIS data originating from the model by Dobslaw et al. [2015], and from 13 years of DDK4 [Kusche et al. 2009] filtered ITSG-Grace2016 solutions.

The only major difference is the shift of the summer extremum by one month between June and July for the model data and the GRACE data and the shift in amplitude for the a coefficient. The shift in amplitude can be accounted for by introducing a scale factor of about 2, resulting in a match between the dashed red and solid blue curve. Such a difference in scaling can also be accounted for by setting a suitable α-value in the design of the W_α filter matrix. A reason for the initial estimate of the factor a being smaller than the real world estimate can be inherent in the model data. In case the model shows smaller signal amplitudes than the real world signal, the estimate of the signal variance accordingly reflects these lower amplitudes by a lower value for a. Another aspect contributing to the different scale of the value of a is the signal content reflected by the model and the real world data. For a derived from the model only HIS data is used, whereas the real world data also contains residual AO and other signals, thus leading to potentially higher signal amplitudes. A plausible reason for the shift of the local extremum between June and July could be the differing timeframes covered by the real GRACE data and the model. The model ranges from 1995 to 2006, whereas the GRACE data ranges from 2003 to end-2015. Therefore they do not reflect the same signals. Another cause, resulting in differences between model and GRACE data estimates, can be random scatter, as the estimates from the DDK filtered solution turned out to be very sensitive to the in- or exclusion of single noise dominated months.

Apart from this difference, the experiment shows a clear cyclo-stationary behavior in the magnitude of the geophysical signal in terms of degree amplitudes. From a climatological point of view such a variation makes sense, since the main amplitude causing mass redistribution is also seasonal (e.g. global water cycle [Kandel 1980]). Advantages and drawbacks of employing a signal variance with variations according to the seasons is discussed in the application section 7.2. The impact of cyclo-stationary signal variance on the average filter strength in terms of the approximated smoothing radius is discussed in section 5.3.4.

For the following experiments a static and cyclo-stationary calendar month approximation of the signal variance is tested. The other options presented are excluded because of inapplicability.

5.3.3 Measures of performance: Regularization bias

As briefly discussed in section 2.3, applying regularization introduces a bias [Xu 1992; Metzler 2007]. The following section addresses this issue by deriving the magnitude of the bias from the closed loop experiments. The bias is considered as an inevitable contribution to the whole error budget of the filtered solution. The total error of a filtered solution is accordingly consisting of the formal error, derived by covariance propagation, and the regularization bias or error, only possible to derive from the closed loop experiments. Both constituents together form the mean square error (MSE). A real world determination of the bias is not possible, since the true solution x is unknown, but needed to assess the bias (cf. equation (2.23) with (2.22)). The idea is to derive the proportion of the formal error with respect to the full error and to investigate the applicability of deriving a scaling factor for the formal error to match the full MSE error. The data shown in Figure 5-14 is computed from 9 different regularization or VADER filter strengths for the white noise closed loop time series. The respective α-value is given on the abscissa. All curves show the median result for the whole time series. The curve labeled "MSE" is computed by taking the cumulative square root of the diagonal of the MSE matrix. This MSE error is equivalent to the cumulative residuals derived from the closed loop experiments, shown e.g. in Figure 5-9, Figure 5-12, Figure 5-15, or Figure 5-16. The red curve labelled "bias" represents the cumulative bias derived from the relation expressed in equation (2.22). The propagated covariance is derived according to equation (2.20). For the blue line, the cumulative square root of the diagonal is shown.

Close to the α-value of 0.5, the MSE shows its minimum, composed of equal contributions from the propagated error covariance (square root is shown) and the bias introduced by the regularization. The filter strength driven by an α-value between 0.5 and 1 is, following the findings from the sections above, considered to be suitable in terms of signal recovery. The scaling value, in order to match the full MSE error with the propagated covariance, would be around $\sqrt{2}$ for $\alpha = 0.5$.

The propagated covariance (from the formal error covariance information of the respective time series) is, according to the result of the MSE and the magnitude of the regularization bias, considered as being a too optimistic lower bound of the true error. Filtering a solution by damping the higher order SH coefficients also lowers the error or noise of the respective solution. The cumulative error of a filtered solution is therefore smaller than the one of the unfiltered one which is illustratively shown by the blue curve. The stronger the filtering, the smaller the propagated formal error covariance gets. The actual signal is affected the opposite way. The stronger a solution is filtered, the larger the distortion of the original signal gets. A commonly known result of this effect is the damping of amplitudes of e.g. hydrological signals within filtered GRACE solutions [Landerer and Swenson 2012]. The red line, representing the bias or distortion of the original signal induced by the application of the regularization filter, shows this clearly. The larger the α-value gets, the larger the bias becomes.

In order to transfer the findings regarding the scaling bias on the real data application, care needs to be taken with respect to the filter strengths. Comparing the filter strength derived for the CL-VADER with the real data ITSG-Grace2016 VADER reveals slightly smaller half width radii for the closed loop case (cf. discussion regarding average filter radii displayed in Figure 5-17 and the average filter radii indicated in Table 5-1). The systematically smaller values for the closed loop radii are due to the existing, although small (cf. section 5.3.1), differences in the correlation structures between the various time series. Filter radii between closed loop experiments and real data results differ by about 25 km for $\alpha = 0.5$ or 1. For identical filter design, the filter strength for the closed loop experiment is smaller than for the real data case. Accordingly the stronger filtering with the same α-value is expected to result in a higher bias. Therefore the transfer of the scaling factor (e.g. $\sqrt{2}$) is considered to be a valid approximation for raising the too optimistic

assumptions regarding the formal error derived by the covariance propagation, since the scaling still reflects a conservative assumption.

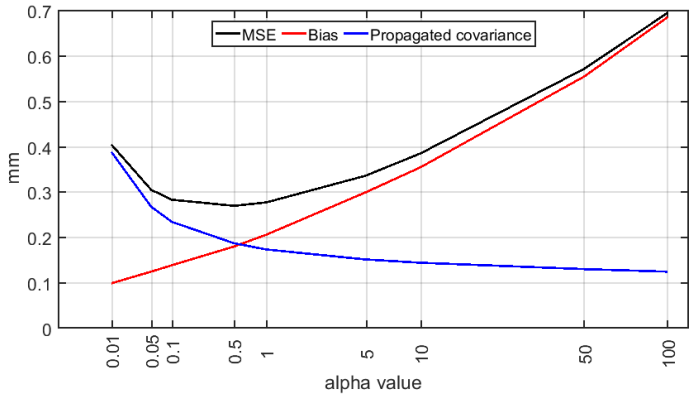

Figure 5-14: Median cumulative regularization bias (red), propagated covariance (blue), and MSE (black) for the white noise time series.

5.3.4 Effect of time variable filters vs. static filters on estimated signals

Since until now only median results of cumulative residuals have been shown, a more detailed look into the scattering of the solutions is presented in the following. The investigation is also covering the issue of applying non-stationary signal and/or error covariance information in more detail than before. Figure 5-15 shows the cumulative geoid error for different VADER filter strengths and setups. Each individual monthly cumulative geoid error is shown against its individual average filter radius for the respective filter strength, illustrated by the colored dots. The black crosses indicate the median cumulative geoid error against the median filter strength. Consequently, the black crosses correspond to the discrete steps of the median curves shown in the preceding analysis. The title of each panel indicates the respective setup of the filter matrix, being composed of both static or cyclo-stationary signal variance information, and static or non-stationary error covariance information. As mentioned before in section 5.3.2 and illustrated by Figure 5-12, the choice of the composition of the signal variance information plays only a minor role with respect to the resulting cumulative geoid error.

By comparing the upper left and lower right panel, both with same error covariance design but differing signal variance, no significant difference can be seen. Comparison of the standard deviation of the most relevant solution clusters (green to blue colored clusters, representing the local minimum of the residuals) reveals a decrease of 8% switching from static to cyclo-stationary signal variance. Comparing the lower left against the upper right panel indicates the same effect from differing signal variance compositions. The lower and upper right panels reveal significant differences for changing the error covariance information from the static to the non-stationary state. A decrease of the standard deviation of the cumulative geoid error by 35% for the cluster representing the local minimum can be seen. The large discrepancy for some single months, showing residuals amplified by a factor of 2 to 4, are not present anymore when using the respective error covariance for each individual month, instead of using a static one. This circumstance is also addressed in the next section regarding a suggested filter design (cf. Figure

5-18). The lower left case, composed of only static components, shows for all solutions the same average smoothing radius. This must be expected, since the filter matrix is the same for every month. The standard deviation, switching from the all static version of the filter matrix to the one with cyclo-stationary signal variance, is decreasing again by 8%.

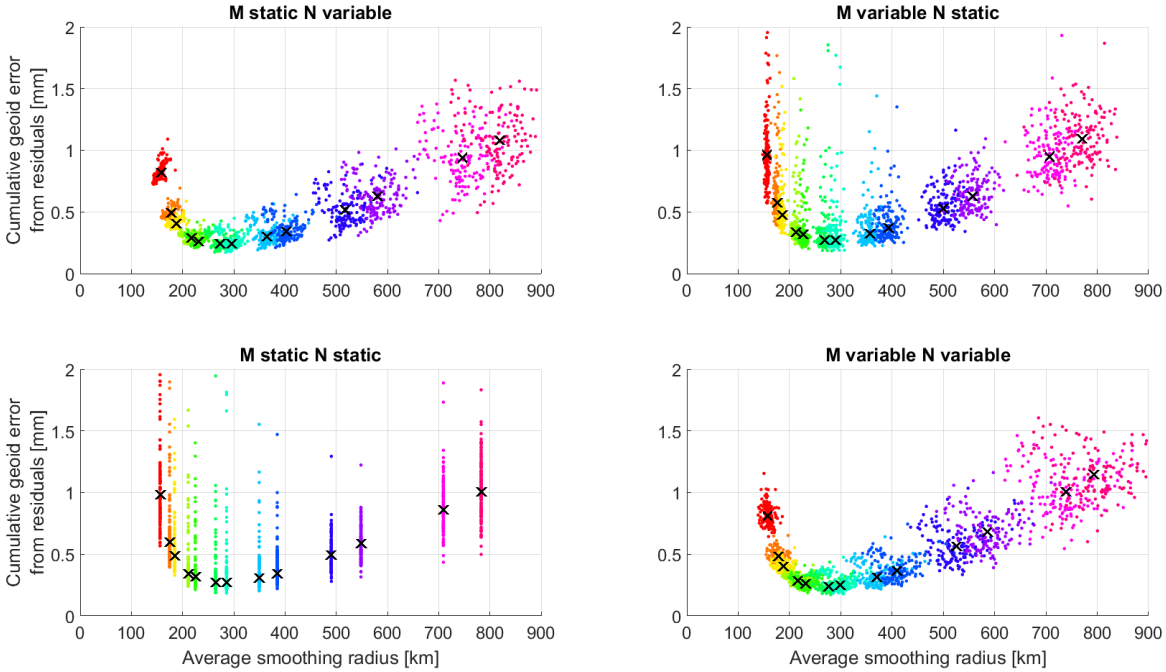

Figure 5-15: Cumulative geoid error from residuals for different static and non-static states of the error covariance matrix and signal variance matrix fed into the design of the VADER filter. Colors indicate the respective result for specific filter strength for the individual months of a 143 month time series. Black x-marks indicate the median cumulative geoid error at the median average smoothing radius of the respective cluster of results.

Figure 5-16 shows the median values of each cluster (black x-marks from Figure 5-15) in a single graph. Comparing the median lines, a clear performance gain can be derived from employing non-stationary error covariance instead of a static one. The performance gain from employing cyclo-stationary or static signal variance is, like the discussion of Figure 5-15 revealed, only marginal on average.

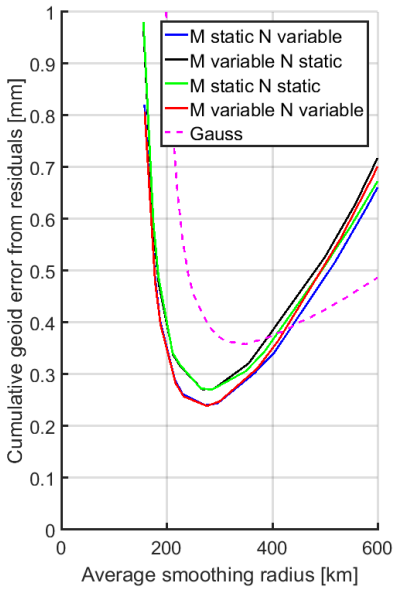

Figure 5-16: Median lines of cumulative geoid error from residuals showing the results from cases with variable and static states of the error covariance and signal variance information fed into the VADER filter design.

An additional aspect of importance, when filtering time series with an adaptive filter, is to analyze how the filter behavior changes with time. Systematic effects, potentially leading to falsified results in the course of geophysical signal determination might produce artefacts misinterpreted as signals. The analysis presented below focuses on the influence of the different filter constituents on the monthly average smoothing radius or filter strength.

Figure 5-17 shows a comparison of different designs of the VADER filter matrix W_α, resulting in the respective variation of the average filter strength. The results shown by the green, red, and blue curve originate from the closed loop simulation environment. The black curve is derived from real data, namely the ITSG-Grace2016 non-stationary error covariance in combination with a cyclo-stationary signal variance using an α-value of 1. The impact on the variability of the average smoothing radius by introducing a cyclo-stationary signal variance, whilst keeping the error covariance contribution constant, is indicated by the blue curve. The variations in signal variance cause a variability of the average smoothing radius of about 25km. Comparing the effect of varying the error covariance contribution (shown in green), whilst keeping the signal variance constant, reveals a larger variation of about 60 km.

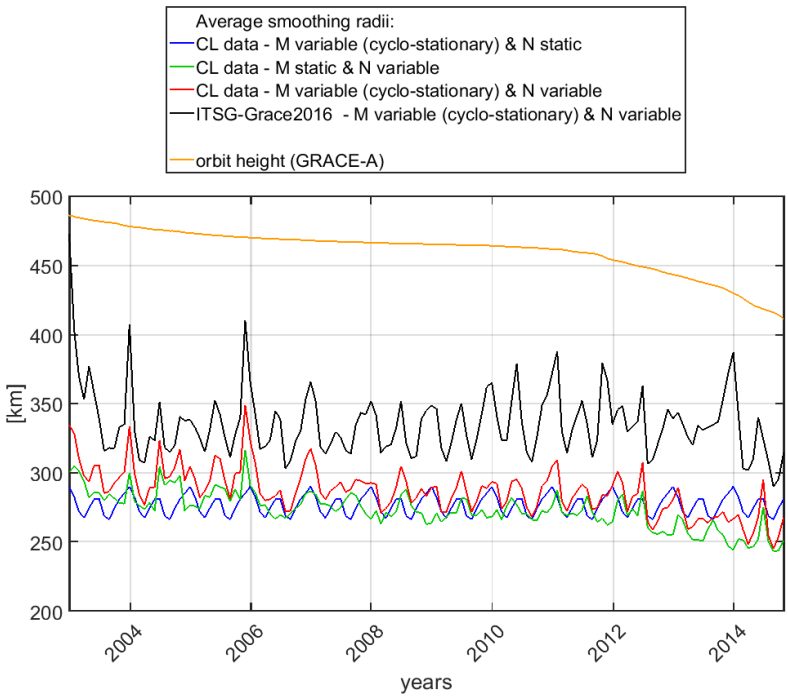

Figure 5-17: Average smoothing radii in km over time for different compositions of the VADER filter matrix W_α (cf. Figure 5-15). For comparison the average orbit height of GRACE-A is indicated in orange.

Contrary to the blue curve, which is varying around a constant mean value, the green curve shows a time dependent behavior which is correlated with the orbit height of the GRACE orbit (orange curve). To compute the orbit height, the semi-major axis of GRACE-A is used as daily mean values from the 10-second orbits provided by TU Graz [Zehentner and Mayer-Gürr 2016]. To arrive at the average orbit height, the Earth's radius R is subtracted from the semi-major axis. For November 2016 the mean orbital altitude decreased even further to about 350km (not shown in figure). Both curves, green and orange, show a decrease in average smoothing strengths respectively average orbital height. It is apparent that for lower orbits less stronger filtering is required. This correlation can be explained by the lower noise level in solutions originating from observations closer to Earth. As equation (2.3) shows, the gravitational potential at a specific location outside the acting body (the Earth) is related by $(R/r)^{l+1}$. A lower value for r implies retrieving the gravitational signal of the acting body in better resolution respectively strength

whilst being in a lower orbit. The average smoothing radius for varying both the signal and error covariance matrix (red) agrees in general with an example from real data analysis (black). The black curve shows the resulting average smoothing radius for the ITSG-Grace2016 time series using non-stationary error covariance and cyclo-stationary signals variance in combination with $\alpha = 1$. Both the red and black curves exhibit a correlation with the evolution of the semi-major axis, decreasing from the beginning of the measurement period in 2003 towards end-2014. Especially the decrease for the time period beginning-2003 until mid-2004 and again from beginning-2013 until end-2014 is visible. The shift of the average smoothing radius between the red and black curve is subject to the choice of the filter parameter α (which is equal in this case) and the level of correlations embedded in the respective error covariance matrices. As the comparison between the formal ITSG-Grace2016 and the closed loop error covariances in Figure 5-11 reveals, the correlations, embedded in the closed loop error covariance matrices, show a lower magnitude than the ITSG-Grace2016 ones. This leads to a scaling of the average filter strength. As the closed loop environment is built on the very same orbits as the ITSG-Grace2016 estimates, the correlation between the two results is high. Only for the period towards the end of the time frame investigated some differences occur. They can be related to differences between real world GRACE and closed loop operations, as the design of the simulator does not include system degradation (e.g. battery problems, unintended outages of scientific instruments, degradation of instrument performance etc.).

Applying a constant smoothing radius for the whole GRACE time series seems unjustified from this analysis, since a systematic attenuation of the retrieved geophysical signal might occur by filtering the later years with filters smoothing too much. Varying filter strength over time results in varying signal content, especially signal amplitudes. This needs to be taken into account whilst estimating geophysical signals from such time series. In this context section 7.2 provides a case study where different VADER filter designs and other filters are tested in the context of retrieving hydrological signals from river basins. Focus is set on the retrievability of phase and amplitudes with respect to the truth in the closed loop environment.

5.4 Suggested process of optimized filtering for decade long GRACE time series

From the findings in section 5.2 regarding the beneficial design of the S&W decorrelation filter and section 5.3, discussing the VADER filter, a suggestion for filtering decadal GRACE time series is derived.

The S&W filter, designed with favorable parameters, can be seen as a powerful tool for filtering gravity field estimates expanded to $l_{\max} = 60$ or even 90. For higher degrees of expansion, a clear recommendation cannot be made since the steady patterns of correlated SH coefficients are not present anymore for high SH degrees, thus leading to artefacts and falsified results. A broad intercomparison of different filters in the context of retrieving hydrological information from GRACE by Werth et al. [2009] left the S&W type filter only delivering superior results for 2 out of 22 major river basins, both of them at high latitudes. For low latitudes the performance of the S&W empirical decorrelation filter suffers from problems, as also visible by the residual striping in equatorial and low latitude regions, as presented in Figure 5-18 (panels in row 3 and 4). The regularization filter approach, implemented by Werth et al. [2009], results contrary to the empirical decorrelation in superior results for 18 out of 22 basins. Although the regularization approach applied cannot be rated as optimal in the context of the findings regarding a favorable design of the VADER filter, it still clearly outperforms all other filters tested by Werth et al. [2009].

The comparison of cumulative geoid errors for different filter setups, as presented in Table 5-2, substantiates these findings. All numbers indicate the median value of the cumulative geoid error from residuals, originating from the 143 month closed loop time series. For all S&W filter setups the minimum order is $m_{start} = 12$ for the comparison. The S&W filter outperforms the Gaussian filter for all degrees of expansion, except $l_{max} = 40$, where version two and the Gaussian filter (at the chosen strength) show equal median performance. No clear recommendation can be derived whether version one or two of the S&W filter is performing better for expansion up to $l_{max} = 60$. For $l_{max} = 75$ and higher, clear upsides in the performance of version one can be observed. This is mainly due to the aforementioned risk of oscillation effects falsifying the solution for applying version two. In the lower row the respective cumulative geoid errors for the VADER filter (non-stationary error covariance, cyclo-stationary signal variance, and $\alpha = 0.5$) are shown. The performance is clearly superior to all other filter methods depicted in the table. Even for $l_{max} = 120$, the cumulative geoid error from the residuals is with 0.49 mm smaller than for any of the other methods for $l_{max} = 90$.

Table 5-2: Comparison of median cumulative geoid errors [mm] of the white noise closed loop time series (143 months, incl. OT & 20% AO) for different S&W and Gaussian type filter setups up to different degrees of SH expansion in comparison to the VADER filter.

Filter:	l_{max} =40	l_{max} =60	l_{max} =75	l_{max} =90
Version 1 S&W only	0.56	0.63	0.88	1.34
Version 2 S&W only	0.54	0.58	0.61	0.69
Version 1 S&W+Gauss 200km	0.56	**0.58**	**0.58**	**0.59**
Version 2 S&W+Gauss 200km	**0.53**	0.59	0.60	0.61
Gauss 300km	**0.53**	0.58	0.63	0.64
VADER $\alpha = 0.5$	0.45	0.46	0.47	0.48

Although the performance for the Gaussian filter for $l_{max} = 90$ shows no major drawback, compared to the version one or two of the S&W filter, one should note the presence of a stronger scattering of the monthly cumulative residuals, as the median does not reflect these properties. The VADER filter shows, as applied in the experiment, the lowest scattering of all filters indicated in the table, thus not only showing the lowest median cumulative geoid error, but also the most adaptive filter properties.

Figure 5-18 gives real data examples of filter performance. The time series used is the ITSG-Grace2014 time series up to $l_{max} = 90$, with a mean field subtracted. The unit of all panels is mm EWH. All panels in the left column show results of a residual filtered solution for April 2004. This month is rated, according to the orbital configuration, representative for the majority of high-quality results of the GRACE mission. The month for all panels in the right column is September 2004, which is suffering from a short repeat cycle, thus representing a non-nominal configuration. The heading of each panel indicates the filter technique applied, being either VADER, DDK, S&W filter version one or two, or Gauss. The DDK filtered solution is obtained as pre-filtered product from the ICGEM web portal (http://icgem.gfz-potsdam.de/ICGEM/).

For April 2004, all filters deliver results allowing to recognize major geophysical signals all over the globe. An illustrative indicator for comparing the leakage and attenuation of signal amplitudes are, among others, features like the mass signal around the Gulf of Alaska, Greenland, and the Amazon or Congo River basins. As signals from hydrology or ice mass variations can be expected

to occur on land, the grade of leakage into ocean areas is an explicit indicator of the filter performance in terms of preserving the target signals. Comparing the leakage in the area of the Gulf of Alaska reveals very good performance of the VADER filter, compared to the other ones. The comparably high level of residual striping for the DDK result can be caused by the wrongful application of the DDK filter on monthly estimates of a time series which deviates significantly from the mean (nominal) situation that formed the basis for the filter setup. As the DDK filter is based on a synthetic error covariance matrix of only block-diagonal population, derived from the orbital pattern of August 2003 [Kusche et al. 2009], it cannot be expected to meet the non-stationary behavior in terms of correlation structures (cf. Figure 4-17). It is also not able to account for the difference between the various available solutions, which all use their own level-2 processing algorithms, resulting in variations of the correlation structures between the solutions (cf. Figure 4-18).

For September 2004 the picture looks different than for April. Most solutions suffer from severe residual errors or signal artefacts induced by inadequate filtering in an equatorial and low latitude band. The correlation structure embedded in the respective error covariance matrix shows, according to the resonance orders in Figure 4-17 (m=61), a clear deviation from the nominal state. Whilst using a non-adaptive filter, such events or circumstances cannot be accounted for. The result for the VADER filter reveals a clearly superior picture in terms of the features of retrieved hydrological or ice mass signals. The version two of the S&W filter apparently shows also a low-noise result. However, comparing the signal amplitudes at multiple locations (e.g. Greenland, Gulf of Alaska, Antarctica, etc.) in high latitudes to the ones derived from the VADER filter, a clear attenuation of the signal becomes apparent. The better performance of the version two of the S&W filter in the case of September 2004 compared to the version one result contradicts the conclusion from Table 5-2. One should note, that this better performance only occurs since the correlation patterns in this specific month fit the properties of the version two better. Drawing the conclusion that version two is better suited for periods with short repeat orbits has no grounds. Tests in other months with non-standard repeat orbits did not allow reproducing the comparably good filter result for the S&W version two filter as in September 2004. The Gaussian filter shows for both examples the highest signal attenuation, but is comparably robust in problematic months, since it is not data driven. Therefore it applies its downweighting to the higher SH degree coefficients, no matter what signal to noise ratio or correlations they exhibit.

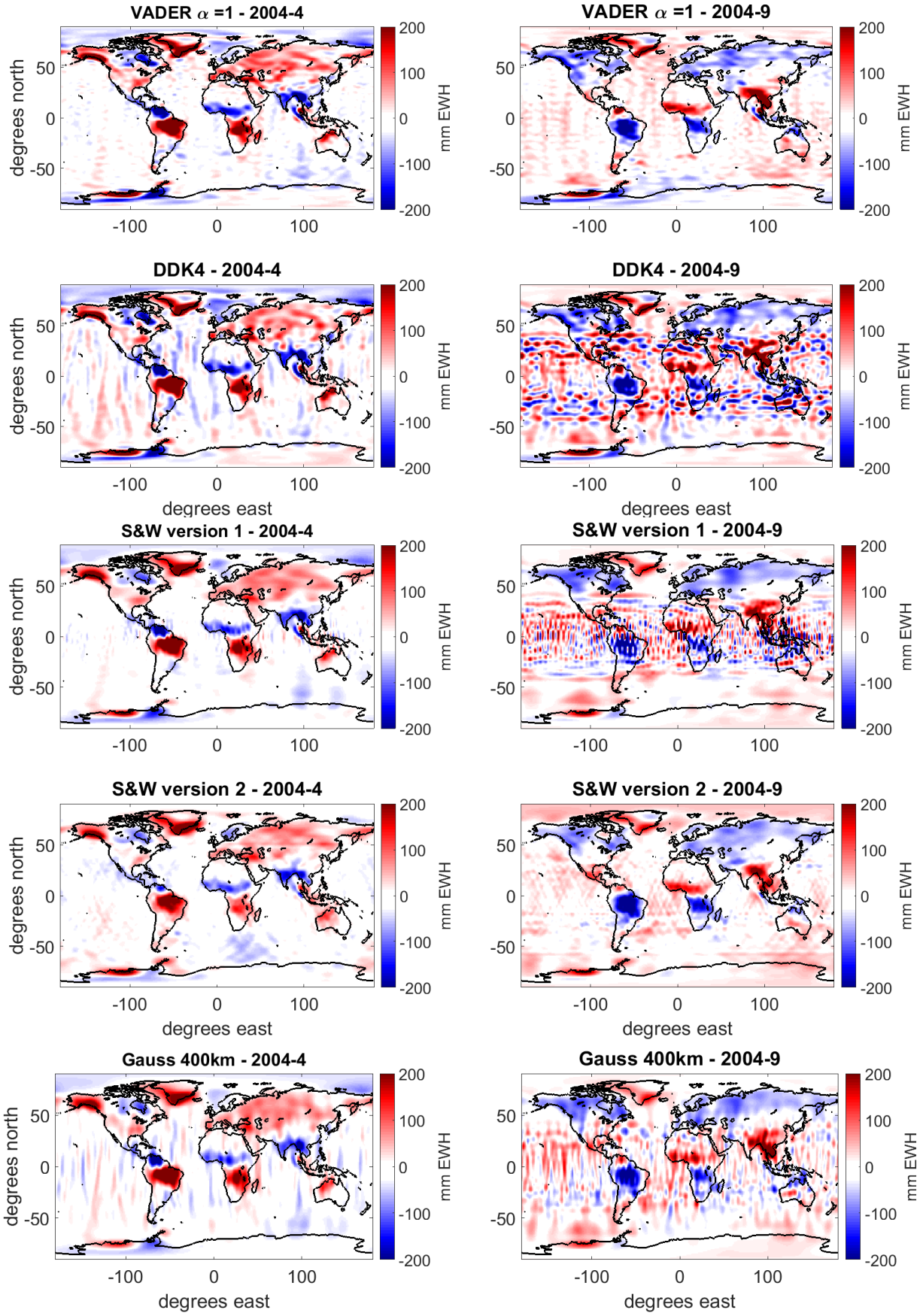

Figure 5-18: Example of real data (ITSG-Grace2014) filtering with different filter approaches for April 2004 (left column) and September 2004 (right column).

Another advantage of the VADER filter, apart from the comparably superior smoothing performance, is its impact on the patterns of error correlations in the spatial domain. Figure 5-19 shows the correlation structure of the propagated formal error covariance information for a location near the Amundsen Sea sector (106° west, 78° south). The left panel shows the pattern after applying the VADER filter with $\alpha = 1$, delivering an almost isotropic pattern. Propagated error covariance through the Gaussian type filter delivers a highly anisotropic pattern, as depicted in the right panel. As errors are correlated due to the observational geometry in along-track direction, elongated north-south oriented auto-covariance functions result. If averaging kernels are applied for a specific region in order to average out error contributions, the VADER filter shows clear advantage, since for a region like Antarctica the error is correlated only with confined spatial extent.

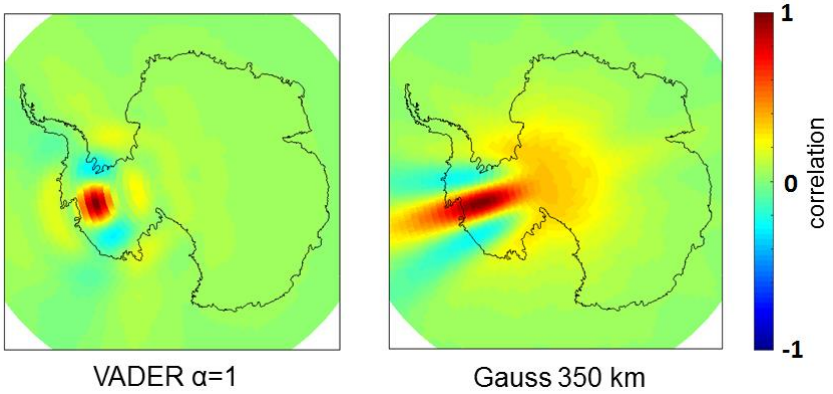

Figure 5-19: Error correlation structure expressed in the spatial domain for a location near the Amundsen Sea sector in Antarctica, derived from propagated error covariance after VADER (left panel) and Gaussian filtering (right panel).

From the performance metrics of the closed loop experiments (cf. Table 5-2) and the real data filter intercomparison (cf. Figure 5-18), the two versions of the S&W filter show, measured by their complexity and requirements in auxiliary data, good performance. They are clearly superior to the Gaussian type filter and allow retrieving geophysical signals with comparably little effort. The main advantage of the S&W filter can be identified in its independence of auxiliary data like the error covariance information. This makes it applicable to most of the available GRACE time series. The S&W filter performance is nevertheless inferior with respect to the VADER filter, which clearly outperforms all other filters tested. The adaptive characteristics of the VADER filter allow applying the needed filter strength for each individual solution in a way that the desired degree of smoothing is achieved in order to suppress noise, whilst simultaneously signal attenuation and leakage is limited. Following the preceding investigations and experiments, a clear recommendation is made for applying regularization type filters of non-stationary design, and incorporating full error covariance information, for retrieving geophysical signals in an optimal way.

6. Filter strategies for future missions

In this chapter the impact of introducing a second pair of satellites into the mission configuration is investigated. The future mission scenario consists, as introduced in section 1.2, of a double pair mission with one near-polar and one inclined orbit (cf. Table 1-1 and Figure 1-3). Until now, all filter strategies were assessed, taking the noise and error characteristics of a single pair mission into account. Section 6.1 addresses the changes in correlation switching from a single to a double pair constellation. As one can derive from the preceding analysis, the correlation structure of errors plays a major role in terms of retrieving geophysical signals from the observations. Upon the analysis of the error correlation patterns, the applicability of the single pair post-processing concepts onto the double pair scenario is assessed in section 6.2. A discussion regarding the performance of the preferred filter strategy in the retrieval of geophysical signals in polar and low latitude locations, assuming either a single or double pair constellation, is presented in section 6.3.

6.1 Correlation structure of errors for future mission scenarios

The analysis strategy presented in section 4.3.2, investigating the properties of error covariance matrices of real GRACE and closed loop error covariance matrices, is applied to future mission single and double pair error covariance matrices in order to detect potential changes in the correlation structures induced by the mission design. The orbital configuration from the SC4MGV project [Iran Pour et al. 2015] baseline scenario 5 is applied (cf. Table 1-1). Figure 6-1 shows the resulting RMS of correlations sorted by the SH order, as derived by the relation in equation (4.14), in the upper left panel for a single month expanded to $l_{\max} = 120$. The underlying noise model is the colored noise case, as described in chapter 3. The red curve represents the RMS of correlations per SH order for the polar pair only. A distinctive peak can be observed e.g. for m=174. Comparing the results for the double pair correlation, indicated in blue, a significantly lower amplitude of the peak can be determined. The lower left panel shows the ratio of the red and blue curve (red divided by blue). The general form of the relation reveals a significantly lower RMS for the double pair than for the single pair constellation (value >1) with distinct discontinuities every 15 respectively 16 orders. To have a better understanding of the effect causing the discontinuities, the upper right panel shows a zoom-in to the RMS of correlations in the range between orders 60 and 180. Please note the different scaling of the y-axis. The observed discontinuities, inherent in the quotient between single pair and double pair RMS of correlations, are due to a shift of the order peaks. Since the chosen design of the inclined orbits involves a lower orbital altitude (20 km lower, cf. Table 1-1), the order resonances (peaks) are shifted. A second reason contributing to the shift is the change of the inclination angle. Changing the inclination from near-polar to smaller angles implies a shift of the order resonances, as such resonances are according to the relation expressed in equation (2.33) also a function of the inclination angle (cf. section 2.5). A detailed discussion regarding the relation between inclination, orbital altitude, semi-major axis, and other orbit defining Kepler elements, resulting in specific order resonances, can be found in Murböck et al. [2014].

The RMS of the overall correlations embedded in the error covariance matrices is reduced by 41% and the magnitude of the resonance bands is also reduced significantly. Therefore one can conclude that the introduction of an inclined pair results in a decorrelation of the error covariance matrix.

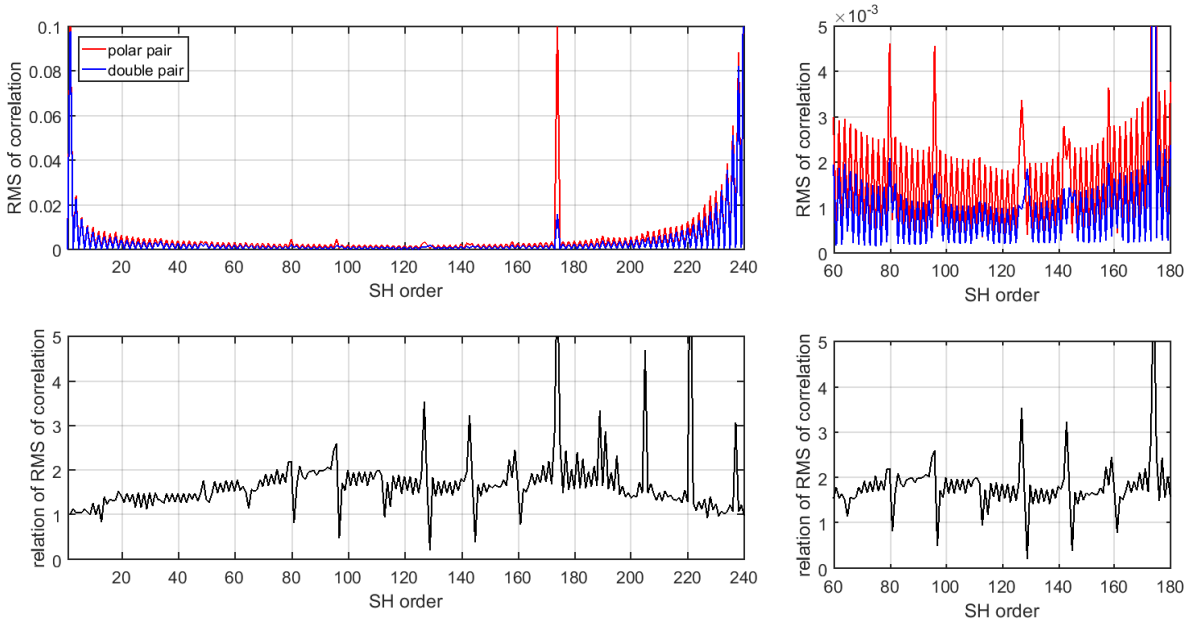

Figure 6-1: RMS of correlation according to equation (4.14) in the upper left panel. Upper right panel shows a zoom–in of the upper left panel for SH orders 60 to 180. Note the different scaling of the y-axes of both upper panels. Lower panels show the ratio of single to double pair (red curve divided by blue curve) for the respective orders from the panels above.

Comparing the correlation of the error covariance matrix in the spatial domain substantiates this finding. Figure 6-2 shows the resulting spatial correlation pattern for the double pair (left three bins) and single pair (right three bins) constellation. The evaluation point is located at ±75°, ±45°, and ±10° latitude centered within the respective bin. The results are shown in one figure for illustrative reasons, but each bin is independent of each other. From the correlation patterns of the different GRACE solutions analyzed, elongated along-track and oscillating cross-track patterns are revealed (cf. Figure 4-13 and Figure 4-14). Similar patterns can be seen for the right part, being the result of a single pair scenario. The only difference between the results shown for the closed loop experiments in section 5.3.1 (Figure 5-10) are the properties of the noise time series employed (colored noise instead of white noise) and the orbits (simulated orbits according to the parameters in Table 1-1 instead of real GRACE orbits). For the left three bins of Figure 6-2, the elongated along-track correlation pattern is reduced significantly in length. The cross-track oscillating patterns is reduced almost completely, resulting in a near isotropic pattern of error correlations already in the unfiltered state. The very left and right bins show the error correlation pattern for ±75° latitude being higher than the inclination of the inclined second pair. Comparison reveals very similar patterns for both cases, the single and double pair constellation, as it has to be expected since only one pair is delivering observations above 65° latitude. An evaluation of correlation patterns, after Gaussian or VADER type filtering is applied, is depicted in Figure 6-9.

The change in the properties of correlations, switching from GRACE-like classical striping patterns to nearly isotropic ones, has a significant impact on the requirements of data driven post-processing methods applied. For methods that are independent of data, like the Gaussian filter, this does not apply in the same way, but for empirical filters like the S&W version one and two filters, such changes have a major impact. Section 6.2 is addressing this issue in detail.

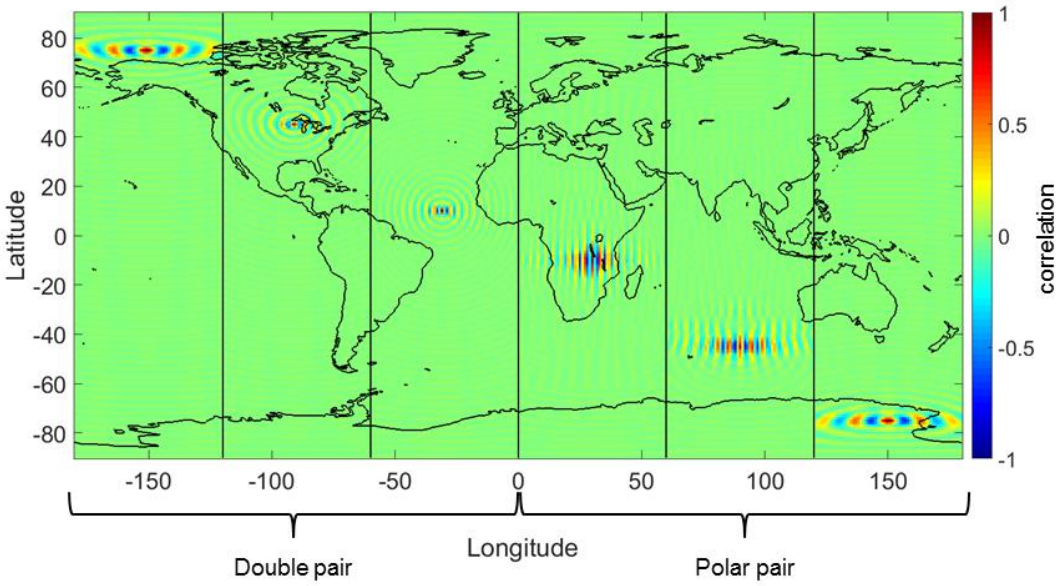

Figure 6-2: Spatial correlation patterns from double pair (left three bins) and single pair (right three bins) constellation in 60° wide bins. Evaluation point is on ±75°, ±45°, and ±10° latitude.

Figure 6-3 shows a spatial representation of the variances (standard deviations are shown) for one month of the double pair scenario. Contrary to the uniform zonal shape of single pair scenarios (cf. Figure 4-11), a distinct jump in the value of the standard deviations at the latitude of the inclination angle (±65° latitude) can be observed. The band in between ±65° latitude shows a comparable pattern with respect to a single pair solution. The larger standard deviations in low latitudes are due to the ground track spacing, respectively the density of observations, which are fewer per unit area as in higher latitudes. The variances of the double pair solutions are significantly reduced compared to the single polar pair solution. Figure 6-4 shows the SH error degree RMS for both scenarios. As the red curve indicates, the formal errors, respectively the standard deviations, are about one order of magnitude lower than for the single polar pair.

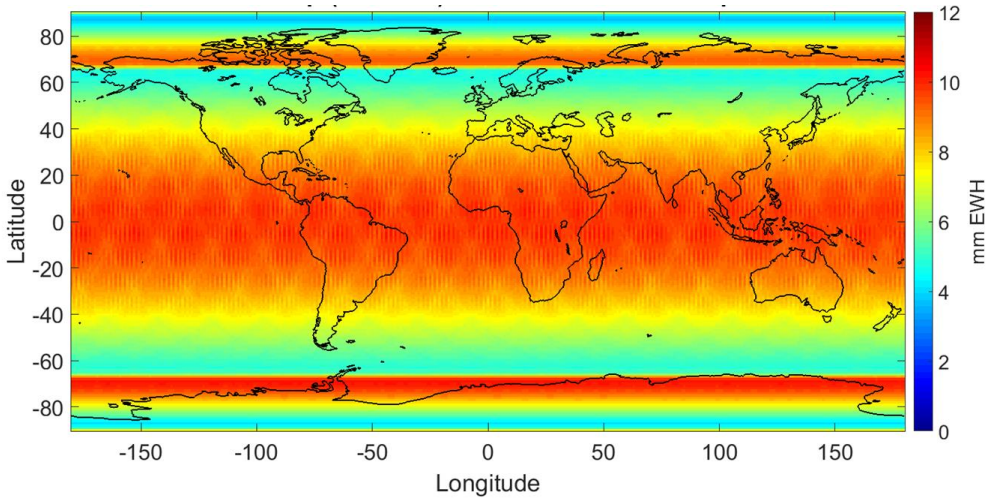

Figure 6-3: Spatial representation of the square root of the variances from a single month of the double pair error covariance matrix.

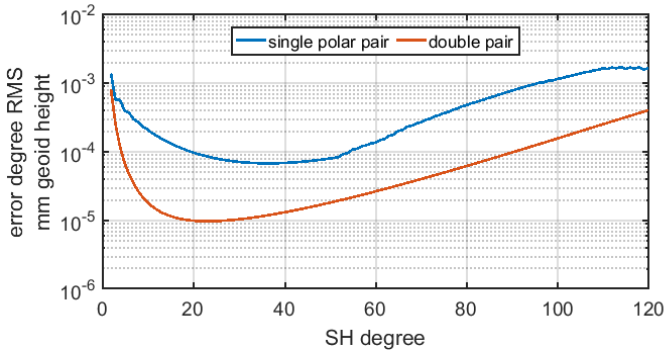

Figure 6-4: Error degree RMS of single and double pair scenario for one exemplary month.

An important question to answer is, in the context of double pair versus single pair missions, the impact and requirements towards filtering above or below the transition zone from double pair coverage to only single pair coverage. The following section 6.2 investigates the applicability of post-processing methods to double pair scenarios.

6.2 Applicability of GRACE post-processing methods on future mission scenarios

As the Gaussian filter is contrary to the S&W filter not data driven, it is assumed to be applicable on any GRACE or future mission gravity field solution. The S&W filter is due to its empirical design dependent on the validity of the assumption regarding the presence of correlated coefficients. If the assumption is not met, wrongful results can occur whilst applying the filter. The VADER filter is, since it incorporates information from the respective normal equation system, carrying information regarding the characteristics of the system design, and thus adaptive to varying mission scenarios. The following section analyzes the applicability of the aforementioned concepts to future mission scenarios, especially to the double pair constellation. The S&W type filter is shown only for the version one, the variant with the moving window, as the performance of version two turned out to be inferior for SH expansions up to $l_{max} = 120$ and for the correlation structures present for future and especially double pair scenarios (cf. Figure 6-7 and Table 6-1).

Figure 6-5 presents a comparison of the signals respectively the residuals occurring for different closed loop scenarios and the performance of Gaussian and VADER type filtering. All curves show the median of all 12 monthly solutions simulated. The dashed gray line represents the residual unfiltered signal (dark for the polar-inclined double pair scenario, light for the single polar pair scenario). For the left panel no AO and OT de-aliasing error is assumed, whereas for the right panel 20% AO signal together with an OT model difference is assumed as de-aliasing error (cf. Table 3-1; closed loop scenarios). Characteristic for the presence of OT de-aliasing error is the distinct peak around SH degree 45. The HIS signal, being the target signal, is indicated in yellow. Red and blue curves represent the residual signal after applying a VADER or Gaussian type filter for the polar-inclined double pair case. Purple and light blue represent the respective results for the polar pair case.

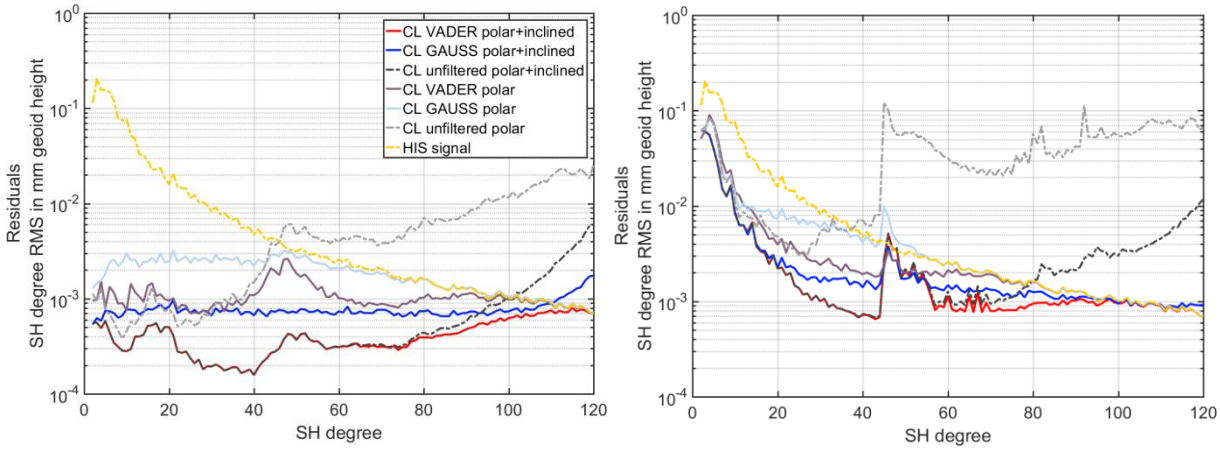

Figure 6-5: Median SH degree RMS from different closed loop simulation runs assuming complete AO and OT dealising (left panel) and residual AO and OT de-aliasing errors (right panel) for a double (red and blue) and single polar pair (purple and light blue) constellation. Median lines from 12 monthly solutions are shown. HIS signal curve (yellow) represents the overall mean of the observed input signal for the closed loop experiment.

The choice for the filter parameters, in terms of filter strength, is based on the global minima as depicted in Figure 6-6. From both panels in Figure 6-5 one can see that compared to the Gaussian filter, the VADER filter is starting to apply downweighting of the unfiltered coefficients only from higher SH degrees onwards. As the residuals of the unfiltered SH coefficients show smaller residuals than the target signal up to SH degree 45 (left panel), respectively 35 (right panel), the need for filtering the coefficients in the spectral band $l < 35/45$ is not pressing. Due to its design, the Gaussian filter is not able to leave certain groups of coefficients untouched. As it is not data driven, it applies the weighting coefficient straightforwardly according to equation (4.16). The VADER filter shows in its design (full non-stationary error covariance matrix with cyclo-stationary signal variance) an adaptive behavior, allowing to react to the specific properties of the solution to be filtered. The cyclo-stationary signal variance, used in the future mission scenario, is identical to the one used within the evaluation of the GRACE and GRACE-like results in section 5.3. It is based on the 12 year average of the respective monthly signals. This long term average is taken to avoid designing the filter with the target signal of the respective month itself. One can conclude from the observations in Figure 6-5 that the VADER filter seems suited for application to future mission double pair environments.

Figure 6-6 gives an overview of global performance levels of VADER and Gaussian filters of different strength in the context of future missions. The cumulative geoid error in mm geoid height, derived from the residuals, is shown with respect to the average smoothing radius (in case of Gaussian type filters the actual half width radius). For the VADER filter the average smoothing radius is derived according to the procedure outlines in section 5.3, the same way as for the GRACE examples. The red and purple curves indicate the performance of the VADER filter. Two options regarding the deterministic noise contribution are shown. In solid lines the performance without any additional deterministic errors is shown. This case would correspond to a scenario with complete AO and OT de-aliasing, which is fairly unrealistic in the near future. Nevertheless such a scenario allows to rate the performance of filters isolated from the deterministic noise contributions systematic effects. Clear performance gain can be observed for the VADER filter in the double pair (red) with respect to the single pair (purple) scenario. The average smoothing radius of about 140 km is larger than for the Gaussian filter half width of the same scenario (blue). A Gaussian filter half width of about 100 km represents a compromise of not or only very light filtering of coefficients of lower SH degrees, whereas at some point filtering

needs to be applied for the higher SH degrees, as depicted in the left panel of Figure 6-5. Tests revealed good results whilst applying the Gaussian filter only from e.g. SH degree 20 or 30 onwards, leaving coefficients with lower SH degree untouched. As this modified Gaussian filter is highly empirical regarding a suitable choice of design parameters, clear preference is given to the VADER filter approach, whose inherent characteristics allow for exactly such filter behavior. The performance of the VADER filter in the double pair scenario (red dashed) with additional AO and OT de-aliasing errors (marked with AO&OT in the figures legend) appears almost equal to the Gaussian filter (blue dashed) performance on global scale in terms of cumulative geoid height errors. Investigations in basin scale areas of interest disprove this impression, although one can notice a decreasing need for filtering for double pair, compared to single pair, scenarios. The single pair scenarios exhibit, similar to the results for the GRACE-like missions, a clear performance gain and less strong average smoothing for the VADER (purple dashed) compared to the Gaussian type filter (light blue dashed). As the variances in the double pair case are almost one order of magnitude smaller than for the single pair case (cf. Figure 6-4), the average smoothing radius consequently decreases (if signal variance and α-value remains unchanged), as a comparison of the red and purple lines reveals.

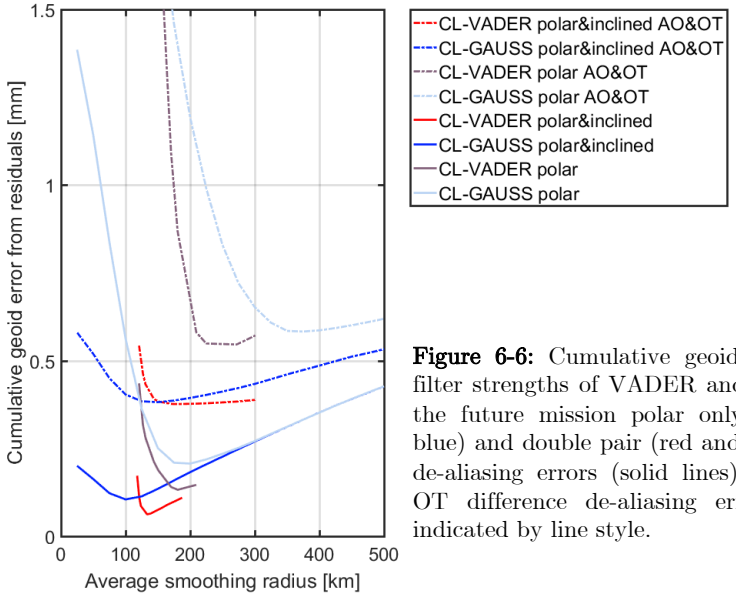

Figure 6-6: Cumulative geoid errors for varying filter strengths of VADER and Gaussian filters in the future mission polar only (purple and light blue) and double pair (red and blue) scenarios. No de-aliasing errors (solid lines) and 20% AO and OT difference de-aliasing errors (dashed lines) indicated by line style.

The results presented in the three panels of Figure 6-7 show the performance in terms of average residual EWH in mm for the respective area of interest for the VADER (blue), Gaussian (red), and S&W version one (black) empirical decorrelation filter. The three areas selected are two high latitude areas, Greenland and Antarctica, with coverage only (respectively mostly) by the polar pair, and one low latitude area, the Amazon basin, with coverage from both the polar and inclined pair. The polygon for defining the Amazon basin is derived from the STN-30p dataset [Vörösmarty et al. 2000], whereas the other two polygons for Antarctica and Greenland are derived from Zwally et al. [2012]. Shown are the results for the twelve monthly solutions of the simulation period. The solid lines represent the results of the polar pair, whereas the dashed lines represent the performance of the double pair. A general observation valid for all three panels is the smaller difference between dashed than solid red and blue lines. This is in agreement with the aforementioned reduced need of filtering for the double pair solutions. The better the solutions get in terms of residual noise and aliasing errors, the lower the strength of the filter needs to be. The differences between Gaussian and VADER filter in terms of filter characteristics are reduced, since the solutions tend to show isotropic error characteristics with reduced striping, not demanding highly sophisticated filters to be applied. For Greenland (left panel) and Antarctica (center panel), the residuals show stable behavior over time. For the Amazon basin the residuals show

seasonal behavior. The oscillations are not induced by e.g. the cyclo-stationary signal variance applied within the VADER filter, since also the residuals resulting from the non-variable Gaussian filtering show such performance as well. Differences in the signal properties over time, mainly the seasonal cycle of hydrological mass redistribution, are the reason for the variations. Investigating the hydrological component of the underlying Earth model reveals that the residuals are, compared to the signal amplitude per month, virtually constant. This implies that the system can always observe a certain proportion of the observed signal. As signal strength is varying over time, these properties call for the application of a filter taking such variability into account. The variability of the residuals for the double pair VADER result is, compared to the Gaussian one, lower (dashed blue versus dashed red curve). This observation can be understood as a reason for applying adaptive and non-stationary filters. But not every time variable filter does meet the required characteristics, as the results of the S&W filter show.

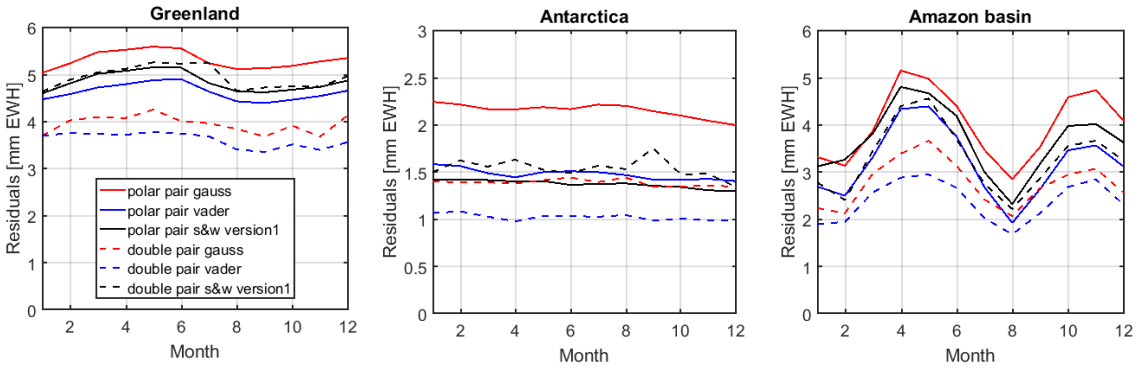

Figure 6-7: Residuals in mm EWH as average per respective area from closed loop future mission experiments. Areas are Greenland (left panel), Antarctica (center panel), and the Amazon basin (right panel). Solid lines represent the results from single polar pair and dashed lines from double pair constellation, both polar and inclined. Filters compared are Gauss (red), VADER (blue), and S&W version one (black). Note the different scaling on the y-axes.

Since the performance of the S&W filter version two, fitting one polynomial per order, shows significant oscillation effects for a solution expanded up to SH degree 120, resulting in erroneous artefacts, only version one is considered to be included in this part of the experiment. For all three panels the resulting performance in terms of residuals is indicated by the black curves. Contrary to the Gaussian and VADER filter, the residuals in the double pair case of the S&W filter version one show larger residuals for Greenland and Antarctica than for the single pair case. This can be attributed to the non-conformity of the correlations embedded in the coefficients violating the assumption regarding the correlation patterns. By visual inspection of the S&W version one filtered monthly solutions, erroneous artefacts, induced by the polynomial fit and subsequent reduction, which are not present in the original observations, are detected. In the right panel for the Amazon basin, the double pair is better than the single pair result, as one would expect since the general noise level is expected to be lower than for the polar pair only solutions.

One result, being unexpected from what all investigations regarding the VADER and S&W filter showed in the preceding experiments, is the better performance of the S&W filter in the case of Antarctica for the single pair scenario (solid black against solid blue curve). Apparently the correlation pattern inherent in the solutions corresponds to the assumed one, resulting in good filter performance. As this is not true for the other two regions, there are no solid grounds for concluding that the S&W filter version one is outperforming the VADER filter in the region of Antarctica. The S&W filter is tuned for every region to optimal performance by defining the optimal half width of the Gaussian filter in the second step of the filter cascade individually for each area of interest. Such optimizations can be carried out in the closed loop environment as the true solution is known. For real world applications this does not hold anymore, as the tuning becomes a highly empirical matter.

A conclusion one can draw from the results presented above is the clear benefit in performance using the VADER filter for both single and double pair future mission scenarios. Table 6-1 is summarizing the findings from Figure 6-7 by indicating the RMS of the residuals of the respective solutions for the three areas of interest. A very encouraging result, also regarding the discussion of the benefit of an inclined pair for cryospheric analysis, is the gain in performance for the retrieval of geophysical signals in areas without direct coverage of the inclined pair, namely most of Greenland and the whole of Antarctica. The introduction of a second pair allows for retrieving more stable results containing less noise contribution due to temporal aliasing, leading to the GRACE typical striping patterns. As results from the different filters are closer in terms of nominal residuals than for the single pair scenario, this is an indicator for less need of post-processing and filtering, since the number of observations is about doubled and the noise characteristics are more beneficial for geophysical signal retrieval as the correlation length of errors is significantly reduced.

Table 6-1: RMS of residuals (mm EWH per area) of different filter types in different regions according to the examples in Figure 6-7.

	Single polar pair			Double polar and inclined pair		
Area	Gauss	S&W v1	VADER	Gauss	S&W v1	VADER
Greenland	5.31	4.85	4.63	3.95	4.95	3.62
Antarctica	2.15	1.37	1.48	1.39	1.54	1.02
Amazon basin	4.08	3.73	3.28	2.82	3.38	2.42
Global	0.26	2.35	0.20	0.17	0.52	0.16

On global scale (last row of the table), the performance deficits of the S&W filter are mainly due to the limited capabilities of the filter approach in low latitude areas. The filter is applied with a second step of the cascade consisting of an average Gaussian filter, making a compromise in filter strength for all areas of low, mid, and high latitude. For the optimal design in the case studies depicted in Figure 6-7, the filter strength of the Gaussian filter as second part of the S&W filter cascade is changing from 80 km half width in the polar areas to 240 km for the near equator and low latitude areas. Such changes for a suitable filter design are easy to determine in the closed loop environment. For real world applications this does not hold because the true target signal is unknown.

Figure 6-8 gives an impression of the spatial resolution and attenuation of signal amplitudes for retrieving linear trend signals from the closed loop time series, showing examples for the regions of Greenland (upper panels) and South America (lower panels). One should not misinterpret the spatial pattern and signal amplitudes as real world signals, as the underlying dataset originates from model assumptions (year 1996) of HI signals, and a certain grade of alteration from the geophysically true signal must be expected.

A second limitation is the very short period the linear trend signal is estimated from. For geophysically meaningful results one should employ at least a several-year long time series. Nevertheless, the results allow to get an impression of how well the observed signals can be retrieved by the respective mission design and the subsequently applied post-processing method. The VADER filter (left panels) delivers, as the preceding experiments suggested, superior results with respect to the Gaussian filtering (right panels). Especially for the high latitude areas above 65° north (most of Greenland) the features retrieved in the double pair case match the reference HI trend (middle panel) better than for the single polar pair only case. For the example of South America, the double pair coverage significantly increases the recoverability of the observed HI signals for both Gaussian and VADER filtering. For the Gaussian filtering in general, residual

striping patterns remain, as the filter is not capable of suppressing groups of correlated coefficients causing such patterns.

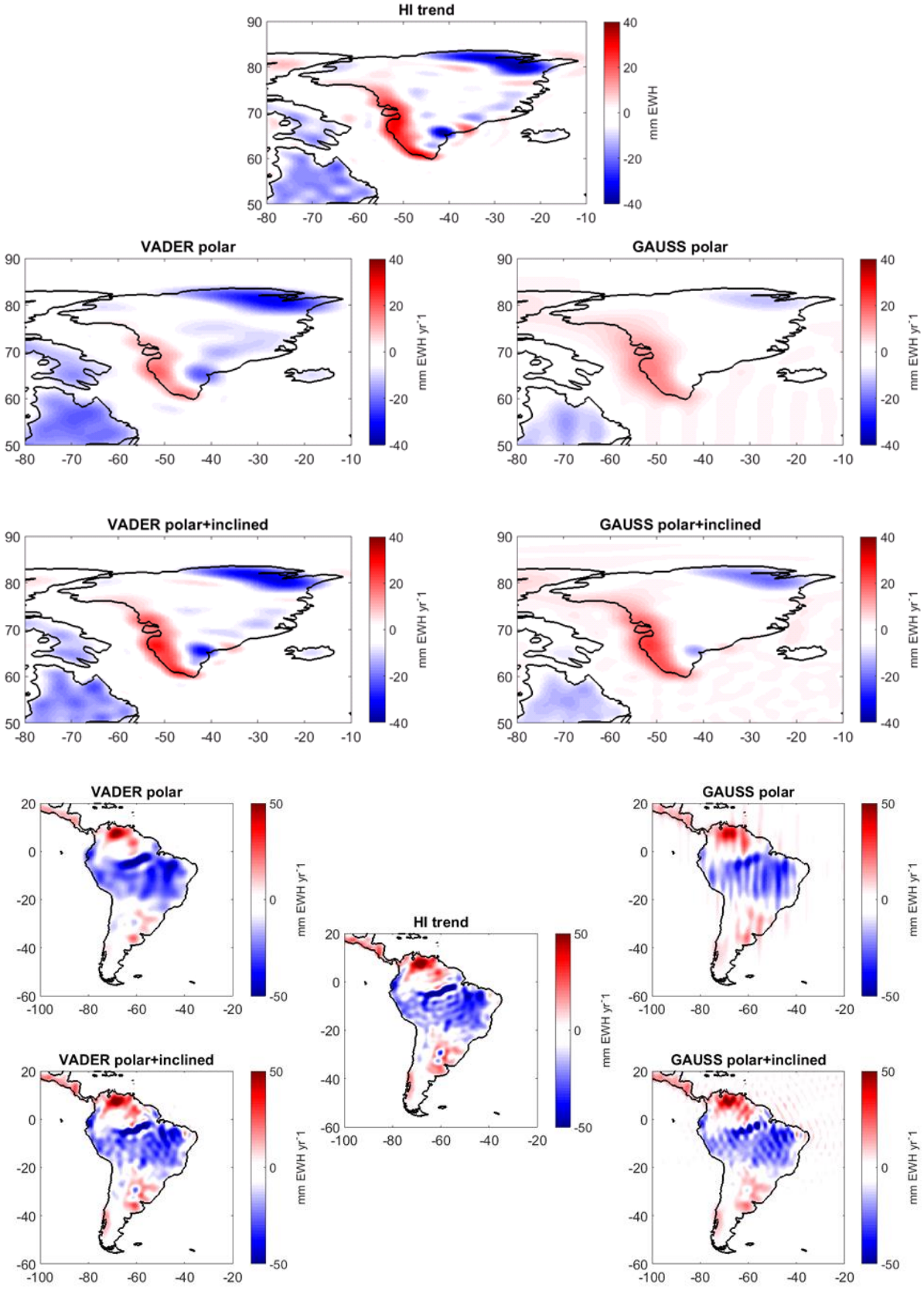

Figure 6-8: Examples of linear trends (mm EWH per year) from VADER (left panels) and Gaussian (right panels) filtering in Greenland (upper five panels) and South America (lower five panels). The underlying true trend is depicted by the respective middle panel. Note the panel heading for details regarding the respective constellation.

6.3 Suggested process of optimal post-processing for future mission time series

Upon the findings from the analysis in section 6.1 and 6.2, a clear preference for employing the VADER filter can be concluded. Either for the single pair or for the double pair scenario, the filter outperforms the other filters tested in terms of cumulative geoid errors on global scale or the analysis of the residuals of EWH in the three local areas.

A second criterion, favorable for the VADER filter, is the pattern of spatial error correlation structures after filtering. Figure 6-9 gives an impression of how the patterns look like for the Gaussian (upper panels) and VADER filtering (lower panels) in the single (left panels) and double pair scenario (right panels). From the left three bins in Figure 6-2, representing the correlations in the unfiltered state, one can already see the positive effect in terms of error correlation patterns introducing the second pair, leading to comparably isotropic results.

The choice for the applied filter strength used for the results displayed is derived from the local minima in Figure 6-6. The difference between Gaussian and VADER filtering in the single pair case is much more prominent as for the double pair case. As one would expect, the shortest correlation length for the VADER filter appears in the double pair case. The shorter correlation length of the VADER filter has a clear advantage whilst integrating over basins or areas of interest. Averaging observations with uncorrelated errors leads to a decrease in the uncertainty of the averaged quantity.

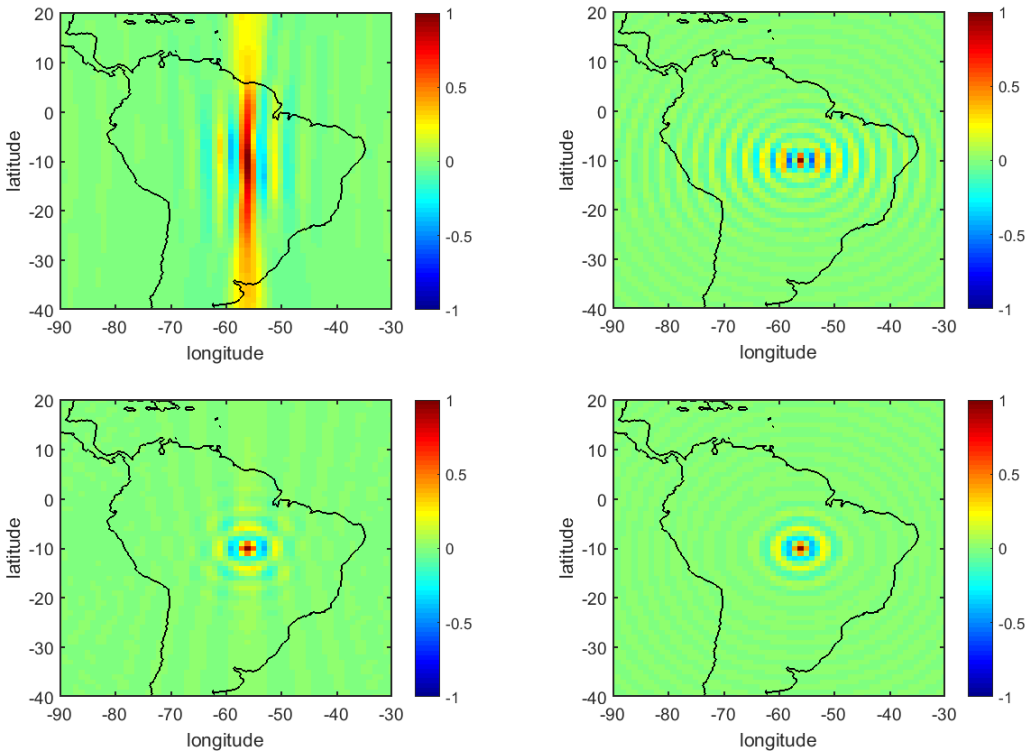

Figure 6-9: Spatial correlation of errors from single (left panels) and double pair (right panels) scenario after Gaussian (upper panels) and VADER (lower panels) filtering applied. Colorbars indicate the correlation.

Interpreting the findings outlined above, one should note that the orbital configuration followed an idealized model. In real world scenarios the satellites will be subject to orbit maneuvers as well as calibration and outage phases, accountable for not delivering scientific data. These data gaps lead to disturbances of the idealized assumptions in the closed loop world. From experiments with GRACE, comparing simulation results from perfect repeat orbits with coherent and steady sampling rates against real GRACE orbits with outages and short repeat phases, a clear performance decrease can be observed. This decrease in performance is caused by non-homogenous observations in space and time, resulting in amplified correlated errors and a worse signal to noise ratio in general. In real world conditions one can expect an adaptive filter, defined by the observational geometry and error characteristic of each individual solution, best suited for employment in future mission post-processing based on the experience with GRACE data and upon the experiments for the mission scenario.

7. Applications

The following chapter presents two applications of the filter and post-processing strategies investigated respectively developed in preceding chapters. The application cases are applied on both real and simulated GRACE data.

The first example is dealing with the retrieval of Antarctic ice mass variations, especially linear trend components, derived from a decadal real GRACE time series. The processing comprises the steps from selecting a suitable time series, applying all necessary corrections and retrieving the linear mass change component using an adequate functional model as well as suitable integration or averaging kernels. The whole process is accompanied by an estimation of an overall error budget, resulting in mass rates on basin scale with their associated accuracies.

The second example is built on a series of simulated GRACE-like monthly gravity field estimates, studying the impact of applying static or time variable filters on hydrological signals in a selection of river basins. Especially the impact on the retrieval of amplitude and phase estimates of the river catchment is of interest. The target is to evaluate whether static or time variable filters cause an erroneous shift of phase or attenuate the amplitudes of the estimated signals with respect to the true reference.

7.1 Mass change in Antarctica measured by GRACE

Within this section an example of geophysical mass change estimates derived by using the VADER filter is presented. It covers the process of estimating linear mass change in Antarctica and its subregions from the selection of a suitable GRACE time series to the final change rates, including an estimate of their uncertainty. The main processing details regarding the corrections applied are aligned with the IMBIE project [Shepherd et al. 2012], allowing comparison to independently derived mass transport estimates. The definition of the region boundaries is derived from the dataset by Zwally and Giovinetto [2011]. The averaging or integration kernel follows the approach outlined in section 4.2.4 and is displayed as an example for the whole AIS in Figure 4-9.

The selection of a suitable time series is based on three main criteria. First, the time series needs to provide full error covariance information since the VADER filter is not applicable without them. Second, the time series should be maintained over and cover an as long as possible time frame. Third, it should comprise latest processing techniques and incorporate up-to-date auxiliary data sets like de-aliasing products or tide models. Upon the investigations carried out in section 4.3.2, the model of choice is the ITSG-Grace2016 time series [Mayer-Gürr et al. 2016a], since it fulfills all the abovementioned criteria. Especially the formal error covariance estimates appear to show better quality compared to the other available series (cf. section 4.3.2).

Before corrections are applied, the monthly sets of coefficients are filtered using the VADER filter. Upon the findings outlined in chapter 5, a cyclo-stationary signal variance, a non-stationary error covariance, and an α-value of 0.5 is employed to build the VADER filter. According to Table 5-1 the α-value corresponds to an average smoothing radius of about 287 km. An α-value of 1 would result in an average smoothing radius of 312 km and is also rated to be suitable for Antarctic mass balance estimates incorporating the ITSG-Grace2016 time series. One should note that the choice for the optimal α-values is not directly transferable to the use of other GRACE time series,

since they can have a different structure within their normal equation matrices, calling for other α-values.

The filter process is accompanied by an error propagation of the unfiltered covariance matrix according to equation (2.20). The variances of the propagated error covariance matrix (diagonal of the full error covariance matrix) are subsequently evaluated for the respective target region to derive month-to-month variances in the spatial domain. This allows either deriving month-to-month weights for the trend estimation process or scaling factors for the monthly GRACE error budget contribution. The month-to-month GRACE error budget contribution is derived similar to the approach described by Nagler et al. [2016]. As well as for the evaluation of the error budget contribution of degree one and C_{20} coefficients (cf. section 4.2.2, C_{20} paragraph), a residual mass time series is computed for the respective area of interest. To obtain the residual time series, a nine-parameter reduction model is applied. It consists of a constant, linear, quadratic, and 365.25, 182.6, and 161 days sine/cosine parameter. A 13-month Gaussian low-pass filter (cf. section 4.2.2, C_{20} paragraph) is subsequently applied to suppress remaining geophysically induced signal. One should note that for the preceding analysis the degree one and C_{20} terms are set to zero. These quantities are evaluated separately. The error noise of the respective area of interest is then scaled by the propagated variance, derived from VADER filter covariance propagation, for each month individually. In this case applying a scaling to the propagated monthly variance estimates, due to the underestimation of the true error (revealed by the regularization bias investigations) is not necessary since the scaling only reflects the relative differences between the individual months and not their absolute value.

Towards meaningful trend estimates, corrections are introduced by replacing the degree one and C_{20} coefficients. A discussion regarding the theoretical background, explaining the underlying problems making such corrections necessary, can be found in section 4.2.2. The replacement C_{20} coefficients are obtained from the time series provided by GRACE technical note TN-07 [Cheng and Ries 2016]. The degree one coefficients are obtained from the GRACE Tellus web portal (http://grace.jpl.nasa.gov/), which provides coefficients computed according to the procedure outlined in [Swenson et al. 2008]. SMB corrections are based on the RACMO2-ANT27 regional atmospheric climate model [Lenaerts et al. 2012]. The gridded SMB product is transferred to Stokes coefficients by a SH analysis before being applied as a correction to the GRACE time series. Replacing the C_{20} coefficients after applying the filter causes, as discussed in section 4.2.2, a little bias. The fully populated filter matrix distributes energy of the original C_{20} coefficient to all other coefficients. For the ITSG-Grace2016 time series this bias has only minor impact ($<$0.1 Gt year^{-1} for linear trend component of the AIS), as the original and SLR derived coefficients are more similar than for the other time series. An error budget contribution for individual months is derived according to the procedure outlined in section 4.2.2. Numerical values for the C_{20} error budget contribution in the region of Antarctica and its subregions for an individual monthly solution can be found in Table 7-2. The contribution of the C_{20} error to the total error budget of the linear trend component is derived by evaluating the linear trend of the series of C_{20} coefficients separated from the other coefficients. Table 7-3 indicates the respective numbers for Antarctica.

Another option to assess the uncertainty of C_{20} time series is by comparing different C_{20} time series. Bloßfeld et al. [2015] compare e.g. their own C_{20} time series with the one from CSR [Cheng and Ries 2016]. Their comparison reveals a difference of 12.3 Gt year^{-1} in the linear trend component for the region of Antarctica between the two C_{20} time series. As only a very limited number of C_{20} time series is available, and deriving an error estimate from an ensemble of only 2 models is from the perspective of statistics unsatisfying, this approach is not further pursued here.

Since the degree one coefficients are not part of the initial estimate of the solution, the error covariance matrix does not contain any information regarding these coefficients. They are therefore treated as uncorrelated and they are not part of the propagated error, as the ITSG-

Grace2016 error covariance matrices contain only information for coefficients with $l \geq 2$. The introduction of values different from zero causes, as explained in section 4.2.2, a shift of the origin of the solutions away from the center of mass. In the case of the applied correction, the origin is shifted to the center of figure. To account for the uncertainty introduced with the degree one coefficients, a dedicated error budget is assigned for the final linear trend error budget (cf. Table 7-3), as well as for the individual monthly solutions (cf. Table 7-2). The approach is the same as the one described above for the error budget assessment of the C_{20} coefficients.

The GIA error estimate applied to the final error estimates shown in Table 7-2 originates from the standard deviation of an ensemble of four different GIA model solutions in the respective area of interest. The ensemble of GIA models used for the assessment of the GIA error are: A mean of all three W12a [Whitehouse et al. 2012] solutions, a mean of all six IJ05_R2 [Ivins and James 2005] solutions, the ICE-5G [Peltier 2004] solution, and the reconciled version of the ICE-6G_C [Stuhne and Peltier 2015] solution, which is an update of the original ICE-6G_C model [Peltier et al. 2015]. Unit weight is applied when calculating the standard deviation of the four different results integrated over the respective area of interest. Table 7-1 presents in the lower section numbers for the derived assumptions for the GIA standard deviations in Gt year^{-1} for the respective area of interest. The magnitude for the GIA error budget reaches, except for West Antarctic ice sheet (WAIS), only about 50-60% of the one derived from van der Wal et al. [2015]. For the WAIS the number is almost equal. In this region the magnitude of GIA rates is significantly larger than e.g. in the East Antarctic ice sheet (EAIS) (cf. Figure 4-8). Analysis shows that in this region the deviations between the tested models are largest, resulting in a similar standard deviation for the samples tested by van der Wal et al. [2015]. A reason for the difference can also be found not only in the different sets of samples incorporated for the assessment, but also in the different averaging functions applied for the respective target regions. It shows that results are highly sensitive to the choice of samples taken into account and that differences between models are concentrated in spatially confined regions mainly at the Antarctic coast and the WAIS. When selecting models for an error assessment, considering a representative selection of models built on different ice loading history models, underlying Earth models, and rheology is advisable. Comparing the assessment carried out by Sasgen et al. [submitted 2016a], the agreement between the error budget contributions is better than for the results derived from van der Wal et al. [2015]. The numbers derived by Sasgen et al. [submitted 2016a] find the standard deviation for the respective basin even lower than the ones derived by the analysis within this thesis. Considering the spreading of available GIA solutions in the Antarctic region, the formal uncertainty by Sasgen et al. is considered to represent a lower bound of uncertainty. For a single monthly GRACE estimate the standard deviation scales to a twelfth of the indicated value for one year (cf. Table 7-2). This is done since for the single monthly solution only the error within the time of one month from GIA is of interest.

Table 7-1 shows the applied GIA correction for the mass balance estimates presented at the end of this section. It is derived from the same models as used in the IMBIE project [Shepherd et al. 2012] for reasons of comparability. The correction applied is the one called "W12a & IJ05_R2", which is a combination of the W12a [Whitehouse et al. 2012] and the IJ05_R2 [Ivins and James 2005] GIA estimates. The combination is computed by taking the mean of the IJ05_R2 ensemble and the W12a so called best estimate. Since the IMBIE project comprises five different estimates of gravimetric mass balance over Antarctica and its subregions, it serves as the main benchmark for the VADER results.

Table 7-1: GIA correction and standard deviation of GIA correction for the Antarctic region and its subregions compared to independent estimates. All numbers in Gt year^{-1}.

Region:	AP	WAIS	EAIS	AIS
GIA correction applied for region of AIS [Gt year^{-1}]:				
Mean of IJ05-R2 and W12a	6.9	41.1	24.8	72.8
Standard deviation per area [Gt year^{-1}]:				
This study	3.3	12.5	20.7	30.2
Derived from van der Wal et al. 2015	6.2	12.1	37.9	52.7
Formal uncertainty by Sasgen et al. [submitted 2016a]	9.8	13.8	14.7	22.7

One could estimate mass trends from GRACE also on smaller scales than the three subregions EAIS, WAIS, and Antarctic Peninsula (AP). Apart from the challenges and limits set by leakage problems and suitable averaging functions, other problems arise whilst evaluating GRACE results for small basins with spatial extents of only a few hundred kilometers in each direction (e.g. areas like basin 17, 20, or 23 as displayed in Figure A 5 in the appendix section). Refining e.g. GIA estimates and their uncertainty to areas of scales below several hundred kilometers seems problematic if the approach of assessing such quantities is not changed from the above described. GIA models show especially in the region of the WAIS corrections, differing by tens of gigatons (cf. Figure 4-8 for variability in spatial domain). Analyzing the rheological structure one must not expect such strong variations on scales of only some hundred kilometers, since the GIA signals are predominantly composed of large scale signals (hundreds to thousands of kilometers), resulting in relatively smooth rebound patterns (cf. Figure 4-8). According to e.g. Morelli and Danesi [2004], the structure of the Earth's crust of East and West Antarctica show significant differences. They report the tectonic setting for West Antarctica being significantly more heterogeneous than for East Antarctica. This explains the generally better agreement (less spread of the GIA solutions) in East compared to West Antarctica, as the properties of the Earth's crust are easier to constrain in a homogeneous environment. Lowering the size of the areas of interest in West Antarctica results in increasing GIA uncertainties, as the effect of averaging becomes less effective. Tests reveal GIA uncertainties for individual small basins, defined by the boundaries according to Zwally and Giovinetto [2011] or Rignot et al. [2011, 2013], of higher magnitude than the GRACE signals themselves. This makes the GRACE gravimetric mass balance (GMB) estimates not reliable anymore. Consequently no refinement of the areas of interest is performed at this stage. From the perspective of GIA models and the estimation of their uncertainty, a separation of areas into basins, separated by the underlying rheological structure, might be reasonable. Therefore breaking down the three sub regions of the AIS into smaller regions, separated by varying properties of the Earth's crust and mantle viscosity and not the drainage basins, is a promising option needing further analysis. As for climatological and ice mass change analysis the separation into drainage basins is desired, one can think of aggregating small scale drainage basins to subregions constrained by coherent tectonic structures. This idea to refine the size of areas of interest, other than Antarctica, does not necessarily prove useful for all regions. In most regions around the globe GIA signal can usually be better constrained by e.g. GNSS observations or seismic analysis. The remote location, harsh conditions, thick ice coverage (up to kilometers), and surfacing bedrock only in a very limited number of locations not evenly distributed over the entire ice sheet (only Transantarctic Mountains and coastal/near coastal areas), make it difficult to constrain GIA estimates easily.

Table 7-2 summarizes the error budget contributions of a single monthly solution for the AIS and its subregions WAIS, EAIS, and AP. The value for the GRACE contribution itself is given as median value of the month-to-month scattering. The other error budget contributions (C_{20}, degree one, and GIA) are assumed to be static. The total error budget for a monthly solution is derived by taking the square root of the quadratic sum of the individual contributors.

Table 7-2: Error budget contributors and total error budget of a single monthly mass balance estimate derived from GRACE in gigatons [Gt] for Antarctica and its subregions AP, WAIS, and EAIS.

Area	AP	WAIS	EAIS	AIS
GIA	0.3	1.0	1.7	2.5
C20	3.7	11.7	47.7	63.1
Degree one	2.0	5.7	22.1	29.2
GRACE (median)	19.1	25.1	41.8	59.6
Total	19.6	28.3	67.1	91.6

The SMB correction is treated as error free. It mainly reduces interannual variability of signals related to geophysical processes like snowfall and wind driven snow transport (cf. section 4.2.2).

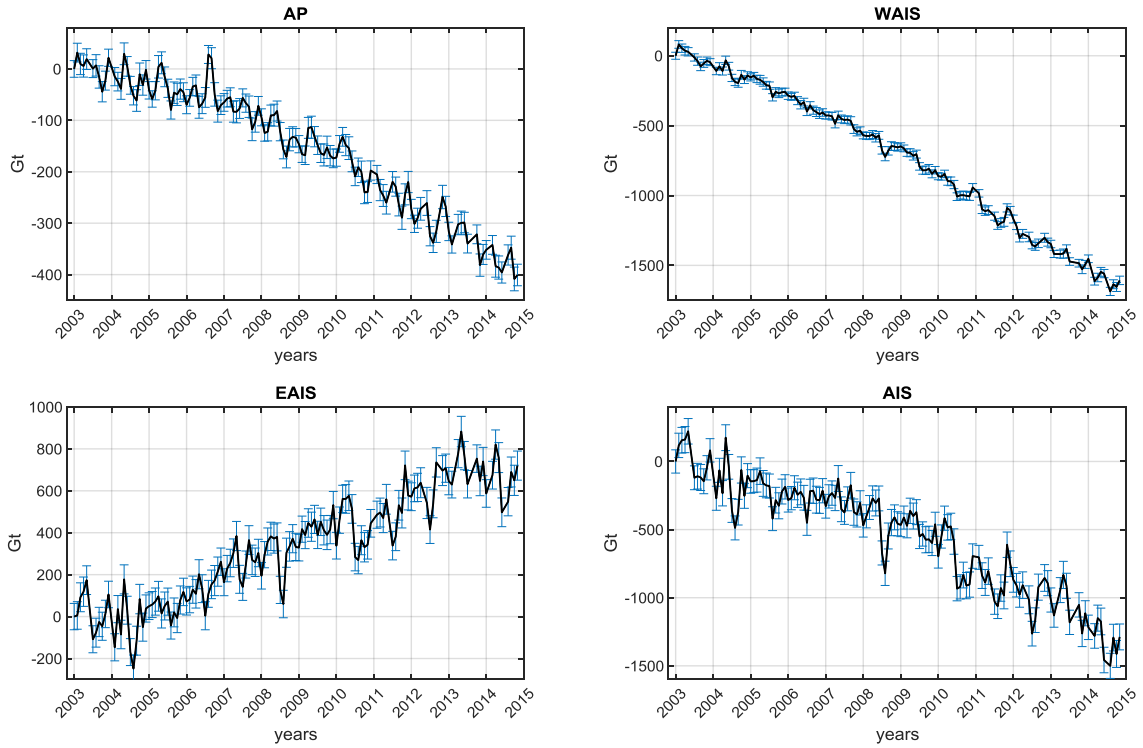

Figure 7-1*: Monthly mass balance estimates (black curves) between 2003-01 and 2014-11 for the AIS and its three subregions AP, WAIS, and EAIS. Blue error bars indicate the individual total error budget for the respective month.

Figure 7-1 shows the monthly mass balance estimates for the region of the AIS and its subregions AP, WAIS, and EAIS derived from the ITSG-Grace2016 time series. Corrections are applied as indicated above, including the reduction of interannual surface mass balance estimates. The

timeframe presented ranges from 2003-01 to 2014-11. The first month (2003-01) is set to have a mass balance of 0 gigatons. The blue error bars indicate for each monthly estimate the total error budget derived from the procedure outlined above (cf. Table 7-2). A clear negative trend can be observed for the AIS in general. For its subregions a positive trend is derived for the EAIS and negative trends are derived for the WAIS and AP. These findings are in agreement with the results in literature. To classify the results, trends for each of the four areas of interest are calculated for different time periods. Table 7-4 gives numbers of the linear trend component for the whole period displayed above in Figure 7-1 as well as for a shorter period spanning from 2003-10 until 2008-12. The functional model for the fit consists of constant, linear, and seasonal sine/cosine parameters with 365.25, 182.6 and 161 days frequencies.

The associated uncertainty of the linear trend component and its constituents is shown in Table 7-3 in Gt year^{-1} for the period 2003-01 until 2014-11 (upper row in Table 7-4). The last row indicates the total error budget for the respective areas of interest. The upper four rows indicate the individual error budget contributors. It is apparent that the GIA uncertainty is clearly dominating the total error budget. The GRACE error itself is only of minor impact on the total budget. One error budget contributor not listed in Table 7-3 is the uncertainty due to leakage. Nagler et al. [2016] suggest to introduce an error of 3 Gt year^{-1} for the whole AIS. According to the presented numbers in Table 7-3, a contribution of such magnitude does only have a minor impact on the total budget.

Table 7-3: Linear trend error budget and its contributors in Gt year^{-1}

Area	AP	WAIS	EAIS	AIS
GIA	3.2	12.4	20.7	30.2
C20	0.2	0.4	1.6	2.2
Degree one	0.1	0.2	1.0	1.3
GRACE (median) 2003-01 until 2014-11	0.8	2.9	2.6	2.9
Total 2003-01 until 2014-11	**3.3**	**12.8**	**21.0**	**30.5**
GRACE (median) 2003-09 until 2008-12	2.4	2.5	6.0	9.1
Total 2003-09 until 2008-12	**4.1**	**12.7**	**21.7**	**31.7**

The error budget contributions of GRACE itself for the period between 2003-01 and 2014-11 for the regions of the WAIS and AIS are on equal level (2.9 Gt year^{-1}). The comparably small value for the whole AIS is due to the averaging over a long time period over a large region containing ample areas showing no or only very little trend signal and low error. Nagler et al. [2016] report a GRACE only error budget of 4 Gt year^{-1} for the same period (2003-2014), being a bit larger than the number estimated within this thesis. Van der Wal et al. [2015] estimate a trend uncertainty from calibrated standard deviations of GRACE monthly gravity field solutions of 1.9 Gt year^{-1} for AP, 3.2 Gt year^{-1} for WAIS, 6.7 Gt year^{-1} for EAIS, and 9.2 Gt year^{-1} for AIS in the period between 2003-02 and 2013-06. Their numbers are larger than the other estimates discussed but are expected to also incorporate error budget contributions from at least the C_{20} terms (not explicitly specified in manuscript). For the shorter period ranging from 2003-09 until 2008-12 the GRACE error budget contribution is, as one can expect, larger since the time period is shorter. Only for the WAIS this does not hold. Here the error budget contribution from GRACE increases from 2.5 to 2.9 Gt year^{-1}. A reason for this effect can be found in the high dynamics of ice mass change in this region.

Table 7-4 presents the linear mass change component estimated from the ITSG-Grace2016 time series for the respective areas of interest in the region of the AIS with associated uncertainties. Note that the IMBIE GMB uncertainty indicated is, according to Shepherd et al. [2012], derived as an arithmetic mean of the given individual uncertainty levels of the participating group members. For further details regarding the IMBIE datasets please consult the supplementary material of Shepherd et al. [2012].

Table 7-4: Mass trend for the region of Antarctica and its subregions derived from the VADER filtered ITSG-Grace2016 time series for the periods of 2003-01 until 2014-11 and 2003-10 until 2008-12.

Area	AP	WAIS	EAIS	AIS
Period 2003-01 until 2014-11	-35.2 ±3.3	-149.5 ±12.8	67.2 ±21.0	-117.5 ±30.5
Period 2003-10 until 2008-12	-26.0 ±4.1	-71.2 ±12.7	21.0 ±21.7	-76.2 ±31.7
IMBIE GMB average “03-08”	-21 ±14	-68 ±23	35 ±40	-57 ±50
IMBIE overall average “03-08”	-28 ±10	-67 ±21	24 ±36	-72 ±43

The shorter period (second row) is presented to allow intercomparison against the results obtained within the IMBIE project [Shepherd et al. 2012]. In the third and fourth row the respective average results for the gravimetric mass balance (GMB), the overall mass balance aggregating input-output method (IOM), radar altimetry (RA), laser altimetry (LA), and GMB obtained from the supplementary material of Shepherd et al. [2012], are given. The label “03-08” is adapted from the documentation of the IMBIE project and corresponds to the period 2003-10 until 2008-12. The GIA correction applied is as mentioned above consistent for all estimates summarized in Table 7-4.

The trend results for the IMBIE period (second row) agree well with the results published by the IMBIE project. Especially the agreement with the overall average mass trend is noticeable. For the period 2003-01 until 2014-11 the trend estimates appear amplified. This becomes apparent by inspecting the mass balance estimates displayed in Figure 7-1 for e.g. the first and second half of the presented time interval.

If an acceleration of mass trend signals appears to be present, attention should be drawn on not erroneously misinterpreting inter-decadal variability as general change of environmental conditions. Kusche et al. [2016] conduct experiments in a probabilistic framework to evaluate whether major changes in mass transport mechanisms (extreme conditions; intensification) can be detected in a statistically significant manner by GRACE yet. They conclude that the necessary length of the time series used for determining changes in the global hydrological cycle is at least 18 years of continuous observations (will be reached around 2020). Hydrological signals have not the same forcing as ice mass change but are still coupled with each other. The findings regarding the necessary length of observations for hydrological signals cannot be transferred directly to ice mass change signals. Nevertheless care must be taken whilst interpreting signals of only decadal length since well-known forcing mechanisms of global climate variability such as the El Niño southern oscillation (ENSO) [Trenberth 2013] have periods of 7 years. According to Turner [2004] the ENSO is partially linked with the Antarctic climate system. Therefore short scale variability like the apparent acceleration can be due to either external forcing by e.g. the ENSO or real acceleration due to increased regional warming. But independent of the underlying forcing, an increase of the mass loss rate for the AIS in the recent past is present, whether it proves statistically significant in terms of the climate systems variability or not.

In summary one can conclude that the VADER filtered ITSG-Grace2016 time series allows estimating linear trend components with associated error budget estimates in a competitive and profound way.

7.2 Estimating hydrological variations in large and medium sized basins

The following section analyzes the impact of the filter and post-processing techniques investigated in sections 4.3.3 (Gaussian filter), 5.2 (S&W filter), and 5.3 (VADER filter) on the retrieval of hydrological signals on basin scale. The environment for the experiment is the closed loop white noise time series as described in chapter 3 (cf. Table 3-1). Evaluating post-processing methods in the closed loop environment allows to rate the recoverability of the original input signal. This is not the case for real world applications, where the true signal is not known. Benchmark values are the amplitude and phase of the retrieved signal per month compared with the amplitude and phase of the initially observed signal.

The comparison is made on the level of total water storage (TWS) change time series per basin (cf. Figure 7-2). To determine the phase lag between retrieved (after post-processing) and observed signal (truth), the following procedure, similar to an approach described by Eicker et al. [2016], is applied. Based on the time series of TWS change, a Hilbert transform is performed, leaving a complex representation H of the original time series Z.

$$H = re(Z) + i\,im(Z) \tag{7.1}$$

The relation in equation (7.1) can be used to determine the phase angle P for each observation by evaluating

$$P = \arctan\left(\frac{im(Z)}{re(Z)}\right) \pm 2\pi k,\ k \in \mathbb{N} \tag{7.2}$$

In case jumps $\geq \pi$ between two consecutive phase angles P occur, these jumps are corrected by adding multiples of $\pm 2\pi$. The phase lag P_{lag} between observed HI signal, transferred to TWS per basin (subscript *HI*), and the retrieved TWS signal after post-processing (subscript *OBS*) is determined for each month by subtracting the respective phase angles P from each other.

$$P_{\mathrm{lag}} = P_{\mathrm{HI}} - P_{\mathrm{OBS}} \tag{7.3}$$

The post-processing methods compared are: (a) The VADER filter in its preferred design of cyclo-stationary signal variance combined with non-stationary error covariance, (b) the VADER filter in a variant with stationary signal variance and non-stationary error covariance, the S&W filter in version one (c) and two (d), and (e) the Gaussian filter. The benchmark is always the monthly average HI signal for the respective basin. The average is computed from the 6-hourly sampling intervals of the Earth system model by Dobslaw et al. [2015b].

As the Earth model used for the closed loop environment spans from 01-Jan-1995 to 31-Dec-2006, the observed signals for the basins must not be understood as truth with respect to the GRACE measurement period. GRACE orbits incorporated are ranging from 01-Jan-2003 until 30-Nov-2014, thus delivering 143 months of solutions observing the respective basins from 01-Jan-1995 until 30-Nov-2006. This does not make the investigation less meaningful or informative. One just has to keep in mind not to compare the presented results with data from other sources without considering the shift in time.

Figure 7-2 shows the location of the six river basins investigated for the evaluation of the comparison of the aforementioned post-processing methods (a-e). The basins are located on different continents and at different latitudes, thus showing varying seasonal and long term behavior. The basin boundaries are derived from the STN-30p dataset [Vörösmarty et al. 2000]. They are the Ganges (1.628.404 km²), Amazon (5.853.804 km²), Danube (788.002 km²), Mississippi (3.202.958 km²), Murray (1.031.512 km²), and Parana (2.661.391 km²) river basin. The numbers in brackets indicate the respective basin size in square kilometers.

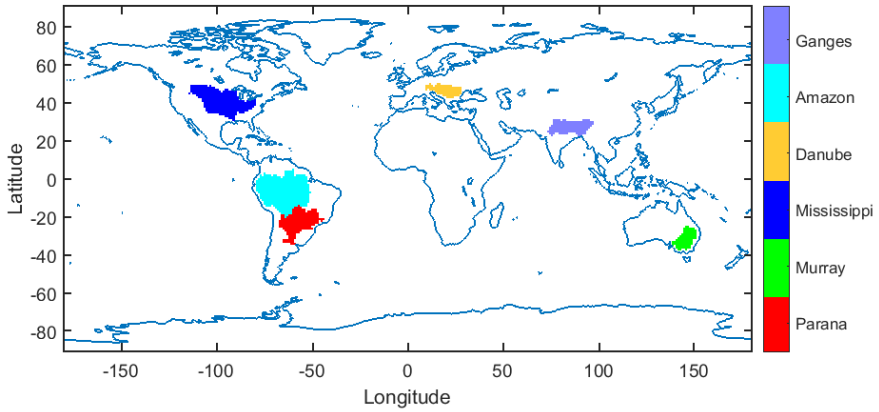

Figure 7-2: River basins investigated for the post-processing method comparison for retrieving hydrological signals.

Figure 7-3 shows the average absolute HI signal (cyan curves) for the six basins in mm EWH. The term HI is used since the input for the simulation are hydrological and ice mass signals. For the river basins under investigation, almost no ice contribution must be expected. The target signal is assumed to originate from almost solely hydrological variations. To create a more realistic simulation environment, 20% of the AO signal and an ocean tide model difference are added to the noise free HI datasets (cf. chapter 3), before computing the five versions of the GRACE-like post-processing results. The residuals with respect to the target HI signal, originating from the GRACE-like observations after applying the post-processing methods a-e, are shown in the red (Gauss), blue (VADER), magenta (VADER with stationary/median signal variance), black (S&W filter version one), and green (S&W filter version two) curves. Two distinct features are the steep peaks in the residuals (red, black, and green) present for all basins around 2004-09 and 2012-05. Both periods are subject to a short repeat cycle of GRACE. This is in agreement with the findings regarding the order resonances for GRACE as shown in the left panel of Figure 5-11. The VADER filter results (blue and magenta) do not show such peaks in residuals as the filter is capable to account for such anomalous events. As one can expect, the rate of signal recovery is depending on the shape and extent of the target regions and the signal strength. For basins like the Murray River (second smallest of the six tested basins), the signal is very small compared to the other basins investigated and does not show significant seasonal variation. Residuals are in the range of the target signal itself, thus suggesting no significance of the retrieved signals. For the Danube river basin the situation is, although even smaller, different, because it shows larger signal

amplitudes compared to the Murray River. This leads, depending on the post-processing methods, to residuals significantly smaller than the target signal. Of course one must not expect the residuals to become zero or near zero since observing the Earth from space comes along with a dampening and filtering of the original signals on ground. Especially signals from small scale features are damped. The different post-processing methods add additional attenuation of the target signals as they imperfectly separate signal from noise. Part of the residual signals shown is also the intentionally introduced residual AO and OT signal simulating the de-aliasing error. Not all of it is being reduced by the post-processing strategies applied. It is apparent that the two VADER filter versions do show best performance (smallest residuals) compared to the other filter approaches tested.

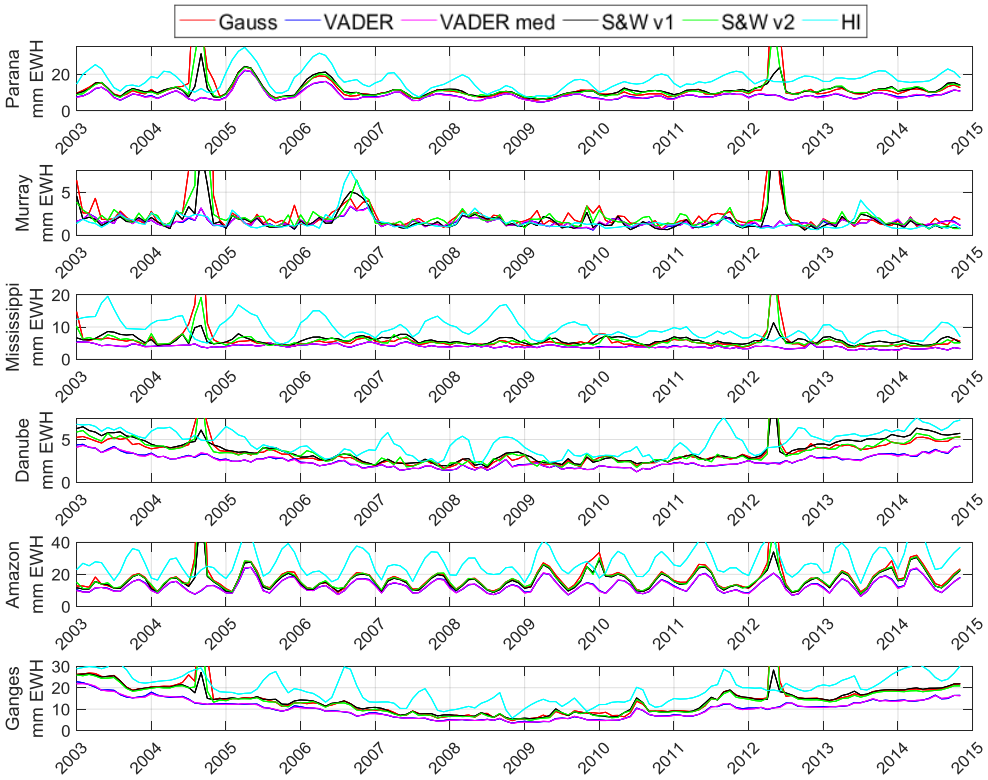

Figure 7-3*: Average absolute signal in mm EWH for each month for 6 river basins (cyan curve). Other curves show residual signal (true signal minus signal after post-processing) for the respective post-processing method.

Using cyclo-stationary or stationary signal variance does not cause significant deviations, especially no systematic calendar-month dependent effects. The blue curve, representing the results obtained with the cyclo-stationary signal variance, is hardly visible since it almost coincides with the magenta curve, representing the results from the stationary signal variance. The label VADER med is chosen, since the stationary signal variance is derived by taking the median of the cyclo-stationary signal variance.

A distinct feature is also the temporal behavior of the residuals comparing e.g. the case of the Amazon and Mississippi River basin. For the Amazon the residuals follow the pattern of the target signal, whereas for the Mississippi River the residuals remain at a certain more constant level.

To analyze the impact of the different post-processing strategies on phase and amplitude of retrieved signals, a seven parameter model is adjusted to the respective time series. Each time series represents the integrated mass change per basin computed from the monthly solutions. The

seven parameters are a constant, linear, annual sine/cosine, semiannual sine/cosine, and quadratic term. Figure 7-4 shows the representation of the adjusted model for each basin over time. Indicated are the results for the different post-processing methods and the original HI target signal. Apart from the Murray River, the agreement between target signal and the different GRACE signals is very good in terms of seasonal patterns.

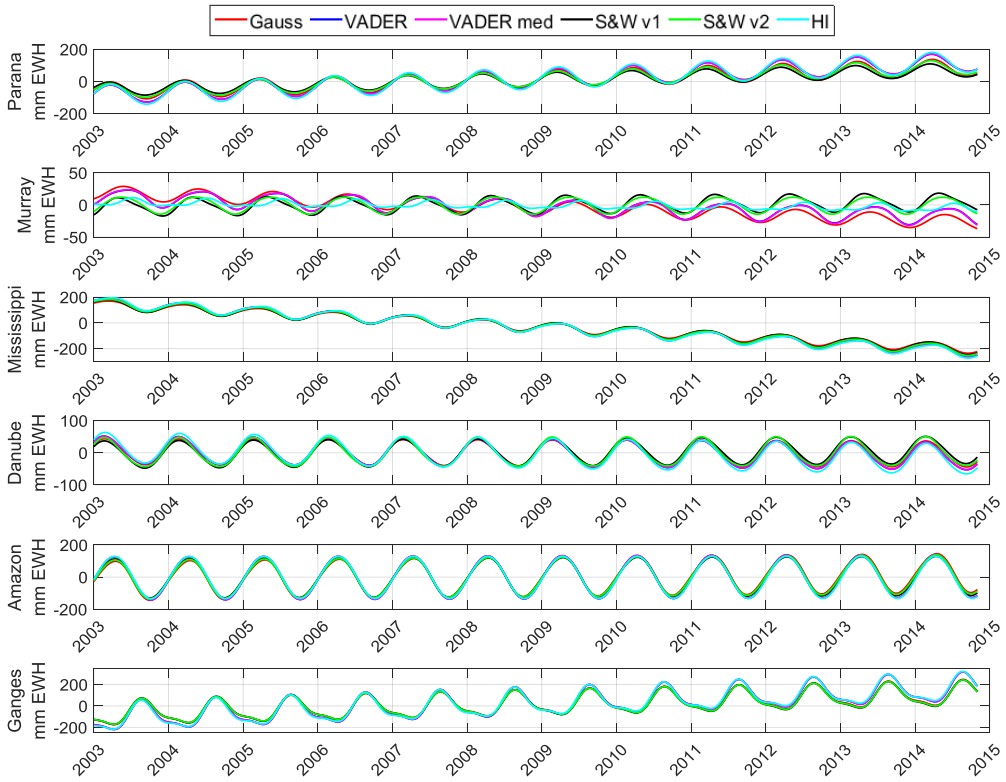

Figure 7-4*: Estimated signals (6 parameters) for 6 river basins in mm EWH from the respective post-processing output and the original observed HI signal.

Characteristic seasonal patterns can be observed for the different basins. The Amazon shows strong seasonal amplitudes with maxima in spring and minima in autumn and the Ganges River shows a peak signal in late summer due to the south-west monsoon and an extended minimum from December until June. The large residuals in Figure 7-3 observed for the Murray River can be explained by the signal being very small compared to all other basins investigated. Accordingly the adjusted model parameters for the GRACE-like results do not represent the true target signal characteristics as they are dominated by noise. The significant slope for the Mississippi River and the Ganges are not considered to represent realistic features and are attributed to a potentially erroneous modeling of the hydrological features in the Earth model. Analysis of the model reveals a significant negative trend for the area of the Mississippi River basin inherent in the model [Dobslaw et al. 2015a]. Comparison with real world hydrological data [USGS 2016] confirms the characteristics of the seasonal variability for the Mississippi River basin, but not the slope.

The phase lag between target HI signal and filtered GRACE-like results is derived by firstly estimating seasonal signals from the original time series and secondly by applying the relations expressed in equation (7.1) to (7.3) on the estimated signals. Figure 7-5 shows the phase lag for the six river basins in terms of days. The phase lag between HI and GRACE-like estimates is within the interval $\pm\pi$, representing ± 182.5 days (assuming a year of 365 days). The jumps occurring e.g. in the case of the Murray River are due to subtracting phase angles across the

interval boundaries. Whilst analyzing the phase lag, one should note the different scaling on the y-axes of the six examples. As visible by eye, the fit between target signal and retrieved signals is poor for the Murray River (cf. Figure 7-4). Accordingly the phase lag is high and does not allow meaningful interpretation of the retrieved results. In real world applications such a scenario would belong to the hydrological examples not or only partially captured by GRACE (cf. left panels of Figure 4-1). For the other basins the phase lag is within reasonable bounds, varying between close to 0 and about 25 days. The reason for different phase lags in different basins is the effect of leakage. Although surrounded by other basins with strong seasonal amplitudes, the Amazon River basin shows comparably little phase lag. Primarily this is due to its enormous size, which reduces the influence of surrounding basins.

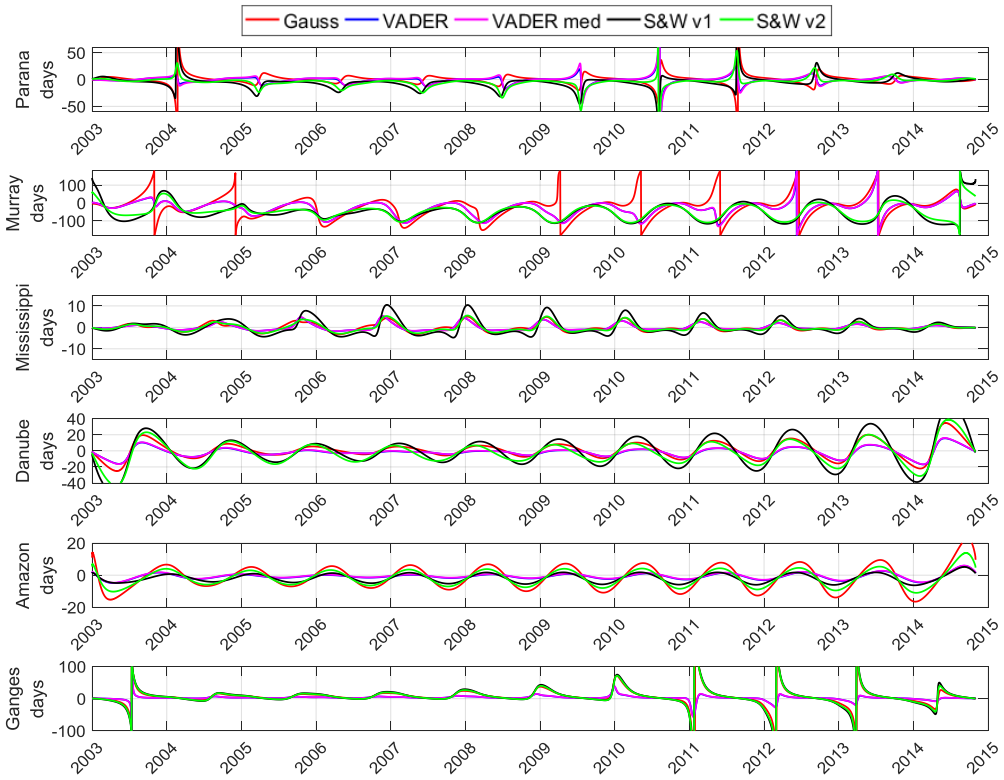

Figure 7-5*: Phase difference in days of estimated signals (6 parameters) between HI and respective post-processing output.

A second effect is the phase of the neighboring basins. In case the phase runs in parallel, a phase shift due to leakage becomes a minor issue. In this scenario the amplitude difference plays a more prominent role. The presence of a significant offset in phase for two neighboring basins can cause, depending on the post-processing method applied, a phase shift due to leakage resulting in a distorted estimate of seasonal signals. For most basins, the largest phase lag can be observed whilst using the Gaussian filter (red curves). The smallest phase lag is observed upon using the VADER filter. Both tested VADER filter versions deliver comparable results. The performance of the S&W filter results is between these two ends. Table 7-5 presents an evaluation of the phase lag per basin and per post-processing method. For comparison the RMS and the mean value of each curve from Figure 7-5 is indicated. The RMS allows evaluating the spread of retrieved results for the phase lag. For all six basins tested, the VADER filter shows best performance. The difference between the two versions is of very small scale. For the mean value, given in brackets, best performance (in terms of smallest value) is achieved by different filter techniques. Nevertheless a RMS of 8.7 days around a mean value of -0.7 days for the VADER filter is

considered to be superior with respect to a RMS of 12.1 days around a mean value of -0.1 days for the Gaussian filter for the Parana River basin example. If a solution exhibits a stable and constant phase shift over time, one can estimate and apply a correction more easily than for a solution with scattering phase shifts.

Table 7-5: RMS and mean value of phase shift in days derived from decadal time series as depicted in Figure 7-5. Mean value in brackets. Unit is days for all values.

River	VADER	VADER med.	S&W v1	S&W v2	Gauss
Parana	**8.7** (-0.7)	9.4 (-0.5)	13.5 (-4.8)	11.6 (-4.2)	12.1 (**-0.1**)
Murray	**48.4** (-28.4)	49.2 (-28.4)	70.2 (-50.3)	62.7 (-48.3)	63.8 (**-22.4**)
Mississippi	**1.4** (<0.1)	**1.4** (<0.1)	3.3 (<0.1)	1.8 (<0.1)	1.8 (<0.1)
Danube	**5.7** (-1.8)	**5.7** (-1.6)	18.6 (**-0.9**)	14.2 (-2.7)	10.2 (1.0)
Amazon	1.9 (-0.7)	**1.8** (**-0.6**)	3.1 (-1.9)	5.1 (-1.7)	7.4 (-1.5)
Ganges	**8.0** (**2.5**)	8.3 (**2.5**)	29.8 (5.8)	28.4 (5.7)	26.5 (5.9)

From the analysis of post-processing performance, a clear advantage using the VADER filter can be deducted. It shows most robust behavior in terms of e.g. the appearance of short repeat cycles (cf. Figure 7-3). Showing the smallest residuals per basin over the whole 143 month sample period indicates best performance in terms of retrieved signal amplitudes (or least attenuation). The phase shift induced by applying the VADER filter as post-processing method is smallest for all basins compared to all other filters tested. Altogether this leads to the conclusion that applying the VADER filter in the context of hydrological analysis for large and medium sized basins delivers the most promising results. The presented analysis suggests encountering only a low risk of misinterpretation of geophysical features due to erroneous shift in amplitude or strong signal attenuation by using the VADER filter.

8. Summary, discussion & outlook

The first part of this last chapter gives a summary of the major findings and results extracted from the work conducted within the framework of this thesis. The second part presents some ideas and considerations on possible amendments of the investigations presented and future experiments to be conducted.

Summary and discussion

The findings regarding the evaluated post-processing methods reveal superior performance of the VADER filter concept. The in-depth analysis in the context of the GRACE mission shows clear advantages with respect to the challenges of real space mission operations. In deep resonance phases or months with inhomogeneous data coverage the VADER filter delivers, due to its non-stationary design, superior results compared to all other filter methods investigated. The availability of full month-to-month error covariance information from an increasing number of GRACE level-2 processing centers allows for applying the VADER filter concept using different time series. One advantage using formal month-to-month error covariance information is the option to perform error propagation throughout the whole filter process not omitting any stochastic information from the original estimate. The analysis of correlation structures within formal error covariance matrices reveals time dependent behavior and evolution. This variability calls for a clear recommendation to use non-stationary filter designs. A relation between orbital geometry and especially SH order dependent patterns of correlations is confirmed. This relation agrees with well described resonances in SH coefficients [Sneeuw 2000; Seo et al. 2008; Murböck et al. 2014], also depending on the SH order.

The question whether the formal error covariance matrices, provided by the GRACE processing centers, are reliable at all, can be answered positively only for some time series. One in this respect positive example is the ITSG-Grace2016 time series. Based on empirical assessments it appears to exhibit realistic errors. Error covariances from other processing centers are identified to exhibit significant deviations between formal and empirically derived estimates.

A relevant result from the application experiments is the reduced attenuation and phase shift of seasonal signals whilst using the VADER filter. Tests for six river basins reveal the smallest phase shift compared to all other filters tested. This is of great importance since using post-processing methods should ideally not alter the target signal to avoid misinterpretation of the estimated signals.

The VADER filter has also a favorable impact on the patterns of post-filter error correlations. It reduces the elongated correlations, especially in along-track direction, significantly. The almost isotropic pattern of the correlations and the reduced correlation length allow applying more simple and confined averaging kernels for retrieving mass balance estimates in the respective target region. The average smoothing radius is, applying the VADER filter, on average shorter than e.g. using a Gaussian filter as post-processing method. This implies a reduction of spatial leakage effects between e.g. river basins.

The design of the closed loop experiments can be considered to be realistic in terms of the error correlation structure of the retrieved error covariance matrices. Accordingly the findings made within the closed loop experiments are rated to be a realistic proxy for real world applications.

The transfer of the processing strategies evaluated for the GRACE mission to future mission scenarios shows again superior performance for the VADER filter. Due to its adaptability, attributable to the use of full month-to-month error covariance matrices, it can not only be applied in single pair, but also in double pair scenarios without major modifications. With respect to the GRACE-FO mission, direct applicability of the VADER filter concept without modifications can be expected.

An important finding in the context of the double pair scenarios, independent of the respective post-processing method applied, is the performance gain in terms of retrieved signal in the polar areas, not covered by the inclined pair, while operating in double pair mode. The presence of the second pair is identified to stabilize and improve the solution globally. The overall error level is also drastically reduced by introducing a second inclined pair. The error correlation patterns derived from the formal error covariance matrices show significantly shorter error correlation lengths compared to a single pair scenario. In addition to the reduction of correlation length they also exhibit almost isotropic behavior compared to the elongated strip-like pattern in along-track direction for the single polar pair. This behavior is expected to result in lower filter strength necessary to extract target signals from future missions.

Outlook and future experiments

For the assessment of the VADER filter, error covariance matrices have been evaluated in detail, showing variability of error correlation patterns between different time series. Since other than the spherical harmonics representations of GRACE time variable gravity field solutions are used as well, a detailed comparison of the error correlation patterns, especially of mascon solutions, is an interesting, but still open question. Extending the simulation environment to the mascon parameterization would allow assessing strong and weak points of the respective solutions. To extend the closed loop simulation environment by implementing a parametrization to derive mascon solutions from the acceleration differences would be the next step to assess the potential of the different parameterization methods on a broader scale.

For the averaging function in the case study of Antarctica, only relatively simple assumptions regarding leakage have been fed into the design of the function. Amending the approach of estimating averaging functions, described by e.g. Groh and Horwath [2016], built on high resolution approximations of mass change signals to account for leakage by incorporating error correlation patterns is a promising further development. Since the month-to-month formal error covariance matrices of e.g. the ITSG-Grace2016 time series show realistic errors, not only the impact of static or empirical estimates of the error correlation patterns, but also time variable patterns, depending on the quality of the monthly GRACE solution, call for investigation of building averaging functions. Such refinements of the averaging functions are considered necessary to allow more robust mass change estimates on the scale of individual small and medium sized drainage basins (cf. Figure A 5) in e.g. the region of Antarctica.

The favorably small impact on amplitudes and phase of hydrological signals by the VADER filter approach in the closed loop environment is waiting to be evaluated in real data experiments. A validation of the filter performance, comparing the results with up-to-date independent datasets, can serve as basis for a broader inclusion of GRACE for hydrological studies of not only large scale, but also medium and small scale effects and phenomena. The performance of the VADER filter can be understood as shifting the performance curves of the GRACE mission indicated in Figure 4-1 towards smaller signals and finer scales, thus resolving a larger proportion of the geophysical phenomena.

Further investigations in order to derive tailored regularization designs towards respective target regions with dominating target signals are advisable. This means e.g. applying a different filter

strength (steered by different signal variances) and filter design for retrieving ice mass change in polar and near-polar regions than for retrieving hydrological variations in low latitude and equatorial regions.

An important investigation with respect to future mission double pair scenarios is the evaluation of post-processing methods in realistic scenarios. In such scenarios the mission operations are disturbed from the nominal state by encountering outages of either the inclined or polar pair, appearance of short repeat phases of the orbital configuration, or significant data gaps (not providing even data coverage). As the VADER filter is adaptive to changing environments, a better understanding of the capabilities and limits of performance is necessary for deriving sound and consistent time series. Especially the filter performance at the margins between double and single pair coverage is an interesting area to assess since e.g. drainage basins in Greenland are located at or near such zones.

As mentioned in the context of the temporal aliasing problem (cf. section 2.5), a co-parameterization of geophysical signals is a promising way to pursue. Some processing centers co-estimate time variable signals up to a certain SH degree on e.g. daily basis to improve the stability of their monthly solutions. Changing the parameterization within the closed loop environment towards the co-estimation of trend parameters is an interesting experiment. One can study the correlations between constant and variable part and one can assess the strong and weak points of post-processing with subsequent trend parameter estimation versus directly co-estimating trend parameters while estimating the gravity field solution itself.

Appendix

Formal and empirical errors from formal and empirical covariance matrices for the GRACE time series ITSG-Grace2014, CSR-RL05, and GFZ-RL5a.

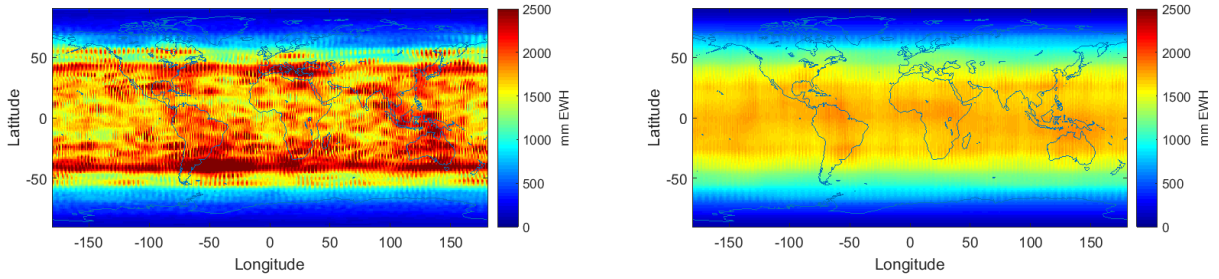

Figure A 1: Empirical (left) and formal (right; 2004-04) errors from the ITSG-Grace2014 time series.

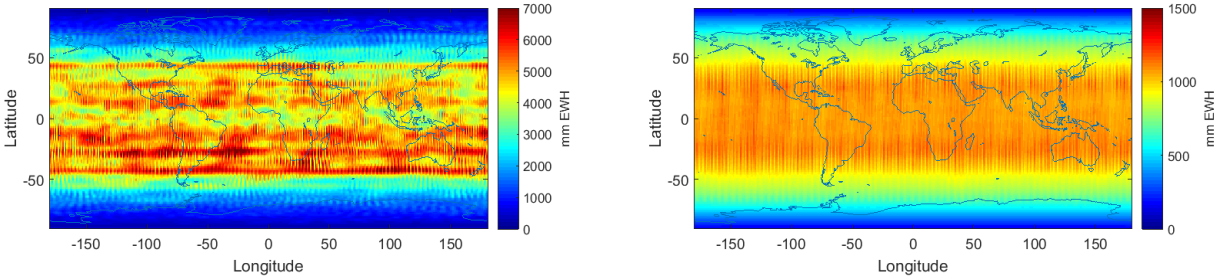

Figure A 2: Empirical (left) and formal (right; 2004-04) errors from the GFZ-RL5a time series.

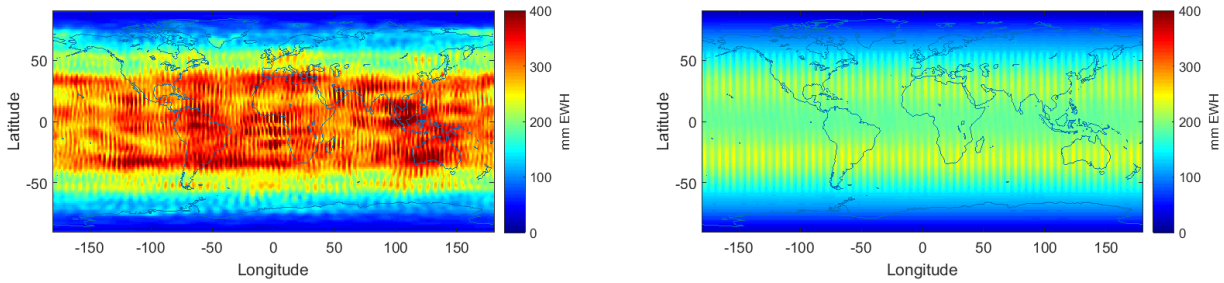

Figure A 3: Empirical (left) and formal (right; 2004-06) errors from the CSR60 RL05 time series.

Formal and empirical errors displayed in Figure A 1 to Figure A 3 show as mentioned in chapter 4.3.2 larger differences than visible for the results originating from the ITSG-Grace2016 series. Please note the use of different limits for the colorbar in Figure A 2 between left and right panel for better readability.

Map of Antarctica illustrating the different regions East and West Antarctica, the Antarctic Peninsula and other regions including major lakes and research station.

Figure A 4: Map of Antarctica (courtesy of the LIMA project, US Department of the Interior, US Geological Service) http://lima.usgs.gov/documents/LIMA_overview_map.pdf, last access: 23.09.2016)

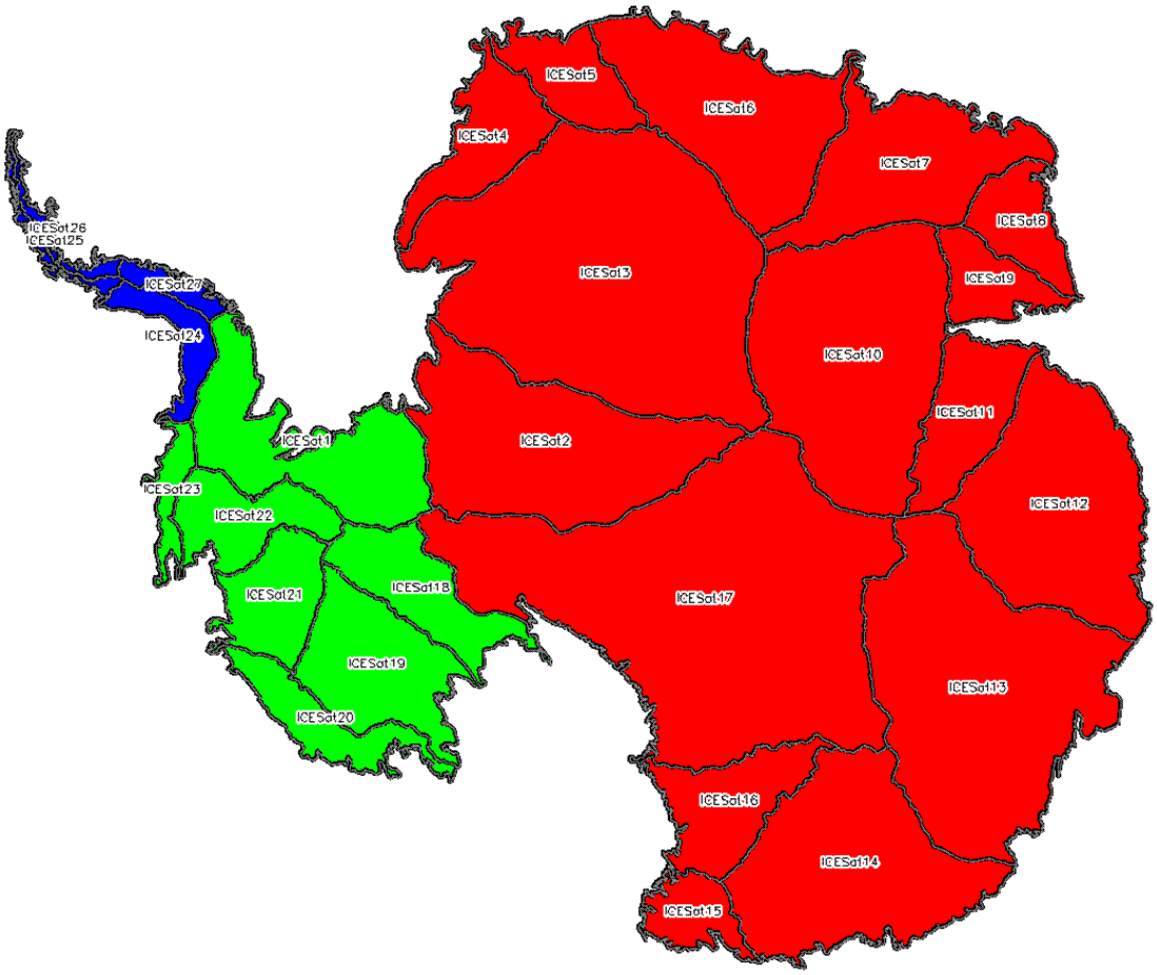

Figure A 5: Regional integration basins 1 to 27 forming the Antarctic Ice Sheet (AIS) after Zwally and Giovinetto [2011]. Red basins belong to the region of East Antarctica (EAIS), green basins to West Antarctica (WAIS), and blue basins to the Antarctic Peninsula (AP).

Source: http://homepages.see.leeds.ac.uk/~earkhb/Drainage_sectorsZ_img_large.html (last access: 23.09.2016)

List of tables

List of figures

Bibliography

Altamimi, Z.; Collilieux, X.; Métivier, L. (2011): ITRF2008: an improved solution of the international terrestrial reference frame. In: *J Geod* 85 (8), p. 457–473. DOI: 10.1007/s00190-011-0444-4.

Balsamo, G.; Albergel, C.; Beljaars, A.; Boussetta, S.; Brun, E.; Cloke, H.; Dee, D.; Dutra, E.; Muñoz-Sabater, J.; Pappenberger, F.; Rosnay, P. de; Stockdale, T.; Vitart, F. (2015): ERA-Interim/Land: a global land surface reanalysis data set. In: *Hydrol. Earth Syst. Sci.* 19 (1), p. 389–407. DOI: 10.5194/hess-19-389-2015.

Barletta, V. R.; Sørensen, L. S.; Forsberg, R. (2013): Scatter of mass changes estimates at basin scale for Greenland and Antarctica. In: *The Cryosphere* 7 (5), p. 1411–1432. DOI: 10.5194/tc-7-1411-2013.

Bettadpur, S. (2012): GRACE 327-742 UTCSR Level-2 Processing Standards Document. For Level-2 Product Release 0005. CSR - The University of Texas at Austin. Online available: ftp://podaac.jpl.nasa.gov/allData/grace/docs/L2-CSR0005_ProcStd_v4.0.pdf, last accessed 11.09.2016.

Blewitt, G. (2003): Self-consistency in reference frames, geocenter definition, and surface loading of the solid Earth. In: *J. Geophys. Res.* 108 (B2). DOI: 10.1029/2002JB002082.

Bloßfeld, M.; Müller, H.; Gerstl, M.; Štefka, V.; Bouman, J.; Göttl, F.; Horwath, M. (2015): Second-degree Stokes coefficients from multi-satellite SLR. In: *J Geod* 89 (9), p. 857–871. DOI: 10.1007/s00190-015-0819-z.

Bouman, J. (1998): Quality of regularization methods. Delft: Delft University Press (DEOS report, no. 98.2). Online available: http://resolver.tudelft.nl/uuid:3d6c4f81-92fc-434a-b84c-89708c09d305, last accessed 02.09.2016.

Bruinsma, S.; Lemoine, J.-M.; Biancale, R.; Valès, N. (2010): CNES/GRGS 10-day gravity field models (release 2) and their evaluation. In: *Advances in Space Research* 45 (4), p. 587–601. DOI: 10.1016/j.asr.2009.10.012.

Butterworth, S. (1930): Theory of filter amplifiers. In: *Experimental wireless & the wireless engineer* (October), p. 536–541.

Cazenave, A.; Dominh, K.; Guinehut, S.; Berthier, E.; Llovel, W.; Ramillien, G.; Ablain, M.; Larnicol, G. (2009): Sea level budget over 2003–2008: A reevaluation from GRACE space gravimetry, satellite altimetry and Argo. In: *Global and Planetary Change* 65 (1-2), p. 83–88. DOI: 10.1016/j.gloplacha.2008.10.004.

Chambers, D. P. (2006a): Evaluation of new GRACE time-variable gravity data over the ocean. In: *Geophys. Res. Lett.* 33 (17). DOI: 10.1029/2006GL027296.

Chambers, D. P. (2006b): Observing seasonal steric sea level variations with GRACE and satellite altimetry. In: *J. Geophys. Res.* 111 (C3). DOI: 10.1029/2005JC002914.

Chambers, D. P. and Bonin, J. A. (2012): Evaluation of Release-05 GRACE time-variable gravity coefficients over the ocean. In: *Ocean Science* 8 (5), p. 859–868.

Cheng, M. K. and Ries, J. C. (2016): Monthly estimates of C20 from 5 SLR satellites based on GRACE RL05 models (GRACE Technical Note 07). Online available: ftp://podaac.jpl.nasa.gov/allData/grace/docs/TN-07_C20_SLR.txt, last accessed 11.09.2016.

Cheng, M. K.; Ries, J. C.; Tapley, B. D. (2013a): Geocenter Variations from Analysis of SLR Data. In: Z. Altamimi; X. Collilieux (Eds.): Reference Frames for Applications in Geosciences, Vol. 138. Berlin, Heidelberg: Springer Berlin Heidelberg (International Association of Geodesy Symposia), p. 19–25.

Cheng, M. K. and Tapley, B. D. (2004): Variations in the Earth's oblateness during the past 28 years. In: *J. Geophys. Res.* 109 (B9). DOI: 10.1029/2004JB003028.

Cheng, M. K.; Tapley, B. D.; Ries, J. C. (2013b): Deceleration in the Earth's oblateness. In: *J. Geophys. Res. Solid Earth* 118 (2), p. 740–747. DOI: 10.1002/jgrb.50058.

Dahle, C. (2014): Release Notes for GFZ GRACE Level-2 Products - version RL05. GFZ Potsdam. Online available: http://isdc.gfz-potsdam.de/index.php?name=UpDownload&req=getit&lid=574.

Dahle, C.; Flechtner, F.; Gruber, C.; König, D.; König, R.; Michalak, G.; Neumayer, K. (2012): GFZ GRACE Level-2 Processing Standards Document for Level-2 Product Release 0005. Revised Edition, January 2013. GFZ Potsdam. Potsdam (Scientific Technical Report, STR12/02).

Daras, I. (2016): Gravity field processing towards future LL-SST satellite missions (Deutsce Geodätische Kommission der Bayerischen Akademie der Wissenschaften / Reihe C, Dissertatonen, 770). Online available: https://dgk.badw.de/fileadmin/user_upload/Files/DGK/docs/c-770.pdf, last accessed 25.11.2016.

Daras, I.; Pail, R.; Visser, P.; Weigelt, M.; Iran Pour, S.; Murböck, M.; Gruber, Th.; Teixera da Encarnacao, J.; Sneeuw, N.; Tonetti, S.; Siemes, C.; van den IJssel, J.; Cornara, S.; van Dam, T.; Cesare, S.; Haagmans, R. (2015): Temporal aliasing effects on future gravity satellite missions and their assessment. Lessons from the ESA-SC4MGV project. EGU General Assembly 2015. European Geoscience Union. Wien, 14.04.2015. Online available: http://meetingorganizer.copernicus.org/EGU2015/EGU2015-10992-1.pdf, last accessed 27.11.2016.

Devaraju, B. (2015): Understanding filtering on the sphere. Experiences from filtering GRACE data. München: Verlag der Bayerischen Akademie der Wissenschaften (Deutsche Geodätische Kommission der Bayerischen Akademie der Wissenschaften : Reihe C, Dissertationen, Heft Nr. 756).

Devaraju, B. and Sneeuw, N. (2016): On the Spatial Resolution of Homogeneous Isotropic Filters on the Sphere. In: N. Sneeuw, P. Novák, M. Crespi und F. Sansò (Eds.): VIII Hotine-Marussi Symposium on Mathematical Geodesy, Vol. 142. Cham: Springer International Publishing (International Association of Geodesy Symposia), p. 67–73.

Dobslaw, H.; Bergmann-Wolf, I.; Dill, R.; Forootan, E.; Klemann, V.; Kusche, J.; Sasgen, I. (2015a): The updated ESA Earth System Model for future gravity mission simulation studies. In: *J Geod* 89 (5), p. 505–513. DOI: 10.1007/s00190-014-0787-8.

Dobslaw, H.; Bergmann-Wolf, I.; Dill, R.; Forootan, E.; Klemann, V.; Kusche, J.; Sasgen, I. (2015b): The Updated ESA Earth System Model for Future Gravity Mission Simulation Studies. In: *GFZ German Research Centre for Geosciences. DOI:* 10.5880/GFZ.1.3.2014.001.

Dong, D.; Dickey, J. O.; Chao, Y.; Cheng, M. K. (1997): Geocenter variations caused by atmosphere, ocean and surface ground water. In: *Geophys. Res. Lett.* 24 (15), p. 1867–1870. DOI: 10.1029/97GL01849.

Dunn, C.; Bertiger, W.; Bar-Sever, Y.; Desai, S.; Haines, B.; Kuang, D.; Franklin, G.; Harris, I.; Kruizinga, G.; Meehan, T.; Nandi, S.; Nguyen, D.; Rogstad, T.; Thomas, JB.; Tien, J.; Romans, L.; Watkins, M.; Wu, SC.; Bettadpur, S.; Kim, J. (2003): Instrument of Grace:GPS augments gravity measurements. In: *GPS World* (14), p. 16–28.

Eicker, A.; Forootan, E.; Springer, A.; Longuevergne, L.; Kusche, J. (2016): Does GRACE see the terrestrial water cycle "intensifying"? In: *J. Geophys. Res. Atmos.* 121 (2), p. 733–745. DOI: 10.1002/2015JD023808.

ESA (1999): Gravity Field and Steady-State Ocean Circulation Mission. ESA Publications Division. ESTEC, Noordwijk, The Netherlands (Special Publication, 1233(1)).

ESA (2010): Assessment of a next generation mission for monitoring the variations of earth's gravity. Final Report. ESTEC Contract No. 22643/09/NL/AF. Online available: http://emits.esa.int/emits-doc/ESTEC/AO7317_RD4-NGGM_FinalReport_Issue2.pdf, last accessed 15.09.2016.

ESA (2011): Assessment of a next generation gravity mission to monitor the variations of earth's gravity field. Final Report. ESTEC Contract No. 22672/09/NL/AF. Online available: http://emits.esa.int/emits-doc/ESTEC/AO7317_RD5-Final_Report_Issue_1_w_ESA_dissemination_rights.pdf, last accessed 15.09.2016.

Famiglietti, J. S.; Lo, M.; Ho, S. L.; Bethune, J.; Anderson, K. J.; Syed, T. H.; Swenson, S. C.; de Linage, C. R.; Rodell, M. (2011): Satellites measure recent rates of groundwater depletion in California's Central Valley. In: *Geophys. Res. Lett.* 38 (3). DOI: 10.1029/2010GL046442.

Farrell, W. E. (1972): Deformation of the Earth by surface loads. In: *Rev. Geophys.* 10 (3), p. 761. DOI: 10.1029/RG010i003p00761.

Flechtner, F.; Dobslaw, H.; Fagiolini, E. (2015): AOD1B Product Description Document for Product Release 05. GRACE 327-750. Rev. 4.3, April 23, 2015. GFZ Potsdam. Potsdam. Online available: http://www.gfz-potsdam.de/fileadmin/gfz/sec12/pdf/GRACE/AOD1B/AOD1B_20150423.pdf, last accessed 03.10.2016.

Flechtner, F.; Neumayer, K.-H.; Dahle, C.; Dobslaw, H.; Fagiolini, E.; Raimondo, J.-C.; Güntner, A. (2016a): What Can be Expected from the GRACE-FO Laser Ranging Interferometer for Earth Science Applications? In: *Surv Geophys* 37 (2), p. 453–470. DOI: 10.1007/s10712-015-9338-y.

Flechtner, F.; Webb, F.; Watkins, M.; Bettadpur, S.; Landerer, F.; Grunwaldt, L.; Dahle, C. (2016b): Status of the GRACE Follow-On Mission. GRACE Science Team Meeting. GFZ Potsdam. Potsdam, 05.10.2016.

Ghelichkhan, S.; Murböck, M.; Colli, R.; Pail, R.; Bunge, H. P. (submitted 2016): On the observability of epeirogenic movement in current and future gravity missions. In: *Gondwana Research (Special Issue: Rifting to Passive Margins)*.

Goiginger, H.; Rieser, D.; Mayer-Guerr, T.; Pail, R.; Schuh, W.-D.; Jäggi, A.; Maier, A.; GOCO Consortium (2011): The combined satellite-only global gravity field model GOCO02S. EGU General Assembly 2011. European Geoscience Union. Wien, 04.04.2011. Online available: http://www.goco.eu/data/egu2011-10571-goco02s.pdf, last accessed 24.07.1016.

Groh, A.; Ewert, H.; Rosenau, R.; Fagiolini, E.; Gruber, C.; Floricioiu, D.; Abdel Jaber, W.; Linow, S.; Flechtner, F.; Eineder, M.; Dierking, W.; Dietrich, R. (2014): Mass, Volume and Velocity of the Antarctic Ice Sheet: Present-Day Changes and Error Effects. In: *Surv Geophys* 35 (6), p. 1481–1505. DOI: 10.1007/s10712-014-9286-y.

Groh, A. and Horwath, M. (2016): The method of tailored sensitivity kernels for GRACE mass change estimates. EGU General Assembly 2016. Wien, 18.04.2016. Online available: http://presentations.copernicus.org/EGU2016-12065_presentation.pdf, last accessed 14.10.2016.

Gruber, T. (2000): Hochauflösende Schwerefeldbestimmung aus Kombination von terrestrischen Messungen und Satellitendaten über Kugelfunktionen. GFZ Potsdam. Potsdam (Scientific Technical Report, STR 00/16).

Gruber, T.; Bamber, J. L.; Bierkens, M. F. P.; Dobslaw, H.; Murböck, M.; Thomas, M.; van Beek, L. P. H.; van Dam, T.; Vermeersen, L. L. A.; Visser, P. N. A. M. (2011): Simulation of the time-variable gravity field by means of coupled geophysical models. In: *Earth Syst. Sci. Data Discuss.* 4 (1), p. 27–70. DOI: 10.5194/essdd-4-27-2011.

Gruber, T.; Murböck, M.; NGGM-D Team (2014): e².motion. Earth System Mass Transport Mission (Square) - Concept for a Next Generation Gravity Field Mission - Final Report "Satellite Gravimetry of the Next Generation (NGGM-D"). München: Beck (Deutsche Geodätische Kommission bei der Bayerischen Akademie der Wissenschaften : Reihe B, Angewandte Geodäsie, 318).

Gruber, T.; Murböck, M.; Pail, R.; Daras, I. (2016): Earth System Mass Transport Mission 2 e.motion2 - Proposal for an Earth Explorer 9 Mission. AOGS 13th Annual Meeting. Asia Oceania Geoscience Society. Peking, China, 03.08.2016. Online available: http://www.iapg.bgu.tum.de/mediadb/10361992/10361993/20160803_Gruber_emotion2.pdf , last accessed 21.10.2016.

Gunter, B. C.; Didova, O.; Riva, R. E. M.; Ligtenberg, S. R. M.; Lenaerts, J. T. M.; King, M. A.; van den Broeke, M. R.; Urban, T. (2014): Empirical estimation of present-day Antarctic glacial isostatic adjustment and ice mass change. In: *The Cryosphere* 8 (2), p. 743–760. DOI: 10.5194/tc-8-743-2014.

Han, S.-C.; Jekeli, C.; Shum, C. K. (2004): Time-variable aliasing effects of ocean tides, atmosphere, and continental water mass on monthly mean GRACE gravity field. In: *J. Geophys. Res.* 109 (B4). DOI: 10.1029/2003JB002501.

Han, S.-C.; Shum, C. K.; Jekeli, C.; Kuo, C.-Y.; Wilson, C.; Seo, K.-W. (2005): Non-isotropic filtering of GRACE temporal gravity for geophysical signal enhancement. In: *Geophysical Journal International* 163 (1), p. 18–25. DOI: 10.1111/j.1365-246X.2005.02756.x.

Hauk, M.; Schlicht, A.; Pail, R.; Murböck, M. (submitted 2016): Gravity field recovery in the framework of a Geodesy and Time Reference in Space (GETRIS). In: *Advances in Space Research*.

Heiskanen, W. A.; Moritz, H. (1967): Physical Geodesy. San Francisco, USA: W. H. Freeman and Company.

Horwath, M. (2008): Zur Ermittlung geophysikalischer Massensignale mit Schwerefeldmissionen: Eine Analyse des gegenwärtigen Standes am Beispiel der Antarktis. Dresden: Technische Universität Dresden (Dissertation).

Horwath, M. and Dietrich, R. (2009): Signal and error in mass change inferences from GRACE: the case of Antarctica. In: *Geophysical Journal International* 177 (3), p. 849–864. DOI: 10.1111/j.1365-246X.2009.04139.x.

Horwath, M.; Horvath, A.; Pail, R.; Peterseim, N. (2013a): Signal and error content in different Release-05 monthly solution series, with applications to polar regions. Poster. GRACE Science Team Meeting. Austin, Texas, 23.10.2013.

Horwath, M.; Legrésy, B.; Rémy, F.; Blarel, F.; Lemoine, J.-M. (2012): Consistent patterns of Antarctic ice sheet interannual variations from ENVISAT radar altimetry and GRACE satellite gravimetry. In: *Geophysical Journal International* 189 (2), p. 863–876. DOI: 10.1111/j.1365-246X.2012.05401.x.

Horwath, M.; Pail, R.; Rexer, M.; Horvath, A.; Sasgen, I.; van der Broeke, M. (2013b): Exploiting Satellite Gravimetry for Glacial Isostatic Adjustment and Ice Mass Trends in Antarctica (STSE Project REGINA). Poster. ESA Living Planet Symposium. Edinburgh, 10.09.2013.

Iran Pour, S.; Sneeuw, N.; Daras, I.; Pail, R.; Murböck, M.; Gruber, T.; Tonetti, S.; Cornara, S.; Weigelt, M.; van Dam, T.; Visser, P.; Teixera da Encarnacao, J.; Cesare, S. (2015): Assessment of Satellite Constellations for Monitoring the Variations in Earth Gravity Field "SC4GM". Final Report. ESA - ESTEC Contract No. AO/1-7317/12/NL/AF.

Ivins, E. R. and James, T. S. (2005): Antarctic glacial isostatic adjustment: a new assessment. In: *Antarctic Science* 17 (04), p. 541. DOI: 10.1017/S0954102005002968.

Jekeli, C. (1981): Alternative methods to smooth the earth's gravity field. Columbus, Ohio: Ohio State University Dept. of Geodetic Science and Surveying (Reports of the Department of Geodetic Science, no. 327).

Kandel, R. S. (1980): Earth and cosmos. A book relating the environment of man on earth to the environment of earth in the cosmos. Oxford, New York: Pergamon Press (Pergamon international library of science, technology, engineering, and social studies).

Kaula, W. M. (1966): Theory of Satellite Geodesy. Toronto: Blaisdell.

King, M. A.; Bingham, R. J.; Moore, P.; Whitehouse, P. L.; Bentley, M. J.; Milne, G. A. (2012): Lower satellite-gravimetry estimates of Antarctic sea-level contribution. In: *Nature* 491 (7425), p. 586–589. DOI: 10.1038/nature11621.

Klees, R.; Revtova, E. A.; Gunter, B. C.; Ditmar, P.; Oudman, E.; Winsemius, H. C.; Savenije, H. H. G. (2008): The design of an optimal filter for monthly GRACE gravity models. In: *Geophysical Journal International* 175 (2), p. 417–432. DOI: 10.1111/j.1365-246X.2008.03922.x.

Klinger, B. and Mayer-Gürr, T. (2016): The role of accelerometer data calibration within the ITSG-Grace2016 release: impact on C20 coefficients. GRACE Science Team Meeting. GFZ Potsdam. Potsdam, 06.10.2016.

Klinger, B.; Mayer-Gürr, T.; Behzadpour, S.; Ellmer, M.; Kvas, A.; Zehentner, N. (2016): The new ITSG-Grace2016 release. EGU General Assembly 2016. European Geoscience Union. Wien, 20.04.2016.

Koch, K.-R. (1987): Parameterschätzung und Hypothesentests in linearen Modellen. 2., bearb. u. erw. Aufl. Bonn: Dümmler (Dümmlerbuch, 7892).

Kruizinga, A. (2015): CSR Release-05 GRACE Level-2 Data Products. CSR - The University of Texas at Austin. Online available: http://www.csr.utexas.edu/grace/RL05.html, last accessed 13.10.2016.

Kruizinga, A. (2016): Geocenter motion derived from SLR. CSR - The University of Texas at Austin. Online available: ftp://ftp.csr.utexas.edu/pub/slr/geocenter/GCN_L1_L2_60d.png, last accessed 20.10.2016.

Kurtenbach, E. (2011): Entwicklung eines Kalman-Filters zur Bestimmung kurzzeitiger Variationen des Erschwerefeldes aus Daten der Satellitenmission GRACE. Dissertation. Bonn: IGG Universität Bonn (Schriftenreihe / Institut für Geodäsie und Geoinformation, 24).

Kusche, J. (2007): Approximate decorrelation and non-isotropic smoothing of time-variable GRACE-type gravity field models. In: *J Geod* 81 (11), p. 733–749. DOI: 10.1007/s00190-007-0143-3.

Kusche, J.; Eicker, A.; Forootan, E.; Springer, A.; Longuevergne, L. (2016): Mapping probabilities of extreme continental water storage changes from space gravimetry. In: *Geophys. Res. Lett.* 43 (15), p. 8026–8034. DOI: 10.1002/2016GL069538.

Kusche, J.; Schmidt, R.; Petrovic, S.; Rietbroek, R. (2009): Decorrelated GRACE time-variable gravity solutions by GFZ, and their validation using a hydrological model. In: *J Geod* 83 (10), p. 903–913. DOI: 10.1007/s00190-009-0308-3.

Lambeck, K. (1988): Geophysical geodesy. The slow deformations of the earth. Oxford [England], New York: Clarendon Press; Oxford University Press (Oxford science publications).

Landerer, F. W. and Swenson, S. C. (2012): Accuracy of scaled GRACE terrestrial water storage estimates. In: *Water Resour. Res.* 48 (4). DOI: 10.1029/2011WR011453.

Lenaerts, J.; Van den Broeke, M.; van de Berg, W.; van Meijgaard, E.; Kuipers Munneke, P. (2012): A new, high-resolution surface mass balance map of Antarctica (1979-2010) based on regional atmospheric climate modeling. In: *Geophys. Res. Lett.* 39 (4). DOI: 10.1029/2011GL050713.

Liu, X. (2008): Global gravity field recovery from satellite-to-satellite tracking data with the acceleration approach. doctoral thesis. TU Delft, Delft, The Netherlands. Online available: http://resolver.tudelft.nl/uuid:af1f1ad0-2066-48e0-949a-6b17291c111d, last accessed 16.09.2016.

Liu, X.; Ditmar, P.; Siemes, C.; Slobbe, D. C.; Revtova, E.; Klees, R.; Riva, R.; Zhao, Q. (2010): DEOS Mass Transport model (DMT-1) based on GRACE satellite data: methodology and validation. In: *Geophysical Journal International. DOI:* 10.1111/j.1365-246X.2010.04533.x.

Loomis, B. D.; Nerem, R. S.; Luthcke, S. B. (2012): Simulation study of a follow-on gravity mission to GRACE. In: *J Geod* 86 (5), p. 319–335. DOI: 10.1007/s00190-011-0521-8.

Louis, A. K. (1989): Inverse und schlecht gestellte Probleme. Stuttgart: B.G. Teubner (Teubner Studienbücher. Mathematik).

Lyard, F.; Lefevre, F.; Letellier, T.; Francis, O. (2006): Modelling the global ocean tides: modern insights from FES2004. In: *Ocean Dynamics* 56 (5-6), p. 394–415. DOI: 10.1007/s10236-006-0086-x.

Mayer-Gürr, T.; Behzadpour, S.; Ellmer, M.; Kvas, A.; Klinger, B.; Zehentner, N. (2016a): ITSG-Grace2016 - Monthly and Daily Gravity Field Solutions from GRACE. GFZ Data Services. DOI: 10.5880/icgem.2016.007.

Mayer-Gürr, T.; Klinger, B.; Kvas, A.; Zehentner, N.; Ellmer, M.; Behzadpour, S. (2016b): Insights into the ITSG-Grace2016 processing. GRACE Science Team Meeting. GFZ Potsdam. Potsdam, 06.10.2016.

Mayer-Gürr, T.; Zehentner, N.; Klinger, B.; Kvas, A. (2014): ITSG-Grace2014: a new GRACE gravity field release computed in Graz. GRACE Science Team Meeting. GFZ Potsdam. Potsdam, 29.09.2014.

McMillan, M.; Shepherd, A.; Gourmelen, N.; Dehecq, A.; Leeson, A.; Ridout, A.; Flament, T.; Hogg, A.; Gilbert, L.; Benham, T.; van den Broeke, M. R.; Dowdeswell, J. A.; Fettweis, X.; Noël, B.; Strozzi, T. (2014): Rapid dynamic activation of a marine-based Arctic ice cap. In: *Geophys. Res. Lett.* 41 (24), p. 8902–8909. DOI: 10.1002/2014GL062255.

Metzler, B. (2007): Spherical Cap Regularization - A spatially restricted Regularization Method Tailored to the Polar Gap Problem. Dissertation. TU Graz, Graz.

Morelli, A. and Danesi, S. (2004): Seismological imaging of the Antarctic continental lithosphere: a review. In: *Global and Planetary Change* 42 (1-4), p. 155–165. DOI: 10.1016/j.gloplacha.2003.12.005.

Murböck, M. (2015): Virtual constellations of next generation gravity missions. Techn. Univ., Diss.--München, 2015. Online available: http://nbn-resolving.de/urn/resolver.pl?urn:nbn:de:bvb:91-diss-20150619-1241150-1-7.

Murböck, M.; Horvath, A.; Pail, R. (2016): Correlation analysis of GRACE gravity field models. GRACE Science Team Meeting. GFZ Potsdam. Potsdam, 2016. Online available: https://media.gfz-potsdam.de/gfz/sec12/GSTM-2016/GSTM2016-A1.zip, last accessed 23.11.2016.

Murböck, M.; Pail, R.; Daras, I.; Gruber, T. (2014): Optimal orbits for temporal gravity recovery regarding temporal aliasing. In: *J Geod* 88 (2), p. 113–126. DOI: 10.1007/s00190-013-0671-y.

Nagler, T.; Horwath, M.; Groh, A.; Horvath, A.; Shepherd, A.; Antarctic Ice Sheet CCI Project Team (2016): Comprehensive Error Characterisation Report. Collaborators: Antarctic Ice Sheet CCI Project. ESA. Online available: https://data1.geo.tu-

dresden.de/ais_gmb/source/ST-UL-ESA-AISCCI-CECR-Draft_GMB.pdf, last accessed 28.10.2016.

Niemeier, W. (2002): Ausgleichungsrechnung. Eine Einführung für Studierende und Praktiker des Vermessungs- und Geoinformationswesens. Berlin, New York: De Gruyter (De-Gruyter-Lehrbuch).

Pail, R.; Bingham, R. J.; Braitenberg, C.; Dobslaw, H.; Eicker, A.; Güntner, A.; Horwath, M.; Ivins, E. R.; Longuevergne, L.; Panet, I.; Wouters, B. (2015): Science and User Needs for Observing Global Mass Transport to Understand Global Change and to Benefit Society. In: *Surv Geophys* 36 (6), p. 743–772. DOI: 10.1007/s10712-015-9348-9.

Panet, I.; Flury, J.; Biancale, R.; Gruber, T.; Johannessen, J.; van den Broeke, M. R.; van Dam, T.; Gegout, P.; Hughes, C. W.; Ramillien, G.; Sasgen, I.; Seoane, L.; Thomas, M. (2013): Earth System Mass Transport Mission (e.motion): A Concept for Future Earth Gravity Field Measurements from Space. In: *Surv Geophys* 34 (2), p. 141–163. DOI: 10.1007/s10712-012-9209-8.

Pellinen, L. P. (1966): A method for expanding the gravity potential of the Earth in spherical harmonics. Hg. v. Trans Central Scientific Res Inst Geodesy, Aereal Survey and Cartography. Nedra, Moscow (171).

Peltier, W. R. (1983): Constraint on deep mantle viscosity from Lageos acceleration data. In: *Nature* 304 (5925), p. 434–436. DOI: 10.1038/304434a0.

Peltier, W. R. (2004): Global Glacial Isostasy and the Surface of the Ice-Age Earth: The ICE-5G (VM2) Model and GRACE. In: *Annu. Rev. Earth Planet. Sci.* 32 (1), p. 111–149. DOI: 10.1146/annurev.earth.32.082503.144359.

Peltier, W. R.; Argus, D. F.; Drummond, R. (2015): Space geodesy constrains ice age terminal deglaciation: The global ICE-6G_C (VM5a) model. In: *J. Geophys. Res. Solid Earth* 120 (1), p. 450–487. DOI: 10.1002/2014JB011176.

Peters, T. (2007): Modellierung zeitlicher Schwerevariationen und ihre Erfassung mit Methoden der Satellitengravimetrie. Techn. Univ., Diss--München, 2007. Online available: http://mediatum2.ub.tum.de/doc/620905/document.pdf.

Ray, R. D.; Rowlands, D. D.; Egbert, G. D. (2003): Tidal Models in a New Era of Satellite Gravimetry. In: *Space Science Reviews* 108 (1), p. 271–282. DOI: 10.1023/A:1026223308107.

Reager, J. T.; Thomas, B. F.; Famiglietti, J. S. (2014): River basin flood potential inferred using GRACE gravity observations at several months lead time. In: *Nature Geosci* 7 (8), p. 588–592. DOI: 10.1038/ngeo2203.

Reigber, C.; Balmino, G.; Schwintzer, P.; Biancale, R.; Bode, A.; Lemoine, J.-M.; König, R.; Loyer, S.; Neumayer, H.; Marty, J.-C.; Barthelmes, F.; Perosanz, F.; Zhu, S. Y. (2002): A high-quality global gravity field model from CHAMP GPS tracking data and accelerometry (EIGEN-1S). In: *Geophys. Res. Lett.* 29 (14), p. 37.1–37.4. DOI: 10.1029/2002GL015064.

Reigber, C.; Schwintzer, P.; Lühr, H. (1999): The CHAMP geopotential mission. In: *Bollettino di Geofisica Teoretica ed Applicata* 40 (3-4), p. 285–289.

Rietbroek, R. (2015): Visualized DDK kernels, 04.12.2015. ftp://skylab.itg.uni-bonn.de/roelof/DDK/Visualized_DDKkernels.pdf.

Rignot, E.; Jacobs, S.; Mouginot, J.; Scheuchl, B. (2013): Ice-shelf melting around Antarctica. In: *Science (New York, N.Y.)* 341 (6143), p. 266–270. DOI: 10.1126/science.1235798.

Rignot, E.; Mouginot, J.; Scheuchl, B. (2011): Antarctic grounding line mapping from differential satellite radar interferometry. In: *Geophys. Res. Lett.* 38 (10). DOI: 10.1029/2011GL047109.

Riva, R. E. M.; Gunter, B. C.; Vermeersen, B.; Lindenbergh, R. C.; Helsen, M. M.; Bamber, J. L.; van de Wal, R. S. W.; van den Broeke, M. R.; Schutz, B. E. (2009): Glacial Isostatic Adjustment over Antarctica from combined ICESat and GRACE satellite data. In: *Earth and Planetary Science Letters* 288 (3-4), p. 516–523. DOI: 10.1016/j.epsl.2009.10.013.

Rummel, R. (1979): Determination of short-wavelength components of the gravity field from satellite-to-satellite tracking or satellite gradiometry. An attempt to an identification of problem areas. In: *manuscripta geodaetica* 4 (2), p. 107–148.

Rummel, R. (1986): Satellite gradiometry. In: H. Sünkel (Ed.): Mathematical and Numerical Techniques in Physical Geodesy, Vol. 7. Berlin/Heidelberg: Springer-Verlag (Lecture Notes in Earth Sciences), p. 317–363.

Rummel, R.; Yi, W.; Stummer, C. (2011): GOCE gravitational gradiometry. In: *J Geod* 85 (11), p. 777–790. DOI: 10.1007/s00190-011-0500-0.

Sasgen, I.; Martinec, Z.; Fleming, K. (2006): Wiener optimal filtering of GRACE data. In: *Stud Geophys Geod* 50 (4), p. 499–508. DOI: 10.1007/s11200-006-0031-y.

Sasgen, I.; Martín-Español, A.; Horvath, A.; Klemann, V.; Petrie. E.J.; Wouters, B.; Horwath, M.; Pail, R.; Bamber, J. L.; Clarke, P. J.; Konrad, H.; Drinkwater, M. R. (submitted 2016a): Estimate of regional glacial isostatic adjustment in Antarctica considering a lateral varying Earth structure. Part II: data combination and impact analysis (ESA STSE Project REGINA). In: *Geophysical Journal International*.

Sasgen, I.; Martín-Español, A.; Horvath, A.; Klemann, V.; Petrie. E.J.; Wouters, B.; Horwath, M.; Pail, R.; Bamber, J. L.; Clarke, P. J.; Konrad, H.; Wilson, T.; Drinkwater, M. R. (submitted 2016b): Estimation of glacial isostatic adjustment in Antarctica considering a laterally varying Earth structure. Part I: data analysis and viscoelastic modelling (ESA STSE Project REGINA). In: *Geophysical Journal International*.

Savcenko, R. and Bosch, W. (2008): EOT08a - empirical ocean tide model from multi-mission satellite altimetry. Hg. v. DGFI. München, Germany (DGFI Report, 81).

Savcenko, R. and Bosch, W. (2012): EOT11a - empirical ocean tide model from multi-mission satellite altimetry. Deutsches Geodätisches Forschungsinstitut. München, Germany (Report, 89).

Savitzky, A. and Golay, M. (1964): Smoothing and Differentiation of Data by Simplified Least Squares Procedures. In: *Anal. Chem.* 36 (8), p. 1627–1639. DOI: 10.1021/ac60214a047.

Schrama, E. J. O.; Wouters, B.; Lavallée, D. (2007): Signal and noise in Gravity Recovery and Climate Experiment (GRACE) observed surface mass variations. In: *J. Geophys. Res.* 112 (B8). DOI: 10.1029/2006JB004882.

Schuh, W.-D. (1996): Tailored numerical solution strategies for the global determination of the earth's gravity field. Dissertation. Techn. Univ. Graz, Graz. Inst. für Theoret. Geodäsie.

Schuh, W.-D. (2003): The Processing of Band-Limited Measurements; Filtering Techniques in the Least Squares Context and in the Presence of Data Gaps. In: *Space Science Reviews* 108 (1/2), p. 67–78. DOI: 10.1023/A:1026121814042.

Seo, K.-W.; Wilson, C. R.; Chen, J.; Waliser, D. E. (2008): GRACE's spatial aliasing error. In: *Geophysical Journal International* 172 (1), p. 41–48. DOI: 10.1111/j.1365-246X.2007.03611.x.

Shannon, C. E. (1949): Communication in the Presence of Noise. In: *Proc. IRE* 37 (1), p. 10–21. DOI: 10.1109/JRPROC.1949.232969.

Sheard, B. S.; Heinzel, G.; Danzmann, K.; Shaddock, D. A.; Klipstein, W. M.; Folkner, W. M. (2012): Intersatellite laser ranging instrument for the GRACE follow-on mission. In: *J Geod* 86 (12), p. 1083–1095. DOI: 10.1007/s00190-012-0566-3.

Shepherd, A.; Ivins, E. R.; A, G.; Barletta, V. R.; Bentley, M. J.; Bettadpur, S.; Briggs, K. H.; Bromwich, D. H.; Forsberg, R.; Galin, N.; Horwath, M.; Jacobs, S.; Joughin, I.; King, M. A.; Lenaerts, J. T. M.; Li, J.; Ligtenberg, S. R. M.; Luthcke, S. B.; McMillan, M.; Meister, R.; Milne, G. A.; Mouginot, J.; Muir, A.; Nicolas, J. P.; Paden, J.; Payne, A. J.; Pritchard, H.; Rignot, E.; Rott, H.; Sørensen, L. S.; Scambos, T. A.; Scheuchl, B.; Schrama, E. J. O.; Smith, B.; Sundal, A. V.; van Angelen, J. H; van de Berg, W. J; van den Broeke, M. R.; Vaughan, D. G.; Velicogna, I.; Wahr, J.; Whitehouse, P. L.; Wingham, D. J.; Yi, D.; Young, D.; Zwally, H. J. (2012): A reconciled estimate of ice-sheet mass balance. In: *Science (New York, N.Y.)* 338 (6111), p. 1183–1189. DOI: 10.1126/science.1228102.

Siemes, C. (2008): Digital Filtering Algorithms for Decorrelation Within Large Least Squares Problems. Dissertation. Universität Bonn, Bonn. Institut für Geodäsie und Geoinformation.

Sneeuw, N. (2000): A semi-analytical approach to gravity field analysis from satellite observations. München: Verl. der Bayer. Akad. der Wissenschaften (Deutsche Geodätische Kommission bei der Bayerischen Akademie der Wissenschaften : Reihe C, Dissertationen, 527).

Stetter, M. (2012): Stochastische Modellierung von GOCE-Gradiometriebeobachtungen mittels digitaler Filter. Master thesis. TU München, München. Institut für Astronomische und Physikalische Geodäsie.

Stuhne, G. R. and Peltier, W. R. (2015): Reconciling the ICE-6G_C reconstruction of glacial chronology with ice sheet dynamics: The cases of Greenland and Antarctica. In: *J. Geophys. Res. Earth Surf.* 120 (9), p. 1841–1865. DOI: 10.1002/2015JF003580.

Swenson, S. C.; Chambers, D. P.; Wahr, J. (2008): Estimating geocenter variations from a combination of GRACE and ocean model output. In: *J. Geophys. Res.* 113 (B8). DOI: 10.1029/2007JB005338.

Swenson, S. C. and Wahr, J. (2002): Methods for inferring regional surface-mass anomalies from Gravity Recovery and Climate Experiment (GRACE) measurements of time-variable gravity. In: *J. Geophys. Res.* 107 (B9), p. ETG 3-1. DOI: 10.1029/2001JB000576.

Swenson, S. C. and Wahr, J. (2006): Post-processing removal of correlated errors in GRACE data. In: *Geophys. Res. Lett.* 33 (8). DOI: 10.1029/2005GL025285.

Swenson, S. C.; Wahr, J.; Milly, P. C. D. (2003): Estimated accuracies of regional water storage variations inferred from the Gravity Recovery and Climate Experiment (GRACE). In: *Water Resour. Res.* 39 (8). DOI: 10.1029/2002WR001808.

Tapley, B. D.; Bettadpur, S.; Watkins, M.; Reigber, C. (2004): The gravity recovery and climate experiment: Mission overview and early results. In: *Geophys. Res. Lett.* 31 (9). DOI: 10.1029/2004GL019920.

Thompson, P. F.; Bettadpur, S. V.; Tapley, B. D. (2004): Impact of short period, non-tidal, temporal mass variability on GRACE gravity estimates. In: *Geophys. Res. Lett.* 31 (6). DOI: 10.1029/2003GL019285.

Tikhonov, A. N.; Arsenin, V. IÃˇ(1977): Solutions of ill-posed problems. Washington, New York: Winston; Distributed solely by Halsted Press (Scripta series in mathematics).

Tiwari, V. M.; Wahr, J.; Swenson, S. (2009): Dwindling groundwater resources in northern India, from satellite gravity observations. In: *Geophys. Res. Lett.* 36 (18). DOI: 10.1029/2009GL039401.

Torge, W.; Müller, J. (2012): Geodesy. 4th ed. Berlin, Boston: De Gruyter (De Gruyter textbook).

Trenberth, K. E. (2013): El Niño Southern Oscillation (ENSO). In: *Reference Module in Earth Systems and Environmental Sciences. DOI:* 10.1016/B978-0-12-409548-9.04082-3.

Turner, J. (2004): The El Niño–southern oscillation and Antarctica. In: *Int. J. Climatol.* 24 (1), p. 1–31. DOI: 10.1002/joc.965.

USGS (2016): USGS Water Data for USA. National Water Information System. U.S. Geological Survey. Online available: http://waterdata.usgs.gov/nwis, last accessed 09.11.2016.

van der Wal, W.; Whitehouse, P.; Schrama, E. (2015): Effect of GIA models with 3D composite mantle viscosity on GRACE mass balance estimates for Antarctica. In: *Earth and Planetary Science Letters* 414, p. 134–143. DOI: 10.1016/j.epsl.2015.01.001.

Velicogna, I.; Sutterley, T. C.; van den Broeke, M. R. (2014): Regional acceleration in ice mass loss from Greenland and Antarctica using GRACE time-variable gravity data. In: *Geophys. Res. Lett.* 41 (22), p. 8130–8137. DOI: 10.1002/2014GL061052.

Vishwakarma, D. B.; Devaraju, B.; Sneeuw, N. (2016): Minimizing the effects of filtering on catchment scale GRACE solutions. In: *Water Resour. Res.* 52 (8), p. 5868–5890. DOI: 10.1002/2016WR018960.

Visser, P.; Sneeuw, N.; Reubelt, T.; Losch, M.; van Dam, T. (2010): Space-borne gravimetric satellite constellations and ocean tides: aliasing effects. In: *Geophysical Journal International* 181 (2), p. 789–805. DOI: 10.1111/j.1365-246X.2010.04557.x.

Vörösmarty, C. J.; Fekete, B. M.; Meybeck, M.; Lammers, R. B. (2000): Global system of rivers: Its role in organizing continental land mass and defining land-to-ocean linkages. In: *Global Biogeochem. Cycles* 14 (2), p. 599–621. DOI: 10.1029/1999GB900092.

Wahr, J.; Molenaar, M.; Bryan, F. (1998): Time variability of the Earth's gravity field: Hydrological and oceanic effects and their possible detection using GRACE. In: *J. Geophys. Res.* 103 (B12), p. 30205–30229. DOI: 10.1029/98JB02844.

Wahr, J.; Swenson, S. C.; Velicogna, I. (2006): Accuracy of GRACE mass estimates. In: *Geophys. Res. Lett.* 33 (6). DOI: 10.1029/2005GL025305.

Wang, L.; Shum, C. K.; Simons, F. J.; Tapley, B. D.; Dai, C. (2012): Coseismic and postseismic deformation of the 2011 Tohoku-Oki earthquake constrained by GRACE gravimetry. In: *Geophys. Res. Lett.* 39 (7). DOI: 10.1029/2012GL051104.

Watkins, M.; Wiese, D. N.; Yuan, D.-N.; Boening, C.; Landerer, F. W. (2015): Improved methods for observing Earth's time variable mass distribution with GRACE using spherical cap mascons. In: *J. Geophys. Res. Solid Earth* 120 (4), p. 2648–2671. DOI: 10.1002/2014JB011547.

Weigelt, M.; Sneeuw, N.; Schrama, E. J. O.; Visser, P. N. A. M. (2013): An improved sampling rule for mapping geopotential functions of a planet from a near polar orbit. In: *J Geod* 87 (2), p. 127–142. DOI: 10.1007/s00190-012-0585-0.

Werth, S.; Güntner, A.; Schmidt, R.; Kusche, J. (2009): Evaluation of GRACE filter tools from a hydrological perspective. In: *Geophysical Journal International* 179 (3), p. 1499–1515. DOI: 10.1111/j.1365-246X.2009.04355.x.

Whitehouse, P. L.; Bentley, M. J.; Milne, G. A.; King, M. A.; Thomas, I. D. (2012): A new glacial isostatic adjustment model for Antarctica: calibrated and tested using observations of relative sea-level change and present-day uplift rates. In: *Geophysical Journal International* 190 (3), p. 1464–1482. DOI: 10.1111/j.1365-246X.2012.05557.x.

Wingham, D. J.; Shepherd, A.; Muir, A.; Marshall, G. J. (2006): Mass balance of the Antarctic ice sheet. In: *Philosophical transactions. Series A, Mathematical, physical, and engineering sciences* 364 (1844), p. 1627–1635. DOI: 10.1098/rsta.2006.1792.

Wouters, B. and Schrama, E. (2007): Improved accuracy of GRACE gravity solutions through empirical orthogonal function filtering of spherical harmonics. In: *Geophys. Res. Lett.* 34 (23). DOI: 10.1029/2007GL032098.

Xu, P. (1992): The value of minimum norm estimation of geopotential fields. In: *Geophysical Journal International* 111 (1), p. 170–178. DOI: 10.1111/j.1365-246X.1992.tb00563.x.

Xu, P. and Rummel, R. (1994): A Simulation Study of Smoothness Methods In Recovery of Regional Gravity Fields. In: *Geophysical Journal International* 117 (2), p. 472–486. DOI: 10.1111/j.1365-246X.1994.tb03945.x.

Yoder, C. F.; Williams, J. G.; Dickey, J. O.; Schutz, B. E.; Eanes, R. J.; Tapley, B. D. (1983): Secular variation of Earth's gravitational harmonic J2 coefficient from Lageos and nontidal acceleration of Earth rotation. In: *Nature* 303 (5920), p. 757–762. DOI: 10.1038/303757a0.

Zehentner, N. and Mayer-Gürr, T. (2016): Precise orbit determination based on raw GPS measurements. In: *J Geod* 90 (3), p. 275–286. DOI: 10.1007/s00190-015-0872-7.

Zhang, Z.-Z; Chao, B. F.; Lu, Y.; Hsu, H.-T. (2009): An effective filtering for GRACE time-variable gravity: Fan filter. In: *Geophys. Res. Lett.* 36 (17). DOI: 10.1029/2009GL039459.

Zwally, H. J. and Giovinetto, M. B. (2011): Overview and Assessment of Antarctic Ice-Sheet Mass Balance Estimates: 1992–2009. In: *Surv Geophys* 32 (4-5), p. 351–376. DOI: 10.1007/s10712-011-9123-5.

Zwally, H. J.; Schutz, B.; Abdalati, W.; Abshire, J.; Bentley, C.; Brenner, A.; Bufton, J.; Dezio, J.; Hancock, D.; Harding, D.; Herring, T.; Minster, B.; Quinn, K.; Palm, S.; Spinhirne, J.; Thomas, R. (2002): ICESat's laser measurements of polar ice, atmosphere, ocean, and land. In: *Journal of Geodynamics* 34 (3-4), p. 405–445. DOI: 10.1016/S0264-3707(02)00042-X.

Zwally, J.; Giovinetto, M.; Beckley M.; Saba, J. (2012): Antarctic and Greenland Drainage Systems. GSFC Cryospheric Sciences Laboratory. USA. Online available: http://icesat4.gsfc.nasa.gov/cryo_data/ant_grn_drainage_systems.php, last accessed 21.10.2016.